Transactions of the ASME

EDITORIAL STAFF
Editor, J. J. JAKLITSCH, JR.
Production Editor, CORNELIA MONAHAN
Editorial Production Assistant, BETH DARCHI

FLUIDS ENGINEERING DIVISION
Technical Editor
FRANK M. WHITE (1981)
Executive Secretary
L. T. NELSON (1981)
Calendar Editor
M. F. ACKERSON

Associate Editors
Fluid Machinery
H. JAMES HERRING (1981)
BUDUGUR LAKSHMINARAYANA (1983)
Fluid Measurements
BHARATAN R. PATEL (1983)
Fluid Mechanics
RICHARD A. BAJURA (1980)
OWEN M. GRIFFIN (1981)
BRIAN E. LAUNDER (1981)
WILLIAM G. TIEDERMAN (1981)
Fluid Transients
DAVID C. WIGGERT (1980)
Polyphase Flow
CLAYTON T. CROWE (1980)
ROBERT L. STREET (1981)
Review Articles
KENNETH E. HICKMAN (1981)

FOREIGN CORRESPONDENTS
Europe and Russia
JACQUES CHAUVIN
Europe and Russia
JOHN H. HORLOCK
India and Middle East
ARUN PRASAD
Japan and China
YASUTOSHI SENOO

POLICY BOARD, COMMUNICATIONS
Chairman and Vice-President
I. BERMAN

Members-at-Large
W. J. WARREN
J. E. ORTLOFF
M. J. RABINS
J. W. LOCKE

Policy Board Representiatives
Basic Engineering, FRED LANDIS
General Engineering, C. F. PHILLIPS
Industry, J. E. ORTLOFF
Power, R. E. REDER
Research, G. P. COOPER
Codes and Stds., L. L. ELDER
Nom. Com. Rep., J. W. LOCKE

Business Staff
345 East 47th St.
New York, N. Y. 10017
(212) 644-7789
Mng. Dir., Publ., C. O. SANDERSON

OFFICERS OF THE ASME
President, CHARLES E. JONES
Exec. Director & Sec'y, ROGERS B. FINCH
Secretary and Treasurer, ROBERT A. BENNETT

The Journal of FLUIDS ENGINEERING (USPS 278-480) is edited and published quarterly at the offices of The American Society of Mechanical Engineers, United Engineering Center, 345 E. 47th St., New York, N. Y. 10017. Cable Address, "Mechaneer," New York.
Second-class postage paid at New York,
CHANGES OF ADDRESS must be received at Society headquarters seven weeks before they are to be effective. Please send old label and new address.
PRICES: To members, $30.00, annually: to nonmembers, $60.00. Single copies, $20.00 each. Add $5.00 for postage to countries outside the United States and Canada.
STATEMENT from By-Laws. The Society shall not be responsible for statements or opinions advanced in papers or . . . printed in its publications (B13, Par. 4).

INDEXED by the Engineering Index, Inc.

Journal of Fluids Engineering

Published Quarterly by The American Society of Mechanical Engineers

VOLUME 102 • NUMBER 4 • DECEMBER 1980

394 Obituary

396 Editorial

397 Foreign Report

398 Fluids Engineering Calendar

402 An Axial Flow Research Compressor Facility Designed for Flow Measurement in Rotor Passages
B. Lakshminarayana

412 A Laser-Two-Focus (L2F) Velocimeter for Automatic Flow Vector Measurements in the Rotating Components of Turbomachines
R. Schodl

420 Velocity and Pressure Distributions in the Impeller Passages of Centrifugal Pumps
M. Murakami, K. Kikuyama, and E. Asakura

427 System to Measure the Pressure Distribution on Fan Aerofoil Surfaces During Flutter Conditions
John W. H. Chivers

433 Supercaviting Cavity Observations by Means of Laser Velocimeter (80-WA/FE-5)
R. Oba, T. Ikohagi, and S. Yasu

441 Theoretical Prediction of Onset of Horizontal Slug Flow (80-WA/FE-6)
Kaichiro Mishima and Mamoru Ishii

446 A Theoretical Study on Air Bubble Motion in a Centrifugal Pump Impeller (80-WA/FE-3)
Kiyoshi Minemura and Mitsukiyo Murakami

456 Flow Prediction in Rotating Ducts Using Coriolis-Modified Turbulance Models (80-WA/FE-1)
J. H. G. Howard, S. V. Patankar, and R. M. Bordynuik

462 Numerical Analysis of Turbulent Wakes of Turbomachinery Rotor Blades
C. Hah and B. Lakshminarayana

473 Rotational Inviscid Flow in a Variable Area Annulus, Pipe or Channel (80-WA/FE-14)
B. R. Munson

478 The Influence of Swirl on the Flow Characteristics of a Reciprocating Piston-Cylinder Assembly (80-WA/FE-8)
A. Morse, J. H. Whitelaw, and M. Yianneskis

481 Two Aspects of Cavitation Damage in the Incubation Zone: Scaling by Energy Considerations and Leading Edge Damage
D. R. Stinebring, J. William Holl, and Roger E. A. Arndt

486 Aerodynamic Performance of a Centrifugal Compressor With Vaned Diffusers
Y. Yoshinaga, I. Gyobu, H. Mishina, F. Koseki, and H. Nishida

494 Leading Edge Separation From a Blunt Plate at Low Reynolds Number
J. C. Lane and R. I. Loehrke

497 Derivation of Kline Line a-a for Straight Walled Diffusers From Stratford's Separation Criterion
S. D. Savkar

499 A Device for Measuring Very Low Pressure Differences
Takeo Nakagawa

502 The Linear Instability Due to the Compressible Crossflow on a Swept Wing
S. G. Lekoudis

510 A Theoretical Model for the Transverse Impingement of Free Jets at Low Reynolds Numbers
R. Winton

519 Discussion on Previously Published Papers

525 Book Reviews

Announcements and Special Notices

393 ASME Prior Publication Policy

393 Submission of Papers

393 Statement of Experimental Uncertainty

432 Call for Papers – 1982 Spring Meeting

440 ASME Announces the Sixth ASME Freeman Scholar Program

477 Call for Papers – 1981 Joint ASCE-ASME Mechanics Conference

493 Call for Papers – International Symposium

527 Call for Papers – 1982 Spring Meeting

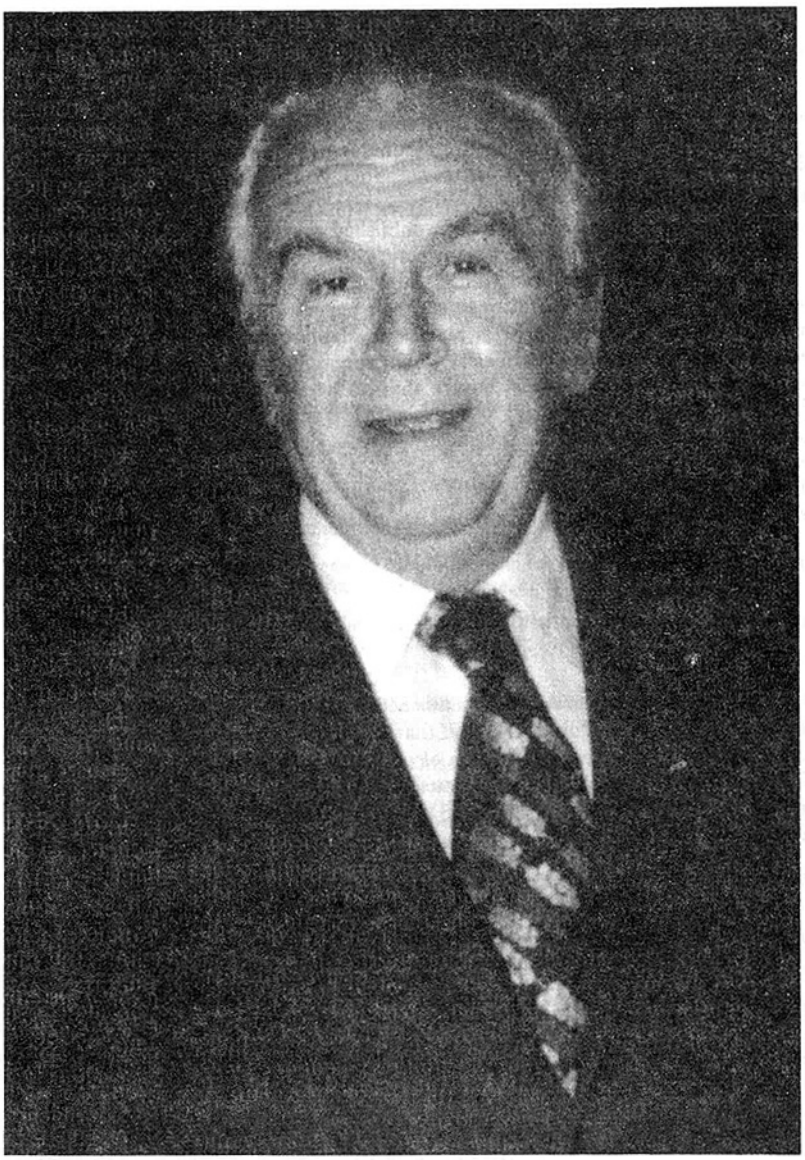

LESLIE S. G. KOVASZNAY

Leslie Kovasznay died suddenly on 17 April 1980 at the age of 62. He was a world leader in turbulent flow research, best known for novel experimental techniques and crucial measurements. He also contributed significantly to theory and to technology.

Born in Budapest, 14 April 1918, Kovasznay earned his Dr. Tech. Sci. at the Royal Hungarian Institute of Technology in 1943, in the laboratory of E. Abody-Anderlik. After five years on that faculty, 1941–1946, he spent a year at Cambridge University's Cavendish Lab with G. I. Taylor, then joined the new Aeronautics Department organized by F. H. Clauser at The Johns Hopkins University, where he remained for more than 31 years. In December 1978 he resigned to become Professor of Mechanical Engineering at The University of Houston.

He was a Fellow of the American Physical Society and the American Academy of Arts and Sciences, a Senior Member of the Institute of Electrical and Electronics Engineers, and a Member of the American Institute of Aeronautics and Astronautics, as well as Tau Beta Pi, Sigma Xi, and Phi Beta Kappa.

Shortly after his arrival at Johns Hopkins, he became a consultant for the National Bureau of Standards, for which he designed an improved hot-wire anemometry electronic system. As consultant for the Ballistics Research Lab, Aberdeen Proving Ground, he devised a condenser configuration which suppressed the troublesome "ringing" of micro-second spark discharge circuits used for short duration photographs. Meanwhile, at Johns Hopkins he developed the first basic procedures for hot-wire anemometers in supersonic flows, procedures still in use. He was also one of the first to apply the statistical "information theory" of Claude Shannon to photographic measurements, with the film graininess as the noise.

Creative electronic image processing work, much of it with H.M. Joseph, earned them the AIEE (now IEEE) Mid-Atlantic Region First Prize for 1954.

Kovasznay's other advances in technique included generalization (with M. S. Uberoi) of the hot-wire "length correction" to any 3-dimensional, non-uniform sensing device, invention of a hot-wire array whose output is streamwise vorticity, design of a modified hot-wire microphone for measuring suface pressure fluctuations (with C.J. Remenyik), several other procedures for hot-wire measurements of turbulent velocities (with R. Chevray, V. Kibens, R. Blackwelder, A. Favre, R. Dumas, L. Fulachier, J.

P. Gaviglio, F. Ali, and others). Conditionally sampled data were the hallmark of his later experiments, not only in normally intermittent turbulent regions, but also in boundary layer transition to turbulence and in turbulent "spots" (with H. Komoda and B. R. Vasudeva), and in a "puffing" jet (with H. Fujita and K. Oshima). In the 1970's he focussed also on aerodynamic sound generation and interactions of sound and turbulence (with Fujita and C. M. Ho).

Kovasznay's theoretical fluid dynamic contributions relevant to turbulence began with the simplest plausible turbulence spectrum, and included categorization of gas dynamic fluctuations into vorticity, sound, and entropy "modes", and the analysis of the lowest order nonlinear interactions (with B. T. Chu). After work on laminar instability (with W. O. Criminale) and magneto-fluid dynamic fluctuations (with M. M. Stanisic), he introduced a practical turbulent shear equation closure model (with V. Nee). That was followed by partially deterministic turbulence models (with R. Lee and R. Takaki).

He was the author or co-author of more than eighty papers published in over thirty different periodicals.

In his prepared lectures, Kovasznay was enthusiastic and illuminating, and at Johns Hopkins he offered courses in both theoretical and experimental fluid mechanics. His outstanding effort was a sophomore-level course on experimental procedures in engineering science. Its infusion with the research spirit contrasted sharply with most elementary lab courses.

He was a premier teacher of research students, and a lively listener to anyone seeking advice, often asking interesting new questions. This was one of many reasons that he was a welcome visitor at fluid dynamics research centers all over the world.

In fact, travel was one of Kovasznay's enthusiasms. He rarely declined an invitation to lecture at another university or a conference, and made several extended visits to France and to Japan, In France his deepest involvement was with A. Favre and his Institut de Mécanique Statistique de la Turbulence, Université d'Aix-Marseille. One principal result was their 1976 monograph on turbulent flow, co-authored with R. Dumas, J. Gaviglio, and M. Coantic.

In Japan his initial host and guide was I. Tani of the University of Tokyo, and he eventually collaborated with researchers at several universities, especially during two years as scientific officer at the new ONR Tokyo liaison group 1975–1977. He was awarded honorary doctorates by Aix-Marseille University in 1968 and Nihon University in 1977. As early as 1956, he had been awarded a Medal of the Université Libre of Brussels.

He was a frequent consultant to industries and governmental agencies, and played a major role in organizing international symposia. His engineering breadth is illustrated by the fact that aerospace, electronic and chemical companies sought his counsel. The governmental agencies included those of the United States, Canada and France.

At the University of Houston, his new colleague A.K.M.F. Hussain had already developed a lively turbulence lab, and Kovasznay was optimistically designing a neighboring one.

He was gregarious and affable, a raconteur, a man who treasured friends all over the world. He took his hobbies seriously, and was a collector of bizzare and entertaining information, particularly about human foibles and appetites of all kinds, a gourmet cook, and a creative artist in several media.

Leslie Kovasznay was a fully plugged-in citizen of world fluid dynamics. He is already seriously missed.

S. CORRSIN

Journal of Fluids Engineering

Editorial

Chicago is a fine place for a Winter Annual Meeting. Indeed, contrary to opinions ascribed to Dave Winfield, Chicago is a splendid city well worthy of two major league baseball teams. As applied to the particular case of WAM 1980, the hotel and meeting accommodations were excellent, as were the technical sessions themselves.

The Fluids Engineering Division packed a lot into its fourteen allotted sessions. There were four major symposia and five additional individual sessions. Some seventy papers were sponsored by the division - not that we went to them all, but the attendees we spoke to certainly seemed to enjoy themselves both technically and socially.

Perhaps most timely and popular was the Symposium on Small Hydropower Fluid Machinery, with fifteen papers in four sessions plus a panel discussion. It was SRO even at the improbable 5:30–7:30 PM session, with 250 people crowded into every session. Although most of the papers were either case studies or reviews of current technology, interest remained high throughout. This is an active field of fluids engineering, with thousands of megawatts of undeveloped or abandoned low-head sites waiting for us throughout the U.S. and other contries. Of particular interest were two broad-brush papers: a selection and optimization review by R. K. Fisher, and an economic overview by W. Nuessli, et al. If site work already exists, as in the restoration of an abandoned plant, the economic prospects are glittering and unchallenged. If one must build from scratch, the chief benefit is most likely inflation: paying off construction costs with the cheap dollars of the 1980's and 1990's. No one was betting against inflation. These papers may be found in bound volume # G-00180.

The Symposium on Vortex Flows presented 17 papers in three sessions: confined flows, radial and axial flows, and external flows. Those of us whose education in vortex motion begins and ends with the law of Biot and Savart would do well to order bound volume G-00181. There's a whole new technology out there: vortex breakdown, merging, coherent structures, vortimeters, vortex diodes, cascading, shedding. A highlight for us was the keynote address by O. M. Griffin on vortex structures in the atmosphere, the oceans, and the laboratory.

The Symposium on Basic Mechanisms in Two Phase Flow and Heat Transfer was cosponsored by the Heat-Transfer Division. There were 14 papers in two sessions, all printed in bound volume G-00179. Emphasis was upon interfacial phenomena, wetting effects, and our growing ability to make theoretical predictions of these complex flows.

The fourth symposium was Flow and Heat Transfer Processes in Recirculating Flows, also cosponsored by HTD. There were 12 papers in two sessions which make up bound volume G-00186. Basically, a recirculating flow usually contains a large separation bubble, perhaps due to an abrupt expansion or a backward-facing step. When we were young we drew sketches on the board, guided by Prandtl's movies. There was no theory: we measured what we could and visualized the rest. Now, as this symposium attests, there is much new theory and experiment, both steady and unsteady. A highlight for us was the new probe described by R. V. Westphal, et al., which measures instantaneous reversing wall shear in a recirculation zone. After so many decades, we seem to be very near the long-awaited coherent analysis of separating flows.

This year's annual FED winter party was rounded off by five individual sessions: one on two-phase flow, two on experimental methods, one on analytical fluid mechanics, and one in fluid machinery current interest topics.

Needless to say, it was a fine meeting which made it almost impossible to tear oneself away from a hotel filled with such technical brilliance. We found time only for a whirlwind tour of the smashing Art Institute of Chicago, plus a 46-second rocket shot elevator ride to the 96th floor of the John Hancock building at dusk. The beautiful glassed-in bar at the top is an absolute necessity before one can contemplate riding back down again.

For 1981 there are six symposia approved by our division, as follows:

I. Spring 1981 FED Meeting, Boulder, Colorado, June 22–24:

1. Fluid Mechanics of Combustion.
2. Cavitation Erosion in Fluid Systems.
3. Transient Fluid-Structure Interaction in Liquid Handling Systems.

II. WAM 1981, Washington, D.C., November 15–20:

1. Fluid-Structural Interaction in Turbomachinery.
2. Computers in Flow Predictions and Fluid Dynamic Experiments.
3. Materials of Construction of Fluid Machinery.

Further details can be found in the calls for papers published earlier and in the Calander of the present issue. In the March issue we will print a complete list of all approved future symposia for the Fluids Engineering Division.

FRANK M. WHITE
Technical Editor

Journal of Fluids Engineering

Foreign Report

IHAR Tenth Symposium of the International Association for Hydraulic Research (IAHR), Section on Hydraulic Machinery, Equipment and Cavitation was held in Tokyo from September 28 to October 2, 1980. There were 116 overseas participants from 21 countries along with 180 participants from Japan. The academic part of the symposium consisted of three general lectures and 16 technical sessions where 61 technical papers were presented. No sessions were scheduled in parallel so that everybody could attend all sessions if they wished to do so. In each session the co-chairman summarized the papers in the session and each author made a short supplementary speech. Then active discussions followed.

The breakdown of the papers presented was as follows: Twenty-four papers were related to cavitation, out of which 14 papers handled basic cavitation problems and cavitating flow, and the remaining 10 papers dealt with cavitation of hydrofoils and pumps. Fourteen dealt with flow in pumps which included three papers for flow in volute casing and 11 papers for flow in impellers. There were 11 papers dealing with hydraulic turbines, among which there were 6 papers on Francis-type, 2 papers on Kaplan and Axial-flow type, and one paper each on Pelton, Deriaz-type and Balb type. There were 12 papers which dealt with the operation of hydraulic power plants including four papers on vibration and surging of the system. Among the 23 papers related to hydraulic turbines and hydraulic power plant mentioned above, and about one half of them dealt with pump turbines.

All 61 papers are bounded in Volume 1 of the proceedings. The summary reports made by the co-chairmen, and the supplementary notes delivered by each author will be published in Volume 2 together with the texts of the three general lectures. For information concerning purchasing of proceedings, write to: Turbomachinery Society of Japan, 3-18, Nishikanda 2-chrome, Chiyodaku, Tokyo 101, Japan.

YASUTOSHI SENOO

An Axial Flow Research Compressor Facility Designed for Flow Measurement in Rotor Passages

B. Lakshminarayana
Director of Computational Fluid Dynamics Program and Professor of Aeorspace Engineering, The Pennsylvania State Uvinersity, University Park, Pa. 16802

An axial-flow research compressor facility, which is designed for relative flow measurement, is described in this paper. The facility has a rotating-probe traverse mechanism which is capable of traversing hot-wire, pitot and other probes at 0.09 deg intervals across the rotor blade passage. The data transmission system includes rotating transducers, pressure transfer device, ten-channel mercury slip-ring unit, scanivalve, etc. The instrumentation includes on-line data processing capability. A brief description of probes used as well as some typical data on the rotor blade static pressure, rotor endwall flow, and rotor wake characteristics are given in the paper.

Introduction

The design and analysis of the next generation of turbomachinery will require a thorough knowledge of the three-dimensional turbulent flows in the rotor passages. A detailed understanding of the wall and rotor blade boundary layers, leakage and secondary flows, the rotor blade wake characteristics, as well as the propagation of inlet distortion and stator wakes through rotor passages, the inception of stall and surge, and the sources of flow unsteadiness and noise in rotor passages will be necessary. There is also an urgent need for three-dimensional flow data inside the rotor passages to provide verification of computer codes for three-dimensional analyses and design procedures currently under development.

Most of the measurements carried out hitherto are confined to either the rotor exit flow or flow through stationary passages (IGV, cascade, stator). Hence, there is a great need for a facility where the relative flow inside the blade passages can be measured. With this as an objective, a research compressor facility having unique probe traversing mechanisms and a data transmission system was constructed at The Pennsylvania State University. Design of some of these devices are based on our earlier experiences with the inducer facility [1].

The research compressor facility, as described in this paper, has provision for measurements to be taken in a relative frame of reference. This capability is achieved by means of a probe traversing mechanism rotating with the rotor. The probe is actuated across the passage, both inside and at the exit of the rotor blade row, while the rotor is in motion. The device is specifically designed for probing thin shear layers that are present in annulus, hub, and blade boundary layers and wakes, as well as for measuring the transport of IGV and stator wakes across the rotor passage. Some typical data acquired in these areas are presented.

Facility Description and Design Features

The Axial-Flow Research Compressor Facility built at The Pennsylvania State University has provisions, among other things, for carrying out the following measurements:

1. Three-dimensional relative flow measurement (including turbulence intensity and stresses) near the rotor blades, inside the rotor passage, rotor endwalls, entry as well as exit, using a hot wire, pitot probe, and skin friction gauge.
2. Radial-flow survey at the exit and at the inlet of each blade row (IGV, stator) as well as three-dimensional flow in IGV and stator passages.
3. Rotor blade static pressures including one at the blade tip.
4. Rotor flow measurement with inlet distortion and nonsteady flow.

In addition, provision is made for the following:

1. Operation at deep stall as well as at high flow coefficients. This is accomplished by an auxiliary fan and an aerodynamically designed and acoustically treated throttle. The rotor can be operated at various speeds with precise speed control.
2. Testing as a single stage, rotor only, annular cascade, or with differing rotor-stator and rotor-IGV spacing.

The facility is shown in Fig. 1. It consists of an enclosure at the inlet (not shown) made of wire mesh coated with 3.1 mm thick foam and has the dimension 3m × 1.5m × 3 m. This enclosure provides dust-free smooth entry flow to the inlet.

The data transmission system is upstream of the nose cone

Contributed by the Fluids Engineering Division of THE AMERICAN SOCIETY OF MECHANICAL ENGINEERS and presented at the Symposium on Measurement Methods in Rotating Components of Turbomachinery, Gas Turbine and Fluids Engineering Conference, New Orleans, La., March 10-13, 1980. Manuscript received by the Fluids Engineering Division, April 22, 1980.

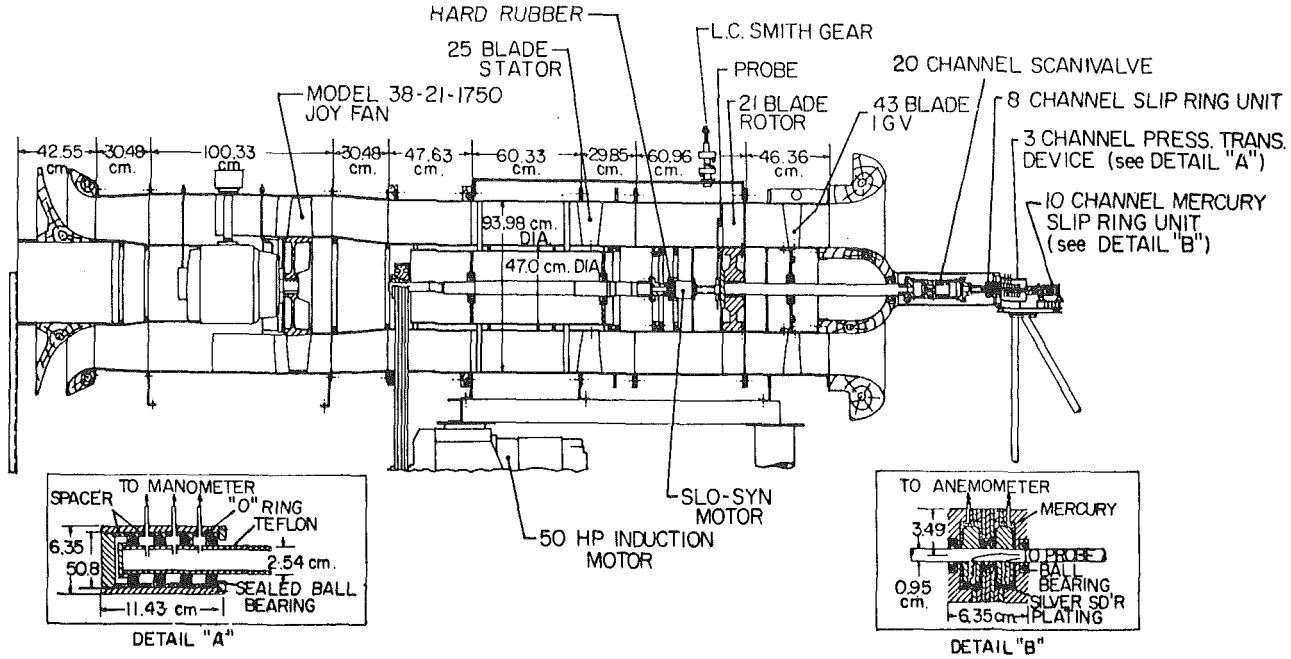

Fig. 1 Axial flow research compressor facility

and is mounted on a tripod stand with vibration dampers. This is followed by an aerodynamically designed inlet. The nose cone and inlet bell mouth are of wooden construction. The hub/annulus wall diameter ratio is 0.5, with diameter of the annulus wall being 0.9398 m. The inlet guide vane, consisting of 43 blades, is followed by the rotor. The rotor presently in operation was designed by Smith [2]. However, the facility can easily be modified to accommodate other rotors. The shaft from the rotor to the data transmission system is hollow to accommodate electrical and pneumatic lines from the probes as well as the traversing mechanism system to be described later. Downstream of the rotor inside the rotating hub, the probe traversing mechanism described in the next section is located. The rotating hub is followed by a stator row with 25 blades.

The drive motor is selected with a view towards future expansion. The motor is of 37.3 kw (50 hp) capacity with eddy current drive and "Dynamatic-Adjusto-Speed" control system. The speed of the motor can be continuously varied from 175 to 1695 rpm, with accurate and precise control. The speed can be held constant to ±1 rpm, even with normal fluctuation in line voltages.

The drive system is followed by an Axial-Flow Fan with variable blade setting for the variation of pressure rise and mass flow. The maximum pressure rise is 12.7 cm of water at a volume flow rate of 18 m^3 per s (38,000 cfm). The purpose of the auxiliary fan is to enable the operation of the compressor at various flow coefficients. This is achieved by controlling the mass flow and compensating for the losses through ducting, IGV, rotor, stator, belt housing, and inlet screens (for possible use later). The fan is of sufficient capacity to enable the operation of the facility as a single-stage compressor, annular cascade, etc.

The facility is terminated downstream with an aerodynamically designed throttle which provides an additional control on the stage operating characteristics. The throttle is lined with perforated metal with fiberglass backing to attenuate the noise from the auxiliary fan. The treatment

Nomenclature

C = chord length
C_p = pressure rise coefficient $(p_2 - p_1)/\frac{1}{2}\rho W_2^2$
E_1, E_2, E_3 = hot-wire voltages (mean)
e_1, e_2, e_3 = fluctuating voltages from hot wires 1, 2, and 3, respectively
p = static pressure
P_0 = aragnation pressure
r, θ, z = radial, tangential, and axial directions, respectively
s, n, r = streamwise, normal, and radial directions, respectively ($s = 0$ at trailing edge)
R = r/r_t
S = blade spacing
T = turbulence intensity (RMS fluctuating velocity normalized by the local total velocity)
U_t = blade tip speed
V = absolute velocity
W = relative velocity
X = chordwise distance from leading edge
$2Y/S$ = tangential distance normalized by half the blade spacing ($Y = 0$ at the wake center)
Z = z/c
ϕ = average flow coefficient $(\bar{V}_z/U_t)$
ψ = mass averaged pressure rise coefficient $\left[(P_{0_2} - P_{0_1})/\frac{1}{2}\rho U_t^2\right]$
η = Euler's efficiency of rotor (actual/Euler head rise)

Subscripts

1, 2 = inlet and outlet to rotor
0 = inlet to guide vane/value at the trailing edge
s, n, r = components in s, n, r directions, respectively
r, θ, z = components in r, θ, z directions, respectively

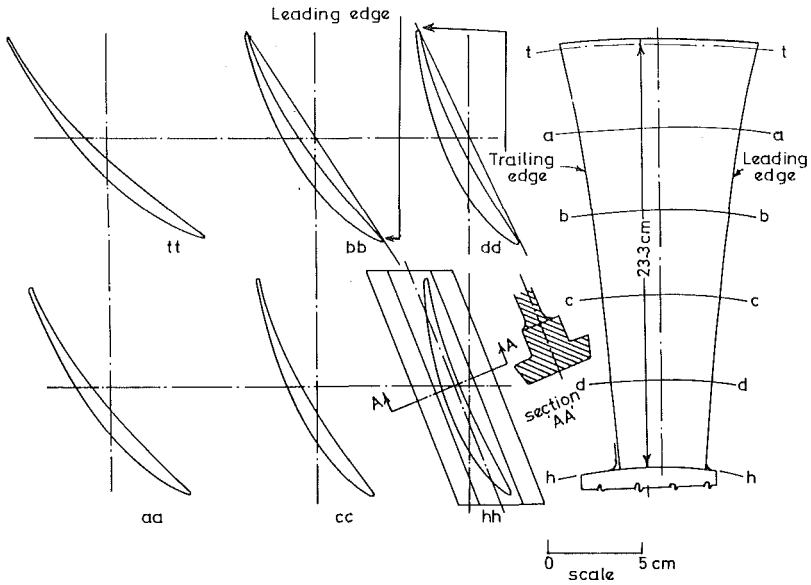

Fig. 2 Rotor blade geometry

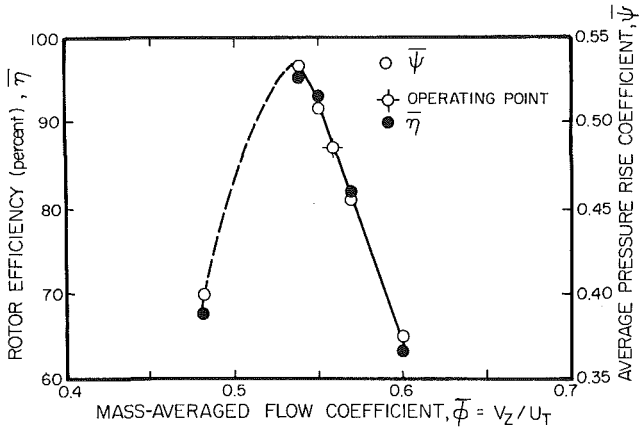

Fig. 3 Overall performance characteristics of rotor

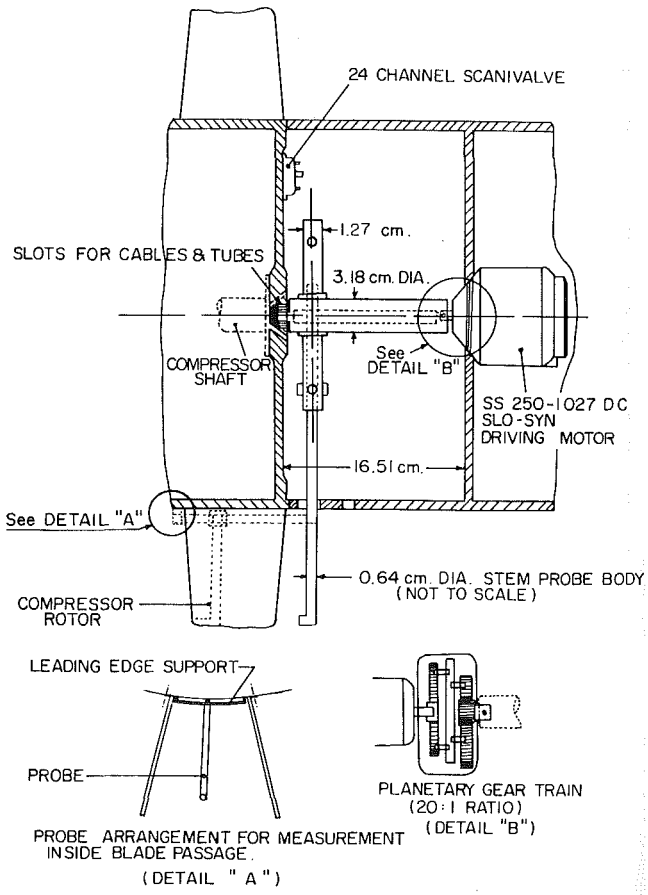

Fig. 4 Rotating probe traverse mechanism – unit 1

provided 6 db reduction in fan noise at the blade-passing frequency.

A detailed vibration and stress analysis of the shaft-rotor-bearing-rotating hub assembly was carried out to determine the maximum bending and torsional stresses encountered. The calculation of the critical speed was based on the finite element program (NASTRAN) developed by NASA. The critical speed was found to be 4900 rpm, well above the design operating speed of the assembly.

The rotor presently has 21 cambered and twisted blades and was designed by Smith [2] using the cascade data of Herrig, et al. [3]. The rotor blade geometry at various locations are shown in Fig. 2 and the overall characteristics in Fig. 3. Good peak efficiencies are exhibited by the rotor. Details of the rotor, IGV, stator blade row can be found in reference [2].

Probe Traversing Mechanisms

Two different units were designed and built at Penn State for traversing a rotating probe (hot wire, pitot, etc.) downstream and inside the blade row in the rotor frame of reference.

Rotating-Probe Traverse Unit 1. The first type of unit is simpler in construction and enables only the tangential traverse of hot wire and other probes during the rotation. A description of this unit follows.

The unit is shown in the compressor assembly (Fig. 1). A detailed drawing is shown in Fig. 4. The unit is designed to provide very accurate movement of the probe in the tangential direction, the radial and axial movement being manual. The mechanism is idealy suited for the blade-to-blade mea-

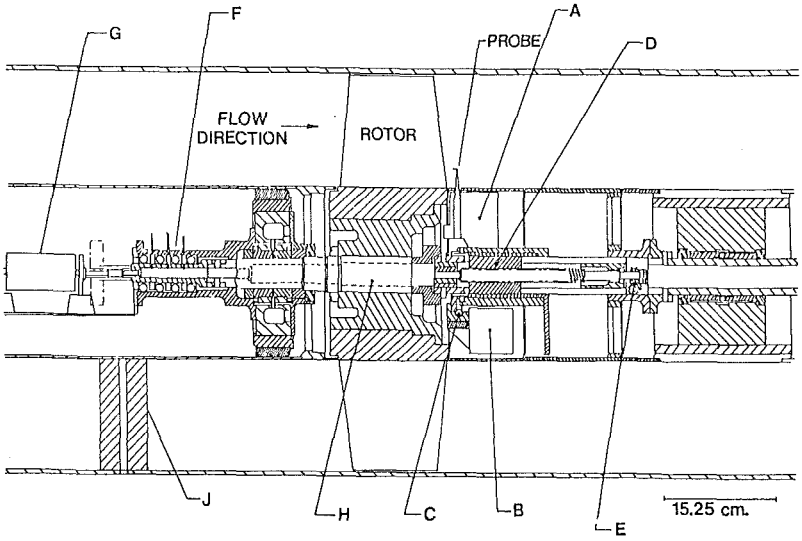

Fig. 5 Rotating probe traverse mechanism – unit 2

surement of the flow properties, including blade boundary layers and wakes as well as end wall flows. Several passages can be probed to determine the non-periodic nature of the flow.

The probe traversing mechanism consists of a Slo-Syn motor of 1.59 Nm (2.25 in-oz) torque driving a 3.18 cm diameter shaft through a 20:1 planetary gear train. The gear train steps down the circumferential stepping from 1.8 deg to 0.09 deg/step. The shaft and the motor are along the axis, thus eliminating the balancing problem. The shaft carries a rider on which the probe is mounted. The mounting block provides two degrees of freedom and is designed to accommodate various types of probes. Rotation about its own axis enables alignment of the probe in any desired yaw direction. The movement in the radial direction can be locked during the rotation. The entire assembly is inside the hub and does not interfere with the flow. The probe traverses in slots on the hub. The motor is powered and controlled by a Slo-Syn preset index in the stationary instrumentation panel through an eight-channel slip-ring unit shown in Fig. 1. The index has provision for variable step size from 1 (0.09 deg) through 1000 (90 deg). It can also be reversed. The traverse gear and the probe are locked except when indexed. Thus, all the circumferential traverse can be accomplished during the rotation.

For measurements inside the passage, the probe length and overhang become long. Hence, the arrangement shown in Fig. 4 was built. The probe is supported at the leading edge as well as the trailing edge of the blade to avoid vibration as well as radial displacement of the probe due to centrifugal forces. The support bracket is fastened to the hub near the blade leading edge. This arrangement enables flow measurement from leading to trailing edge of the blade, passage to passage, and from hub to tip.

The electrical and pneumatic cables from the probes are brought through the rider into the hollow shaft and connected to the data transmission system, shown in Fig. 1, and described later.

A scanivalve assembly with 25 channels, available commercially, is also mounted inside the traverse assembly. The scanivalve assembly enables multipressures (such as blade static or five-hole probes) to be measured consecutively using a single master channel connected to a transducer (rotating) or a pressure transfer device (Fig. 1). Description of the scanivalve assembly is given in reference [4] and will not be repeated here.

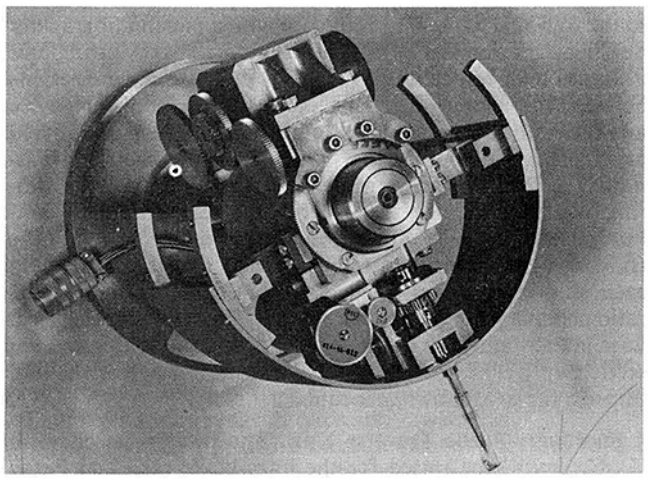

Fig. 6 Photograph of the rotating probe traverse mechanism – unit 2

Rotating-Probe Traverse Unit 2. The second unit built for traversing a rotating probe is shown in Fig. 5. This unit has provision for the rotation of the probe about its own axis as well as the circumferential traverse in the rotating mode. Only the circumferential traverse mode is operational at the present time. This unit was built for the rotor wake measurement at the Axial-Flow Fan Facility at Penn State [5] and can be easily adopted for use in the compressor facility. A schematic of the unit is shown in Fig. 5 and a photograph is provided in Fig. 6.

The data transmission system as well as the traverse assembly is shown schematically in Fig. 5. The probe is mounted in the probe traverse assembly (A) downstream of the rotor test blades within the rotating hub section. With the probe traverse device and the step motor (B) fixed to the cylindrical section (D), tangential motion of the probe is performed. The cylindrical section (D) is stepped tangentially with a gearing assembly at (C) between the rotor fixed frame of reference and that of the step motor assembly (B). The step motor is actuated by a Slo-Syn preset indexer through a set of brush contacts as indicated in Fig. 5. Tangential steps small enough (0.0192 deg/step) to allow an accurate measurement of the rotor wake were achieved.

The axial position of the probe is adjusted by turning a

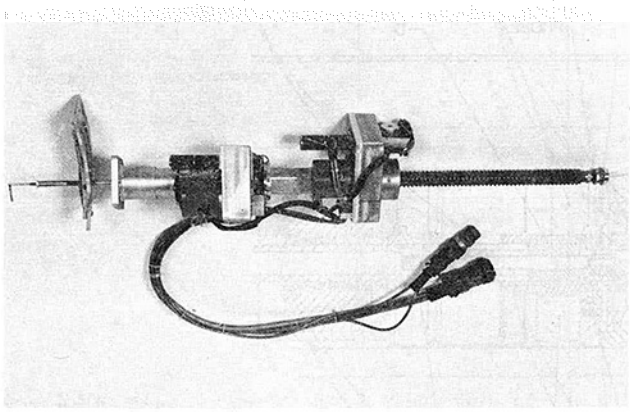

Fig. 7 Stationary probe traverse unit

worm gear at E as shown in Fig. 5. Turning of the worm gear at E moves the entire traversing mechanism in the axial direction. The probe is manually moved in the radial direction. The traversing mechanism was statically and dynamically balanced for all of the probe positions used.

Pressure or electrical signals from a probe are transmitted to the stationary frame of reference with a pneumatic transfer device at location F (Fig. 5) and with a mercury slip-ring unit at location G, respectively. Electrical or pressure connections between the mercury slip-ring or pneumatic transfer device and the probe are located within the rotating shaft designated as H. Three pressure signals can be simultaneously transmitted to the stationary frame. A ten-channel mercury slip-ring was installed for the experiments reported in this investigation, of which only six channels were needed with the tri-axial hot-wire probe. Triple-distilled mercury is used in each slip-ring channel to give the negligible noise-to-signal ratio necessary for the hot-wire signal. Pressure and electrical lines in the stationary frame located within the stationary hub section upstream of the rotor are transferred out of the hub through the strut shown at location J.

Stationary-Probe Traverse Unit. The traverse mechanism (L. C. Smith, Inc.) used for the intra-blade radial survey is shown in Fig. 1 and a photograph of the unit is presented in Fig. 7. The probe actuator is driven by two step motors, one for nulling the probe (about its own axis) and the other for the radial movement. The radial movement provides a step size of 0.05 mm/step and the angular movement is 0.0239 deg/step. Both the angular and the linear movement are controlled by a Slo-Syn preset indexer described later. This unit is common to both the rotating- and the stationary-probe traverse mechanisms. The support on which the traverse assembly is mounted enables accurate movement of the entire assembly in the axial and tangential directions for the intra-stage (radial) as well as blade-to-blade measurement of the flow in the stationary frame of reference.

Data Transmission System

The data transmission system, which is an integral part of the facility, is shown in Fig. 8. It consists of a 20-channel scanivalve unit (similar to the one described earlier) and a transducer unit, both of which rotate with the rotor and are attached to the shaft upstream of the nose cone (Fig. 1). This unit is self-contained and utilizes a rotating pressure transducer. Conversion of the pressure signal to electrical signals in the rotating frame of reference simplifies the measurement of the pressure from a multi-tube probe or blade static or wall static pressures, since the transmission of the output signal to the laboratory frame requires only a slip-ring unit. Furthermore, the scanivalve assembly in the rotating system allows the use of the same output channel for the measurement of blade static pressures at several locations. Check-out of the system for rotational effects indicated that the transducer mounted with its axis parallel to the shaft is very accurate under all operating conditions. The scanivalve motor is operated by an indexer described later.

The scanivalve assembly is followed by an eight-channel brush slip-ring unit, mainly used for power transmission to all scanivalve motors as well as the Slo-Syn motor driving the traverse mechanism.

This is followed by a three-channel pressure transfer device (PTD) for transferring pressure signals from a rotating system to a stationary system. Construction details are given in Figs. 1 and 8. This is an alternate system for transferring pressures from rotating blades, walls or probes through a scanivalve to a stationary transducer or a manometer. The unit consists of a rotating hollow shaft connected to the rotor shaft. Four sealed bearings are mounted at equal intervals with "0"-ring spacers, thus providing three channels for the pressure transfer. The outer casing is stationary. The pressure from the rotating system is transferred to the stationary system through these sealed channels. The device is calibrated, both statically and dynamically, at very frequent intervals to ensure that there is no leakage between channels.

The PTD is followed by a ten-channel mercury slip-ring unit (Meridian Laboratory, Inc.) shown in Figs. 1 and 8. Each channel consists of a thin disk rotating in a small housing filled partially with triple-distilled mercury. During rotation, the shear pumping effect of the disk carries mercury to the gap between the housing and the disk. This thin layer of mercury acts as a conductor. The signals from the hot wire or the wall stress gauge are transferred from the inner shaft through the rotating disk and the mercury pool to the stationary conducters on the casing of the slip-ring unit. This system provides extremely low noise/signal ratio and is ideally suited for transferring weak (AC and DC) signals from the

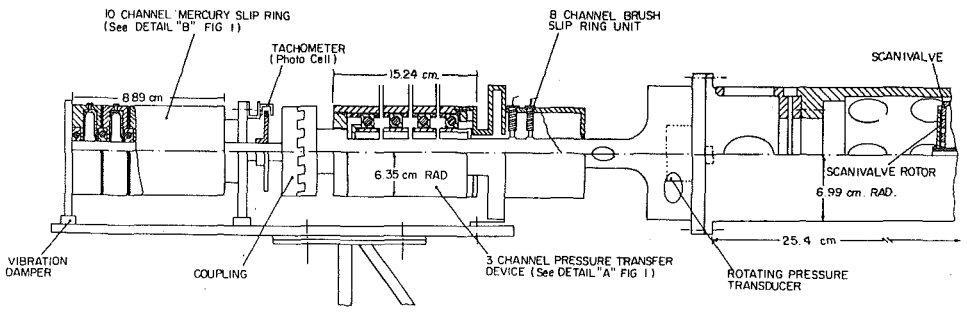

Fig. 8 Data transmission system

rotating system to the stationary instruments. This also provides negligibly small distortion of the amplitude and frequency characteristics of electrical signals from the sensors (hot wire, wall stress gauge, etc.). The system is calibrated, both statically and dynamically, to ensure accuracy. The mercury has to be changed at regular intervals as contamination of the triple-distilled mercury results in higher noise/signal ratio. The unit can run satisfactorily up to 10,000 rpm, even though it has been mostly used at this facility at 1100 rpm. The entire slip-ring unit is mounted on a four-arm vibration damper.

At the end of the shaft is a photocell unit (Fig. 8) for accurate measurement of the rotor frequency (and rpm). This signal is recorded on one of the channels of the tape recorder for processing of the rotor flow data using the ensemble-average technique [6].

Probes and Measurement Techniques

Some of the measurement techniques developed at Penn State and employed in this facility are described in the published literature, and hence will not be repeated here.

The following probes and measurement techniques are presently employed for relative flow measurement in this facility. A photograph of some of the probes used are shown in Fig. 9.

Blade Static and Hub Wall Static Pressures. To facilitate the measurement of the rotor blade static pressures, pressure ports of 1.5 mm diameter are provided on blade pressure and suction surfaces (eight locations on each surface) at seven radial locations including one at the tip. The hub wall has similar static pressure taps. These measurements are essential for the complete understanding of the blade-to-blade flow, wakes, and secondary flow near the hub wall regions. The pressures are brought through the scanivalve and the transducer assembly shown in Figs. 1 and 8.

Hot-Wire Measurement Technique. Single sensor, "X" configuration and triple-sensor hot-wire probes are used extensively in the relative and absolute flow measurement. Major emphasis has been on the use of the triple-sensor wire (No. 5 in Fig. 9) for three-dimensional mean velocity and turbulence measurements.

The technique employed for the absolute flow measurement using a single sensor is similar to that of reference [7], and is limited to the mean velocity measurement at the exit of the blade row or inside the IGV and the stator blade row. This technique was utilized for measuring the IGV and stator blade wakes reported in reference [8].

The "X" configuration hot-wire probe is employed for measurement of the rotor blade boundary layer close to the blade surface. The plane containing the wire is parallel to the blade surface and hence has very little spatial error or interference with the flow.

A special three-sensor (boundary layer type) probe is used for the relative flow measurement. A photograph of the probe is shown in Fig. 9 (No. 5). The probe sensors are built out of tungsten wire and have a length/diameter ratio of 270. The three wires are nearly orthogonal to each other and are placed in the flow such that the flow vector lies in the cone formed by the sensors. The active part of the sensor (etched part) is 1.25 mm, with the active part of the wires inside a sphere of 3 mm. Two techniques are employed to measure the relative flow inside the rotor passages and at the exit. The first technique, valid for the exit flow measurement, utilizes the ensemble-average technique developed at Penn State [6, 10] and employs a three-sensor hot wire. The second technique, which utilizes a rotating three-sensor wire, can measure the relative flow at the exit as well as inside the blade row [1, 9]. These methods are very accurate, and provide three components of mean velocity as well as six components of Reynolds stresses and the turbulent energy spectrum.

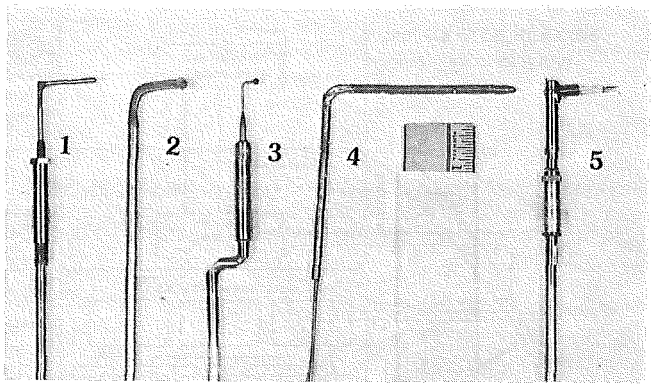

Fig. 9 Probes Used in the Facility – (1) five hole probe, (2) disk probe, (3) direction insensitive pitot-static probe, (4) Prandtl probe, and (5) three sensor hot wire probe

Static Pressure in Three-Dimensional Flow. The difficulties associated with the measurement of the static pressure in three-dimensional and turbulent flow is well known. The probe is very sensitive to the flow angle. To overcome this difficulty, a static-stagnation pressure probe has been developed, the design of which is partly based on a commercially available probe [11]. A photograph of the probe is shown in Fig. 9 (No. 3). It consists of a 3.175 mm brass sphere with trips around it to stabilize the wake flow region. The probe has the pitot tube at the nose, and the stem at the back has four static pressure ports, which measure the static pressure through the equation

$$p = \frac{P_w + kP}{1+k},$$

where p, P are free-stream static and stagnation pressures, respectively, and k is the probe factor, which has a value of 0.305 over a wide range of pitch and yaw angles.

The stagnation pressure measurement is accurate to ± 10 deg changes in flow angle and the static pressure is insensitive to direction changes within ± 30 deg. The probe has been used to measure the static pressure across the rotor blade wake. The agreement between the total relative velocities measured by this probe and those derived from the hot-wire probe is very good [11].

Conventional Probes. Some of the conventional probes that are presently employed in this facility are: a five-hole pitot probe (No. 1 in Fig. 9) for three dimensional flow measurement, a disk probe (No. 2 in Fig. 9) for pitch angle and stagnation pressure measurements near the rotor blade surface, and a pitot-static probe (No. 4 in Fig. 9). The five-hole probe has been calibrated simultaneously for both yaw and pitch angles at various Reynolds numbers. This probe has been used for endwall flow measurement in a rotor.

The disk probe is 6.35 mm in diameter and 1.59 mm thick with two 0.79 mm diameter hole at 45 deg to each other (circumferentially). The probe has been used for the boundary layer measurement on an inducer rotor blade. In the present facility, it will be used to measure the blade boundary layer near the surface to complement the hot-wire results. The extremely small dimensions of the probe provides the least aerodynamic interference to the flow near the wall, where the flow is nearly parallel to the blade surface.

Attempts are being made to measure the wall shear stress on the rotor blade surface using a somewhat modified version of the technique developed by McCroskey and Durbin [12]. The technique under development utilizes commercially available

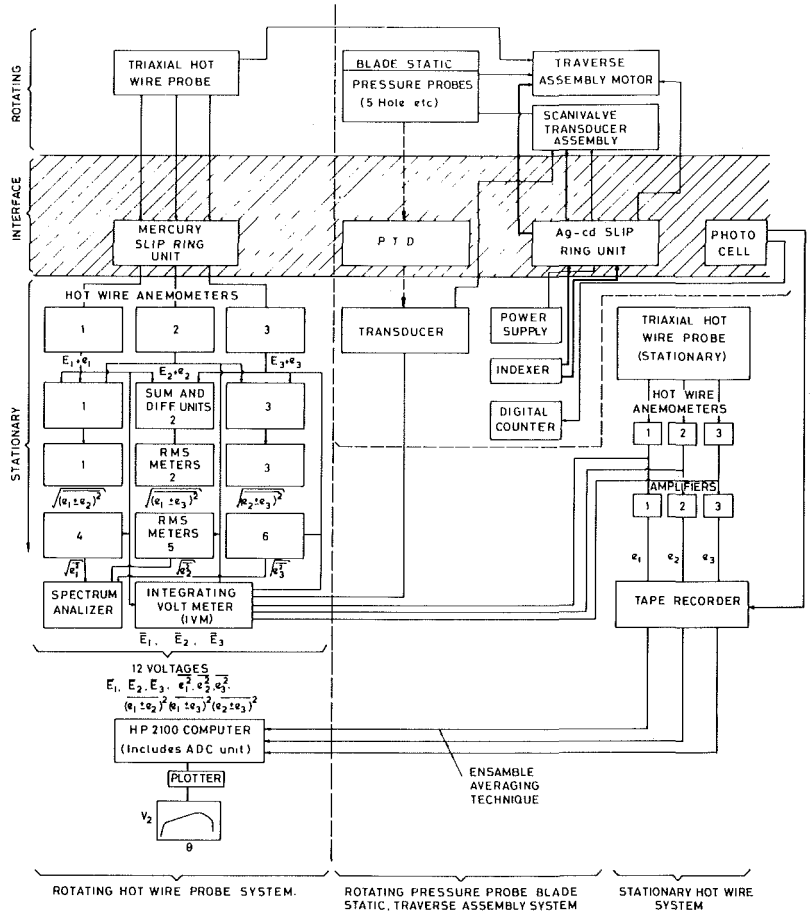

Fig. 10 Schematic of the instrumentation, control and data processing system

hot films, which will be embedded on the rotor blades. The signal will be processed through hot-wire anemometers.

Instrumentation and Data Processing System

A schematic of the instrumentation and control system used for the control of the probe traversing mechanism as well as scanivalve units, and for processing the signal from rotating and stationary three-sensor hot-wire and pitot probes (five-hole, etc.) is shown in Fig. 10. The hot wire and other probes are traversed by the traversing mechanism, which has a step size of 0.09 deg. The indexing device controls the forward and backward motion of the probe as well as the step size. The rotating hot-wire signal is processed through a three-channel hot-wire anemometer system, sum and difference circuits, and RMS meters. This will provide three mean voltages and nine RMS values of fluctuating voltages. These can be processed using the method of reference [9], to derive three components of mean velocity and six components of Reynolds stresses (shear stress and normal intensity) in any chosen coordinate direction. The data can be processed through an online HP 2100 S computer and plotter, shown schematically in Fig. 10, to derive the mean-velocity profile, etc. The spectrum analyzer is utilized to derive the energy spectrum of each component of turbulent stresses and intensities.

The pitot probe as well as the blade static pressure probe data are sent through the scanivalve assembly (or the pressure transfer device – PTD) to the integrating voltmeter to derive the mean (steady) value of the pressures.

The stationary hot-wire probe technique utilizes an ensemble-average technique [6, 10]. This program is built into the HP 2100 S computer, thus enabling simultaneous processing of the data. The hot-wire data are sent through an amplifier and recorded on a magnetic tape. The signals are converted into digital values through the analog-digital conversion unit in the computer before activating the program to do the ensemble average of the signal. The samples are then processed to derive three components of velocity, six components of stresses, length scale, and spectrum using the HP 2100 S computer in the laboratory.

The HP 2100 S computer system consists of the main computer (32 K memory size), disk operating system, magnetic tape system, optical data recorder, ADC unit, teletype terminal, low- and high-speed optical terminal, electric printer, and digital plotter. All hot-wire data, from both rotating and stationary probes, can be processed on-line to derive the desired velocity and turbulence profiles across the passage and the wake.

Typical Data Acquired in the Facility

Some typical data acquired in this facility are as follows:

1. Intra-blade row traverse at inlet and exit of IGV, rotor, and stator using conventional probes at design and various off-design conditions.
2. Rotor blade static pressure distribution at design condition and at various radii.
3. Rotor wake characteristics using a three-sensor hot-wire probe, both rotating and stationary, with and without an inlet grid.
4. Rotor blade endwall flow using a five-hole probe and

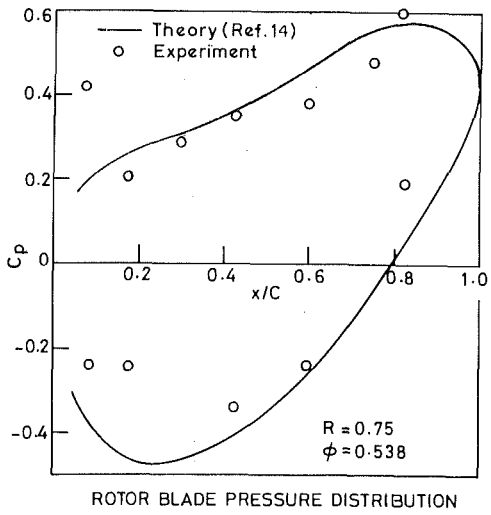

Fig. 11 Rotor blade static Pressure distribution

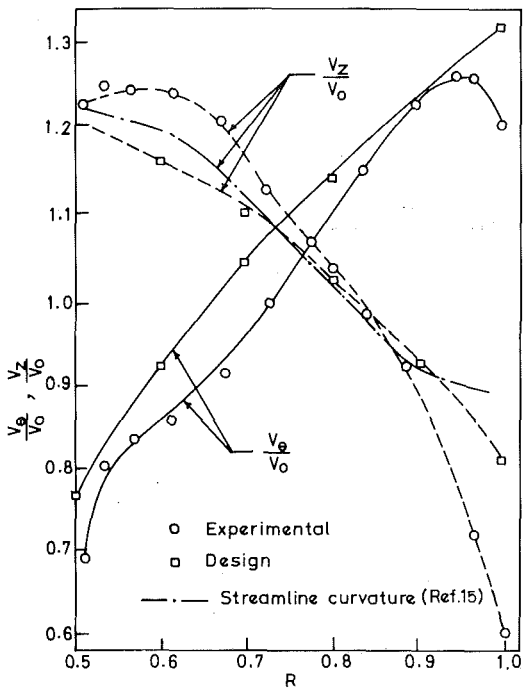

Fig. 12 Radial distribution of absolute velocity at the exit of the rotor

three sensor hot-wire probe; both in the passage and at the exit.

5. IGV and stator wake using a single-sensor probe.

Some of the rotor wake data as well as the IGV and stator wake data are published in reference [13 and 8], respectively, and will not be repeated here.

Overall Performance. The inlet flow properties were measured at three sectors 120 deg apart and found to be nearly uniform. The turbulence intensity is found to be 0.5 percent, except near the hub and annulus walls. Overall performance characteristics of the rotor is shown in Fig. 3.

The rotor blade static pressure distribution at mid-radius is shown in Fig. 11. The measurements are compared with the prediction from the surface singularity method (inviscid) due to Giesing [14]. The agreement is good except near the suction

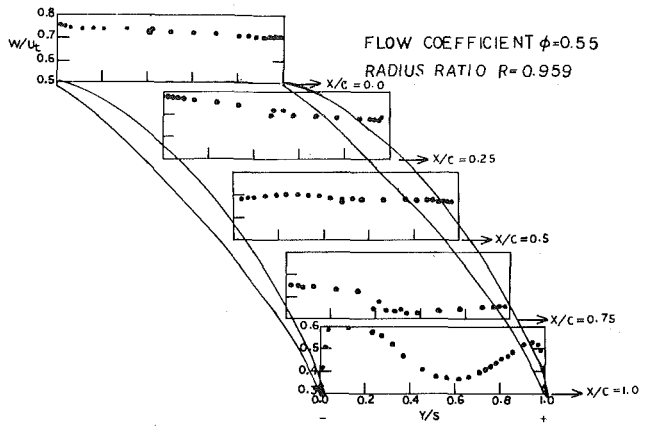

Fig. 13 Blade-to-blade distribution of the total relative velocity near the rotor end wall (five hole probe)

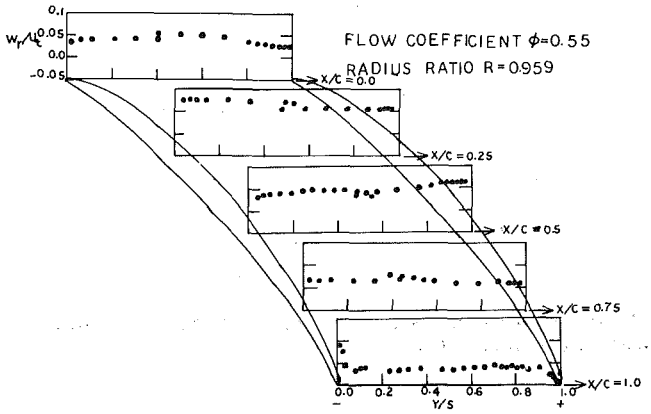

Fig. 14 Blade-to-blade distribution of the radial velocity near the rotor end wall (five hole probe)

peak, where viscid effects may be important. The departure between the theory and the experiment is considerably larger at other radii.

The tangential (absolute) and axial velocity distribution measured at the exit of the rotor is shown in Fig. 12. The measurement location is far downstream at mid-radius, where the departure from two-dimensional flow should be small. It is evident that the departure from the design is less than 5-10 percent at most of the locations.

A streamline curvature program [15] is utilized to predict the hub-to-tip distribution of the axial velocity. The input to this program is the static pressure and the absolute tangential velocity distribution. The comparison between the measured and the predicted distribution is good, except near the annulus and the hub wall (Fig. 12).

Rotor Endwall Flows. The measurements taken near the endwall ($R = 0.959$) region using a five-hole probe are shown in Figs. 13 and 14. The total relative velocity distribution across the passage at four chordwise locations is shown in Fig. 13. A slight jump in the data near the mid-passage is caused by the fact that the probe traversing is done from the pressure surface to mid-passage due to constraints imposed by the twisted blades. A slight radial displacement of the probe probably accounts for the discrepancy in the overlapping region. It is clear that the potential flow effects persist from $x/c = 0$ to 0.5, with the leakage vortex formation taking place between $x/c = 0.5$ and 0.75. The trailing edge distribution ($x/c = 1.0$) shows the existence of the leakage vortex as well

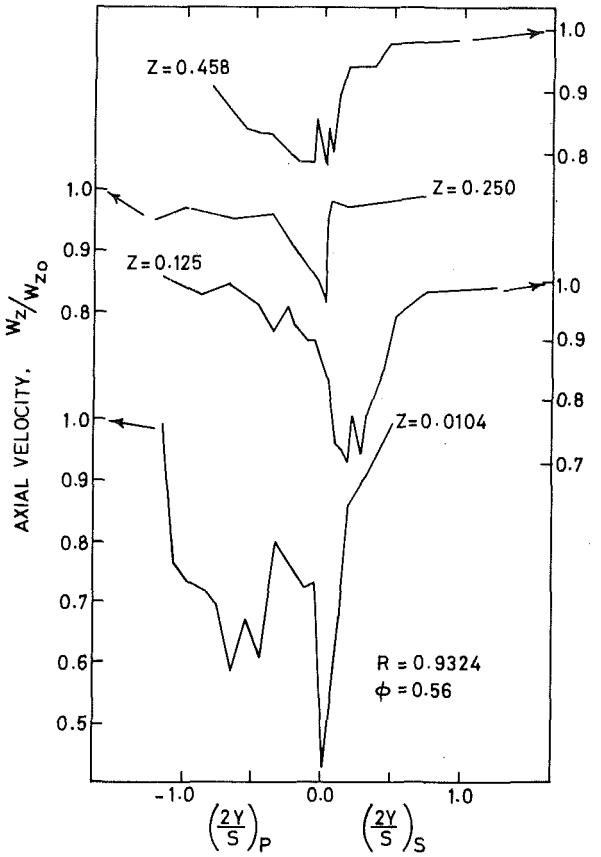

Fig. 15 Blade-to-blade distribution of axial velocity at the exit of the blade row (three sensor hot wire)

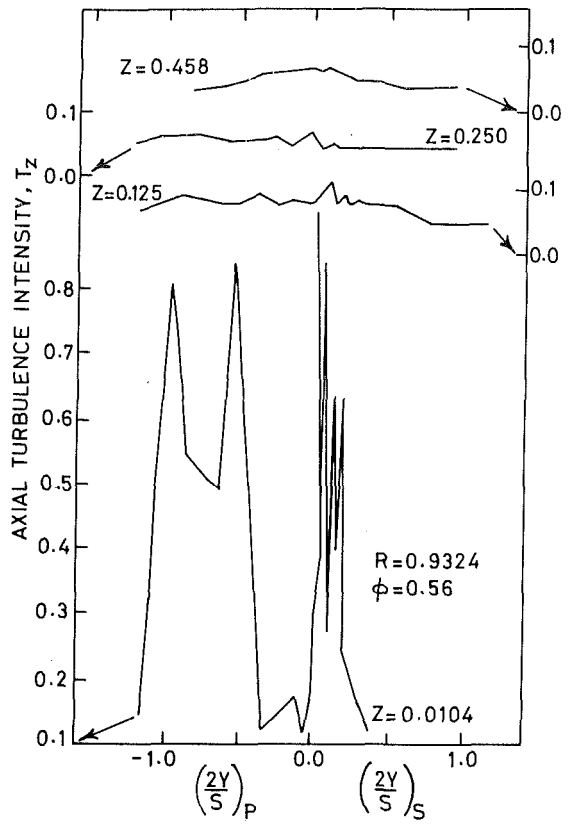

Fig. 16 Blade-to-blade distribution of axial turbulence intensity at the exit of the blade row (three sensor hot wire)

as the blade wake. The circumferential extent of the vortex seems to be large. The blade wake is fairly thin and well defined. Since the blades are curved and twisted, no measurements could be taken very near the blade surface. Attempts are being made to modify the system to measure the thin boundary layers that exist on the blade surface.

The radial velocity distribution across the passage, shown in Fig. 14, indicates the magnitudes are rather small, which is expected in view of the presence of the annulus wall. The measurements at the trailing edge ($x/c = 1$) indicate a vortex type of distribution in the blade wake. Spanwise outward flow on one side and inward flow on the other side of the blade, is evident. Additional measurements are necessary to identify the vortex.

Rotor Blade Wake and Endwall Flow at the Exit of the Rotor. Extensive measurement of the blade-to-blade as well as hub-to-tip flow, including wakes, secondary flow, and tip vorticies at the exit of the blade row using both the stationary and the rotating three-sensor hot-wire probe, have recently been completed. It is beyond the scope of this paper to discuss these results. Some typical unpublished data is presented below; other data and interpretation can be found in references [11, 13, and 16].

The wake and the endwall flow characteristics near the blade tip and downstream of the blade row, measured by a rotating hot-wire probe, is shown in Figs. 15 through 17 at various axial distances downstream of the trailing edge. The axial velocity profile and the axial component of turbulence intensity at $R = 0.9324$, shown in Figs. 15 and 16, respectively, reveal the complex nature of the flow near the tip at the rotor exit. The existence of the wake (at $2Y/S = 0$) as well as the presence of a vortex is clear from the figure. Based on the radial velocity measurement [11], it can be concluded that this

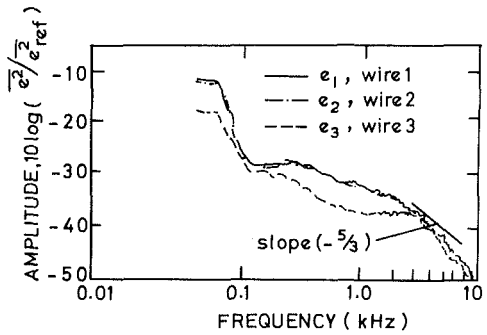

Fig. 17 Turbulent energy spectrum at the wake center ($R = 0.9324$, $\phi = 0.56$)

is the tip leakage vortex. The vortex has a major influence on the blade-to-blade distribution of the flow and turbulence properties. The turbulence intensities are very high, both in the wake and in the vortex region. Surprisingly, the vortex decays more rapidly than the wake as seen in Fig. 15. At $Z = 0.125$, the wake and vortex seem to have merged together. The turbulence intensity also decays very rapidly.

The spectrum of turbulence at the wake center, plotted in terms of fluctuating voltages in Fig. 17, reveals a smaller than usual region of isotropic turbulence. The energy levels are high at low frequencies, showing a substantial change in the turbulence structure due to rotation.

An experiment was recently undertaken to determine the effect of inlet turbulence on the rotor wake structure. The rotor wake was measured at the mid-radius with and without the turbulence-generating grid. The grid was of square mesh of size 2.5 cm × 2.5 cm with 0.47 cm diameter brass rods. The stationary hot-wire probe (triaxial) described earlier was used

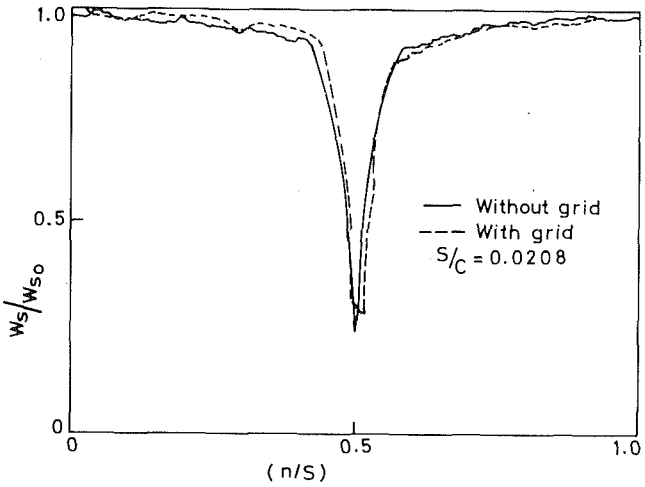

Fig. 18 Effect of inlet Turbulence on streamwise relative velocity distribution across the rotor blade wake (R = 0.75, ϕ = 0.56)

in this program. The free-stream turbulence intensity at inlet was increased from 0.5 to 3.5 percent. The difference in mean velocity profile is found to be negligibly small, as shown in Fig. 18. However, the entry turbulence levels had appreciable influence on the turbulence structure at the exit of the rotor [16].

Concluding Remarks

The facility described in this paper provides some unique experimental capabilities for studying many unresolved problems in turbomachinery. It also facilitates verification of many of the three-dimensional inviscid/viscid, steady/unsteady theories under development. Among the measurement capabilities are three-dimensional flows inside and at the exit of the blade row, turbulence phenomena near and away from the blade, effect of inlet distortion and its propagation through the blade row, and a systematic investigation of sources and magnitude of losses as well as noise in turbomachinery. Some of the measurements completed so far have provided a great insight into the wake, boundary layer and endwall phenomena in the rotor blade row.

Acknowledgment

The facility was constructed and the investigations carried out with the assistance of a grant (NSG 3012) from the National Aeronautics and Space Administration, with M. F. Heidmann as the technical monitor. The endwall flow investigation is presently being carried out under NASA Grant NSG 3212, with P. Sockol as the technical monitor. The author wishes to thank many of his former and present graduate students who helped in the development of the facility and participated in the measurement program. Among these are R. Raj, N. Sitaram, A. Ravindranath, R. Davino, and C. Hah. G. Kane took the major responsibility in the assembly of the facility. G. Gurney and G. Sayers provided assistance in developing the rotating-probe traverse mechanism – Unit 2. The paper was written during the author's sabbatical leave at the Indian Institute of Science, Bangalore, where he was an NSF/CSIR Exchange Scientist.

References

1 Anand, A. K., and Lakshminarayana, B., "Three Dimensional Boundary Layer in a Rotating Helical Channel," ASME JOURNAL OF FLUIDS ENGINEERING, Vol. 97, No. 2, June 1975, pp. 197–210.

2 Smith, L. H., "Three Dimensional Flow in an Axial Flow Turbomachinery," WADC Tech. Report No. 55-348, Vol. 11, Johns Hopkins University, Mar. 1956 (also see Report I-16, Dept. of Mechanical Engineering, Johns Hopkins University, May 1954).

3 Herrig, J. L., Emery, J. C., and Erwin, J. R., "Systematic Two Dimensional Cascade Tests of NACA 54 Series Compressor Blades at Low Speeds," NACA TN 3916, 1957.

4 Pemberton, J. C., and Ellis, G. O., "Flow Measurement in Rotating Machinery," *Instruments and Control Systems,* Mar. 1964.

5 Raj, R., and Lakshminarayana, B., "On the Investigation of Cascade and Turbomachinery Rotor Wake Characteristics," NASA CR 134680, Feb. 1975.

6 Lakshminarayana, B., and Poncet, A., "A Method of Measuring Three Dimensional Rotating Wakes Behind Turbomachinery Rotors," ASME JOURNAL OF FLUIDS ENGINEERING, Vol. 96, No. 2, June 1974, pp. 87–91.

7 Schmidt, D. P., and Okiishi, T. H., "Multistage Axial Flow Turbomachine Wake Production, Transport and Interaction," *AIAA Journal,* Vol. 15, Aug. 1977, pp. 1138–1145.

8 Lakshminarayana, B., and Davino, R., "Mean Velocity and Decay Characteristice of the Guide Vane and Stator Blade Wake of an Axial Flow Compressor," ASME *Journal of Engineering for Power,* Vol. 192, No. 1, 1980, pp. 50–60.

9 Gorton, C. A., and Lakshminarayana, B., "A Method of Measuring the Three Dimensional Mean Flow and Turbulence Quantities Inside a Rotating Blade Passage," ASME *Journal of Engineering for Power,* Vol. 98, Apr. 1976, p. 137.

10 Raj, R., and Lakshminarayana, B., "Three Dimensional Characteristics of Turbulent Wakes Behind Rotors of Axial Flow Turbomachinery," ASME *Journal of Engineering for Power,* Vol. 98, Apr. 1976, pp. 218–228.

11 Ravindranath, A., "Three Dimensional Characteristics of the Wake of a Moderately Loaded Compressor Rotor Blade," M.S. thesis, Department of Aerospace Engineering, The Pennsylvania State University, Nov. 1979.

12 McCroskey, W. J., and Durbin, E. J., "Flow Angle and Shear Stress Measurements Using Heated Films and Wires," ASME *Journal of Basic Engineering,* Vol. 94, No. 1, 1972, p. 1258.

13 Ravindranath, A., and Lakshminarayana, B., "Mean Velocity and Decay Characteristics of the Near and Far Wake of a Compressor Blade of Moderate Loading," ASME *Journal of Engineering for Power,* Vol. 102, No. 3, July 1980, pp. 535–548.

14 Giesing, J. P., "Extension of Douglas Neumann Problems to Lifting Infinite Cascade," Douglas Aircraft Co., Report LB 31653, July 1964.

15 Treaster, A. L., "Computer Application of the Streamline Curvature Method to the Indirect Axisymmetric Turbomachine Problem," ARL TM 514.2491-16, Applied Research Laboratory, The Pennsylvania State University, 1969.

16 Hah, C., "Numerical and Experimental Study of Turbulent Wakes of Turbomachinery Rotor Blade, Isolated Airfoil and Cascade of Airfoils," Ph.D. Thesis, Department of Aerospace Engineering, The Pennsylvania State University, Mar. 1980.

A Laser-Two-Focus (L2F) Velocimeter for Automatic Flow Vector Measurements in the Rotating Components of Turbomachines

R. Schodl
Research Engineer, DFVLR,
Institut für Antriebstechnik,
5000 Cologne 90/W. Germany

Numerous results – most of them are published – have proved the applicability of the L2F-velocimeter to experimental studies of the complex compressor flow: e.g. the blade wakes and the shock-wave system within the blade passages. Furthermore, measurements close to the compressor surfaces provide information about boundary layers and flow separation. However, the measuring procedure is rather time-consuming. It takes about one hour to accumulate 10 to 15 vector measurements within a rotor blade channel. This paper presents a technique whereby the measuring time is reduced by a factor of ten. Mathematical considerations of the L2F-signal statistics lead to a modified calculation model and a new measuring procedure. Now, about 100 to 150 flow points can be acquired in one hour which includes the magnitude and direction of the mean flow vector as well as its turbulent components. This paper describes the innovations in optics, operational procedures, and electronics that have resulted in an enhanced state-of-the-art in flow measurement. Experimental results are also submitted and discussed.

Introduction

Experimental research into modern, highly loaded turbomachines is entering a new, exciting stage, owing to the recently-developed optical methods, [1] of measuring local blade-passage velocities. That is because the experimental data on these flows can be used for further improving the design techniques and the performance capability of these machines.

During the past 4 to 5 years the Laser-2-Focus (L2F) velocimeter developed at the DFVLR [2, 3, 4], has proved to be a useful tool to investigate the internal flow of centrifugal and axial compressors. Detailed data of these measurements illustrate the actual three-dimensional flow field through the blade passages of compressors rotors [5, 6], the shock-wave systems, blade wakes, boundary layers, both attached and separated and gave the basis of comparing these real flow data with results of different calculation methods [7, 8]. In order to further improve these methods more detailed experiments are required.

The well known advantage of L2F-velocimeters is that of measuring high velocities in a backscatter arrangement even at positions close to walls where laser light reflections generate a strong background noise. Unfortunately this is connected with a rather time consuming measuring procedure. Rising energy consumption costs are being felt and either data aquisition must be more efficient or experiments must be limited to a small number. This is especially true in the research field of multi-stage turbomachines in which the experimental flow field data are of special interest today.

Considering this situation, the DFVLR has been engaged in a program for reducing the L2F operating time with special regard to turbomachinery applications.

The paper deals with the results of this investigation and describes the development and testing of the new automated L2F-processor for periodical flows.

Survey of Measuring Principle

The L2F-measuring device generates in its probe volume (Fig.1) two parallel highly focussed light beams such that a "light gate" is created. A particle passing through both the light beams in the measuring section, along the focal (x_1, x_2-) plane, produces then two successive pulses of scattered light. The time elapsed between the pulses yields the component of the particle's velocity perpendicular to the optical (x_3-) axis. However, this scattered light double pulse - which is necessary for time measurement - will only be generated once the plane of the beams has been established parallel to the flow direction. Consequently, the L2F-method responds to the

Contributed by the Fluids Engineering Division of THE AMERICAN SOCIETY OF MECHANICAL ENGINEERS and presented at the Symposium on Measurement Methods in Rotating Components of Turbomachinery, Gas Turbine and Fluids Engineering Conference, New Orleans, La., March 10-13, 1980. Manuscript received by the Fluids Engineering Division, November 1979.

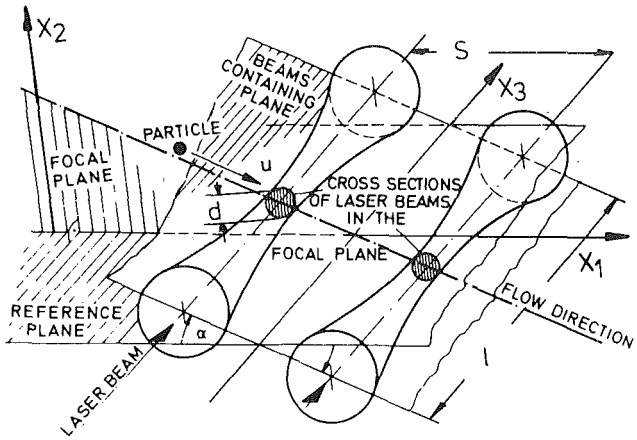

Fig. 1 Laser-two-focus probe volume (principle sketch)

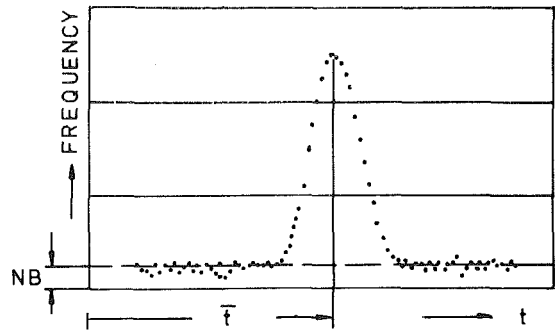

Fig. 2 Frequency distribution of time-of-flight measurements (t)

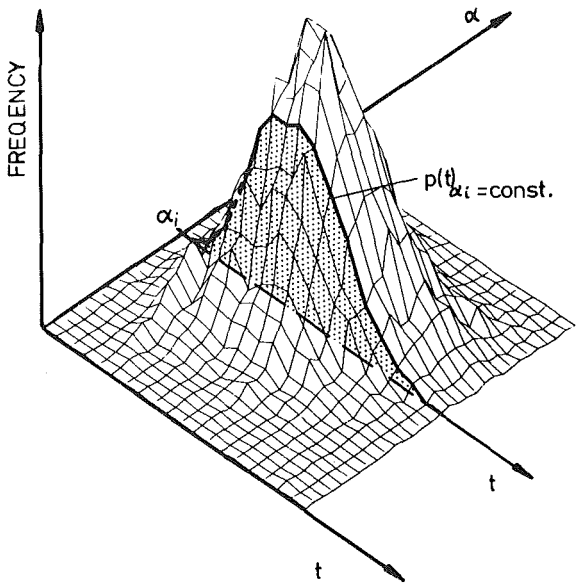

Fig. 3 Two dimensional probability distribution constructed by measured data

flow in different directions. Taking a single measurement of the time interval between two scattered-light pulses, one is never sure that this is a right measure. The reason is, that the two succeeding pulses can be generated in two different ways. First by one particle passing both the beams and causing a useful measurement and second by two different particles independently passing any a beam causing wrong measurements. To distinguish between wrong and right measurements, many measured values taken at a certain probe position are necessary.

In Fig.2, as an example, a probability histogram of such data is plotted, the "noise band" (NB), which is approximately constant along the time axis, is due to non-useable measurements. The net distribution which is shaped like a gaussian curve - it has to be reduced by the averaged value of the noise-band - represents the right measurements.

In the statistical theory of turbulence, the properties of the flow are described by a probability density function. As it is shown in references [2] and [3] this function can be measured by a L2F-velocimeter if it is operated as follows: At a certain position in a turbulent flow the plane of the beams of the L2F-probe volume has to be approximately aligned with the mean flow direction. Due to the turbulent fluctuations of the flow vector only such particles which have this direction will be selected for measurements. Measuring the amount of velocity of a certain number of particles entering the probe volume that leads to a probability histogram as shown in Fig.2. By setting the plane containing the beams to other slightly different angles and by accumulating the same number of particles entering the probe volume, more velocity histograms can be measured as long as the chosen setting angles of the plane are within the range of the velocity angle fluctuations.

This yields a two dimensional probability histogram (see Fig.3) which can be fitted by a two dimensional normalized probability density function $p(\alpha,t)$. As it is expounded by the theory of turbulence (see reference [9]) the function $p(\alpha,t)$ contains all information about the velocity components in the plane perpendicular to the optical axis (x_1,x_2-plane, see Fig.1). Any mean value of the fluctuating velocity components can be calculated by applying equation (1)

$$\bar{F}_x = \int_0^{2\pi} \int_0^{\infty} F(\alpha,t) \cdot p(\alpha,t)\ dt\ d\alpha \qquad (1)$$

wherein $\bar{F}_x$ is the mean value of the desired velocity function $F(\alpha,\ t)$. When inserting an appropriate velocity function

Nomenclature

d = beam diameter at focal point
$\bar{F}_x$ = local mean value of velocity components
$F(\alpha,t)$ = velocity function
$F_u(u), F_v(v)$ = velocity density functions
$f(u,v)$ = two dimensional probability function
$f_1(u,v)$ = product of the density functions
I = light intensity
I_0 = light intensity at probe volume center
1 = axial length of probe volume
$M_{\alpha w}$ = relative Mach number
$p_t(t), p_\alpha(\alpha)$ = velocity density functions
$p(\alpha,t)$ = two dimensional probability function
$p_1(\alpha,t)$ = product of density functions
Re = Reynolds shear stresses
s = beam separation at probe volume
Tu, Tv = turbulence intensities
ΔT, $T1$ = delay times
t = time coordinate
u = velocity component along x_1-coordinate
$\bar{u}$ = mean value of u
v = velocity component along x_2 coordinate
$\bar{v}$ = mean value of v
x_1, x_2, x_3 = cartesian coordinates
α = angle-coordinate
ρ = correlation factor
σ_u, σ_v = variances of the Gaussian function

$F(\alpha,t)$ into equation (1) the components of the mean flow vector, the turbulence intensities, the Reynolds' shear stresses as well as high order moments can be calculated (see reference [3]). All this information is contained within the measured two dimensional probability distribution.

Experience on L2F-Measurements Within Compressors

When applying the L2F velocimeter to rotor flow measurements in turbomachines, positioning of the probe volume can only be carried out in two coordinates – in radial and in axial directions. In order to define the measuring point in circumferential direction, both the laser beams and the electronics are controlled during the rotating through a trigger signal from the rotor.

Measurements are acquired as both laser beams and the electronics are activated while focused upon a common location within each blade passage. It is not sufficient to merely switch the signal from the electronics. It is also necessary to switch the laser beams periodically. The photomultipliers must be protected from becoming saturated by a strong radiation which is generated when the blade surfaces touch the probe volume. Although the photomultiplier will not be damaged by this reflection, the saturation renders measurement impossible for a certain time period which is often not small compared to the blade passing time.

By its exposure time a finite measuring region in circumferential direction rather than a discrete measuring point is determined. The length of the measuring region (measuring window) – chosen to be 1/20 of the blade spacing – corresponds to a time interval which is about two to three times longer than the time of flight of a particle through both of the beams in the probe volume. The measuring window which at first might appear to be rather long is found to be sufficiently small in practice, even in regions of steep velocity gradients. This is acceptable because the unfavourable integration of the velocity profile is caused even more by flow unsteadiness – as perhaps shock fluctuations – than by the finite width of the circumferential measuring position.

At each of the probe positions the operator has to search for the mean flow direction by adjusting the plane of the beam. If a first measurement is made in a completely unknown flow this is a rather time-consuming procedure. However, the experience of the operator increases with the number of measurements carried out such that it becomes easier to estimate the mean flow angle from previous measured positions. By setting the plane containing the beams to certain angles around the estimated mean flow angle, different probability distributions are measured. Six to eight angle settings with about 2000 particles at each angle provides a sufficient number of flow data. This will ensure an accurate calculation of the mean flow vector and the turbulence intensities.

These numbers are mainly determined by the numerical method used for fitting the measured data by a two-dimensional function. Due to the difficult mathematical procedure, a large sample of data is required.

Depending on seeding, signal quality, turbulence intensity and on the experience of the operator in estimating the actual flow direction, a usual measurement takes about 5 minutes on the average including the positioning of the probe, the collecting of data, the angle setting of the plane containing the beams and the data transfer.

The measuring accuracy is not mainly defined by the systems error – which is about 0.2 to 0.5 percent (see reference [4]) – but by errors caused by the applicational case itself, as there are finite width of the measuring window, somewhat different flow in each of the blade channels and unsteadiness effects such as shock fluctuations and vibrations. The resultant error of mean velocity measurement does not exceed ± 1 percent. Only in the regions of shock waves, within the blade wakes and within close proximity of the hub and outer casing wall will measuring errors be somewhat increased. The relative error of the measured turbulence intensities - it is recommended better to talk about r.m.s. - value of local velocity fluctuations (fluctuation factor) - is found to be about 5 to 10 percent depending on the signal quality and the number of measured data.

During three years of operating the L2F-velocimeter upon component test compressors, much experience on the specific condition in turbomachines was gathered. This experience was very helpful toward reducing the L2F-measuring time.

As the following section describes a significant reduction of the measuring time was achieved by a modified mathematical calculation model in connection with a new automated measuring procedure and by some modest improvements in optics and electronics.

Signal Improvement

An automated measuring procedure mainly saves the time which is needed for handling the device but does not affect the measuring time which depends upon the quality of optics and electronics used, on the laser power, on the properties and quantity of the particles, and on the geometry of the probe volume and on its location within the flow channels.

It is especially difficult and time consuming to measure close to the hub and the shroud because of the unfavourable background radiation generated by laser light reflections on solid surfaces. However, measurements are of most interest there today. The former compressor tests have shown that measurements are possible up to minimum probe volume distances of 2 to 3 mm from the solid surfaces. When applying fluorescent particles for improving the signal to noise ratio, this minimum distance is decreased to about 0.5 mm. However, later intensive investigations have shown that these solid fluorescent particles do not follow the flow accurately.

This has been demonstrated by measurements carried out within a transonic axial compressor using different kinds of particles. The probe volume was located just in front of the rotor blade leading edges at 63 percent blade height. The measured relative Mach numbers are shown plotted in Fig.4 against the blade pitch. A shock is indicated by the steep velocity gradient. The significant difference of the measured Mach numbers demonstrates that these fluorescent particles are not suitable for this application. The mean diameter of the particles used was about 1 μm. Because it is difficult to find smaller solid fluorescent particles for seeding the flow, the further development of the fluorescent technique was stopped.

An equivalent reduction of the background noise has been achieved by the use of a specially calculated collimator lens. It focuses the collimated light - generated by particles passing the probe volume - more precisely onto the dual hole aperture (see ref.3) rendering a better spatial filtering.

When a scattering surface is moved along the optical axis (x_3-coordinate, see Fig.1) within the proximity of the probe volume the photo-multipliers detect light intensity changes depending on the position of the scattering surface. Such experiments have been carried out in order to compare results from the new collimator lens with those used previously. The measured intensity referred to its value at $x_3 = 0$ (which corresponds to the probe volume center) is plotted in the diagram of Fig.5 showing that the new lens only gathers the light out of a very narrow axial region. Using the new collimator, a small windtunnel test has been run without seeding the air. The results in Fig.6 - the velocity is plotted against the channel width - illustrate the improved capability of the device to measure within the close proximity of the

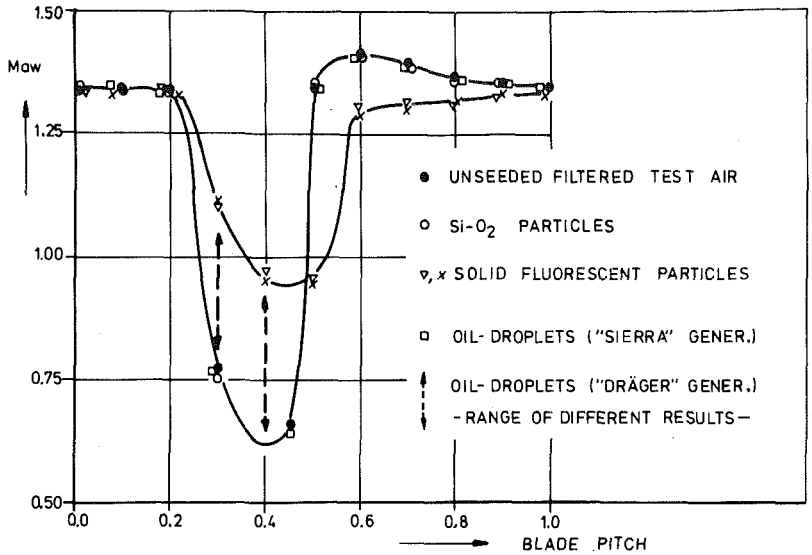

Fig. 4 Relative Mach number distribution against blade pitch measured by use of different seeding material at blade leading edges (63 percent blade height)

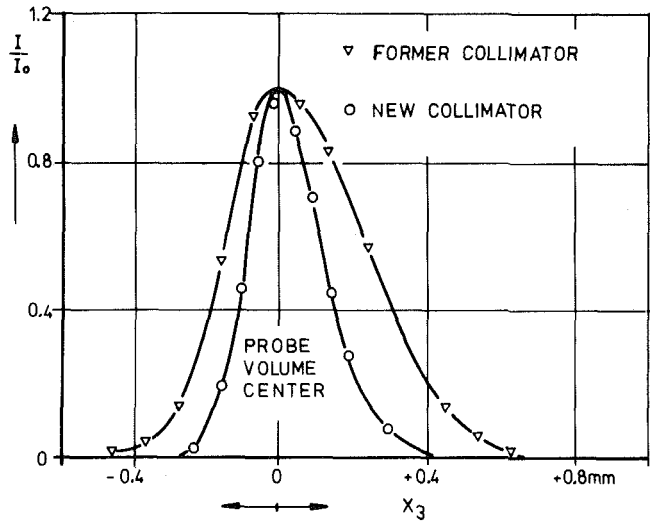

Fig. 5 Detected light intensity from a scattering surface which was moved along the probe volume axis

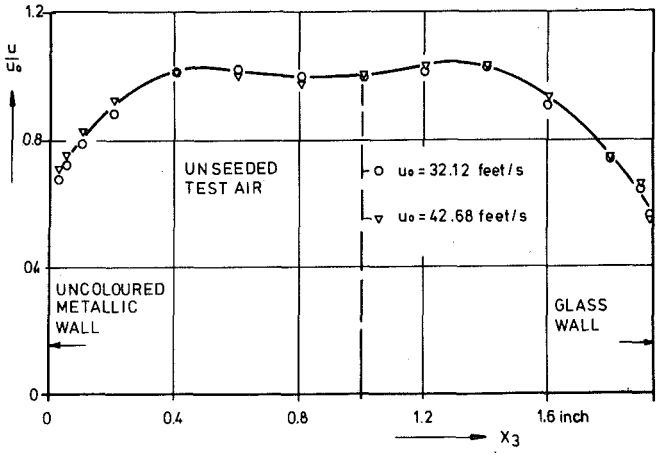

Fig. 6 Velocity distribution measured within a small wind tunnel

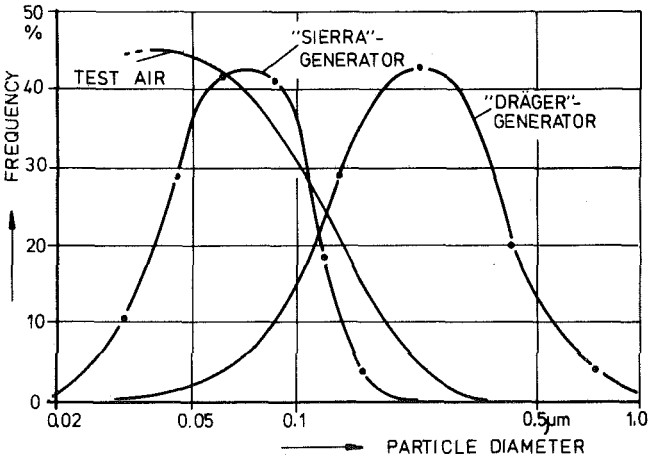

Fig. 7 Particle size distribution of different seeding materials

wall. The noise level was acceptable down to a distance of 0.4 mm.

The seeding problem was also considered in this test. As shown by Fig.4 both natural dust particles of the filtered test air as well as the seeded SiO_2-particles follow a much steeper velocity gradient than the fluorescent particles. Former tests with SiO_2 particles have proved (see reference [3]) that they follow very closely the real flow even within shock regions. This is also true with the natural dust particles used as it is demonstrated by the agreement of both measuring results.

From the number of measuring events obtained within these tests the particle concentration was calculated. Considering the flow velocity and the probe volume geometry (beam diameter 0.01 mm, axial length 0.5 mm) a particle concentration of 1000 to 2000 per cubic centimeter was deduced. If this experimental result – a 150 mW laser was used for the tests – is compared with the well known particle size distribution within filtered air one can conclude that particles of diameter smaller than 0.1 μm are detectable by the L2F-velocimeter. The resulting signal rate – at 200 m/s about 1000 to 2000 events per second – cannot easily be increased by seeding due to the problem of agglomeration within the seeding generators. With no expectation of increasing the number of particles, further improvement in signal amplitude was sought through choice of seeding materials. Two oil droplet generators – oil particles are known to have good scattering properties – were used within the aforementioned compressor tests.

The signal amplitudes resulting from particles produced by

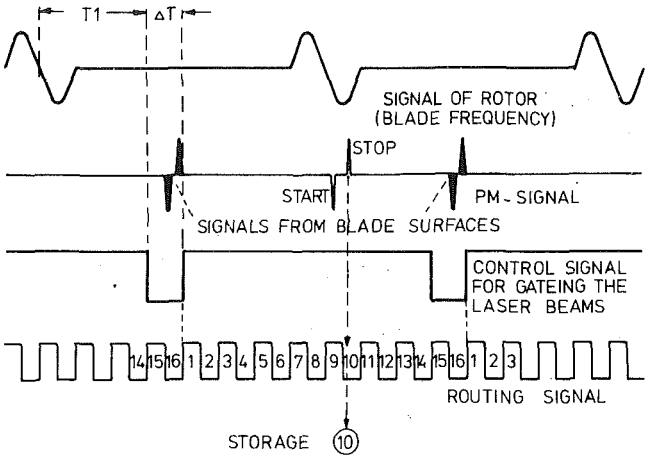

Fig. 8 Timing diagram of the multi window controller

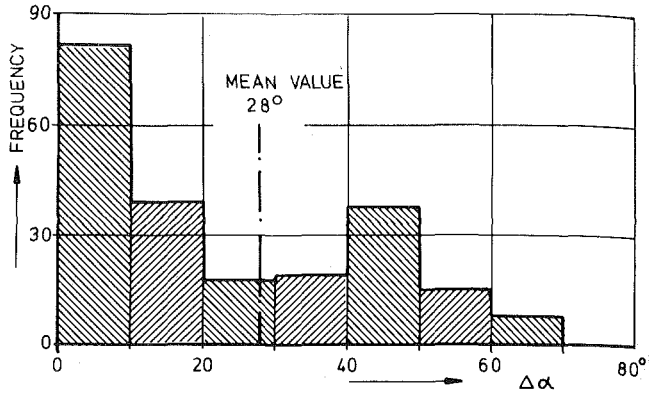

Fig. 9 Histogram of absolute flow angle variations from suction to pressure side

the "Dräger"-generator (see Fig.7) were observed to be much higher than that of natural dust particles. However, these particles do not follow the flow well. The arrow in Fig.4 illustrates the range of different results measured by different threshold settings of the discriminator in the signal electronics (see Fig.11). Additionally a very high fluctuation factor was measured. Both results do indicate that a significant fraction of large particles have been contained within this aerosol, mean diameter 0.3 μm.

Testing the "Sierra"-generator - mean particle diameter about 0.07 μm - the flow-following behaviour of these particles was acceptable (see Fig.4). However their signal amplitude was not higher than that of the natural dust particle.

Therefore these conclusions can be drawn: To insure a good following of the flow within turbomachinery tests, particles smaller than 0.3 μm must be used. This small particle can be detected by the L2F-velocimeter in backscattering with the use of a 150 mW Laser. Due to the very high number of these small particles, even in filtered test air, additional seeding is not needed.

Inserting of additional filters into the signal electronics provided a further improvement of the L2F-velocimeter. The signal to noise ratio of the photomultiplier was increased such that a higher signal rate was achieved as well as a better peak discrimination.

By the small modification of both optics and electronics the measuring time was reduced by a factor from 1.5 to 2.5 depending on the velocity range - the higher value corresponds to the lower speeds.

Multi Window Operation

When the probe position in circumferential direction is determined by switching on the laser during a small time period within each blade channel - single window operation - this is a rather time consuming measuring procedure because only 5 percent of the total operating time is used for measurement.

The possibility exists that all circumferential positions of finite width be measured simultaneously. By this way - lets call it multi window operation - a considerable measuring time reduction should be achievable.

The way of operation can be explained with the help of the timing diagram in Fig.8. A trigger signal from the rotor (upper trace) is required. The periodically generated pulses correspond to the blade frequency. A control signal is generated which switches the laser periodically off for an adjustable time period ΔT just in that moment when the blade passes the probe volume – see P.M. – signal. The delay time T1 depends on the probe position and is also adjustable. By this way the photomultipliers are protected from getting saturated. When the laser is switched on for measurement - control signal at high level - an internal timing (routing signal) divides the blade period in 16 parts corresponding to 16 different circumferential positions.

Just at that moment when a stop signal appears - generated by a particle passing the second beam - the routing value is stored. The measured time interval data is then be stored into that part of a group of memories which corresponds to the indicated routing value. Due to a particle rate of about 2000 per second and a blade frequency of 10 kHz - a measuring event is only probable in each 5th blade passage. Therefore the 10 - 30 μs which are needed for storing the measurements into the multi channel analyzer (MCA) will not affect the measuring time and measurements may take place continuously.

This multi window operation which simultaneously measures 16 different circumferential positions does not require the same order of time required for a single window measurement. However, there is less than a factor of 16 in time reduction in practice.

L2F-measurements are only possible within such windows where the angle setting of the plane of the beams corresponds with the flow angle. The flow angle of the measured absolute velocity varies considerably from suction to pressure side. In Fig. 9 a histogram of the flow angle variation over the blade pitch is shown which is based on the results of about 2500 measurements taken within a transonic compressor rotor. For the mean value of the angle variation from blade to blade is about 28 degrees – depending somewhat on the type of rotor – the mean flow angles within each window are separated by about 2°. Therefore, for a given angle setting of the plane of the beams it is most probable to get measurements only within 2 or 3 windows and not within all at the same time.

As can be shown by experiment, the realistic factor of shortening the measuring time by multi window operation is not 16 but only 2 to 3 on the average.

Simplification of Mean Value Calculation and Error Estimation

At any probe position (radial, axial) within each measuring window the already mentioned 6 to 8 histograms of time interval data - measured by setting the plane of the beams to an equivalent number of different angles - are required for calculating the flow data. With the use of equation (1) various mean values of the flow velocity can be calculated. However, the theorist only ask for the mean velocity components $\bar{u}$ and $\bar{v}$ (in direction of x_1 and x_2) and perhaps for the turbulence intensities, because these values are the only ones which they can compare with theoretical calculations up to now. All the

other information which is contained within the two dimensional probability distribution is not used.

The possibility is suggested here that the condensation of requirements may lead to simpler, more direct procedures for acquisition of the desired parameters.

By experiments it was found that the two dimensional Gaussian function (ref.11)

$$f(u,v) \approx \frac{1}{2\pi\sigma u\sigma v\sqrt{1-\rho^2}} \cdot \exp\left\{\frac{-1}{2(1-\rho^2)} \cdot \left[\left(\frac{u-\bar{u}}{\sigma u}\right)^2 - 2\rho\frac{u-\bar{u}}{\sigma u}\frac{v-\bar{v}}{\sigma v} + \left(\frac{v-\bar{v}}{\sigma v}\right)^2\right]\right\} \quad (2)$$

approaches very closely most of all probability distributions measured within turbulent flows. The mean velocity components of this distribution u and v, the turbulence intensities $Tu = \sigma u/\sqrt{\bar{u}^2+\bar{v}^2}$ and $Tv = \sigma v/\sqrt{\bar{u}^2+\bar{v}^2}$ and the Reynolds shear stresses $\mathrm{Re} = \sqrt{\sigma u \cdot \sigma v \cdot \rho}/\sqrt{\bar{u}^2+\bar{v}^2}$ are well known - σu, σv are the variances and ρ the correlation factor.

Integrating $f(u,v)$ along u and v one gets the density functions

$$Fu(u) = \int_{-\infty}^{+\infty} f(u,v)\ dv \quad (3)$$

$$Fv(v) = \int_{-\infty}^{+\infty} f(u,v)\ du \quad (4)$$

If a new two dimensional function is defined by

$$f_1(u,v) = Fu(u) \cdot Fv(v) \quad (5)$$

the calculations lead to the same mean velocity components and turbulence intensities as above. Further information about the flow – e.g. the Reynolds stresses – is not contained within the density function. If it would be easier to measure density distribution rather than the two dimensional probability distribution this would be a possibility for reducing the measuring time because sufficient information is contained in these.

By the L2F-method, however, the time of flight and the flow angle and not the cartesian components u,v are measured. The resulting probability distribution $p(t,\alpha)$ is really not Gaussian shaped such that the assumption of the aforementioned derivation is not fulfilled.

When applying the density functions

$$p\alpha(\alpha) = \int_0^{+\infty} p(t,\alpha)\ dt \quad (6)$$

$$p_t(t) = \int_0^{2\pi} p(t,\alpha)\ d\alpha \quad (7)$$

and calculating mean values $\bar{u}$, $\bar{v}$, Tu, Tv from

$$p_1(\alpha,t) = p_\alpha(\alpha) \cdot p_t(t) \quad (8)$$

by use of equation (1) errors might occur. To get an estimation of the amount of error, a model calculation was carried out. The two dimensional Gaussian function (2) was presumed such that the correct mean values are known. When transforming $f\ (u,v)$ into t,α-coordinates by use of $u = s \cdot \cos\alpha/t$ and $v = s \cdot \sin\alpha/t$ - s is the beam separation - one gets the function p(α,t) which agrees very well with the measured distributions. Applying equation (6) and (7) by replacing $p_1(\alpha,t)$ (equation (8)) into equation (1) mean values of the velocity components have been calculated, which were compared with the correct one. The results of this model calculation are shown in Fig.10. Different relative errors are plotted against the correct turbulence intensity. The correlation factor was also varied. Limiting the error to ± 1 percent of the mean velocity components and ± 5 percent of the turbulence intensities the calculation based on the density

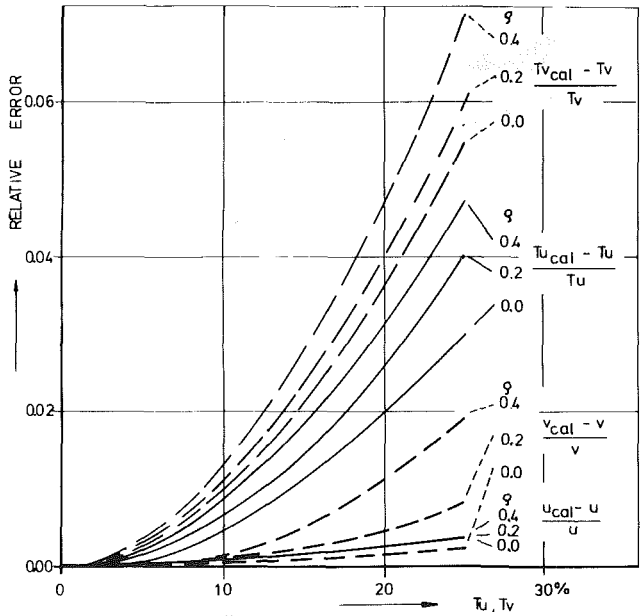

Fig. 10 Relative error of velocity mean values which were calculated from density function plotted against the correct turbulence intensity

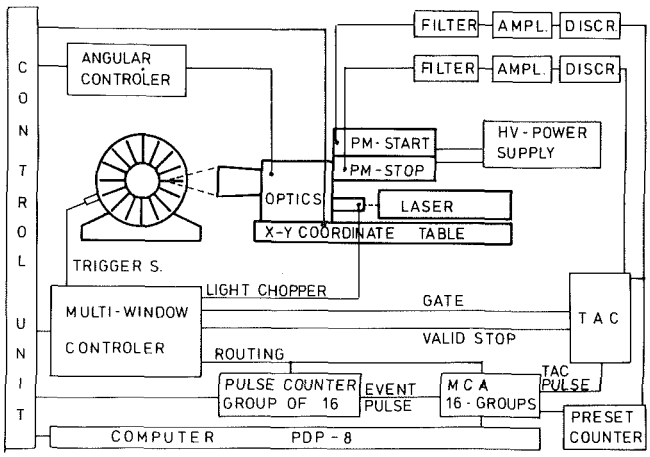

Fig. 11 Scheme of the new automated L2F-measuring system

function $p_\alpha(\alpha)$ and $p_t(t)$ is sufficiently accurate in practice up to turbulence intensities of 20 percent.

Similar small errors occurred when, based on experimental probability distributions, calculations were carried out in two different ways. One was to fit the measured data with a two-dimensional probability function and the other was to integrate the t and α coordinates separately to get two density distributions $p_\alpha(\alpha)$ and $p_t(t)$ and the fitting these by independent single variable functions.

However the main important result was that the number of data which are required to fit the density functions $p_\alpha(\alpha)$ and $p_t(t)$ with sufficient accuracy is much less than that required for fitting the two dimensional function. By the second approach, poorly defined individual distributions are integrated into a well defined density distribution.

Therefore, summing of the measured data into density functions yields a reduction of measuring time of nearly 10 and only about 200 particles are now required for each angle setting. By this way the most productive measuring time reduction was achieved. For directly measuring the two density functions $p_\alpha(\alpha)$ and $p_t(t)$, including the multi window operation and an automated measuring process, new electronics have been developed and are described below.

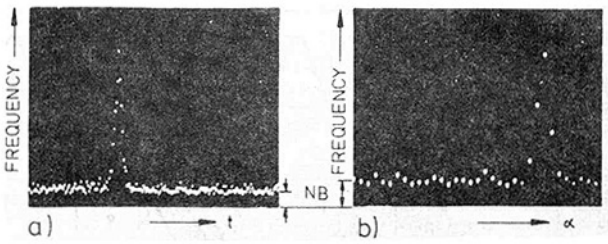

Fig. 12 Measured density distributions

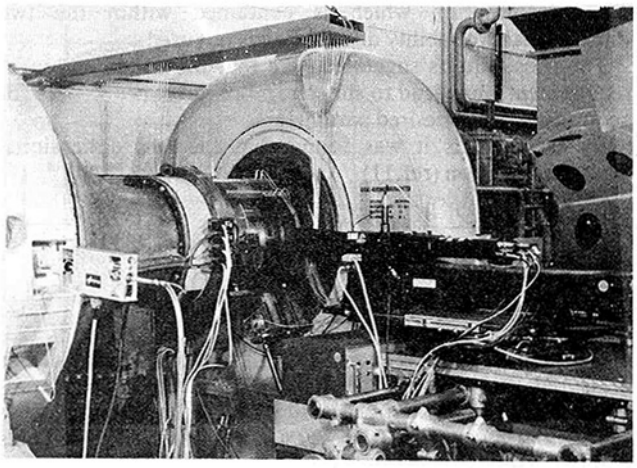

Fig. 13 L2F-velocimeter operating on the single stage transonic axial compressor

L2F-Measurement and Control System

Figure 9 shows the scheme of the complete system. The analog signal chain from the photomultipliers up to the time to pulse height converter (TAC) has undergone little change. New low pass filters are used. The multi window controller (MWC) was developed. A trigger signal from the rotor is used to synchronize the timing (see Fig.8). The laser beam as well as the TAC is switched off during blade passages through the probe volume by means of the light chopper and the gate signal. Depending on the occurrence of a stop event-valid stop signal from the TAC – the MWC determines the respective circumferential position and selects – as it is directed by a routing signal – a corresponding group within each of the 16 MCA memory groups and the 16 pulse counters to enable it for measurement.

When the velocimeter was positioned at a certain axial and radial position by controlling the x-y-coordinate table, a suitable angle range for setting the plane of the beams must be chosen by the operator. Because of the strong flow angle variation from suction to pressure surfaces this range can be selected rather wide (about 70 to 100°) in as much as no careful estimation of the mean flow direction is necessary. After the beams' plane has been set to the first angle the measurement starts. The times of flight measured by the TAC are stored into the different groups of the MCA while the measuring events - only logic pulses without the time of flight - are counted by the respective pulse counter.

If the number of all measuring events achieves a preset number - it is selected on the preset counter - the set angle is increased by + 1°, the contents of the 16 counters is transferred into the computer and the measurement continues. The new time interval data now are added to the different contents of each MCA memory group while the group of counters which have been reset start again counting only the events. In such a way the measurement continues until the last angle of the chosen range is set. Within each of the 16 groups of the MCA a probability distribution of the time interval data is measured which corresponds to the density function $p_t(t)$ (Fig. 12(a)).

To explain the function of the counters we will discuss only one of the 16 counters. The number of measuring events which were counted at each angle setting is precisely the integral of all time interval data measured within the corresponding group of the MCA. If the different contents of the counters are plotted against α, one gets a distribution which represents the density function $p_\alpha(\alpha)$ (Fig. 12(b)).

While the next measuring cycle is running, the computer calculates $\bar{u}$, $\bar{v}$, Tu and Tv out of every two corresponding density distributions of the first set of data such that, after the second measuring cycle is finished, the flow data of 16 different circumferential positions are available.

By increasing the time delay by 1/32 of a period at the same probe volume location, another 16 measuring points just between each of the 16 previous ones can be determined such that 32 measuring points over the blade pitch are selectable.

Control of the measuring process as well as the performance of all mathematical calculation is currently carried out by a PDP-8 computer of 32 KW capacity. A further decrease of the overall measuring time can be expected by use of a PDP-11 which enables the time saving interrupt programming.

Experimental Results

The L2F-velocimeter with the new automated measuring procedure was applied to the same transonic axial compressor in order to check the estimated measuring error and to determine the real measuring time reduction.

Figure 13 shows the L2F-velocimeter acting on the compressor test rig for rotor flow measurements. The measuring device was arranged with the new collimator and a 150 mW argon laser. Due to the replacement of the former beam rotating device - a stepping motor is now used - the optical head was completely rearranged.

Tests have been run at 20,000 rpm. The operational point close to surge line - 15.93 kg/s - was chosen for comparing the measured data with former test results. The probe was located at 63 percent blade height just in front of the leading edges of the rotor blades.

Figure 14 shows the measured relative Mach numbers which are plotted against the dimensionless blade pitch. The circles and triangles indicate the new automated measurements while the solid circles represent former measurements which have been carried out by the single window operation. The new data were deduced presuming the automated measured density distribution while the former ones have been calculated presuming the two dimensional density function. Both results agree within an error range of 1 percent. This is also true when the reproducibility of two runs of the automated measurements is considered. In spite of changes of optics, of electronics, of calculation methods and of manner of operation the resultant uncertainty was not further increased when comparing it with the error of former compressor measurements (reference [4]).

To get a reliable estimate of the measuring time, a series of tests have been run. The flow field within one blade passage measured at 89 percent of blade height with the compressor operation point close to the surge line is shown in Fig.15. The lines of constant relative Mach number illustrate the complex flow within a transonic rotor, e.g. shock location, wake region. This figure – the results of which agree very closely to

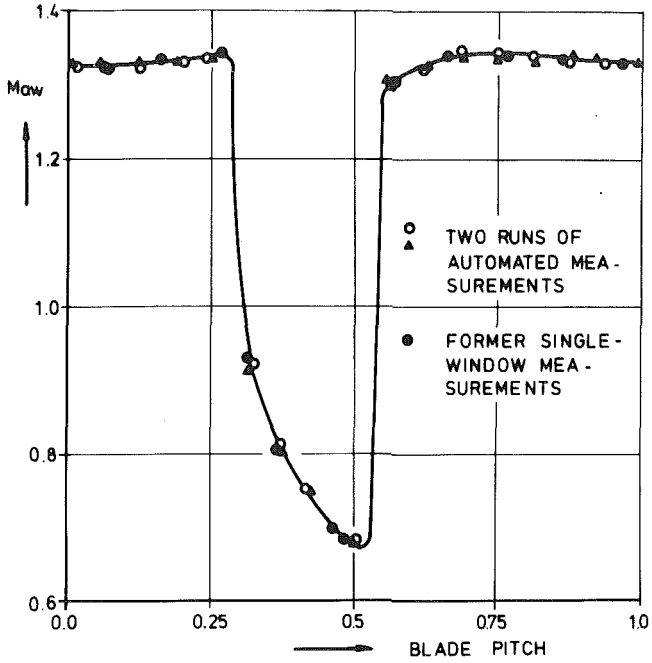

Fig. 14 Comparison of formerly and newly measured relative Mach numbers over the blade pitch (probe position close to the blade leading edges at 63 percent blade height - 100 percent speed)

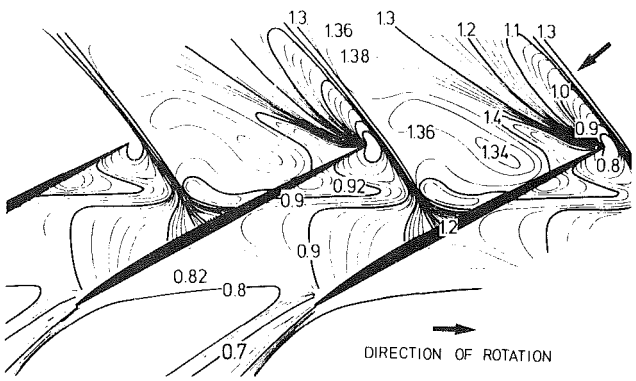

Fig. 15 Lines of constant relative Mach number through the blade passage at 89 percent blade height (100 percent speed)

the former measurements – was drawn using 300 measurements.

In the past about 4 days of operation (nearly 30 hours) were needed to obtain the same number of data. By the new automated measuring procedure, however, this time was reduced to only 2 1/2 hours, indicating an improvement by a factor of 12. Although the flow was not artificially seeded, a single measurement takes only an average of 0.5 minutes, including the calculation time.

Conclusion

Former tests have demonstrated the special advantages of the L2F-velocimeter as

1. the capability of measuring very high velocities (Ma > 2),
2. the advantage of a very good background noise reduction allowing near wall measurements and
3. the high sensitivity which enables even in backscattering the detection of 0.1 μm particles which allow good flow-following.

Due to the favorable properties and due to the stable optical construction which render operations under high noise and vibrational environment the L2F-velocimeter is found to be a useful tool for flow measurements within turbomachines.

To overcome the former disadvantage of a rather long measuring time, an advanced automated L2F-system was developed. A measuring time reduction of a factor of 12 was achieved while maintaining measuring accuracy. The automated computer controlled operation enables measurements at 32 distinct positions over one blade pitch.

The measuring time was reduced to about 0.5 minutes per measuring point and in addition - due to the improved optics - the minimum distance of approaching a wall was reduced to about 0.5 mm. This improved L2F-velocimeter - which is commercially available - will help to get more detailed information about the real flow within turbomachines in the future.

References

1 Various Authors, "Laser Optical Methods for Aero Engine Research and Development," AGARD-LS-90, 1977.

2 Schodl, R., "Laser-Dual-Beam Method for Flow Measurements in Turbomachines," ASME Paper No. 74-GT-157, p. 7.

3 Schodl, R., "Laser-Two-Focus Velocimetry for Use in Aero Engines," *Laser Optical Measurement Methods for Aero Engine Research and Development,* AGARD-LS-90, 1977, pp. 4.1-4.34.

4 Schodl, R., "Development of the Laser Two-Focus Method for Nonintrusive Measurement of Flow Vectors, Particularly in Turbomachines," ESA-TT-528, 1979.

5 Eckardt, D., "Detailed Flow Investigations Within a High-Speed Centrifugal Compressor Impeller," ASME JOURNAL OF FLUIDS ENGINEERING, Vol. 98, No. 3, Sept. 1976, pp. 390-402.

6 Weyer, H.B. and Dunker, R.J., "Dual Beam Laser Anemometry Study of the Flow Field in a Transonic Compressor," *Secondary Flows in Turbomachines,* AGARD-CP-214, 1977, pp. 8.1-8.11.

7 Krain, H., and Eckardt, D., "The Flow Field in a High-Speed Centrifugal Compressor Impeller, A Comparison of Experimental and Theoretical Results," *Proceedings of the First International Conference on Centrifugal Compressor Technology,* Madras, 1978, pp. B1-25.

8 Dunker, R.J., Strinning, P.E., and Weyer, H.B., "Experimental Study of the Flow Field Within a Transonic Axial Rotor by Laser Velocimeter and Comparison With Through Flow Calculations," ASME Paper No. 77-GT-28, 1977.

9 Rotta, J.C., *Turbulente Strömungen,* Teubner, Stuttgart, 1972, pp. 15-25.

10 Helsper, C., and Fissan, H.J., "Bestimmung der Teilchengrößenverteilung in einem Hochgeschwindigkeitsgitterwindkanal der DFVLR-Braunschweig," Bericht No. 19, 1977, Institut fur Aerosolmesstechnik, Gesamthochschule Duisburg.

11 Rasch, D., "Einführung in die mathematische Statistik," Band 1, V.E.B., Berlin 1976, pp. 147-152.

Velocity and Pressure Distributions in the Impeller Passages of Centrifugal Pumps

M. Murakami
Professor.

K. Kikuyama
Associate Professor.

E. Asakura
Research Engineer.

Department of Mechanical Engineering,
Nagoya University,
Nagoya, Japan

The flow patterns in centrifugal pump impellers with three and seven blades, respectively, were measured using a cylindrical yaw probe and an oil surface flow method. The measured distributions of velocities and pressures for the seven (sufficient number) blade impeller at the design flow rate coincide well with the numerical solution obtained from the theoretical equation based on a potential flow. The flow patterns of the three (insufficient number) blade impeller deviate largely from those of the seven blade impeller both at the design and off-design conditions. The values of the slip factor deduced from the data of velocity measurements in the impeller passage were compared with those calculated by commonly-used formulae, and considerably good agreement was obtained for the seven blade impeller.

Introduction

The increase in capacity and speed of turbomachines has given rise to an earnest demand for more detailed knowledge of the flow patterns in the impellers in order to design more efficient machines. Many experimental studies of the distributions of velocities and pressures in the impeller passage have been performed in the past. Ellis [1], Fujie [2], and Hamrick [3], respectively, measured velocity and pressure distributions in impeller passages by means of yaw meters and Pitot probes, and found that secondary flow created by a Coriolis acceleration developed toward the channel outlet, resulting in an accumulation of low energy fluids in the suction side of the passage. Howard and Kittmer [4] measured the velocities (including both primary and secondary flow components) in an impeller passage using a hot film method and a flow visualization technique, and discussed the difference between the secondary flows generated in a shrouded and an unshrouded impeller. Eckardt [5] recently measured the distributions of velocities and turbulence in an impeller of a centrifugal compressor employing a laser velocity meter and discussed the effects of channel curvature and system rotation on the secondary flow and turbulence.

In the past decade [6] great advancement has been made using another approach to the same problem, the application of a numerical method to the flow in an impeller in an invisid condition. This method was applied to the impeller in two or quasi-three dimensional forms and produced fairly good result at the design condition. However, it failed to give a precise prediction of flow patterns at off-design conditions.

Moore [7] made a calculation for a rotating, radial flow passage taking into account the viscosity of fluids. The flow model obtained by this method gives a good approximation for a separation point on the suction side of the wall, toward which low energy fluids are driven by secondary flows.

Much more detailed experimental work on the flow patterns in impellers of various blade shapes and numbers is required in order to promote further progress of numerical calculations. Research of this sort is also necessary to further understanding of pumps dealing with multi-phase fluids. In this case, a decrease in blade number may bring about some improvements in the pump head [8].

The present paper describes the results of measurement of velocities and pressures in centrifugal pump impellers having various blade numbers. Measurements were performed at both design and off-design conditions. A discussion is given for the flow patterns obtained from a cylindrical yaw probe measurement and an oil flow method.

Apparatus and Experimental Method

Impeller Employed. The dimensions and specifications of the impellers tested are given in Fig. 1. Two impellers with three and seven blades, respectively, were employed to check the effects of the number of the impeller blades. Velocity measurements were performed at the radial sections of $r/r_2 =$ 0.44 (impeller inlet), 0.53, 0.70, 0.80, 0.90, and 0.99, where a yaw probe was traversed along the lines parallel to the impeller axis in the regions of the suction side (S), center (C), and pressure side (P), respectively. Additional measurements along the lines S' and P' were also made for the impeller of $Z = 3$. The pressures on the passage wall were measured at the same radial positions as the velocity measurement on both the shroud and hub as well as on the blade surfaces. The distributions of the total pressure loss at each section of the

Contributed by the Fluids Engineering Division of THE AMERICAN SOCIETY OF MECHANICAL ENGINEERS and presented at the Symposium on Measurement Methods in Rotating Components of Turbomachinery, Gas Turbine and Fluids Engineering Conference, New Orleans, La., March 10–13, 1980. Manuscript received by the Fluids Engineering Division, September 1979.

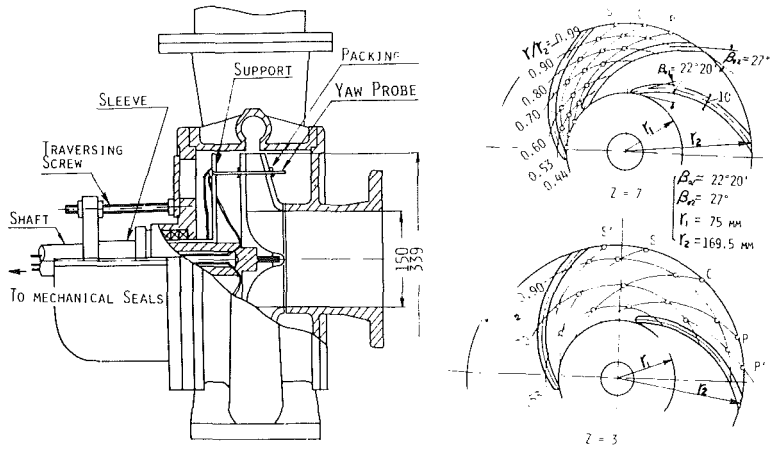

Fig. 1 Apparatus for measuring velocities and impeller tested

impeller passage were obtained from the data of the velocity and static pressure measurements.

This experiment was carried out at a rotational speed of n = 400 rpm, at which the similarity law in the pump performance was ascertained to be established. The flow rate corresponded to ϕ/ϕ_m = 1.28, 1.0, 0.65, 0.33 for the impeller of Z = 7, and ϕ/ϕ_m = 1.05, 1.0, 0.65, amd 0.33 for the impeller of Z = 3, where ϕ_m is the discharge coefficient at each maximum efficiency point, and has an approximate value of 0.098 for both the pumps having the impellers of Z = 3 and 7.

Method of Measurements in the Rotating System. A cylindrical three-hole yaw probe, the diameters of the tube and holes being 2.5 mm and 0.3 mm, respectively, was employed for velocity measurement in the rotating impellers. A schematic outline of the measuring devices is shown in Fig. 1. The yaw probe mounted on a support was fixed to a sleeve which was again mounted on the pump shaft so as to be able to slide smoothly along the shaft during the impeller rotation. The yaw probe thus designed was inserted into the impeller passages through holes on the shroud and hub. The leakage along the probe stem was avoided by rubber packings as shown in Fig. 1. Change in flow patterns in the impeller due to the insertion of the probe was small enough to neglect its effects. The pressures taken by this yaw probe were conducted to mechanical seals through a perforation in the pump shaft, and then transferred to manometers in the stationary system.

The characteristics of the cylindrical yaw probe were calibrated carefully in the stationary system before proceeding with the experiment. The results are given in Fig. 2. The flow angle relative to the bisector of the two diameters going through the holes (2) and (3) is plotted against a parameter defined by $(h_{1-2} - h_{1-3})/(h_{1-2} + h_{1-3})$, where h_{1-2} and h_{1-3} represent the differences of the pressure heads measured at the taps (1) and (2), and the taps (1) and (3), respectively. It was observed that the deviated angle θ can be accurately determined by measuring the values of h_{1-2} and h_{1-3}, if θ is in the range of $-15° \leqq \theta \leqq 15°$ and the probe Reynolds number is in the range of $2 \times 10^3 \leqq \mathrm{Re_p} \leqq 10^4$. The error due to the pitch angle deviations in the velocity measurement was less than 5 percent, when the angle deviation was within the range of $\pm 20°$.

Thus, the yaw probe at a measuring point was aligned at first in the direction parallel to the impeller blade curvature and the flow velocity there could be determined by use of the results in Fig. 2, if θ and Re_p were in the limiting range as described above. If the amount of the dislocation, θ, exceeds 15°, the setting angle of the probe was adjusted so that θ fell in the available range.

Now, the flow velocity can be calculated using the known values of θ and h_{1-2} or h_{1-3}, by

$$V = C_1 C_p \sqrt{2gh_{1-2}} \quad (1)$$

$$= C_2 C_p \sqrt{2gh_{1-3}} \quad (2)$$

Nomenclature

A = area of the impeller exit
$= 2\pi r_2 h_2$
C_1, C_2 = coefficients of yaw probe
h = height of blade
h_{1-2}, h_{1-3} = pressure heads of yaw probe
P = static pressure
P_0 = static pressure at the center of the inlet section
P_t = relative total pressure
P_{t0} = relative total pressure at the center of the inlet section
Q = volumetric flow rate
r = radius of the measuring position
r_1 = radius of the passage inlet
r_2 = radius of the passage exit
Re_p = Reynolds number of cylindrical yaw probe
U_2 = peripheral speed at the passage exit
V = relative velocity component normal to W
W = relative velocity component along the blade
y = normal distance measured from the shroud
Z = number of blades
β_2 = flow angle at the exit
β_{02} = blade angle at the exit
ζ = coefficient of total energy loss
$= [\{P_{t0} - \rho(r_1\omega)^2/2\} - \{P_t - \rho(r\omega)^2/2\}]/(\rho U_2{}^2/2)$
μ = slip factor
ρ = density of fluid
ω = angular velocity of the impeller
θ = flow angle relative to yaw probe
ϕ = coefficient of flow rate, (Q/AU_2)
ϕ_m = value of ϕ at maximum pump efficiency
ψ = coefficient of pressure head
$= (P - P_0)/(\rho U_2{}^2/2)$

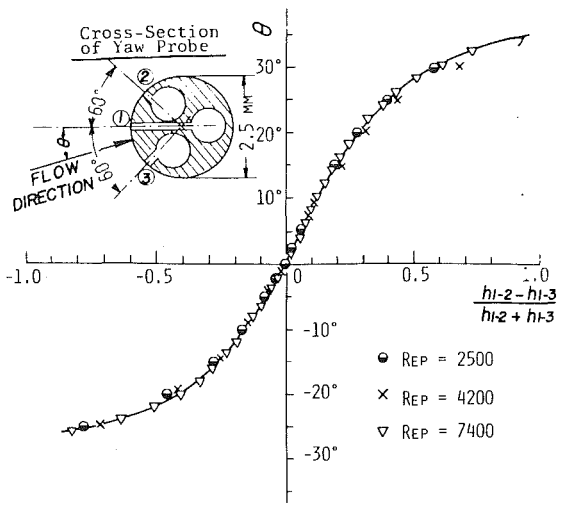

Fig. 2 Calibration curve of cylindrical yaw probe

where the constants C_1 or C_2 are given as a function of θ, and C_p is a velocity coefficient of the probe given as a function of probe Reynolds number and can be determined experimentally in the stationary state when $\theta = 0°$. Static pressures on the passage walls of the impellers were transferred to manometers in the stationary system by means of mechanical seals.

Flow Visualization by Surface Oil Flow Method. Velocity measurement by the yaw probe was either not accurate or impossible in the range near the wall or in the separated flow region. The flow visualization was made at the flow rates of $\phi/\phi_m = 1.0$, 0.65, 0.33, and 0.10 for both the impellers of $Z = 3$ and 7. The oil used was composed of paraffin liquid, carbon black, and oleic acid, the ratio of which was 15 : 5 : 2 by weight. A precoating of automobile oil under the oil sheet was used in order to obtain clear streamline patterns on the impeller walls. The oil surface thus prepared was exposed to a flow of water for fifteen minutes or a little more.

Uncertainties of Experimental Data. The volumetric flow rate of the pumps was measured by an orifice and a manometer, and limit of the coefficient of flow rate ϕ was ± 2 percent. The measurement of the angle and the magnitude of the flow velocity was made by a yaw probe, in which the calibration curves were used. The limit of uncertainty in the flow velocity and angle in the central region of a section for design flow rate were ± 5 percent and ± 2 degrees, respectively. Near the passage wall and the separated region observed at off-design conditions, the error in velocity measurement increased more on account of the large velocity gradient. To check the accuracy of the velocity measurement, the total flow rate through the impeller was assumed from the data of a local flow rate obtained from the graphical integration of velocity profiles in a channel section of $r/r_2 = 0.53$ for each impeller. The difference in the flow rates of the impeller by an orifice flow meter and by this method was less than 7 percent, when $\phi/\phi_m = 1.0$ and 0.65 for the seven blade impeller.

Experimental Results and Discussion

Velocity Distributions in the Impeller of $Z = 7$. The change of flow pattern along the impeller passage is shown in Figs. 3 (*a*) and (*b*) for the optimum efficiency flow rate. At the inlet section of the impeller channel, $r/r_2 = 0.44$, where the flow has just been turned radially from an axial direction, the relative velocity is larger in the low pressure side, and a displacement of flow due to the thickness of the impeller

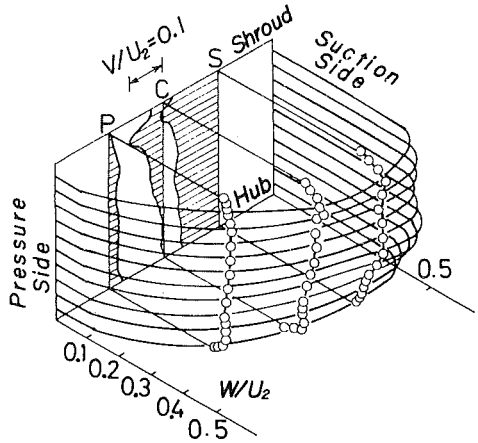

Fig. 3(*a*) Velocity distribution for $Z = 7$ ($\phi/\phi_m = 1.0$ and $r/r_2 = 0.44$)

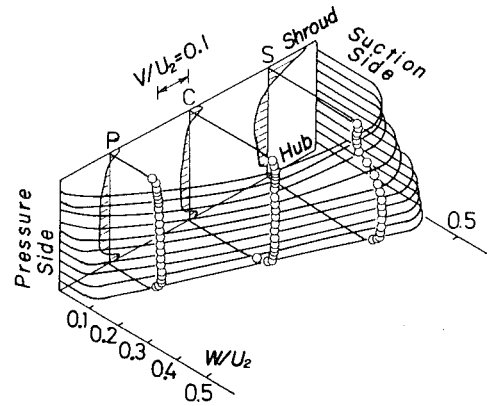

Fig. 3(*b*) Velocity distribution for $Z = 7$ ($\phi/\phi_m = 1.0$ and $r/r_2 = 0.70$)

blades occurs, as is seen clearly in the distribution curves of the secondary flow at the positions of S and P. At the section of $r/r_2 = 0.70$, the main flow velocity has an almost linearly distributed profile and the cross flow caused by the displacement of the blade thickness disappears. Instead, a typical secondary flow directed to the pressure side in the central zone is observed. At this section a low velocity region is created near the suction side of the shroud. This is attributed to a wake caused by the rapid change of flow direction at the channel inlet. The turbulence of flow in the suction side of the channel is largely suppressed by the system rotation and the lower energy fluids which are brought there by the secondary flow stay stably along the suction side of the channel.

When the flow rate ϕ/ϕ_m is reduced to 0.63, the flow pattern changes greatly from that at the optimum efficiency point as shown in Fig. 4. A remarkable decrease in flow velocity at the inlet near the shroud brings about a clockwise secondary flow in the central zone of the section. At the section of $r/r_2 = 0.70$, the flow velocities in the low pressure side decrease considerably and the main flow is shifted to the pressure side. It was observed using the visualization method that a wake which initially formed on the shroud surface at the section of $r/r_2 = 0.44$ grew in dimension towards the suction side of the impeller blade till it reached the hub at about $r/r_2 = 0.71$. An example of streamlines on the hub surface obtained by the oil flow method is shown in Fig. 5, when $\phi/\phi_m = 0.33$. A wake created on the leading edge of the shroud reaches the hub in the suction side at about $r/r_2 = 0.7$, where the secondary flow and hence, the supply of lower energy fluids in the suction side is maximum. The reduction of

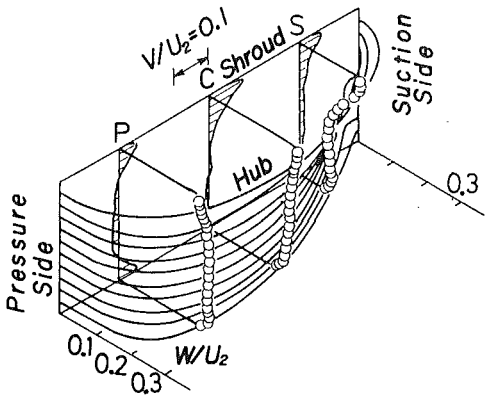

Fig. 4 Velocity distribution ($Z = 7$, $\phi/\phi_m = 0.65$, and $r/r_2 = 0.70$)

the wake near the exit of the channel is due to the reduction in the supply of low energy fluids, which continuously flow there through the boundary of the forward and reverse flows. Near the passage exit, the constraint of blades on the flow decreases and the flow near the hub is no longer directed towards blade surface, but towards the exit as shown in Fig. 5. This change of direction in the flow near the passage walls causes a decrease in the amount of lower energy fluids supplied to the wake.

In order to examine the effects of the volute casing on the flow leaving the impeller, velocity distributions at the section of $r/r_2 = 0.99$ were measured for the flow rates of $\phi/\phi_m = 1.0$ and 0.65. The results are shown in Figs. 6 (a) and (b), respectively. When $\phi/\phi_m = 1.0$, the fluid seems to leave the impeller in a nearly uniformly distributed condition everywhere except in a small region near the suction wall. A secondary flow directed towards the pressure side results from the pressure difference at the impeller tips. Such a secondary flow is developed at points P and C in the section of $r/r_2 = 0.90$. Figures 6 (a) and (b) show that a slip of the flow has already occurred at the section in the impeller where the effect of the constraint of the blades on flow is almost nonexistent at the suction side.

When the flow rate is reduced to $\phi/\phi_m = 0.65$, flow velocities near the suction side decrease remarkably and the resultant velocity vector at the point S lies in a direction tangent to the periphery of the impeller. Thus, it is seen that the fluid in the suction side region comes over the blade tip from the pressure side of the neighbouring passage. A distinct black streamline near the pressure side of the passage in Fig. 5 shows a locus of the stagnation points in the boundary layer, on which the secondary flow coming from the pressure side along the hub and the flow coming from the neighboring passage meet. From these stagnation points in the boundary layer, the flow leaves the surface and proceeds towards the volute region.

Velocity Distributions in the Impeller of $Z = 3$. Figures 7 (a) and (b) show a change of flow patterns along the passage, when $\phi/\phi_m = 1.0$. At the section of $r/r_2 = 0.53$, higher velocities prevail in the suction side, but in a region near the pressure side of the shroud, the flow stagnates and a reverse flow is generated. The number of blades ($Z = 3$) is not sufficient to constrain the flow in the impeller. As a result there is an increase in the acceleration of the flow in the suction side, and the velocity distribution at the section of $r/r_2 = 0.90$ near the impeller exit becomes rather flat. This even velocity profile may cause a reduction of mixing loss in the volute, and brings about a favourable effect in the pump efficiency.

An examination of the velocity profiles at $r/r_2 = 0.53$ shows that the flow tends to expand to the full width of the channel. A picture of the oil surface flow indicates that a wake is formed on the suction side of the passage just behind the inlet and hence, the effective area of flow is reduced there. This inlet wake shrinks rapidly in the downstream sections, and a corresponding increase in the effective area results.

Figure 8 exhibits the flow patterns at $r/r_2 = 0.90$, when $\phi/\phi_m = 0.33$. In this case, there is a great decrease in the flow velocities on both sides of the blades at the inlet but a comparatively flat velocity profile is attained at the downstream section of $r/r_2 = 0.90$. These results are confirmed by an oil

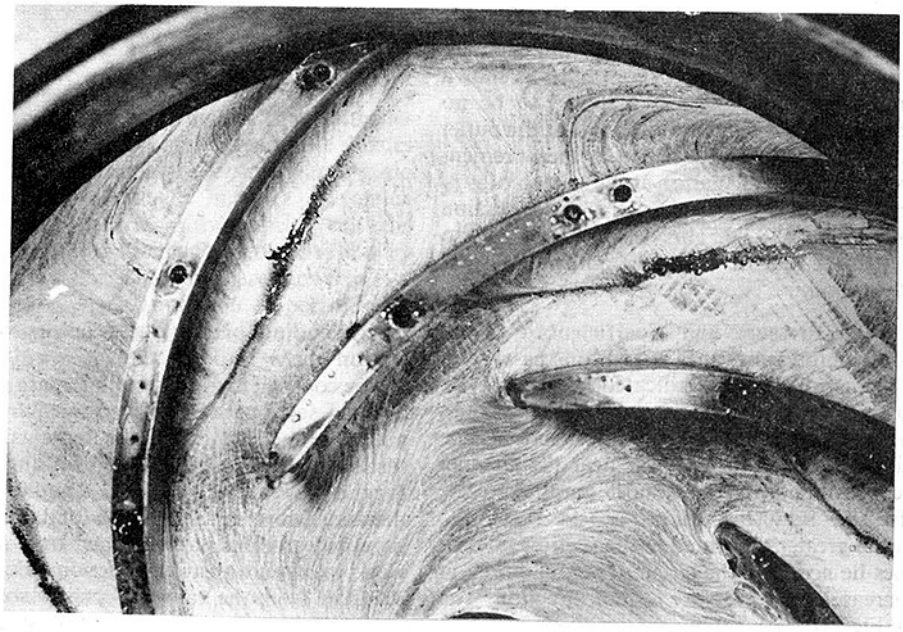

Fig. 5 Oil surface flow pattern on hub ($Z = 7$, $\phi/\phi_m = 0.33$)

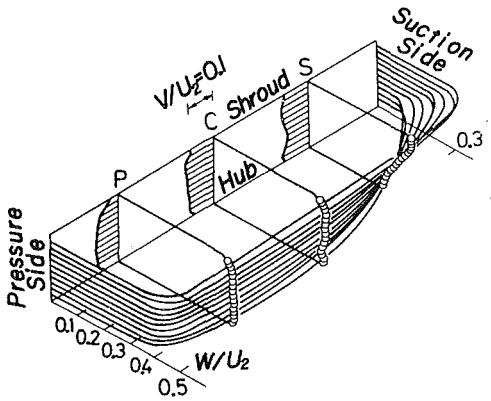

Fig. 6(a) Velocity distribution ($Z = 7$, $r/r_2 = 0.99$, and $\phi/\phi_m = 1.0$)

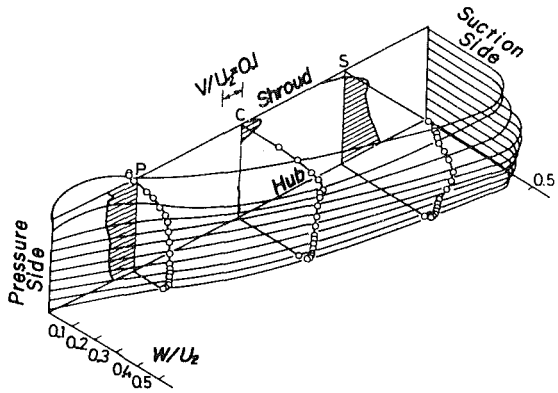

Fig. 7(a) Velocity distribution ($Z = 3$, $\phi/\phi_m = 1.0$, and $r/r_2 = 0.53$)

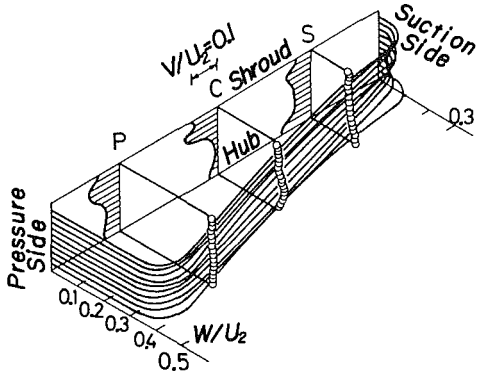

Fig. 6(b) Velocity distribution ($Z = 7$, $r/r_2 = 0.99$, and $\phi/\phi_m = 0.65$)

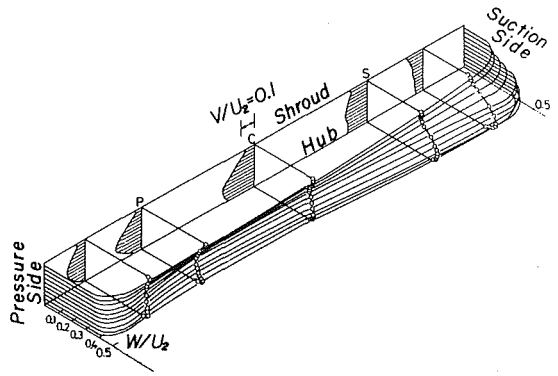

Fig. 7(b) Velocity distribution ($Z = 3$, $\phi/\phi_m = 1.0$, and $r/r_2 = 0.90$)

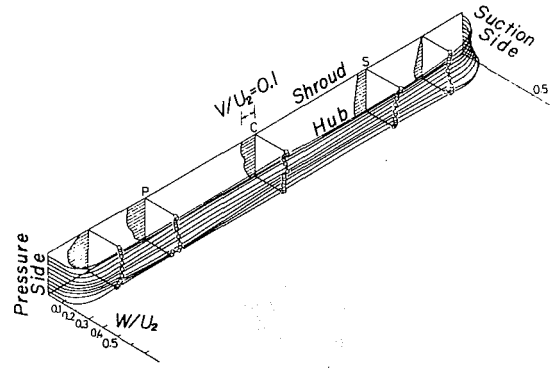

Fig. 8 Velocity distribution ($Z = 3$, $\phi/\phi_m = 0.33$, and $r/r_2 = 0.90$)

flow method as shown in Fig. 9. About half of the inlet section is blocked by the wake at the inlet section, and the wake shrinks rapidly to zero in the downstream sections. In this process the main flow shifts to the suction side and a comparatively flat velocity profile occurs near the impeller exit as is seen in Fig. 9. A comparison of the above flow patterns in the impeller of $Z = 3$ with those in the impeller of $Z = 7$ shows that the flow separation which appears in the impeller of $Z = 7$ may be avoided in the impeller of $Z = 3$.

Comparison Between Experimental and Calculated Results. Distributions of velocities in the seven blade impeller are calculated by Katsanis method (9) for $\phi/\phi_m = 1.0$ as shown in Fig. 10. In this calculation, there is assumed to be no prerotation in the inlet and the relative flow angle at the outlet is taken as 26°. The velocity curves obtained by measurement coincide well with those from calculation at the section of $r/r_2 = 0.70$, but a discrepancy occurs, especially in the suction side, in the section of $r/r_2 = 0.90$. This discrepancy is due to the secondary flow in the real flow, since a potential flow is assumed in the calculation.

Distributions of Wall Pressure and Coefficient of Total Pressure Loss. The equipressure lines drawn on the shroud surface of seven blade impeller are indicated in Figs. 11 (*a*) and (*b*), when $\phi/\phi_m = 1.0$ and 0.65, respectively. These lines are seen to be inclined in the circumferential direction. The angle of this inclination tends to be lower near the channel outlet, where the pressure lines are almost parallel to the circumference. In the flow rate of $\phi/\phi_m = 0.65$, the equipressure lines are greatly deformed in the suction side. In this range, the lines lie nearly in the circumferential direction and there is no increase in the pressure in that direction. The shaded region in Fig. 10 (*b*) shows the wake on the hub obtained by the oil flow method. The wake shrinks and a corresponding pressure rise occurs downstream from the section of $r/r_2 = 0.8$.

The coefficient of the total pressure loss, ζ, at a point in the channel section can be determined from the data on static pressure and velocity measurements. The results for the section of $r/r_2 = 0.70$ are shown dimensionlessly in Fig. 12 for the flow rate of $\phi/\phi_m = 1.0$ and 0.65. When $\phi/\phi_m = 1.0$, the dimensionless value of the total pressure loss, ζ, is seen to be nearly uniformly distributed over the section, showing a weak maximum near the suction side of the shroud. When $\phi/\phi_m = 0.65$, the values of ζ show some deviations and low energy fluids prevail in the suction side. In this case, lines of equal loss lie nearly parallel to the impeller channel.

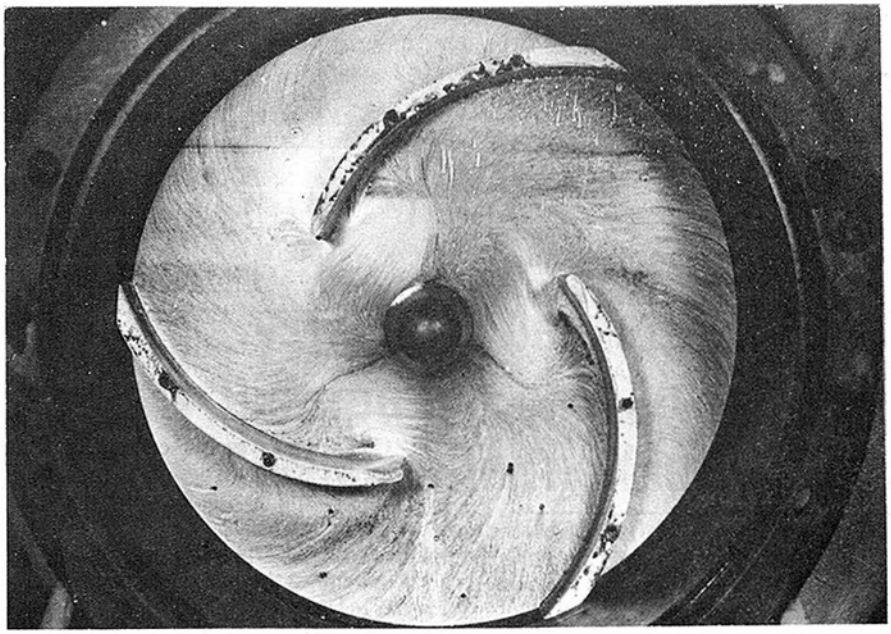

Fig. 9 Oil surface flow pattern on hub ($Z = 3$, $\phi/\phi_m = 0.33$)

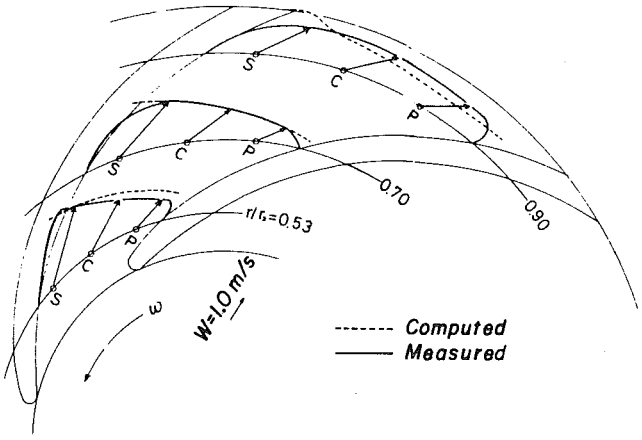

Fig. 10 Measured and computed velocity distributions ($Z = 7$ and $\phi/\phi_m = 1.0$)

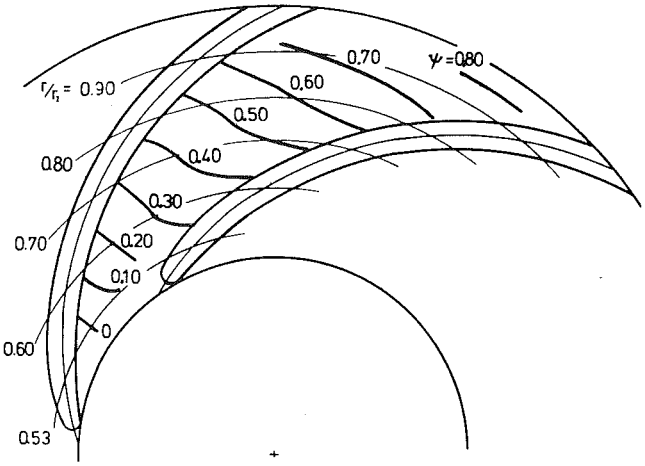

Fig. 11(a) Pressure distribution ($Z = 7$ and $\phi/\phi_m = 1.0$)

Relative Exit Flow Angles and Slip Factors. If the impeller blades are finite in number, the constraint of the blades exerted on the flow is insufficient and the fluid particles do not leave the impeller at the vane angle. In order to examine the mechanism of a slip in the flow at the impeller exit, the relative flow angles β_2 were measured at the section of $r/r_2 = 0.99$ just before the impeller exit. The results are shown in Fig. 13 for the flow rates of $\phi/\phi_m = 1.0$ and 0.65, respectively. In the case of design flow rate, $\phi/\phi_m = 1.0$, the angle β_2 is distributed almost uniformly along the arc from hub to shroud, and a slight increase in the angle is seen near the walls, exhibiting an effect of the secondary flows.

In the case of an off-design condition of $\phi/\phi_m = 0.65$, a remarkable reduction of β_2 is observed in the region near the shroud. The negative values of β_2 at the points S and C may result from the fact that the fluid coming from neighbouring passages over the blade tips enters the lower pressure region in that passage, thus creating reverse flow.

A slip factor μ can be determined from the results in Fig. 13 by taking account of the velocity distribution, and the results for the impellers of $Z = 7$ and 3, respectively, are shown in

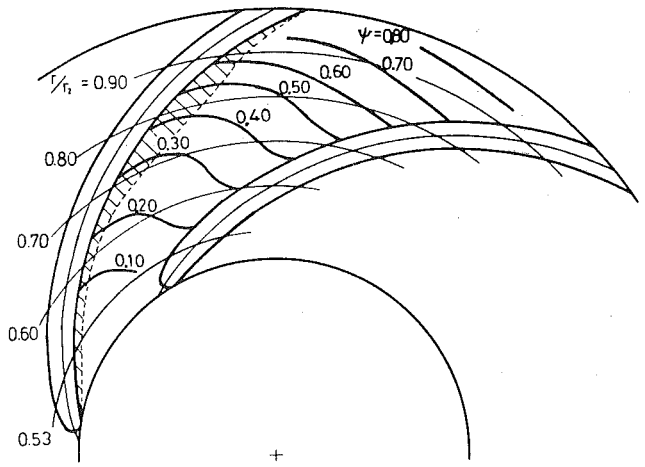

Fig. 11(b) Pressure distribution ($Z = 7$ and $\phi/\phi_m = 0.65$)

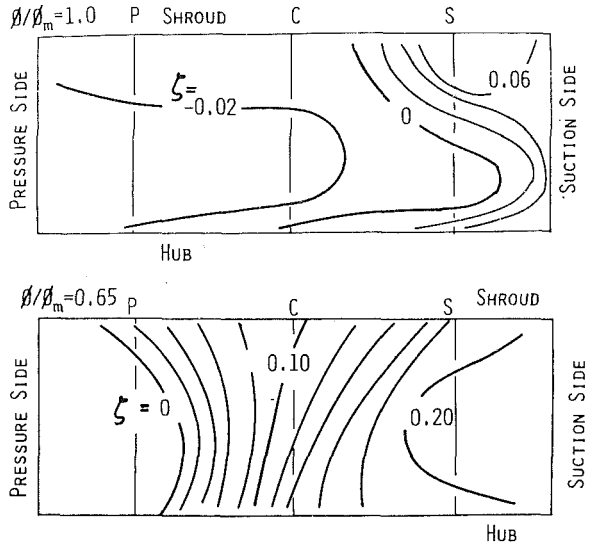

Fig. 12 Total pressure loss at r/r_2 = 0.70 for Z = 7

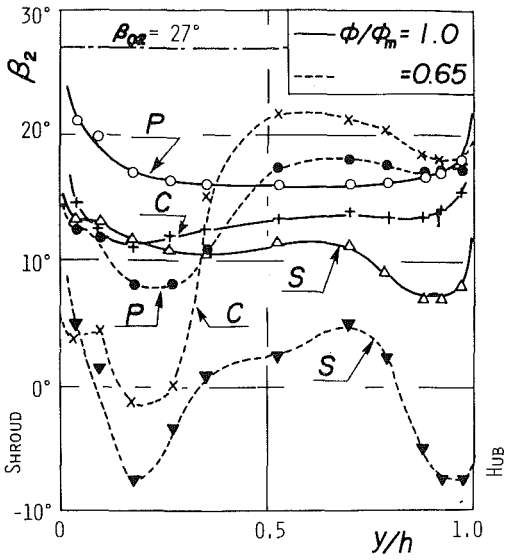

Fig. 13 Relative flow angle at impeller exit for Z = 7

Fig. 14, where each value of μ is averaged by weighting the velocity distributions. The value of μ in the impeller of Z = 3 is always less than that in the impeller of Z = 7. For reference, the values of the slip factors calculated by Stodola [10] and Busemann [11] formulas are also plotted in Fig. 14. Greater agreement is observed for the impeller of Z = 7. In the impeller of Z = 3, the experimental values are considerably larger than the calculated ones, due to the extreme shift of flow toward the suction side of the passage caused by the rapid shrink of the inlet wake.

Conclusions

The results of measurements of velocities and pressures in centrifugal pump impellers with three and seven blades, respectively, are summarized as follows:

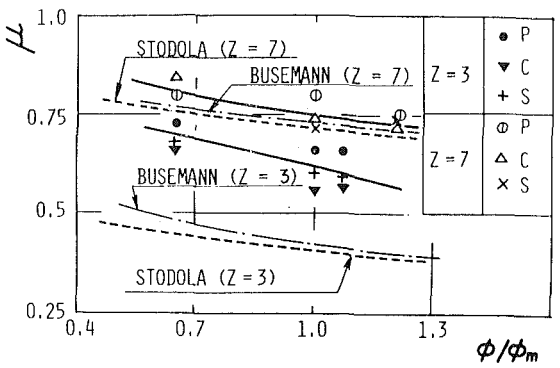

Fig. 14 Slip factor

(1) In the seven blade impeller, almost ideally distributed velocities are observed in the upstream half of the impeller passage, and in the downstream half the distributions are deformed considerably by the secondary flow developed along the passage. The deformation of velocity distributions is extreme in the case of the three blade impeller.

(2) The slip factor deduced from the data of velocity measurements at the sections just before the impeller exit coincides well with that calculated by Stodola and Busemann formulae, respectively, for the seven blade impeller.

Acknowledgment

The authors wish to express their appreciation to Mr. T. Inagaki and Mr. N Kanzaki for their experimental work while carrying out this study.

References

1 Ellis, G. O., "A Study of Induced Vorticity in Centrifugal Compressors," ASME *Journal of Engineering for Power,* Vol. 86, No. 1, 1964, pp. 63-76.

2 Fujie, K., "A Study on the Flow in a Centrifugal Impeller with Passages of Circular-Arc in Meridional Plane," *Bulletin of the Japan Society of Mechanical Engineers,* Vol. 4, No. 13, 1961, pp. 94-101.

3 Hamrick, J. T., "Some Aerodynamic Investigations in Centrifugal Impellors," ASME *Journal of Engineering for Power,* Vol. 78, No. 3, 1956, pp. 591-602.

4 Howard, J. H. G., and Kittmer, C. W., "Measured Passage Velocities in a Radial Impeller With Shrouded and Unshrouded Configurations," ASME *Journal of Engineering for Power,* Vol. 97, No. 2, 1975, pp. 207-213.

5 Eckardt, D., "Detailed Flow Investigations Within a High-Speed Centrifugal Compressor Impeller," ASME JOURNAL OF FLUIDS ENGINEERING, Vol. 98, No. 3, 1976, pp. 390-402.

6 Japikse, D., "Review — Progress in Numerical Turbomachinery Analysis," ASME JOURNAL OF FLUIDS ENGINEERING, Vol. 98, No. 4, 1976, pp. 592-606.

7 Moore, J., "A Wake and an Eddy in a Rotating, Radial-Flow Passage, Part 2: Flow Model," ASME *Journal of Engineering for Power,* Vol. 95, No. 3, 1973, pp. 213-219.

8 Murakami, M. and Minemura, K., "Effects of Entrained Air on the Performance of Centrifugal Pumps, 2nd Report: Effects of number of blades," *Bulletin of the Japan Society of Mechanical Engineers,* Vol. 17, No. 112, 1974, pp. 1286-1295.

9 Katsanis, T., "Computer Program for Calculating Velocities and Streamlines on a Blade-to-Blade Stream Surface of a Turbomachine," *NASA Report* TN D-5427, Sept., 1969.

10 Stodola, A., *Steam and Gas Turbines,* McGraw-Hill, New York, 1927.

11 Busemann, A., "Das Förderhöhenverhältniss Radialer Kreiselpumpen mit Logarithmischspiraligen Schaufeln," *Zeitschrift fur Angewandte Mathematik und Mechanik,* Vol. 8, 1928, pp. 372-384.

System to Measure the Pressure Distribution on Fan Aerofoil Surfaces During Flutter Conditions

John W.H. Chivers
Electronics and Instrumentation Research Group, Rolls-Royce Limited, Derby, England

In order to assist in the understanding of high speed flutter, a series of tests has been conducted on a research fan in which the blade surface pressures have been measured by means of miniature silicon diaphragm pressure transducers embedded in selected fan blades. Prior to this investigation a program of rig tests was conducted to examine the effects of centrifugal force and vibration on the transducer performance and a transducer mounting technique was developed to minimize blade induced stress in the transducer. Instantaneous measurements of the tip stagger angles of the pressure instrumented fan blades have enabled a cross correlation to be performed on the blade surface pressure data and the blade tip angles. Some typical test results are shown.

Introduction

The current series of transonic fans in use on large gas turbine engines have nearly parallel blade channels and it is thought that during high speed flutter the in-blade shock system experiences significant axial movements. The movement of the shock system can produce excitation forces on the blade and under certain conditions a positive feedback situation may arise.

In order to investigate the pressure fields within the fan passages during flutter, improved stability miniature pressure transducers have been installed to measure the pressure distribution on fan blade aerofoil surfaces. On-blade pressure measurement has previously been reported by Sexton, O'Brien, and Moses [1] who describe a single transducer installation on a 460mm (18 in.) diameter axial flow fan. Carrol [2] reports on the effects of support struts and pylons in the gas path of an axial flow compressor as measured by six rotating pressure transducers.

For our flutter research, in conjunction with the on-blade pressure measurements, a system has been developed which will measure the instantaneous tip stagger angles of a pair of fan blades. Throughout fan flutter testing, the pressure and blade untwist data are continuously recorded onto magnetic tape. Subsequent analysis of the data has enabled the blades surface pressures to be cross correlated with the blade tip stagger angles. In addition, as a result of the improved d-c stability of the miniature pressure transducers used, steady blade surface pressure measurements have been obtained and plotted against fan rotor speed whilst running out of the flutter regime.

Contributed by the Fluids Engineering Division of THE AMERICAN SOCIETY OF MECHANICAL ENGINEERS and presented at the Symposium on Measurement Methods in Rotating Components of Turbomachinery, Gas Turbine and Fluids Engineering Conference, New Orleans, La., March 10-13, 1980. Manuscript received by the Fluids Engineering Division, September, 1979.

System Description

Typically five high frequency response miniature pressure transducers are inserted into the chords of two pairs of fan blades, giving a total of 20 transducers. Each pair of adjacent fan blades define a blade passage as shown diagrammatically in Fig. 1. The transducers on each pair of blades are located at similar radial positions and face each other across the relevant blade passage. As shown, the transducers are radially located near the blade tips on one pair of blades and near the fan blade clappers on the second pair of blades. The transducer polarising supplies and outputs are taken down the blades onto the fan disc, into the transducer compensating modules and eventually off the rotor via a conventional silver/graphite brush slip ring unit.

The fan blade stagger angle signals are derived from two pairs of fan tip proximity transducers mounted through the fan casing and spaced circumferentially by one blade pitch. For each pair of transducers one senses the leading edge of a predetermined fan blade and one the trailing edge of the same fan blade. Each pair of probes is aligned at an angle slightly greater than the tip stagger angle of the fan blades. As the fan blade tip stagger angle changes, either steadily due to rotor speed variations, or dynamically due to the onset of flutter, the time delay between the arrival of the trailing and leading edge signals changes.

This time delay is converted into an analogue voltage pulse, the amplitude of which is proportional to the instantaneous angle of the blade tip. By the use of a dual channel system instantaneous angle information is obtained from one pair of adjacent pressure instrumented blades. In this way the torsional geometry of the blade passage under consideration is defined at the instant that the two fan blades are under the two pairs of angle measuring transducers.

During flutter testing the signals from the blade mounted pressure transducers are recorded continuously onto magnetic tape together with the blade angle information and the usual fan strain gauge signals as shown schematically in Fig. 2.

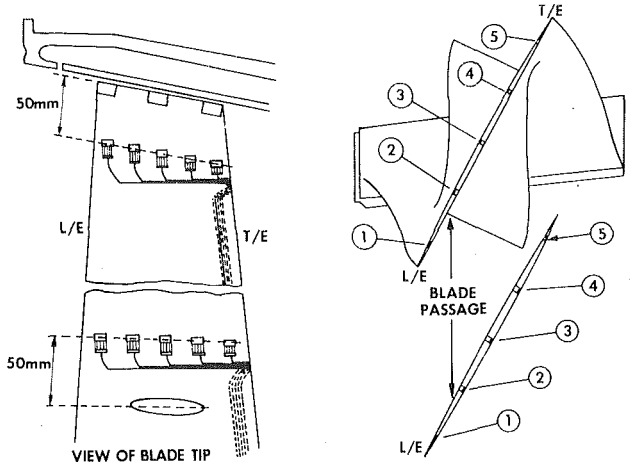

Fig. 1 Fan blade transducer locations

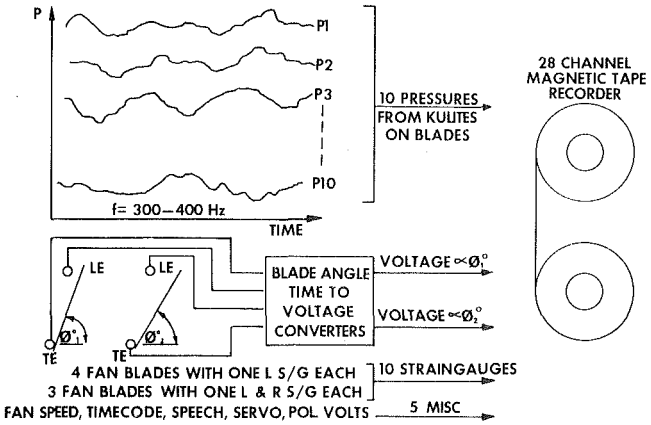

Fig. 2 Blade surface pressure recording system

After a preliminary examination of the blade angle information which has been recorded, a range of blade angles is chosen which represent blade passage geometries of interest.

For each geometry the two blade angles are selected on a coincidence detector and the tape replayed. A block diagram of the data analysis systems is shown in Fig. 3. Each time the two blade angles coincide with the preselected values a "data collect" pulse is transmitted to a computer which in turn triggers 10 data sample and hold circuits. The instantaneous values of pressure for each of the 10 transducers is measured and stored in the computer. This procedure is repeated until sufficient data points have been collected after which the corrected pressure data for each channel is printed out in the form of average pressure (e.g. $P1$) plus the value of each reading used to calculate the average (e.g. $P1(1)$, $P1(2)$,....$P1(n)$). The data are also available on file for further analysis.

System Component Details

The Blade Mounted Pressure Transducers. The transducer chosen for mounting on the fan blades is manufactured by Kulite Semiconductor Products Inc. model LQ-4-156-25A which is based on their third generation CQ-080 sensor. This device appeared to be particularly suitable for on-blade applications because of its low "g" sensitivity and its overall stability which is generally a factor two better than previous models. The transducer is 7.6mm (0.30 in.) square by 1.9mm (0.075 in.) thick with a pressure range of 172kPa absolute (25 psia) and is shown in Fig. 4.

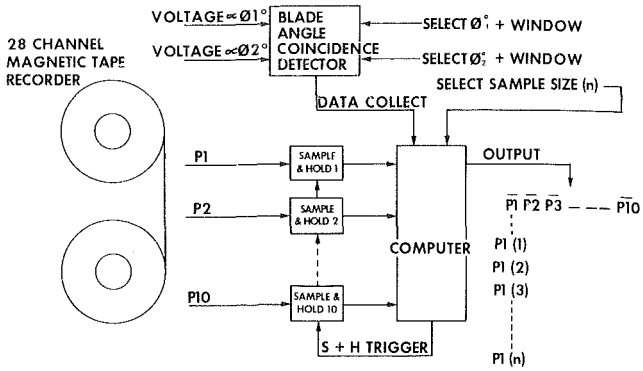

Fig. 3 Blade surface pressure replay and analysis system

An extensive laboratory and spinning rig test program has been conducted to investigate the effects of centrifugal force on the sensitivity and zero offset and the effects of blade induced stress in the transducer. Transducers were spun in a small test facility at speeds of up to 13,000 rpm at a radius of 152mm (6 in.). Minkin [3] has reported a test programme in which the performance of some miniature pressure transducers has been examined under c.f. loading. Additionally, transducers have been mounted in a cantilever which was subjected to a bending load in order to evaluate the effectiveness of the mounting technique. This work has enabled a method to be developed of mounting the transducer in the fan blades in such a way that blade stresses do not affect the transducer performance.

A diagrammatic section through a fan blade and transducer explaining the attachment technique is shown in Fig. 5. Essentially the transducer is rigidly attached to the blade only along one side, this being the side at minimum fan radius. This is achieved by laser welding a piece of stainless steel shim to the transducer which is in turn attached to the blade using an epoxy adhesive. The other three sides of the transducer are secured to the blade using a compliant silicone rubber. An epoxy impregnated patch is built up over the back of the transducer to protect the installation against accidental damage. In this manner the transducer is attached to the fan blade with sufficient strength to resist the 25000g centrifugal loading. However flutter stresses in the fan blade are not transferred to the transducer because of the compliant nature of the silicone rubber.

To summarize the results to date, the effect of a centrifugal force of 25000g in the plane of the transducer diaphragm generates an output equivalent to a pressure of less than 1.7kPa (0.25 psi). Also the maximum combined effect of temperature on transducer zero offset and span is equivalent to a pressure of less than 4kPa (0.6 psi), over a temperature range 20 to 80 degrees centigrade. After installation of the transducers in the fan blades each transducer is individually calibrated over a range of temperature and pressures to enable the test result to be corrected for temperature induced changes in zero offset and span. The transducer temperature during test is estimated from previously derived aerodynamic test data.

An error of ± 10 degrees centigrade in the estimated transducer operating temperature still enables the temperature effects to be reduced to less than 0.7kPa (0.1 psi). Figure 6 shows a photograph of three fan blades in a rotor with transducers installed.

Fan Blade Angle Transducers. The transducers used to detect the proximity of the fan blade tips are magnetic probes manufactured by Orbit Controls Ltd type 70D1102 as shown in Fig. 7. Four such probes are used in the dual channel blade

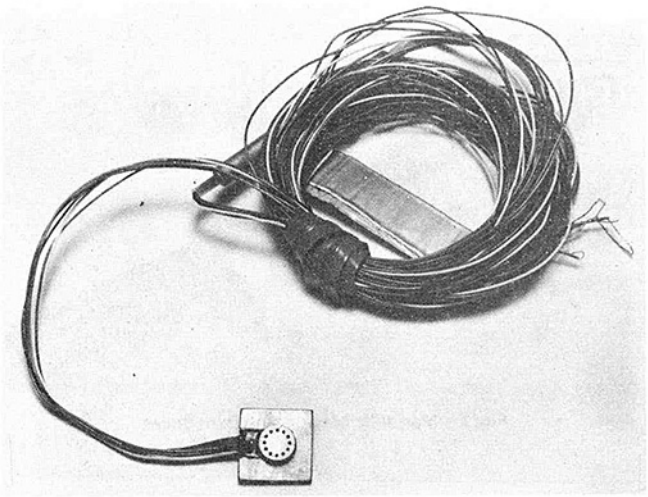

Fig. 4 Miniature pressure transducer with compensation module

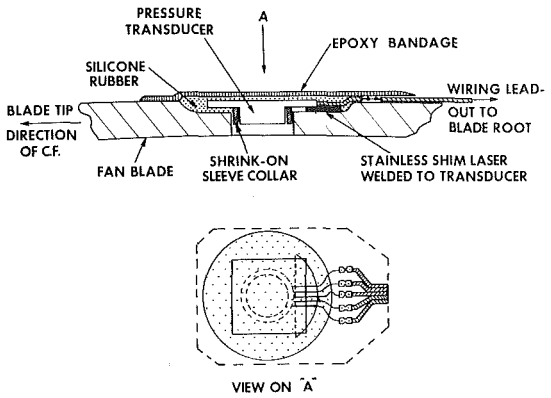

Fig. 5 Pressure transducer blade mounting technique

angle measuring system. These probes are 63mm (2.5 in.) long and are threaded 0.375 inch diameter 24T.P.I. UNF-2A. The once per revolution probe which is used to arm the blade angle system is similar to the four used to measure the blade angles. As the fan blade material is titanium the pressure instrumented blades are identified magnetically either by attachment of a 0.1mm thick magnetic shim, 3mm deep by 10mm long or by a flame sprayed soft iron patch applied to the blade tips.

Blade Angle Measuring System. The fan blade angle measuring system can be considered as two discrete units – a dual channel record unit and a dual channel replay unit.

Record Unit. The function of the record unit is to accept the two pairs of signals from the magnetic proximity probes and convert each time delay between the trailing edge and leading edge signals into a voltage pulse with an amplitude proportional to the times. In this way the formidable problems of

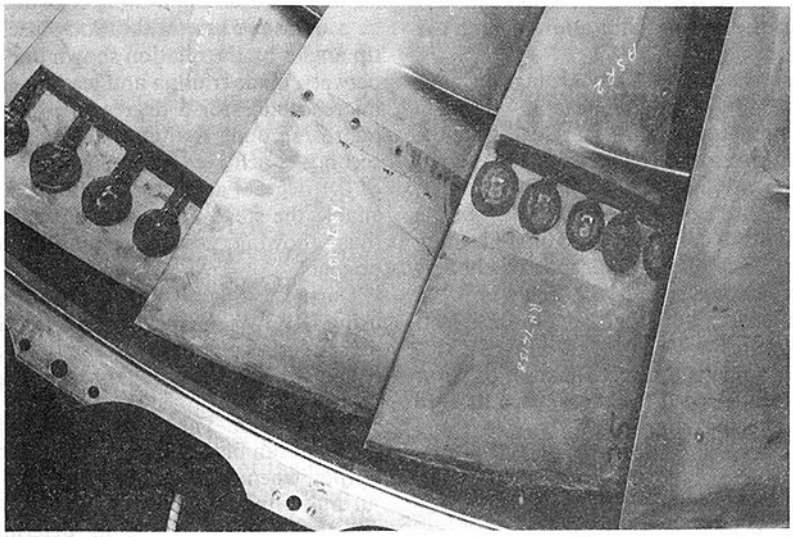

Fig. 6 Installation of transducers in fan blades

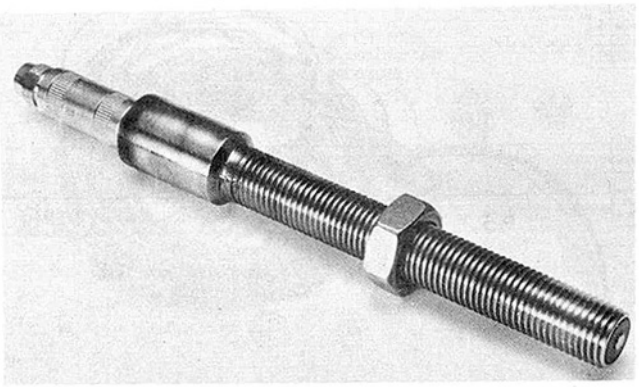

Fig. 7 Magnetic blade angle transducer

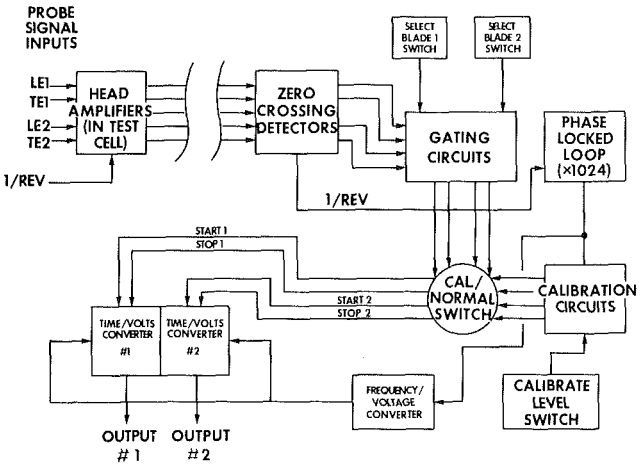

Fig. 8 Blade angle record unit block diagram

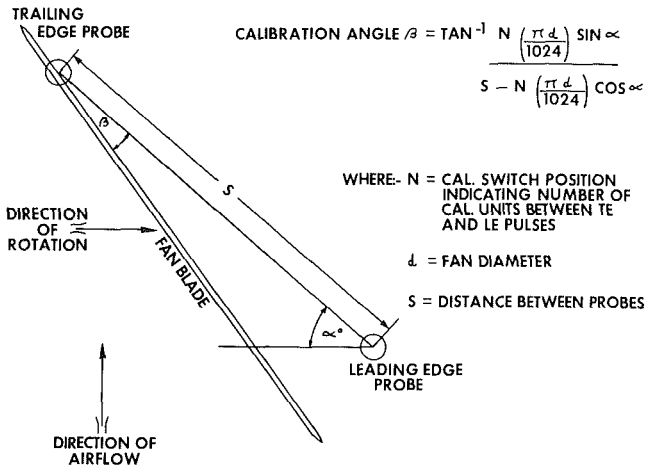

Fig. 9 Calibration of blade angle measuring system

recording and replaying the raw timing data to an accuracy of better than 0.25 microseconds are avoided.

The time to voltage conversion is achieved independently of fan speed and a system for the on line calibration of both the record and replay units is provided.

Figure 8 shows the record system in block diagram. The probe signals are conditioned by unity gain head amplifiers in order to drive the long lines between the test cell and the record unit in the adjacent measurement facility. The signals are then detected by conventional zero crossing detectors. After detection the blade trailing edge pulses each start a voltage ramp generator and the corresponding blade leading edge pulses stop the ramp. The voltage amplitude reached by each ramp is directly proportional to the time delay between the two trailing edge and leading edge signals. However it is obvious that the time taken for a blade tip to cross the two probes for a given untwist angle is a direct function of rotor speed. In order to eliminate the speed factor, a speed derived voltage is used as the charging source for the two ramp generators, thus the ramp slope increases with increasing fan speed.

Calibration of the system is achieved by multiplying the once per revolution pulse by 1024 with a phase locked loop. This has the effect of producing a pulse chain with a repetition rate equivalent to 1/1024 of the fan circumference. By counting pulses in the calibration circuit two calibration signals representing trailing edge and leading edge signals can be provided. These calibration pulses are converted into blade tip angles by the relation shown in Fig. 9. The time difference between blade trailing and leading edge signals is typically 20 microseconds for 5 degrees of untwist at a tip speed of 500 metres/second. A timing accuracy of better than 300 nano seconds is achieved in practice which gives a system accuracy of 0.1 degrees at maximum fan speed. Facilities also exist to enable the steady untwist component of signals to be offset thus allowing greater resolution of the fluctuating components.

During testing all signals are recorded onto magnetic tape using IRIG Wideband Group 1 standard at a tape speed of 30 inches per second to give a d-c to 20kHz data bandwidth, this response being necessary for the untwist data.

Replay Unit. The replay unit is required to detect when two adjacent fan blades are at preselectable angles and provide an output when this condition occurs. Two independently adjustable window discriminators are used which are set to the required voltage levels, as determined by the calibration procedure, and are gated together to trigger a monostable

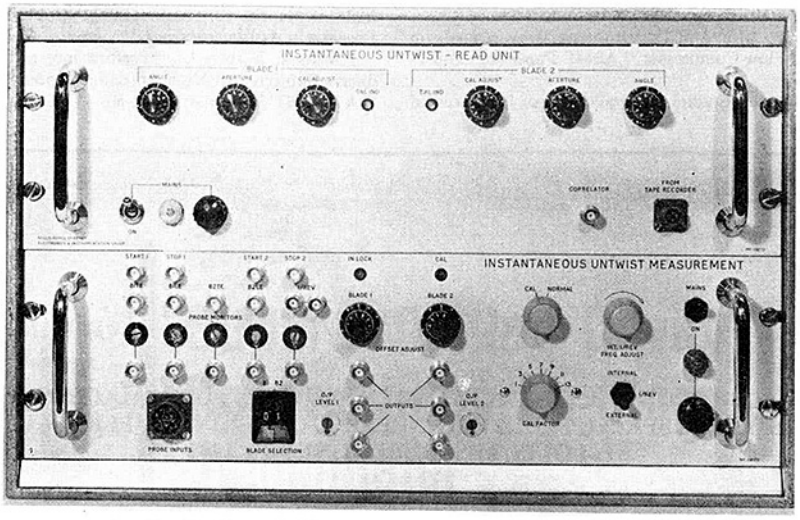

Fig. 10 Front panel of instantaneous blade angle measuring system

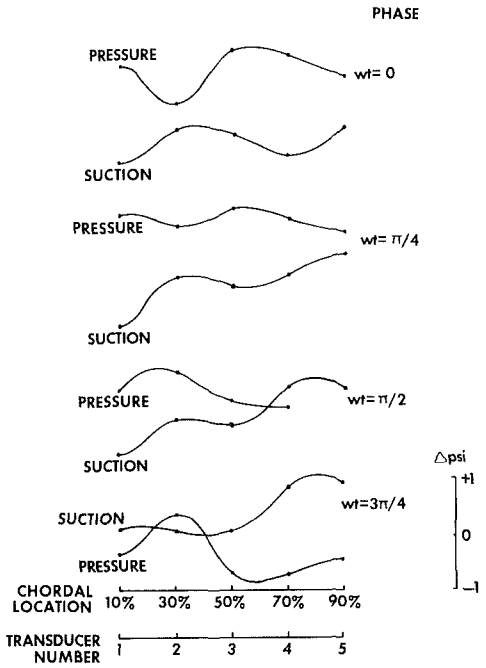

Fig. 11 Typical results – pressure fluctuations on fan aerofoil

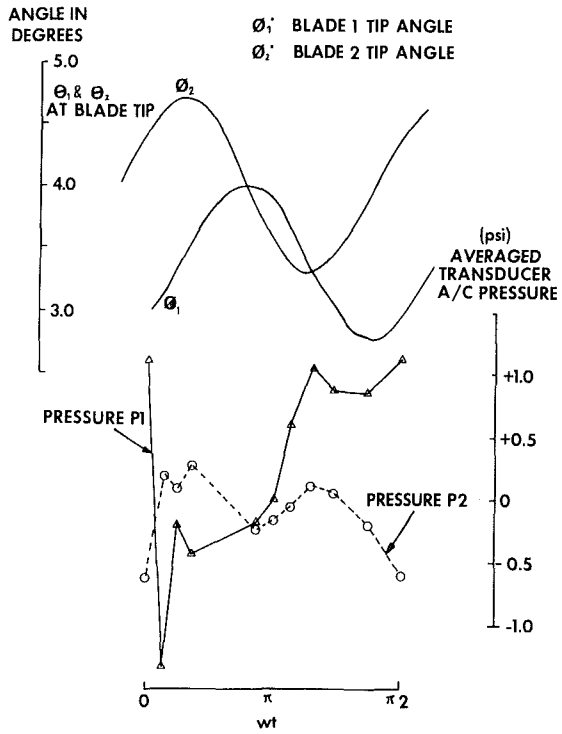

Fig. 12 Typical results – phase relationship between pressure and blade angles

when the required blade angles which correspond to the voltage levels are detected simultaneously.

Results

The instrumentation system described in this paper has been used on four tests of a research fan with very satisfactory results. The reliability of the transducers during the flutter testing has been considerably better than expected with only two failures which could be positively attributed to a transducer fault. Initial problems were concerned with the transducer wiring and retention of the transducer compensation modules on the fan disk. No problems have arisen with the instantaneous untwist system and in later tests capacitance proximity transducers have been used in place of the leading and trailing edge magnetic probes. In this way the need to magnetically identify the instrumented blades is avoided at the expense of more complex electronic circuitry.

Data have been obtained which have enabled the unsteady lift and moment forces to be determined together with their phase relationship. These forces and the resultant unsteady work have been compared with their theoretical derivation from the unsteady aerodynamic coefficients. Although this paper is primarily concerned with the measurement techniques, Figures 11 and 12 show some typical test results obtained while the fan was in flutter.

Acknowledgments

The author wishes to acknowledge the invaluable assistance of Measurement Engineering and members of the Measurement Techniques Group at Derby in the development and implementation of the techniques described. Thanks are also due to Rolls-Royce for their permission to present this paper.

References

1 Sexton, M.R., O'Brien, W.F., Moses, H.L., "Pressure Measurements on the Rotating Blades of an Axial-Flow Compressor," ASME Paper No. 73-GT-79.

2 Carrol, John T., "Dynamic Flow Studies by Application of Pressure and Velocity Sensors on Axial Flow Fan Blades," Paper given at Symposium on Instrumentation for Airbreathing Propulsion, Sept. 1972, contained in *Progress in Astronautics and Aeronautics,* Vol. 34, MIT Press, 1974.

3 Minkin, Herbert L., "Performance of Some Miniature Pressure Transducers Subjected to High Rotational Speeds and Centripetal Accelerations," ISA ASI 76317, 1976, pp. 55 to 60.

R. Oba
Professor.

T. Ikohagi
Assistant.

Institute of High Speed Mechanics,
Tohoku University,
Sendai, Japan

S. Yasu
Engineer,
Ishikawajima-Harima
Heavy Industries Co., Ltd.,
Tokyo, Japan

Supercavitating Cavity Observations by Means of Laser Velocimeter

The behavior of supercavitation as well as of cavitation, especially near the separation point, were carefully observed in a two-dimensional subcritical flow around a cylinder with and without ventilation. Since supercavitating flow generally detaches from the separation point abruptly, the assumption "smooth separation" often applied is evidently unsatisfactory. There is a transient region, where a kind of supercavitation and of subcavitation can be alternately observed. Outside the immediate neighborhood of the separation point, the flow features are uniquely expressed by σ_c based on cavity pressure both with and without ventilation, while within that neighborhood, there arise some different features due to ventilation.

1 Introduction

With increasing speed in hydraulic machinery or in ship propellers, interest has been growing in supercavitating foils. The design or the performance analyses of such machinery require detailed investigations on the flow patterns, especially near the separation point which has to be directly connected with the hydrodynamic forces.

According to literature on the features near the separation point, several investigations [1-4] have been made under the assumption "smooth separation." It is, however, questionable whether the assumption is actually applicable or not. There is very little information about the detailed flow patterns except an empirical correlation [5] for the distance between the boundary layer- and the cavitating-separation by the Schlieren technique, especially in a supercavitating state of the most technical interest, in which small disturbance will easily result in a number of cavitation bubbles.

In this paper, therefore, by means of a laser velocimeter and high speed photography, the behavior of supercavitation as well as of cavitation, especially near the separation point, were carefully observed in a two-dimensional flow with and without ventilation around a cylinder installed in a rectangular test section in which the wall effects were negligible.

2 Experimental Facilities

2.1 Cavitation Tunnel. The experiments were conducted in the two-dimensional horizontal closed tunnel described elsewhere [6], installed with splitter plates, straightening tubes to control the cavitation nuclei as well as the air content, a bypass filtering circuit, a water cooling system and a 4000 mm diameter reservoir to prevent the reentering of cavitation bubbles occurring in the test section or in the pump.

The rectangular test section shown in Fig. 1 was made of lucite. The entire wall surfaces, especially around the test cylinder, were finished precisely and optically smooth for the laser velocimeter measurement. As shown in Fig. 2, the velocity distribution was fairly uniform there and the boundary layer was about 4 mm in thickness on either side wall, so that the two-dimensionality of the flow through the section might be fairly good.

The upstream reference pressure was measured at the tap A where the disturbance due to the cylinder almost vanished. The flow rate and the pressure at the section were continuously regulated in a range of $0 \sim 16$ m/s as well as $0 \sim 200$ kPa by means of a sluice valve, a circulating pump and a valve to regulate the pressure in the reservoir. In place of the turbulence level, the wall pressure fluctuation was measured by a flush-mounted transducer, indicating 1.0 percent of the dynamic pressure [7].

2.2 Test Cylinder. The cylinder was made of brass and its surface was finished hydrodynamically smooth to prevent roughness effects. Figure 3 shows the one used in the vented experiments, in which air was supplied in a two-dimensional manner into the trailing cavity through a 0.5 mm wide two-dimensional slit in the rear of the cylinder. And the cylinder used in the experiments without ventilation has been described elsewhere [6]. The diameter $d = 15$ mm was selected to minimize the wall effects [8], so that the blockage ratio d/H was 0.05, where H was the height of the section.

2.3 Laser Velocimeter LDV. The laser velocimeter is described in detail in reference [9] (see Fig. 4). It was mounted

Contributed by the Fluids Engineering Division and presented at the Winter Annual Meeting, Chicago, Ill., November 16-21, 1980, of THE AMERICAN SOCIETY OF MECHANICAL ENGINEERS. Manuscript received by the Fluids Engineering Division, April 4, 1979. Paper No. 80-WA/FE-5.

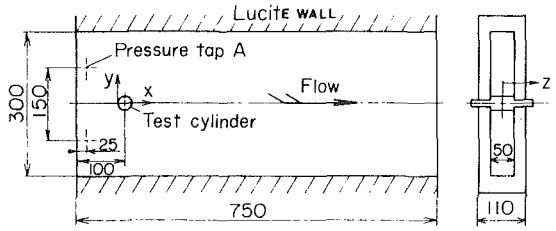

Fig.1 Rectangular test section (all dimensions are in millimeters)

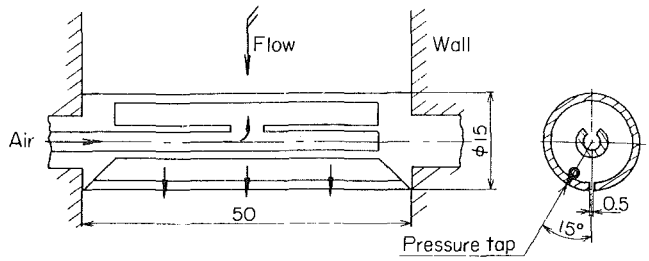

Fig.3 Test cylinder used in the vented experiments

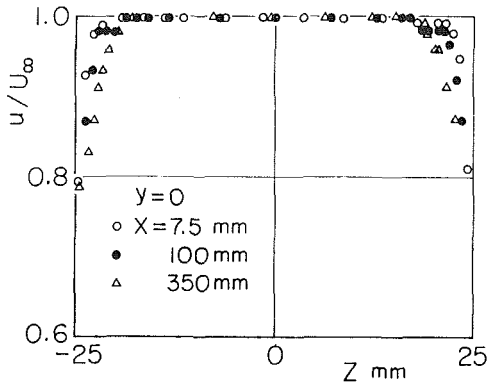

Fig. 2 Velocity profile in the test section (uncertainties for u/U_∞ and z are ± 0.01 and ± 0.05 mm, respectively)

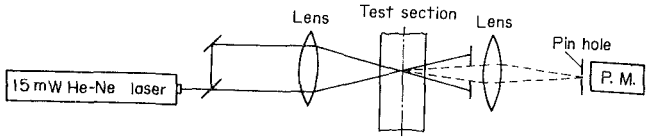

Fig.4 Optical arrangement of laser velocimeter

on a three component traverse mechanism to freely traverse the measuring points without any optical adjustment. The flow velocity was reduced from the output of the photomultiplier through a wideband frequency analyzer (10 kHz ~ 30 MHz) and a frequency tracker (0.1 kHz ~ 10 MHz). The accuracy was within ± 1 percent of the mean velocity.

3 Experimental Procedure

In order to remove the air bubbles attached to the tunnel inner wall, a preliminary circulation of tunnel water was made for ten minutes, and then each test run was started. The flow velocity U_∞ at the test section was measured by a previously calibrated upstream nozzle and was held fixed at about 12 m/s, i.e., the Reynolds number $R_e = U_\infty d/\nu = 1.9 \times 10^5$ so as to hold the scale effects as small as possible. Since the critical Reynolds number [10] is about 2.7×10^5 for non-cavitating cylinder in this tunnel, the present experiments are said to be limited within the subcritical region.

While conducting each run, the change in air content ratio[1] α/α_s and water temperature t_w was negligibly small, and the range was 1.02~1.07 for α/α_s and 22~25°C for t_w throughout the test. The cavitation nuclei distribution in the test water was measured by a specially-made Coulter counter and the typical one has been reported elsewhere [11].

Based on the cavity pressure p_c and the vapor pressure of water p_v, the cavitation numbers are defined as follows:

$$\sigma_c = 2(p_\infty - p_c)/\rho U_\infty^2 \quad (1), \qquad \sigma_v = 2(p_\infty - p_v)/\rho U_\infty^2 \quad (2)$$

where p_∞ and U_∞ are the upstream reference pressure and velocity, respectively, measured at the tap A, and ρ the density of water.

The vented air flow rate Q was reduced to the condition at p_∞ by Boyle-Charles' law and then was reduced to a non-dimensional air supply coefficient as follows:

$$C_Q = Q/A_c U_\infty \quad (3)$$

where A_c is the projected area of the cylinder on a y-z plane.

4 Results

Before going into the main argument, let us try to specify

[1] By Henry's law, saturation rate of air relative to local condition $(\alpha/\alpha_s)_\ell$ is defined as $(\alpha/\alpha_s)_\ell = (\alpha/\alpha_s) \cdot (p_s/p_\infty)$, where p_s is the standard pressure at the normal condition (t_w = 0°C, p_s = 101.3 kPa). In the present experiments,
$\sigma_v > 1.4$; $(\alpha/\alpha_s)_\ell < 1.0$: Undersaturation
$\sigma_v < 1.4$; $(\alpha/\alpha_s)_\ell > 1.0$: Supersaturation

Nomenclature

A_c = projected area of test cylinder
C_Q = $Q/A_c U_\infty$ = air supply coefficient
d = diameter of cylinder
H = height of test section
ℓ = cavity length
p_c = cavity pressure
p_s = standard pressure
p_v = vapor pressure of water
p_∞ = upstream reference pressure
Q = vented air flow rate
q_s = velocity along separation streamline
R_e = $U_\infty d/\nu$ = Reynolds number
$\bar{T}$ = maximum cavity width
t_w = water temperature
U_B = velocity at y = 5d from cylinder
U_∞ = upstream reference velocity
u = velocity component in the x-direction
x,y,z = coordinate system
α/α_s = air content ratio
$(\alpha/\alpha_s)_\ell$ = saturation rate of air relative to local condition
ν = kinematic viscosity
ρ = density
θ_c = separation angle
θ_s = separation point
σ_c = $2(p_\infty - p_c)/\rho U_\infty^2$ = cavitation number based on p_c
σ_v = $2(p_\infty - p_v)/\rho U_\infty^2$ = cavitation number based on p_v
σ_d = desinent cavitation number

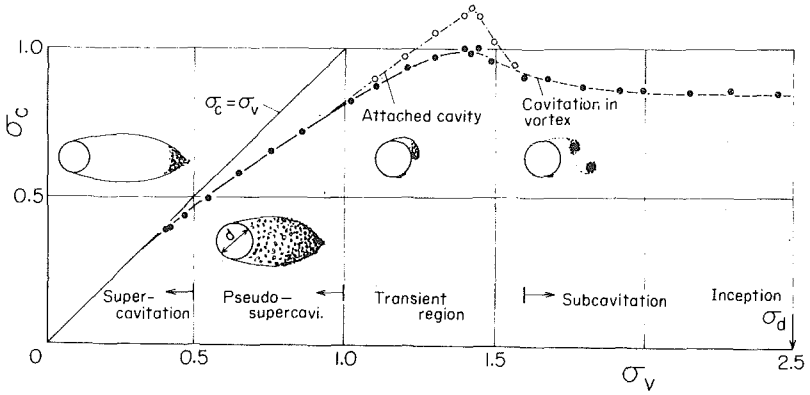

Fig.5 Various flow regime in cavitating flow: cavitation number σ_v based on vapor pressure versus cavitation number σ_c based on measured cavity pressure (uncertainties for σ_v and σ_c are ± 0.01)

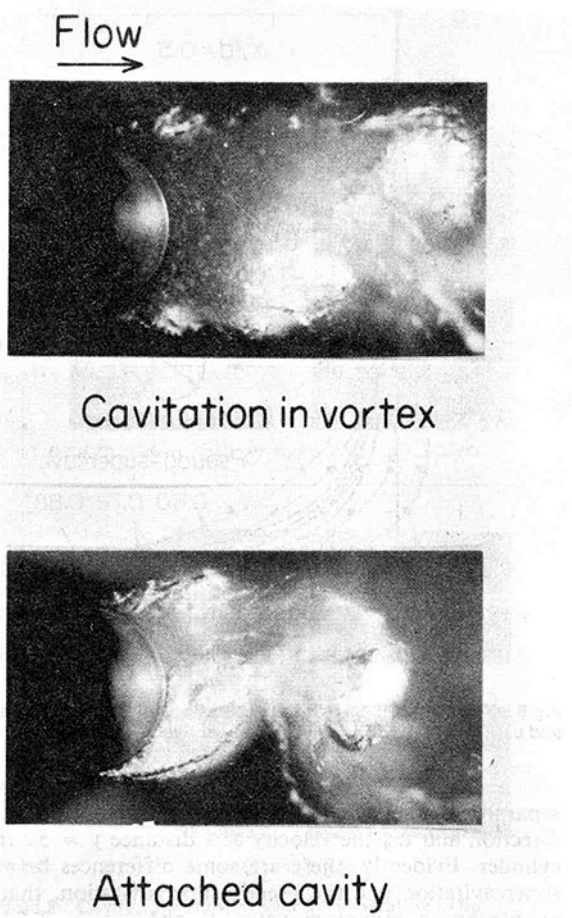

Photo 1 Attached cavity and cavitation in vortex (σ_v = 1.30, xenon flash lamp with exposure time 3 × 10^{-6} s)

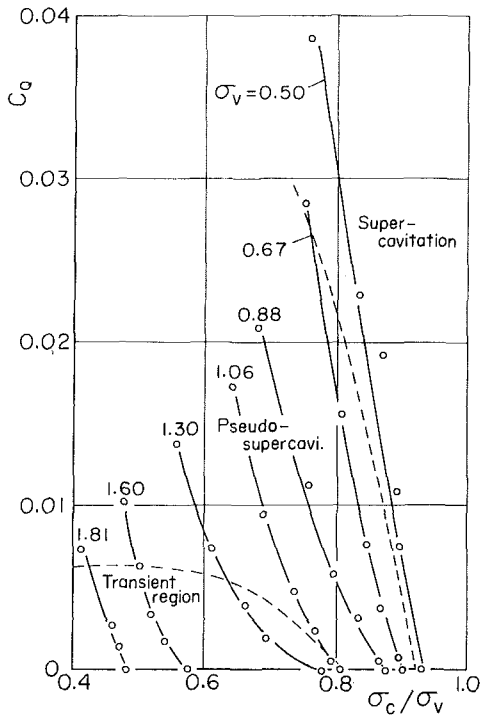

Fig.6 Air supply coefficient C_Q versus cavitation number σ_c (uncertainties for C_Q and σ_c/σ_v are ± 0.001 and ± 0.02, respectively)

essential features in such a cavitating flow. The cavitation observed in the present experiments is classified according to the appearances into the following three types: (i) supercavitation, (ii) pseudo-supercavitation, (iii) subcavitation. The terms supercavitation and pseudo-supercavitation refer to the situation that a large trailing cavity has been observed, in which the liquid flow detaches from the cylinder surface, and the pseudo-supercavitation differs from the supercavitation in existing a cluster of small bubbles in the trailing cavity. In subcavitation, the cavities are periodically found in the cores of shedding vortices from the cylinder.

The two typical cavitation numbers based on the vapor- and the cavity-pressure, σ_v and σ_c, are evaluated in a natural state without ventilation of the most technical interest. Figure 5, showing the relation between them, illustrates that σ_c is very close to σ_v in the supercavitating region of $\sigma_v \leq 0.5$, while it is quite different from σ_v in the subcavitating region (σ_d in the figure shows the desinent cavitation number) of $\sigma_v > 1.6$, as might be expected. Notice here the existence of a transient region between the above extreme regions, where two quite different cavitating states (see Photo 1), that is, the vertically oscillating unsymmetrically attached cavity[2] with a glassy surface (indicated by "o" in the figure) and the cavitation in the Karman vortex [12] (" ● "), are alternately observed at the same value of σ_v, as described elsewhere [6], and thus the difference $\sigma_c - \sigma_v$ rapidly increases with σ_v. This figure also shows the region where a symmetric pseudo-supercavitating cavity is steadily observed.

[2] It is very close to pseudo-supercavitation not only in appearance but also in slope of the $\sigma_c \sim \sigma_v$ curve.

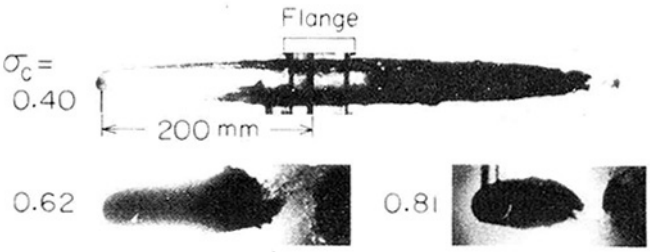

Photo 2 Typical cavities

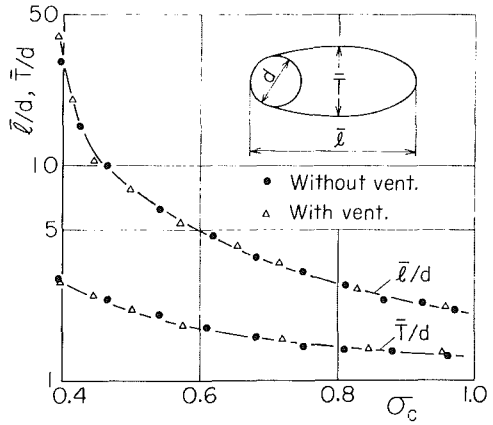

Fig. 7 Variation of cavity dimensions with cavitation number σ_c (uncertainties for $\bar{\ell}$ and $\bar{T}$ are ± 5 percent, and for σ_c ± 0.01)

To avoid the instability taking place in the transient region is the most important object of ventilation. The following experiments on ventilation, therefore, will be limited within a range, $0.5 < \sigma_v < 1.8$, where the instability mostly takes place, and the vented air is naturally supplied. Figure 6 shows the relation between the air supply coefficient C_Q and the resulting cavitation number σ_c for various σ_v, where σ_c decreases approximately proportionally to an increase in C_Q.

The cavitation was photographed with a xenon flash lamp of 3 μs. Photo 2 shows the typical cavities, where black lines found in this photo indicates the flange of the test section and is independent of the main flow. In Fig. 7, the most essential dimensions, i.e., the time-averaged length $\bar{\ell}$ and -maximum width $\bar{T}$, which were measured on the photographs, are plotted against σ_c for both with and without ventilation. It is evident here that for the both cases the dimensions are uniquely expressed by σ_c in almost entirely ranging from subcavitation to supercavitation. In our experiments, no such discontinuous change in ℓ as observed by Silberman [13] seemed to take place.

Next, by means of a laser velocimeter, let us try to measure the flow patterns, especially near the separation point which is closely related to the hydrodynamic forces.

Figure 8 illustrates the velocities q_s measured in the immediate neighborhood of the separation point by comparing the two cases, and also shows the theoretical velocity $q_s = \sqrt{1 + \sigma_c}$, where the pressure at the point is assumed to be equal to p_c. Here, slight discrepancy between the experiment and the theory is seen even in the supercavitating or pseudo-supercavitating region of $\sigma_c \leq 0.8$, and it rapidly increases with σ_c in $\sigma_c > 0.8$. Also, q_s is uniquely expressed by σ_c.

In Fig. 9, the velocity profiles near the separation point ($x/d = 0.5$) are compared with σ_c and with the theoretical ones [14][3] obtained under the assumption "smooth separation," where u is the velocity component in the x-direction and U_B the velocity at a distance $y = 5$d from the cylinder. Evidently, there are some differences between the supercavitation and the pseudo-supercavitation, that is, the profile has a minimum value at about $y = 1.5$d in the supercavitating region of $\sigma_c \leq 0.5$, while it decreases monotonically with increasing y in $\sigma_c > 0.5$. It might also be expected in the supercavitation that the boundary layer on the cavity surface separates more easily with decreasing σ_c, thus it possibly interacts with the cavity separation. As is well known, the assumption "smooth separation" has been widely applied. However, since a considerable difference is indicated between the experiment and the theory in the supercavitating region of $\sigma_c = 0.39$ or 0.5, the assumption is said to be unsatisfactory. But the difference tends to decrease with increasing σ_c and becomes negligibly small at the border of the pseudo-supercavitation of $\sigma_c = 0.6$. Thus, even in this sense, there are some differences between the supercavitation and the pseudo-supercavitation.

To clarify the feature in the immediate neighborhood of the separation point, the separation angle θ_c and the separation

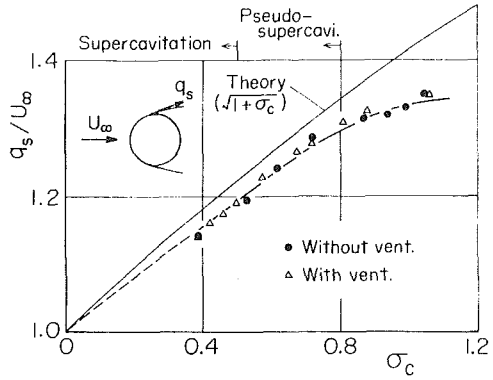

Fig.8 Variation of velocity q_s in the immediate neighborhood of the separation point with cavitation number σ_c (uncertainties for q_s/U_∞ and σ_c are ± 0.02 and ± 0.01, respectively)

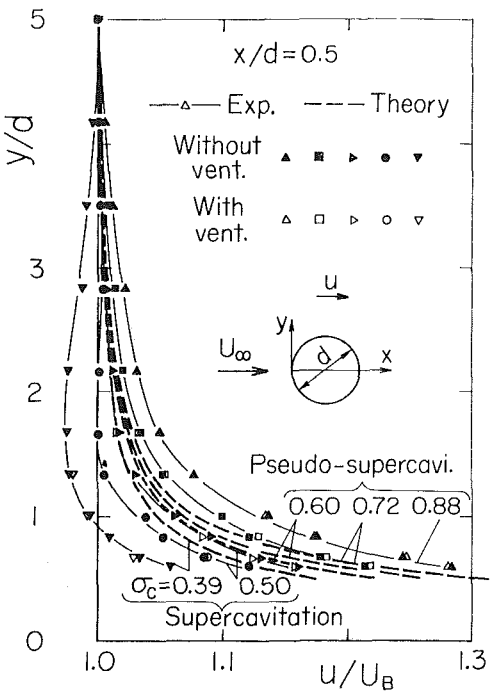

Fig.9 Velocity profiles near the separation point (uncertainties for y/d and u/U_∞ are ± 0.005 and ± 0.01, respectively)

[3] The smooth separation and the constant base pressure are assumed in this free streamline theory. It is why we adopt this theory by replacing the base pressure by the cavity pressure.

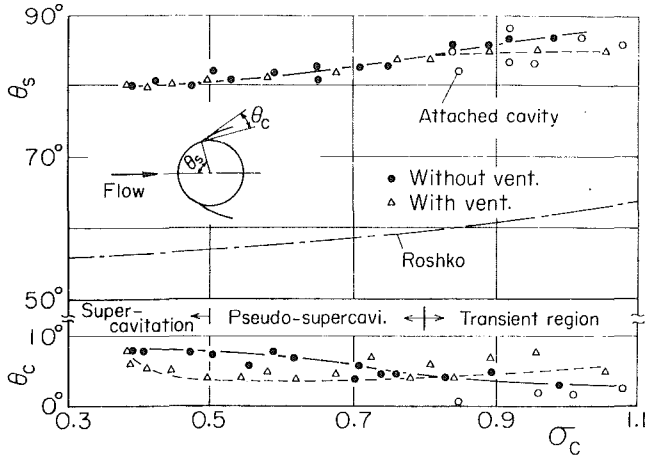

Fig. 10 Angle θ_c and point θ_s of separation (uncertainties for θ_c and θ_s are $\sqrt{2}$ deg, and for σ_c ± 0.01)

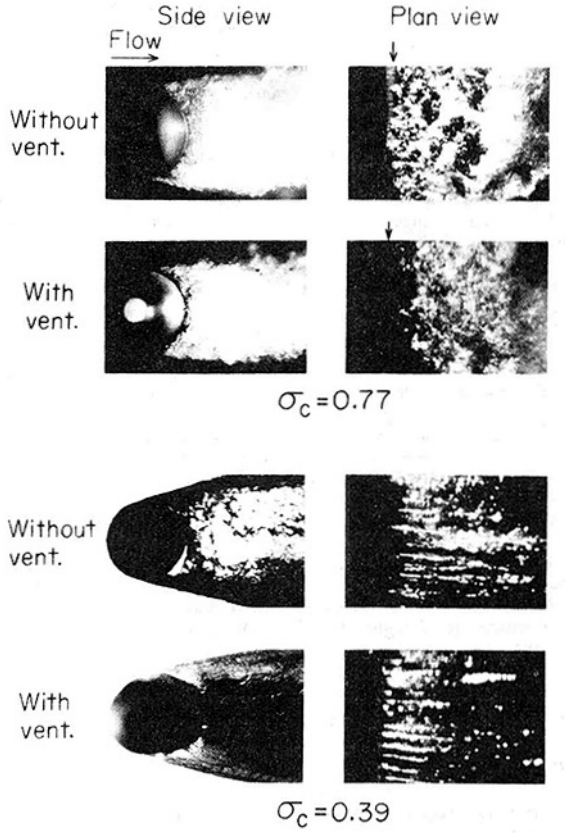

Photo 3 Cavity appearances near the separation point

point[4] θ_s were measured on the photographs, and are plotted in Fig. 10 against σ_c for both with and without ventilation, to compare the Roshko's theoretical data calculated by assuming "smooth separation"; where symbol "o" in the transient region indicates the attached cavity.

First, the effects of ventilation are clearly seen in the immediate neighborhood. Since θ_c is always larger than zero and tends to increase with decreasing σ_c, the flow is said to be detached from the separation point not smoothly as has been widely expected, but rather abruptly; for example, in a supercavitating region of σ_c = 0.4, θ_c is very close to 7 deg

[4] The separation point is defined by the intersection of the extension of visible streamline and the cylinder surface.

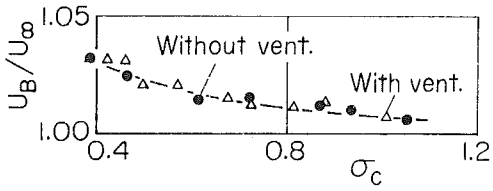

Fig. 11 Blocking factor U_B/U_∞ (uncertainties for U_B/U_∞ and σ_c are ± 0.01)

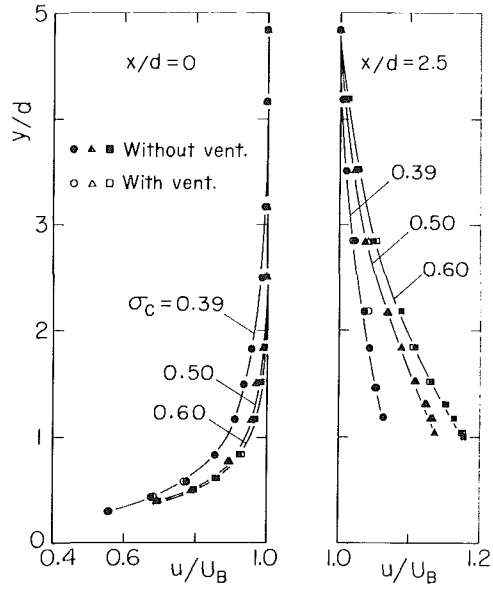

Fig.12 Velocity profiles at a distance from the cylinder (uncertainties for y/d and u/U_∞ are ± 0.005 and ± 0.01, respectively)

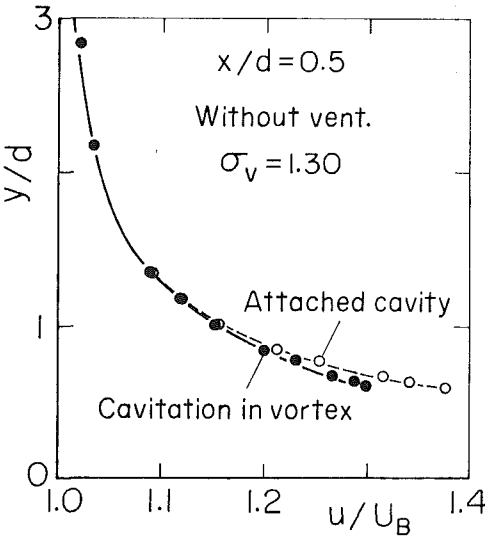

Fig.13 Time averaged velocity profiles around the attached cavity and the cavitation in the vortex (uncertainties for y/d and u/U_∞ are ± 0.005 and ± 0.01, respectively)

indicated on the sphere [3]. There is also a marked difference in θ_s between the experiments and Roshko's theory, though the trend with σ_c is fairly similar.

The cavity appearance is compared in Photo 3 for both with and without ventilation and for typical cases of σ_c = 0.77 (pseudo-supercavitation) and σ_c = 0.39 (supercavitation); where an arrow marked on the plane view shows the separation point, and the wavy pattern appearing in the central part on the side view suggests the dummy flow on the

side wall, which is almost independent of the main flow of interest. In the immediate neighborhood of the separation point, there arises an apparent difference in the appearance due to ventilation in the pseudo-supercavitation; for example, the cavity with ventilation takes place slightly away from the cylinder, while the one without ventilation takes place directly on the cylinder. However in the supercavitation there is no such marked difference. Thus, some differences mentioned above are reaffirmed here. And as may be expected, the pseudo-supercavitating cavity is evidently frothy and the surface is fairly rough, while the supercavitating cavity is clear and the surface is glassy as well as striated.

In such flows, the wall effects so often become serious problems. Figure 11 shows the blocking factor, a kind of the wall effects, U_B/U_∞ against σ_c and indicates that $U_B/U_\infty - 1$ are within 3 percent. Notice here the factor is also uniquely expressed by σ_c.

Figure 12 illustrates the velocity profiles at a distance from the cylinder, $x/d = 0$ and 2.5. Evidently, the profiles are also uniquely expressed by σ_c and the downstream one at $x/d = 2.5$ much varies with σ_c as is expected in such cavitating flows. It is also apparent from the upstream one at $x/d = 0$ that the disturbance due to the cylinder almost vanishes in $y/d = 3$, if the blocking factor is small. In the present experiments, therefore, the upstream reference pressure is measured at $y/d = 5.0, x/d = -5.0$.

To clarify the flow feature when the instability takes place in the transient region, in Fig. 13, the time averaged velocity profile around the attached cavity is compared with that around the cavitation in the vortex near the separation point at a typical case of $\sigma_v = 1.3$. Since the difference between them is extremely limited within a narrow region near the cylinder, the feature is said to scarcely depend on the cavitation appearance, though the cavitation appearances are quite different from each other.

5 Conclusions

By means of LDV and high speed photography, the behavior of supercavitation as well as of cavitation, especially near the separation point, were carefully observed in a two-dimensional subcritical flow around the cylinder installed in the 300 × 50 mm rectangular test section in which the wall effects were negligible, in both with and without ventilation. The following results were obtained:

(i) The flow was not detached from the separation point smoothly as had been widely expected, but rather abruptly in all cases with or without ventilation, in which abruptness increased with decreasing σ_c. Thus, the assumption "smooth separation" is not satisfactory, but somewhat harmful in the supercavitating region.

(ii) There was a transient region, where two quite different cavitating states, i.e., the attached cavity and the cavitation in the vortex, were alternately observed at the same value of σ_v, and in the supercavitating region σ_c was very close to σ_v, while it was quite different from σ_v in the subcavitating region as might be expected.

(iii) The features such as the cavity dimensions, the velocity profiles and the blocking factor U_B/U_∞ were almost independent of the vented condition and were uniquely expressed by σ_c, but not expressed by σ_v, except those in the immediate neighborhood of the separation point. However, in the immediate neighborhood, there arose some differences due to ventilation in the appearance as well as in the separation angle θ_c.

(iv) In the supercavitating region, the boundary layer on the cavity surface could separate more easily with decreasing σ_c, and the boundary layer separation possibly interacted with the cavity separation.

(v) The velocities q_s measured in the immediate neighborhood of the separation point agreed with the theoretical one in the supercavitating or in the pseudo-supercavitating region, but in the transient region, there was a considerable discrepancy between them, and it increased with σ_c. The latter fact was remarkable.

(vi) The difference between the time averaged velocity profiles around two quite different cavitating states in the transient region was extremely limited in a narrow region near the cylinder. Therefore, the flow feature is said to scarcely depend on the appearance.

The authors wish to express their thanks to Prof. B. R. Parkin for his valuable discussions and to Mr. J. Higuchi for his assistance in the experiments.

References

1 Birkhoff, G., and Zarantonello, E. H., *Jets, Wakes, and Cavities,* Academic Press, New York, 1957, p.78.

2 Roshko, A., "A New Hodograph for Free-Streamline Theory," NACA, TN 3168, 1954, pp.1-39.

3 Brennen, C., "A Numerical Solution of Axisymmetric Cavity Flows," *Journal of Fluid Mechanics,* Vol.37, Part 4, 1969, pp.671-688.

4 Fabula, A. G., "Choked Flow About Vented or Cavitating Hydrofoils," ASME *Journal of Basic Engineering,* Vol.86, No.3, 1964, pp.561-568.

5 Arakeri, V. H., "Viscous Effects on the Position of Cavitation Separation From Smooth Bodies," *Journal of Fluid Mechanics,* Vol.68, Part 4, 1975, pp.779-799.

6 Oba, R., and Yasu, S., "Unsteady Characteristics of Cavitation Behind a Circular Cylinder, Especially on Two Modes of Oscillations," *Transactions of the Japan Society of Mechanical Engineers,* Vol.46, 1980, pp.199-207.

7 Oba, R., and Yasu, S., "Non-Linear, Low-Frequency Cavity Oscillations Behind a Circular Cylinder," *Transactions of the Japan Society of Mechanical Engineers,* Vol.46, 1980, pp.208-214.

8 Cohen, H., and DiPrima, R. C., "Wall Effects in Cavitating Flows," *Proceedings of Second Symposium on Naval Hydrodynamics,* 1958, pp.367-390.

9 Oba, R., and Yasu, S., "Spatial Cavitation-Nuclei-Measurements by Means of Laser Velocimeter," The Reports of the Institute of High Speed Mechanics, Tohoku University, Vol.38, 1978, pp.1-12.

10 Schlichting, H., *Boundary-Layer Theory,* McGraw-Hill, New York, 1979, p.20.

11 Oba, R., Ikohagi, T., Kim, K. T., Niitsuma, H., and Sato, R., "Cavitation Nuclei Measurements by a Newly Made Coulter Counter Without Adding Salt into Water," *Transactions of the Japan Society of Mechanical Engineers* (in Japanese), Vol. 48, 1980, pp. 1485-1492.

12 Knapp, R. T., Daily, J. W., and Hammitt, F. G., *Cavitation,* McGraw-Hill, New York, 1970, p.9.

13 Silberman, E., and Song, C. S., "Instability of Ventilated Cavities," *Journal of Ship Research,* Vol.5, 1961, pp.13-33.

14 Parkinson, G. V., and Jandali, T., "A Wake Source Model for Bluff Body Potential Flow," *Journal of Fluid Mechanics,* Vol.40, Part 3, 1970, pp.577-594.

side wall, which is almost independent of the main flow of interest. In the immediate neighborhood of the separation point, there arises an apparent difference in the appearance due to ventilation in the pseudo-supercavitation; for example, the cavity with ventilation takes place slightly away from the cylinder, while the one without ventilation takes place directly on the cylinder. However in the supercavitation there is no such marked difference. Thus, some differences mentioned above are reaffirmed here. And as may be expected, the pseudo-supercavitating cavity is evidently frothy and the surface is fairly rough, while the supercavitating cavity is clear and the surface is glassy as well as striated.

In such flows, the wall effects so often become serious problems. Figure 11 shows the blocking factor, a kind of the wall effects, U_B/U_∞ against σ_c and indicates that $U_B/U_\infty - 1$ are within 3 percent. Notice here the factor is also uniquely expressed by σ_c.

Figure 12 illustrates the velocity profiles at a distance from the cylinder, $x/d = 0$ and 2.5. Evidently, the profiles are also uniquely expressed by σ_c and the downstream one at $x/d = 2.5$ much varies with σ_c as is expected in such cavitating flows. It is also apparent from the upstream one at $x/d = 0$ that the disturbance due to the cylinder almost vanishes in $y/d = 3$, if the blocking factor is small. In the present experiments, therefore, the upstream reference pressure is measured at $y/d = 5.0, x/d = -5.0$.

To clarify the flow feature when the instability takes place in the transient region, in Fig. 13, the time averaged velocity profile around the attached cavity is compared with that around the cavitation in the vortex near the separation point at a typical case of $\sigma_v = 1.3$. Since the difference between them is extremely limited within a narrow region near the cylinder, the feature is said to scarcely depend on the cavitation appearance, though the cavitation appearances are quite different from each other.

5 Conclusions

By means of LDV and high speed photography, the behavior of supercavitation as well as of cavitation, especially near the separation point, were carefully observed in a two-dimensional subcritical flow around the cylinder installed in the 300 × 50 mm rectangular test section in which the wall effects were negligible, in both with and without ventilation. The following results were obtained:

(i) The flow was not detached from the separation point smoothly as had been widely expected, but rather abruptly in all cases with or without ventilation, in which abruptness increased with decreasing σ_c. Thus, the assumption "smooth separation" is not satisfactory, but somewhat harmful in the supercavitating region.

(ii) There was a transient region, where two quite different cavitating states, i.e., the attached cavity and the cavitation in the vortex, were alternately observed at the same value of σ_v, and in the supercavitating region σ_c was very close to σ_v, while it was quite different from σ_v in the subcavitating region as might be expected.

(iii) The features such as the cavity dimensions, the velocity profiles and the blocking factor U_B/U_∞ were almost independent of the vented condition and were uniquely expressed by σ_c, but not expressed by σ_v, except those in the immediate neighborhood of the separation point. However, in the immediate neighborhood, there arose some differences due to ventilation in the appearance as well as in the separation angle θ_c.

(iv) In the supercavitating region, the boundary layer on the cavity surface could separate more easily with decreasing σ_c, and the boundary layer separation possibly interacted with the cavity separation.

(v) The velocities q_s measured in the immediate neighborhood of the separation point agreed with the theoretical one in the supercavitating or in the pseudo-supercavitating region, but in the transient region, there was a considerable discrepancy between them, and it increased with σ_c. The latter fact was remarkable.

(vi) The difference between the time averaged velocity profiles around two quite different cavitating states in the transient region was extremely limited in a narrow region near the cylinder. Therefore, the flow feature is said to scarcely depend on the appearance.

The authors wish to express their thanks to Prof. B. R. Parkin for his valuable discussions and to Mr. J. Higuchi for his assistance in the experiments.

References

1 Birkhoff, G., and Zarantonello, E. H., *Jets, Wakes, and Cavities,* Academic Press, New York, 1957, p.78.

2 Roshko, A., "A New Hodograph for Free-Streamline Theory," NACA, TN 3168, 1954, pp.1-39.

3 Brennen, C., "A Numerical Solution of Axisymmetric Cavity Flows," *Journal of Fluid Mechanics,* Vol.37, Part 4, 1969, pp.671-688.

4 Fabula, A. G., "Choked Flow About Vented or Cavitating Hydrofoils," ASME *Journal of Basic Engineering,* Vol.86, No.3, 1964, pp.561-568.

5 Arakeri, V. H., "Viscous Effects on the Position of Cavitation Separation From Smooth Bodies," *Journal of Fluid Mechanics,* Vol.68, Part 4, 1975, pp.779-799.

6 Oba, R., and Yasu, S., "Unsteady Characteristics of Cavitation Behind a Circular Cylinder, Especially on Two Modes of Oscillations," *Transactions of the Japan Society of Mechanical Engineers,* Vol.46, 1980, pp.199-207.

7 Oba, R., and Yasu, S., "Non-Linear, Low-Frequency Cavity Oscillations Behind a Circular Cylinder," *Transactions of the Japan Society of Mechanical Engineers,* Vol.46, 1980, pp.208-214.

8 Cohen, H., and DiPrima, R. C., "Wall Effects in Cavitating Flows," *Proceedings of Second Symposium on Naval Hydrodynamics,* 1958, pp.367-390.

9 Oba, R., and Yasu, S., "Spatial Cavitation-Nuclei-Measurements by Means of Laser Velocimeter," The Reports of the Institute of High Speed Mechanics, Tohoku University, Vol.38, 1978, pp.1-12.

10 Schlichting, H., *Boundary-Layer Theory,* McGraw-Hill, New York, 1979, p.20.

11 Oba, R., Ikohagi, T., Kim, K. T., Niitsuma, H., and Sato, R., "Cavitation Nuclei Measurements by a Newly Made Coulter Counter Without Adding Salt into Water," *Transactions of the Japan Society of Mechanical Engineers* (in Japanese), Vol. 48, 1980, pp. 1485-1492.

12 Knapp, R. T., Daily, J. W., and Hammitt, F. G., *Cavitation,* McGraw-Hill, New York, 1970, p.9.

13 Silberman, E., and Song, C. S., "Instability of Ventilated Cavities," *Journal of Ship Research,* Vol.5, 1961, pp.13-33.

14 Parkinson, G. V., and Jandali, T., "A Wake Source Model for Bluff Body Potential Flow," *Journal of Fluid Mechanics,* Vol.40, Part 3, 1970, pp.577-594.

DISCUSSION

E. Silberman[5]

Some very useful experimental data and observations on supercavitating flow are reported by the authors. The data will provide grist for the mills of persons doing numerical calculations for many years.

Conclusion (iv) regarding boundary layer separation is speculative and not supported by any data. There appears to be a more reasonable explanation for the non-monotonic behaviour of the velocity profiles at low cavitation numbers shown in Fig. 9. That is the stagnation effect on the front of the body plus cavity shown in Fig. 12; the body plus cavity is thicker at small cavitation numbers than at larger numbers, as shown in Fig. 7.

The authors comment on their inability to obtain cavities of discontinuous length (vibrating cavities) during ventilation as described by the discusser in reference [13]. They should realize from that reference that σ_c/σ_v would have to be very

[5]Professor, St. Anthony Falls Hydraulic Laboratory, University of Minnesota, Minneapolis, Minn.

much smaller than any values plotted in Fig. 6 to obtain vibrating cavities. Furthermore, a narrowly confined closed jet as used by the authors has a different effect on cavity growth than does a free jet or infinite fluid wherein the pressure surrounding the wake is esentially constant.

B. R. Parkin[6]

This writer applauds the efforts of this research group at Sendai for coming to grips with a problem which has been in need of investigation for many years [15, 16]. Although the sources just cited draw upon experiments which were designed to study the onset of cavitation on hemispherical headforms, it is believed that the evidence indicated is applicable to the cavity separation problem as studied by the present authors for fully cavitating flows. The reason is that the present observations and those cited concern cavity separation when the cavity separation point is influenced by an incoming boundary layer which is laminar as reported more recently in those parts of references [17] and [18] which show band cavitation on hemispherical headforms.

This writer suspects that water probably wets the brass cylinders used in the present experiments so that the contact angle between the liquid and the solid is probably less than 90 deg, and if the surface were chemically clean, it could vanish. When one compares this bit of information with the separation angles, θ_c, of the present paper, he immediately suspects that further, but more detailed, experiments might be worthwhile. For example, can the authors give us any information on the details of their use of the laser velocimeter? In particular, can they indicate some characteristic length of the measuring volume, defined by the intersecting beams which can be compared with the laminar boundary layer thickness or other lengths which might characterize various regions in the flow? In a similar vein, we would also like to have their opinion on their photographs of the cavity separation point. Can these photographs resolve those parts of the flow which depend most strongly on surface tension?

The foregoing matters also bear upon the data presented in Fig. 8 of the paper. It is not obvious to this writer than the dashed curve should pass through the origin because the interface between the water and the cavity will still be subject to the more slowly moving fluid from the laminar boundary layer near separation. Could it be possible that the liquid speeds on the interface are even less than those reported because our techniques at present cannot fully resolve such small-scale details? Can the same be said if the results from Fig. 11 were used to correct the data at $s/d = 2.5$ in Fig. 12 from u/U_B to u/U_∞ (which might be close to q_s/U_∞)? Can the data of Fig. 12 for $x/d = 0$ give us any indication of the spatial resolution possible in the present experiments? If this is the case, can any correction to the data be devised which might permit one to extrapolate to the surface? Even an approximate method might be better than none at all.

In conclusion, it is fair to say that the present investigators have taken on a difficult piece of research and this writer is delighted that they have risen to the challenge. It is earnestly hoped that they will persevere.

Additional References

15 Kermeen, R. W., McGraw, J. T. and Parkin, B. R., "Mechanism of Cavitation Inception and the Related Scale-Effects Problem," *Trans. ASME,* May 1955, p. 537, Fig. 6.

16 Cooper, R. D. (Ed.), *Proc. Second Symposium on Naval Hydrodynamics,* ACR-38, Office of Naval Research, Dept. of the Navy, Washington, D.C., 1958, pp. 259–260.

17 Arakeri, V. H., "Viscous Effects in Inception and Development of Cavitation on Axi-Symmetric Bodies," Ph.D. thesis, California Institute of Technology, 1973. (Also released as Report No. 3183.1, Division of Engineering and Applied Science, California Institute of Technology, 1973.)

18 van der Meulen, J. H. J., "A Holographic Study of Cavitation on Axisymmetric Bodies and the Influence of Polymer Additives," Ph.D. thesis, Enschede, 1976.

Authors' Closure

The authors would like to thank Professor E. Silberman and Professor B. R. Parkin for their friendly, fruitful discussions and interesting suggestions.

In our experiments, the very small blockage ratio of 0.05 is selected to make the stagnation effect negligible in the test section composed of solid walls. Therefore, the velocity profiles near the separation point shown in Fig. 9, from which conclusion (iv) is derived, are considered to be scarcely affected by the stagnation effect, and their nonmonotonic behavior at low cavitation numbers experimented is believed to be an inherent character in such a two-dimensional supercavitating flow. Remember here that the behavior emerges initially not within the range of $\sigma_c > 0.6$ but $0.4 < \sigma_c < 0.5$, while the blocking factor U_B/U_∞ shown in Fig. 11, which should be closely related to the stagnation effect, is said to be almost equivalent within the marked range of $0.4 < \sigma_c < 0.6$. At extremely lower cavitation numbers of $\sigma_c << 0.4$, however, there is no way to check how dominant the stagnation effect is, if any.

The instability of supercavitating cavity due to ventilation, that is, the vibrating cavities, which is said to be of great importance, has been precisely investigated by Professor Silberman, the present discusser, on several bodies in a free jet tunnel. Then, the instability has been discussed by many investigators, and several mechanisms have been proposed. Therefore, at the present stage, it is also meaningful to confirm whether such vibrating cavities are observed or not in a solid wall tunnel without any free surfaces. And within our experimental range where σ_c/σ_v is rather higher, no vibrating cavity is confirmed to be observable during ventilation. Also Professor T. Nishiyama, Tōhoku University, has personally communicated to us that no vibrating cavity was observable even in his experiment performed in a solid wall tunnel when σ_c/σ_v was much smaller.[7]

Since our object is to understand the essential behavior of subcavitating and supercavitating flows, the most fundamental outer flow without extremely confined, complex viscous layer, that is, the rather steady, pseudo-potential flow is chiefly investigated. At the present stage, it is not necessarily obvious to the authors that the cited studies on viscous effects in axisymmetric cavitating flows by Arakeri et al. are directly applicable to our cavity separation problem, especially in the supercavitating flow, though we are much interested in these studies.

The separation angle θ_c, which is closely related to the cavity drag, is defined here as an included angle between the tangent of the cavity surface and that of the body surface at the cavity separation point, where the cavity leading edge is steadily observed on the high speed photograph. In general, θ_c is not necessarily related only to the contact angle or the surface tension, because the complicated dynamical forces, such as a suction force, work near the separation point. And, the spatial resolution of high speed photographs is high

[6] Garfield Thomas Water Tunnel, Applied Research Laboratory, The Pennsylvania State University, State College, Pa. 16801.

[7] Nishiyama, T. and Kaga, T., *Trans. JSME*, Vol. 39, 1973, pp. 3699–3706.

enough to determine such separation angles, and our Laser velocimeter has a small measuring volume of about $2 \times 10^{-6}\text{cm}^3$, so that the local mean velocity is sufficiently measurable in such a pseudo-potential flow, as described elsewhere [9].

Professor Parkin's comment is very attractive on the dashed curve on Fig. 8, which has been rather artifically drawn with expecting an asymptotic trend towards the theoretical curve. We have not yet observed the more slowly moving fluid on the cavity surface, though we are also very interested in such a behavior.

In the present study, the accurate measurements by means of the Laser velocimeter have not yet been made in the extreme neighborhood along the cavity surface, concerning Fig. 12 which shows the behaviors upstream and downstream from the separation region. Anyway, we agree with Professor Parkin, upon necessity of further experiments on the actual cavity surface and the viscous layer.

Kaichiro Mishima
Research Reactor Institute, Kyoto University, Japan; presently Visiting Scientist at Applied Physics Division, Argonne National Laboratory, Argonne, Ill. 60439

Mamoru Ishii
Reactor Analysis and Safety Division, Argonne National Laboratory, Argonne, Ill. 60439. Mem. ASME

Theoretical Prediction of Onset of Horizontal Slug Flow

A criterion for the onset of a slug flow in a horizontal duct is derived theoretically. A potential flow analysis is carried out by considering waves of finite amplitude. The stability criterion is obtained by introducing the wave deformation limit and the "most dangerous wave" concept in the stability analysis. The present theoretical criterion for slug formation shows very good agreement with a large number of experimental data and with some empirical correlations.

Introduction

When a gas flows over a liquid surface with large relative velocity in a horizontal duct, the interface will become disturbed and eventually the formation of slug flow will occur. Slug formation has been studied by many investigators [1-4]. In earlier works, it was thought that the Kelvin-Helmholtz instability was the basic mechanism of slug formation. Kelvin-Helmholtz instability will occur when the suction effect due to the pressure variation over a wave becomes sufficiently large to overcome the stabilizing effect of gravity. For long waves of small amplitude, the criterion for the classical Kelvin-Helmholtz instability [5-8] is given theoretically by,

$$V_G - V_L \geqq \sqrt{(\rho_L - \rho_G) g h_G / \rho_G} \tag{1}$$

Equation (1), however, overpredicts the gas velocity for the formation of slug flow by a factor of two.

Kordyban and Ranov [1] pointed out that in the case of two-phase flow in a closed conduit, the effect of Kelvin-Helmholtz instability was significantly enhanced by the proximity of the upper wall. They considered waves of finite amplitude and arrived at an approximate criterion for slug formation,

$$(V_G - V_L)^2 \geqq \frac{\rho_L g}{\rho_G k} \times \frac{1}{\coth(kh_G - 0.9) + 0.45 \coth^2(kh_G - 0.9)} \tag{2}$$

In order to obtain this equation, they used the experimental relationship between wave amplitude and wavelength. Moreover, it was required to know the depth of the air channel and the wavelength in order to use this equation.

Wallis and Dobson [2] proposed the following criterion for slug formation from observation of experimental data,

$$V_G - V_L \geqq 0.5\sqrt{(\rho_L - \rho_G) g \ h_G / \rho_G} \tag{3}$$

Equation (3) correlated their data for flow of air over water over a wide range of changes in geometrical variables and also the data of Kordyban and Ranov [1]. In order to explain this correlation, they extended Benjamin's work [9] for liquid flow around a stagnant gas bubble to the idea of gas flow over a large stationary water wave. Their arguments, however, are questionable because the analogy between Benjamin's model and their model has little theoretical basis.

In 1976, Taitel and Dukler [3] proposed a theoretical model for predicting flow regime transitions in horizontal two-phase flow. They considered the pressure difference over the wavy surface due to the Bernoulli effect. They postulated that slug formation would occur when the pressure difference was large enough to overcome the gravity force acting on the wave and arrived at the following criterion:

$$V_G \geqq K_1\sqrt{(\rho_L - \rho_G) g \ h_G / \rho_G} \tag{4}$$

where

$$K_1 = \sqrt{\frac{2}{h_G/h_c (h_G/h_c + 1)}} \tag{5}$$

for slug formation between horizontal parallel plates; and

$$V_G \geqq K_2\sqrt{\frac{(\rho_L - \rho_G) g \cos \alpha \ A_G}{\rho_G dA_L/dh_L}} \tag{6}$$

where

$$K_2 \simeq A_G/A_G$$

for slug formation in a horizontal or near horizontal pipe.

Contributed by the Fluids Engineering Division for presentation at the Winter Annual Meeting, Chicago, Ill., November 16-21, 1980, of THE AMERICAN SOCIETY OF MECHANICAL ENGINEERS. Manuscript received by the Fluids Engineering Division, October 24, 1979. Paper No. 80-WA/FE-6.

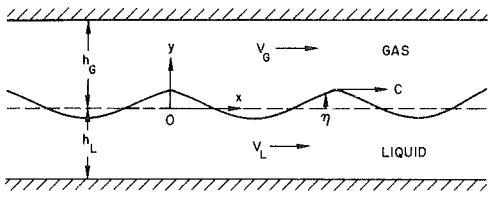

Fig. 1 Finite waves in horizontal duct

However, using qualitative arguments, they estimated K_1 and K_2 to be as follows;

$$K_1, K_2 = 1 - \frac{h_L}{D} \tag{7}$$

This result is consistent with the result of Wallis and Dobson when $h_L/D = 0.5$.

More recently, Kordyban [4] assumed that the pressure difference over the wave might be expressed as follows,

$$\Delta P = \frac{K}{2} \rho_g (V_c^2 - V_t^2) \tag{8}$$

Then, he obtained, from a force balance, following criterion,

$$K \frac{\rho_G}{\rho_L - \rho_G} \cdot \frac{V_c^2}{g h_G} = 1 \tag{9}$$

It is noted that equation (9) is similar to equation (4). The constant value K was estimated to be 1.35 from observations of experimental data.

As described so far, previous works proposed the criterion for the formation of slug flow which had essentially the same expression as equation (4), and the value of K_1 was determined, after all, from observations of experimental data. Present work, extending the analysis of Kordyban and Ranov [1], however, attempts to obtain the value of K_1 theoretically. It will be shown that the value of K_1 can be determined by introducing the wavelength of the "most dangerous wave" into the equation of Kordyban and Ranov.

The Proposed Basic Mechanism of Slug Formation

When gas flows over a wavy liquid surface at sufficiently high gas velocities, the suction effect due to the pressure difference over the wave will become so large that it overcomes the stabilizing effect due to the gravity force, which is so called Kelvin-Helmholtz instability. In case of two-phase flow in a closed conduit (see Fig. 1), the suction effect will be significantly enhanced by the proximity of upper wall, according to the Bernoulli effect. When this instability occurs, a particular wave will continue to grow until it attains a limiting amplitude. In this situation, we can no longer consider waves of infinitesimal amplitude. We suppose that the particular wave should have the length of the "most dangerous wave," which has the largest growth rate. We propose that this is what we observe as slug formation.

Theory of Waves of Finite Amplitude

As mentioned above, we must consider waves of finite amplitude in order to obtain the criterion for slug formation in a closed conduit. Kordyban and Ranov [1] extended the analysis of Lamb [7] by introducing a finite wave displacement η. In their nonlinear analysis, ideal two-dimensional flows of air and water were assumed, and the motions of the fluids were represented by the Laplace equations for velocity potentials and stream functions. Then, the form of the solution of Laplace equations, which satisfied the condition that the stream functions should be constant at the interface, was postulated as,

$$\frac{\phi_L}{C} = x - \beta_L \cosh k(y + h_L) \sin kx \tag{10}$$

$$\frac{\psi_L}{C} = y - \beta_L \sinh k(y + h_L) \cos kx \tag{11}$$

$$\frac{\phi_G}{U} = -x - \beta_G \cosh k(h_G - y) \sin kx \tag{12}$$

$$\frac{\psi_G}{U} = -y + \beta_G \sinh k(h_G - y) \cos kx \tag{13}$$

where ϕ and ψ were the potentials and the stream functions, respectively. A wave profile was determined from the condition that $\psi_L = 0$ at the interface, and thus,

$$\eta = \beta_L \sinh k(\eta + h_L) \cos kx \tag{14}$$

The pressures at the interface were calculated from Bernoulli equation, resulting in the form,

$$\frac{p_L}{\rho_L} = \text{const} - g\eta - \frac{1}{2} C^2 [1 - 2k\eta \coth k(\eta + h_L) + k^2\eta^2 \coth^2 k(\eta + h_L) + k^2\eta^2 \tan^2 kx] \tag{15}$$

$$\frac{p_G}{\rho_G} = \text{const} - g\eta - \frac{1}{2} U^2 [1 + 2k\eta \coth k(h_G - \eta) + k^2\eta^2 \coth^2 k(h_G - \eta)] \tag{16}$$

These pressures have to satisfy the boundary condition at the interface,

$$p_L - p_G + T \frac{\partial^2 \eta}{\partial x^2} = 0 \tag{17}$$

Nomenclature

A_G' = cross-sectional area of gas flow at crest
A_G = mean cross-sectional area of gas flow
C = wave velocity
C_1 = actual wave velocity
C_2 = amplitude growth rate
D = hydraulic diameter
F_k = ($k = G$ or L) functions defined by equations (19) and (20)
g = gravity
h_k = ($k = G$ or L) height
h_c = distance from wave crest to top wall
H = total channel height
K = constant
K_1 = constant
K_2 = constant
k = wave number
p_k = ($k = G$ or L) pressure
T = surface tension
U = gas velocity relative to wave velocity
V_k = ($k = G$ or L) mean velocity
V_c = gas velocity at crest
V_t = gas velocity at trough
x = axial distance
y = transverse distance
z = parameter ($= kh_G$)
β_k = ($k = G$ or L) constant
Δp = pressure difference
η = interface displacement
η_{max} = maximum interface displacement
ρ_k = ($k = G$ or L) density
ϕ_k = ($k = G$ or L) velocity potential
ψ_k = ($k = G$ or L) stream function

Subscripts

L = liquid phase
G = gas phase

Using equations (15), (16), and (17), and assuming that the vertical components of the velocity and the surface tension terms are small at the neutral level ($\eta = 0$), a following equation can be obtained,

$$F_L C^2 = \left[g\eta\left(1-\frac{\rho_G}{\rho_L}\right)-\frac{T}{\rho_L}\frac{\partial^2\eta}{\partial x^2}\right]-F_G\frac{\rho_G}{\rho_L}U^2 \tag{18}$$

where

$$F_L \equiv k\eta \coth k(h_L+\eta)\left[1-\frac{1}{2}k\eta \coth k(h_L+\eta)\right] \tag{19}$$

$$F_G \equiv k\eta \coth k(h_G-\eta)\left[1+\frac{1}{2}k\eta \coth k(h_G-\eta)\right] \tag{20}$$

Neglecting the current velocity in the water and solving for C, equation (18) yields

$$C=\frac{F_G\frac{\rho_G}{\rho_L}V_G}{F_L+F_G\frac{\rho_G}{\rho_L}}+\sqrt{\left(\frac{F_G\frac{\rho_G}{\rho_L}V_G}{F_L+F_G\frac{\rho_G}{\rho_L}}\right)^2+\frac{g\eta\left(1-\frac{\rho_G}{\rho_L}\right)-\frac{T}{\rho_L}\frac{\partial^2\eta}{\partial x^2}-F_G\frac{\rho_G}{\rho_L}V_G^2}{F_L+F_G\frac{\rho_G}{\rho_L}}} \tag{21}$$

The instability occurs when C is imaginary, and thus the criterion for slug formation can be expressed by,

$$\frac{F_G F_L\frac{\rho_G}{\rho_L}}{F_L+F_G\frac{\rho_G}{\rho_L}}V_G^2 = g\eta\left(1-\frac{\rho_G}{\rho_L}\right)-\frac{T}{\rho_L}\frac{\partial^2\eta}{\partial x^2} \tag{22}$$

If the current velocity in the liquid is taken into account, equation (22) should be written in the form,

$$\frac{F_G F_L\frac{\rho_G}{\rho_L}}{F_L+F_G\frac{\rho_G}{\rho_L}}(V_G-V_L)^2 \geqq g\eta\left(1-\frac{\rho_G}{\rho_L}\right)-\frac{T}{\rho_L}\frac{\partial^2\eta}{\partial x^2} \tag{23}$$

Simplified Instability Equation

Some simplifications can be made in equation (23) by taking into account the large density ratio, i.e., $\rho_G/\rho_L << 1$, and, therefore, $F_G\rho_G/\rho_L << F_L$. Moreover, we assume that the surface tension effect is not important except near wave crests where $\partial^2\eta/\partial x^2$ is large. This implies that for the overall stability of surface waves, the last term in equation (23) can be neglected. Then we obtain from equation (22),

$$V_G^2 \geqq \frac{\rho_L g\eta}{F_G\rho_G} \tag{24}$$

The value of η can be determined by assuming that, when the instability occurs, a particular wave attains its limiting amplitude. From equation (14), we find that there is a cusp of the wave, when

$$k\ \eta_{\max} = \tanh\ (k\eta_{\max}+kh_L) \tag{25}$$

Since relatively deep water waves are concerned with slug formation and the function $\tanh x$ approaches quickly to 1 as x increases as shown in Fig. 2, we obtain for deep water waves,

$$k\eta_{\max} = 1 \tag{26}$$

Then, equation (24) becomes

$$V_G^2 \geqq \frac{\rho_L g h_G/\rho_G}{kh_G F_G(kh_G)} \tag{27}$$

where $F_G(kh_G) = \coth(kh_G-1)[1+0.5\ \coth(kh_G-1)]$ (28)

Instead of equation (26), Kordyban and Ranov [1] used the value of 0.9 for $k\eta_{\max}$ from their experimental observations, and obtained the criterion given by equation (2). The value of $k\eta_{\max}$ given by equation (26) is slightly larger than that observed in the experiment [4] and that of the Michell's analysis [10]. However, for the simplicity and consistency, the theoretical limit of 1 has been used in our analysis.

By using the assumptions described above, equation (21) becomes,

$$C=2F_G(kh_G)\frac{\rho_G}{\rho_L}V_G+\sqrt{\frac{2g}{k}-2F_G(kh_G)\frac{\rho_G}{\rho_L}V_G^2} \tag{29}$$

Most Dangerous Wave

Equation (27) can be rewritten in the form,

$$V_G \geqq K_1\sqrt{\rho_L g h_G/\rho_G} \tag{30}$$

where

$$K_1 = 1/\sqrt{kh_G F_G(kh_G)} \tag{31}$$

In order to use equation (30), it is required to determine the value of kh_G.

When the instability occurs, it is assumed that the dominant wave which can be observed, is the "most dangerous wave" with the largest growth rate. In equation (29), the second term in right-hand side becomes imaginary, when the instability occurs. Then, instead of equation (29), we have,

$$C = C_1 + iC_2 \tag{32}$$

where

$$C_1 = 2F_G(kh_G)\frac{\rho_G}{\rho_L}V_G$$

$$C_2 = \sqrt{2F_G(kh_G)\frac{\rho_G}{\rho_L}V_G^2-\frac{2g}{k}}$$

Using the fact that the growth rate of the wave is given by $k|C_2|$, the value of k, which gives the maximum growth rate, can be determined. Thus, the condition imposed on k is

$$\frac{d}{dk}k|C_2| = 0 \tag{33}$$

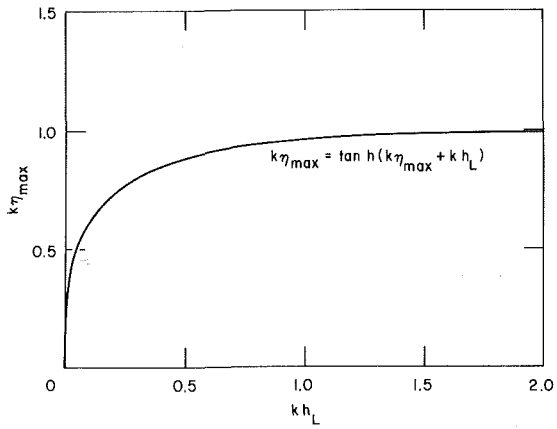

Fig. 2 Relation between $k\eta_{\max}$ and kh_h at appearance of wave cusp

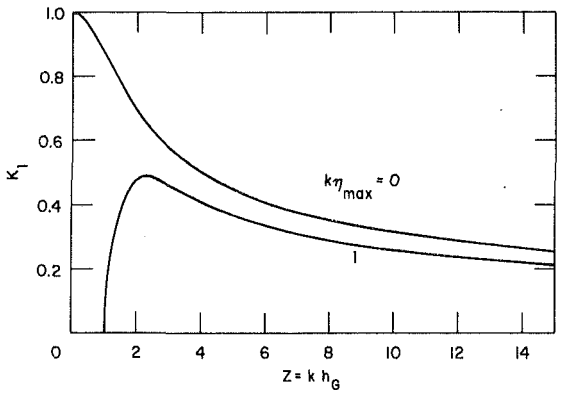

Fig. 3 Proportionality constant K_1 as function of $z = kh_G$

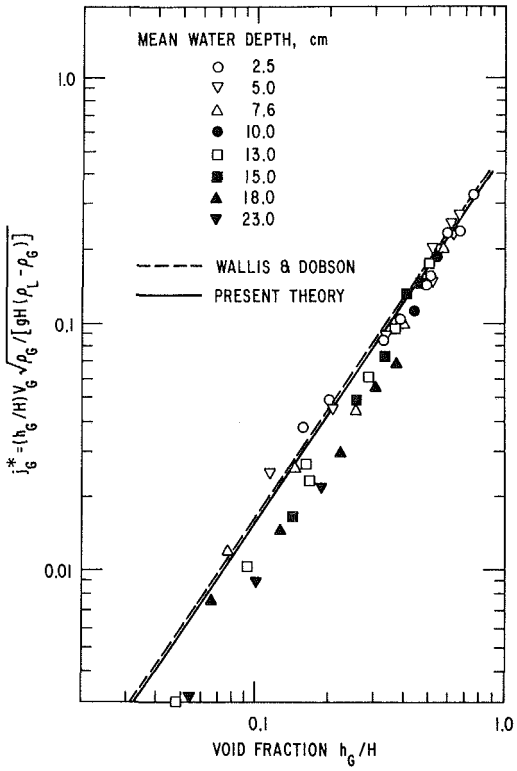

Fig. 4 Theoretical prediction of onset of horizontal slug flow compared to data of Wallis and Dobson (effect of water depth)

From equations (32) and (33), we have,

$$[2F_G(z) + zF_G'(z)]\frac{\rho_G}{\rho_L}V_G^2 - \frac{gh_G}{z} = 0 \tag{34}$$

where

$$F_G'(z) = \frac{dF_G(z)}{dz}$$

$$z = kh_G$$

Since equation (27) should be satisfied just when the instability occurs, we can use equation (27) in order to eliminate the second term in the left-hand side of equation (34). Then we obtain

$$F_G(z) + zF_G'(z) = 0 \tag{35}$$

Note that equation (35) is equivalent to the condition which gives the maximum value of K_1 in equation (30). In fact, equation (35) is satisfied when $kh_G = 2.26$, which gives the maximum value of K_1, 0.487, in equation (31), as shown in

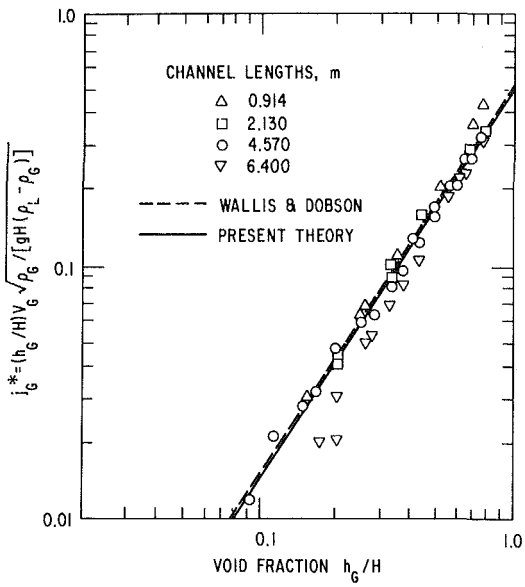

Fig. 5 Theoretical prediction of onset of horizontal slug flow compared to data of Wallis and Dobson (effect of duct length)

Fig. 3. Then, we obtain the criterion for slug formation in the form,

$$V_G \geqq 0.487\sqrt{\rho_L g h_G/\rho_G} \tag{36}$$

and

$$kh_G = 2.26 \tag{37}$$

If the buoyancy in the gas and the current velocity in the liquid should be taken into account, equation (36) becomes,

$$V_G - V_L \geqq 0.487\sqrt{(\rho_L - \rho_G)gh_G/\rho_G} \tag{38}$$

In Fig. 3, the curve corresponding to $k\eta_{max} = 0$ is also shown as a reference case of the linear theory. It is interesting to note that the value of K_1, determined from the idea of the "most dangerous wave," approaches to unity and kh_G approaches to zero, when the limiting amplitude approaches to zero. In this case we obtain equation (1). This result is consistent with the classical Kelvin-Helmholtz instability analysis.

Discussion

It can be seen from Figs. 4 and 5 that equation (36) agrees very well with the empirical correlation of Wallis and Dobson [2] and a number of experimental data. Figure 6 shows that there is fairly good agreement between equation (36) and the experimental data of Kordyban and Ranov [1]. In the correlation of Kordyban and Ranov, the wave length was estimated to be between 2.5 and 5 cm from the experimental observations, while equation (37) predicts the wave length to be between 1.5 and 3.5 cm. This result may be reasonable when we consider the simplifications used in our theory.

The influence of liquid level h_L on the slug formation may not be significant. We can, however, estimate the effect of liquid level from Fig. 2 and Fig. 3. It can be found from Fig. 2 that the limiting amplitude will be reduced in the case of shallow water. Then, from Fig. 3, we obtain a larger value of K_1. This means that higher gas velocity will be required for slug formation when the liquid level is low. This effect, however, is not sifnificant. In fact, if we assume $kh_L = 0.1$, $k\eta_{max}$ becomes 0.6 and the maximum value of K_1 is 0.58, which is only 20 percent larger than the value for the deep water case.

Conclusions

1. The criterion for slug formation has been derived

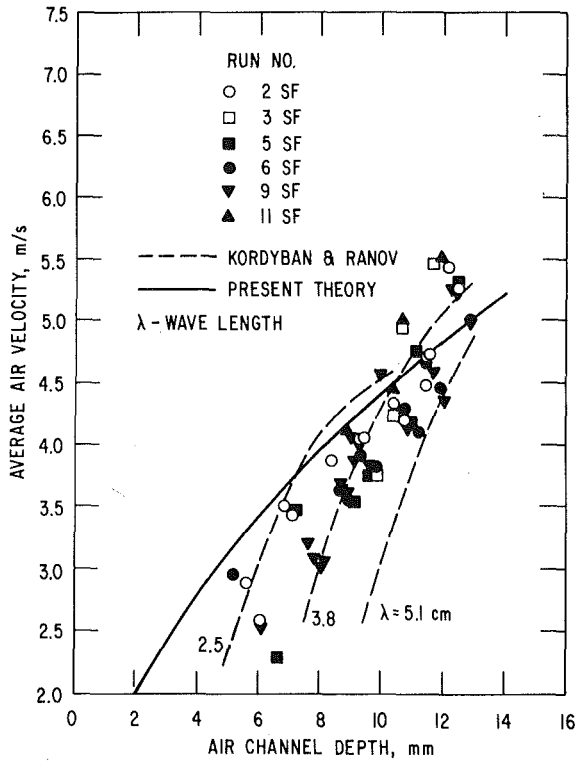

Fig. 6 Comparison of theory to Kordyban and Ranovs' experiment

theoretically, considering waves of finite amplitude with the following assumptions:

(*a.*) the "most dangerous wave" will be observed when the instability occurs,

(*b.*) the "most dangerous wave" will attain the limiting amplitude obtained by equation (25) or equation (26).

(*c.*) surface tension may be neglected if we consider overall behavior of waves.

2. The theoretical criterion for slug formation, represented by equation (38), shows fairly good agreement with other empirical results. However, the criterion may not be valid at very low liquid levels at which the effects of viscosity cannot be neglected any more.

3. Classical Kelvin-Helmholtz instability can be derived as a limiting case of our theory; $k\eta_{max} = 0$.

Acknowledgment

The part of this work was performed under the auspices of the U. S. Nuclear Regulatory Commission.

References

1 Kordyban, E.S., and Ranov, T., "Mechanism of Slug Formation in Horizontal Two-Phase Flow," ASME *Journal of Basic Engineering,* Vol. 92, 1970, p. 857.

2 Wallis, G.B., and Dobson, J.E., "The Onset of Slugging in Horizontal Stratified Air-Water Flow," *Int. J. Multiphase Flow,* Vol. 1, 1973, p. 173.

3 Taitel, Y., and Dukler, A.E., "A Model for Predicting Flow Regime Transitions in Horizontal and Near Horizontal Gas-Liquid Flow," *AIChE Journal,* Vol. 22, No. 1, 1976, p. 47.

4 Kordyban, E., "Some Characteristics of High Waves in Closed Channels Approaching Kelvin-Helmholtz Instability," ASME JOURNAL OF FLUIDS ENGINEERING, Vol. 99, 1977, p. 339.

5 Helmholtz, H., "Über discontinuirliche Flüssigkeits-bewegungen," *Monatsber. Akad. Wiss.,* Berlin, 1868, p. 215.

6 Kelvin, W., "Hydrokinetic Solutions and Observations," *Phil. Mag.,* Vol. 4, 1871, p. 374.

7 Lamb, H., *Hydrodynamics,* Dover, New York, 1945 (Originally published in 1879).

8 Milne-Thomson, L. M., *Theoretical Hydrodynamics,* MacMillan, New York, 1963.

9 Benjamin, T.B., "Gravity Currents and Related Phenomena," *J. Fluid Mech.,* Vol. 31, 1968, p. 209.

10 Michell, J.H., "The Highest Waves in Water," *Phil Mag.,* 5, No. 36, 1893, p. 430.

A Theoretical Study on Air Bubble Motion in a Centrifugal Pump Impeller

Kiyoshi Minemura
Lecturer,
Department of General Education.

Mitsukiyo Murakami
Professor,
Department of Mechanical Engineering.

Nagoya University,
Nagoya, Japan

Equations of motion for air bubbles in a centrifugal pump impeller were obtained and solved numerically for a flow in a radial-flow-type impeller, and the results were compared with experiments. Governing factors for the bubble motion are the force due to the pressure gradient, the drag force due to the flow resistance of the surrounding liquid, and the inertia force due to virtual mass of the liquid. If the bubble diameter is reduced continuously, the effect of the inertia force is also reduced and trajectories of the air bubbles approach more and more to the path of the flowing water.

1 Introduction

The water flowing through the impeller of a centrifugal pump frequently contains cavitation vapor bubbles and air bubbles entrained from outside. The presence of the cavitation bubble constitutes a danger of erosion damage to the impeller and casing of the pump, and most investigators engaging in the cavitation problem have focused their interest on the subject of bubble collapse. The air bubbles entrained from outside generally pass through the impeller without collapse or accumulation.

The trajectories of air bubbles will be shifted more or less from the path of water by the transverse pressure gradient in the impeller. This shift will prevent a precise determination of the collapse point of the cavitation bubbles and erosion region, and may cause, in some cases, a local accumulation of air bubbles in the impeller and bring about a remarkable degradation of the pump performance [1–5].

The bubble behavior in the water flowing through a rotating field is an interesting subject, but researches into it are few, except for those on the flows between co-rotating disks employed in nuclear rockets [6] and skylab [7], or studies on the droplet in vapor [8].

In order to study the motion of air bubbles in a rotating impeller, the path of water particles in the impeller was first discussed on the basis of equations of motion for a single phase liquid. Then, an air bubble of a small diameter was set free in this flow field, and equations of motion for it were deduced on the assumption that the flow field was not affected by the existence of the bubble. The equations were solved numerically to find the bubble trajectory in the water. The process of this analysis can be explained as follows.

Flow of water in the impeller is assumed to be inviscid and steady, and has stream surfaces of revolution, as is generally assumed for computation of flow in a rotating cascade [9]. In this case, the flow is quasi-three-dimensional and can be discussed as having a meridional stream line and a blade-to-blade surface on the axisymmetric stream surface. The flow was calculated by use of a finite difference method, in which the computer program of Katsanis [10] was employed in a modified form. In order to confirm the calculated results, the motion of air bubbles in an impeller was traced experimentally by use of a high speed camera. Agreement of the theory with experiments seems to be quite satisfactory.

2 Theory

2.1 Equations of Motion for a Single Phase Liquid. Figure 1 shows a rotating system of coordinates with an axial symmetry. Assuming an inviscid imcompressible flow, the equation of motion for a single phase liquid is given by

$$\frac{D_a\mathbf{W}_a}{Dt}=\frac{\partial\mathbf{W}}{\partial t}+\mathbf{W}\cdot\nabla\mathbf{W}+\omega\times\mathbf{W}+\mathbf{W}\times(\omega\times\mathbf{r})=-\frac{1}{\rho}\nabla_a p \quad (1)$$

and the static pressure p at an arbitrary point is given by

$$p=p_{is}-\rho\omega\lambda+\rho\{(\omega r)^2-|\mathbf{W}|^2\}/2 \quad (2)$$

where

$$\mathbf{W}=W_r\mathbf{i}_r+W_\theta\mathbf{i}_\theta+W_z\mathbf{i}_z \quad (3)$$

After rewriting with use of equation (2), equation (1) can be solved numerically by means of a three-dimensional procedure, provided that the flow is steady and axisymmetric [11]. The static pressure at any point in the flow field can be determined by equation (2), where effect of the gravity is not

Contributed by the Fluids Engineering Division and presented at the Winter Annual Meeting, Chicago, Ill., November 16–21, of The American Society of Mechanical Engineers. Manuscript received by the Fluids Engineering Division, September 18, 1979. Paper No. 80-WA/FE-3.

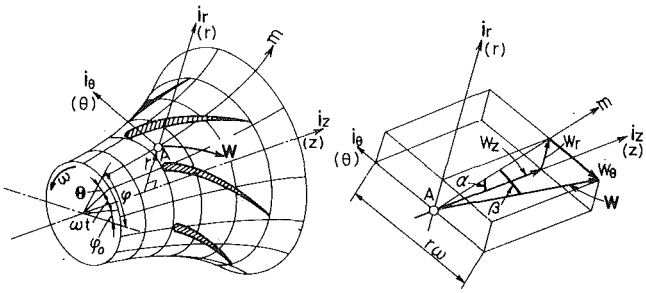

Fig. 1 *(a)* Stream surface *(b)* Velocity vector of water Coordinate system

considered. The effect can be taken into account if the following expression is introduced in equation (2),

$$P = p - \rho g r \sin \varphi \tag{4}$$

2.2 Equations of Motion for Bubbles. If it is assumed that the number of the air bubbles entrained in water is few and the diameter of the bubbles is also small, it can be considered that the flow condition of water remains substantially unaltered by entrainment of the bubbles. In this case, the history of a single bubble can give information on the behavior of the bubbles in the impeller. If it is assumed that neither mass nor heat transfer are present, the equation of motion for an air bubble of mass M moving in water with velocity $\mathbf{V}_a$ can be given in an absolute coordinate system as follows [12],

$$M(\mathrm{D_a}\mathbf{V}_a/Dt) = -\mathbf{F}_d + \mathbf{F}_p + \mathbf{F}_y + \mathbf{F}_v + \mathbf{F}_B \tag{5}$$

The first term of the right-hand side of equation (5) signifies the drag force due to motion of the bubble relative to the water. The second term is the force due to the pressure gradient in the water surrounding the bubble. The third term denotes the body force due to the difference in densities between water and air. The fourth term denotes the force needed to accelerate the water displaced by bubble motion. The last term, due to Basset, is a history term showing the effect of the previous acceleration on the force at present time.

If the bubble maintains the shape of sphere having the diameter d during the motion, the drag force on the bubble is given by

$$\mathbf{F}_d = \left(\frac{1}{2}\rho\right)\left(\frac{\pi}{4}d^2\right) C_d(\mathrm{V}_a - \mathbf{W}_a)\,|\mathbf{V}_a - \mathbf{W}_a| \tag{6}$$

where C_d is a drag coefficient and is usually given in terms of the Reynolds number of bubble defined by,

$$\mathrm{Re} = d\,|\mathbf{V}_a - \mathbf{W}_a|/\nu \tag{7}$$

An air bubble in water like tap water behaves as a solid sphere [13] and it has been shown experimentally that the relationship between the drag coefficient C_d and the Reynolds number of a gas bubble can be given by [14]

$$C_d = (24/\mathrm{Re})(1 + 0.15\ \mathrm{Re}^{0.687}) \tag{8}$$

and

$C_d = 0.44$ for $\mathrm{Re} \geq 989$, $C_d = 24/\mathrm{Re} + 2$ for $\mathrm{Re} \leq 6.5$.

The vector sum of the forces on a bubble due to the pressure gradients in flow field and the weight of the bubble, $(= F_p + F_y)$, may be written as

$$\mathbf{F}_p + \mathbf{F}_y = -\int_S P\mathbf{n}\ dS - Mg\nabla_a(r \sin\varphi) \tag{9}$$

where the integration $\int_S$ should be extended over the total bubble surface and $\mathbf{n}$ is the unit vector of the outward direction normal to the bubble surface. Through use of the

Nomenclature

A_2 = effective discharging area of impeller outlet
C_d = bubble drag coefficient
C_v = virtual mass coefficient
d = bubble diameter
$\mathbf{F}_y$ = buoyancy vector due to the difference in densities between water and air
$\mathbf{F}_d$ = force vector due to flow resistance
$\mathbf{F}_p$ = force vector due to pressure gradient
$\mathbf{F}_v$ = force vector due to acceleration of apparent mass of bubble
$\mathbf{F}_B$ = Basset's force vector
g = acceleration of gravity
$\mathbf{i}$ = unit vector
M = mass of bubble
m = displaced mass of water by bubble
p = absolute static pressure referred to pump center height
p_{is} = total pressure of pump inlet measured on its centerline level
P = static pressure
Q = pump discharge
r = radial distance from axis of rotation
$R, \dot{R}, \ddot{R}$ = radial coordinate, velocity, and acceleration of bubble
Re = Reynolds number
t = time
Δt = increment of time
u = peripheral speed of impeller
$\mathbf{V}$ = velocity vector of bubble in a moving frame rotating with angular velocity
V = volume of a bubble
$\mathbf{W}$ = velocity vector of water in a rotating frame
Z = axial distance from pump inlet
$Z, \dot{Z}, \ddot{Z}$ = axial coordinate, velocity and acceleration of a bubble
β = angle of velocity $\mathbf{W}$ against meridian plane
θ = angular coordinate
$\Theta, \dot{\Theta}, \ddot{\Theta}$ = tangential coordinate, velocity and acceleration of a bubble measured in rotating frame
φ = angular coordinate of bubble referred to stationary coordinate system = $\Theta + \omega t + \varphi_0$
λ = angular momentum flux per unit mass of water at the inlet of a pump (referred to stationary coordinate system)
ρ = density of water
σ = surface tension of water
ν = kinematic viscosity of water
ω = angular velocity of impeller
ϕ = dimensionless expression of pump flow rate = Q/A_2u_2

Subscripts

a = absolute coordinate system
0 = initial condition of bubble
r = radial component
θ = circumferential component
z = axial component
2 = impeller outlet

divergence theorem and substitution of equation (4) for the pressure P, equation (9) may be evaluated as

$$\mathbf{F}_p + \mathbf{F}_y = -(m/\rho)\,\nabla_a p + (m-M)g\,\nabla_a(r\,\sin\varphi) \qquad (10)$$

where m is the mass of water displaced by the bubble. The first term of the right-hand side of equation (10) denotes the force $\mathbf{F}_p$ due to the pressure gradient, which can be evaluated by equation (1) which includes the effects of Coriolis and centrifugal forces in the rotating system. The second term represents the force $\mathbf{F}_y$, due to the difference in the fluid densities.

The inertia force of water influencing the bubble motion $\mathbf{F}_v$ is given by

$$\mathbf{F}_v = mC_v(D_a\mathbf{W}_a/Dt - D_a\mathbf{V}_a/Dt) \qquad (11)$$

where C_v is a coefficient expressing the virtual mass effect.

The so-call Basset term, showing an historical effect of the flow pattern round the bubble, is given as

$$\mathbf{F}_B = \left(\frac{9m}{d}\right)\sqrt{\frac{\nu}{\pi}}\int_0^t \frac{D_a(\mathbf{W}_a - \mathbf{V}_a)}{Dt}\,\frac{1}{\sqrt{t-\tau}}\,d\tau \qquad (12)$$

Let the bubble velocity with respect to the rotating frame of reference be $\mathbf{V}$, then

$$\left.\begin{aligned}\mathbf{V} &= \dot{R}i_r + R\dot{\Theta}\mathbf{i}_\theta + \dot{Z}\mathbf{i}_z \\ D\mathbf{V}/Dt &= (\ddot{R} - R\dot{\Theta})\mathbf{i}_r + (2\dot{R}\dot{\Theta} + R\ddot{\Theta})\mathbf{i}_\theta + \ddot{Z}\,\mathbf{i}_z\end{aligned}\right\} \qquad (13)$$

and

$$D_a\mathbf{V}_a/Dt = D\mathbf{V}/Dt + 2\omega\times\mathbf{V} + \omega\times(\omega\times\mathbf{r}) \qquad (14)$$

or

$$D_a\mathbf{V}_a/Dt = \{\ddot{R} - (\omega+\dot{\Theta})^2 R\}_{\mathbf{i}_r} + \{R\ddot{\Theta} + 2(\omega+\dot{\Theta})\dot{R}\}\mathbf{i}_\theta + \ddot{Z}\mathbf{i}_z \qquad (15)$$

where the dots indicate time derivative.

Substitution of equations (6), (10), (11), and (12) into equation (5) yields the following equation for the bubble motion,

$$M\left(\frac{D_a\mathbf{V}_a}{Dt}\right) = -\left(\frac{3m}{4d}\right)C_d(\mathbf{V}_a - \mathbf{W}_a)\,|\mathbf{V}_a - \mathbf{W}_a| - \frac{m}{\rho}\nabla_a p + (m-M)g\,\nabla_a(r\sin\varphi) + mC_v\left(-\frac{1}{\rho}\nabla_a p - \frac{D_a\mathbf{V}_a}{Dt}\right) + \left(\frac{9m}{d}\right)\sqrt{\frac{\nu}{\pi}}\int_0^t \frac{D_a(\mathbf{W}_a - \mathbf{V}_a)}{Dt}\,\frac{1}{\sqrt{t-\tau}}\,d\tau \qquad (16)$$

Collecting the terms of an expression of $\mathbf{Va} - \mathbf{Wa} = \mathbf{V} - \mathbf{W}$ included in this equation, the acceleration components in the direction of the unit vectors $\mathbf{i}_r$, $\mathbf{i}_\theta$, and $\mathbf{i}_z$ at a point (R, Θ, Z) can be written, respectively, as,

$$\left.\begin{aligned}\ddot{R} &= \left\{-\frac{3m}{4d}C_{dr}(\dot{R} - W_r)\,|\dot{R} - W_r| - \frac{m}{\rho}(1+C_v)\,\frac{\partial p}{\partial r} - (m-M)g\sin\varphi + F_{Br}\right\}/(M + C_v m) + (\omega+\dot{\Theta})^2 R \\ R\ddot{\Theta} &= \left\{-\frac{3m}{4d}C_{d\theta}(R\dot{\Theta} - W_\theta)\,|R\dot{\Theta} - W_\theta| - \frac{m}{\rho}(1+C_v)\,\frac{1}{R}\,\frac{\partial p}{\partial \theta} - (m-M)g\cos\varphi + F_{B\theta}\right\}/(M + C_{vm}) - 2(\omega+\dot{\Theta})\dot{R} \\ \ddot{Z} &= \left\{-\frac{3m}{4d}C_{dz}(\dot{Z} - W_z)\,|\dot{Z} - W_z| - \frac{m}{\rho}(1+C_v)\,\frac{\partial p}{\partial z} + F_{Bz}\right\}/(M + C_v m)\end{aligned}\right\} \qquad (17)$$

where F_{Br}, $F_{B\theta}$, and F_{Bz} indicate the components of the Basset term in the direction of $\mathbf{i}_r$, $\mathbf{i}_\theta$ and $\mathbf{i}_z$, respectively.

Assuming that the bubble volume $V\,(=\pi d^3/6)$ changes in a quasi-steady-state, the pressure difference between the ambient static pressure P and the internal pressure of the bubble $(=P_o V_o/V = P_o d_o^3/d^3)$ can be given by

$$P = P_o d_o^3/d^3 + p_v - 4\sigma/d \qquad (18)$$

where p_v is the saturated vapor pressure. By rewriting the above equation, the following relation for the bubble diameter can be derived

$$(P - p_v)d^3 + 4\sigma d^2 - P_0 d_0^3 = 0 \qquad (19)$$

This equation may be solved for the diameter d as a function of the water pressure P, which can be estimated as a function of position. Thus, equation (17) is sufficient to determine the motion of the bubbles as a function of the position and the velocity of the bubble, and the Basset term.

3 Numerical Solution

3.1 Flow of Water in Impeller. General design for an impeller should keep the depth of the impeller channel such that it will maintain a nearly constant meridian velocity in the radial direction [15]. A two-dimensional impeller having a constant depth in the radial direction as shown in Fig. 2 has its blade thickness changed circumferentially to satisfy the above requirement, resulting in an impeller having blades of a relatively thick trailing edge. A theoretical treatment of the flow around such a thick blade is impossible, except for the blade of a small circular form or of one sharp in the trailing edge, because the position of the rear stagnation point can not be decided theoretically. Impeller blades as shown in Fig. 2 have large separated regions behind them, and the regions were decided by the following approximate procedure in this study.

The separated regions were detected experimentally by use of piezo-metric sensors and a Pitot tube, which were inserted through several openings on the casing wall downstream from the impeller outlet. And the absolute flow angle, together with the circumferential extension of the separated regions and their position relative to the impeller trailing edge were decided. If the free stream lines starting from a separated rear edge are asumed to be the curves connected smoothly through the points on the boundary of the separated region and with the measured flow angles, then the blade-to-blade flow pattern can be solved numerically. In this case, the region enclosed by such free stream lines should be treated as a part of the impeller blade. The computer program of a finite difference method for calculation of blade-to-blade flow employed by Katsanis [10] was slightly modified.

Since the flow properties of water are known at all the mesh

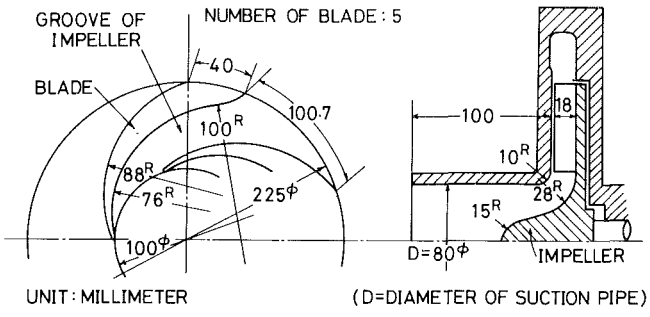

Fig. 2 Shape of meridian section and of pump impeller

points and the boundary points from the above calculation, the values of the water flow everwhere in each mesh grid can be obtained by linear interpolation from the values of the mesh points and the boundary enclosing it, if the mesh length adapted is sufficiently small.

3.2 Flow of Bubbles. Velocity of a bubble is assumed to be the same as that of water at the inlet section of the pump passage. Diameter of the bubble d at any point can be determined as a function only of the coordinate that is found from equation (19) by use of a Newton Raphson method.

Let the bubble position, velocity, and acceleration at a time t be denoted by suffix i, and those at a time $t+\Delta t$ by suffix $i+1$, equation (17) gives the initial bubble acceleration at the time t as

$$\left.\begin{aligned} R_i &= f_r(R_i,\Theta_i,Z_i,\dot{R}_i,\dot{\Theta}_i,\dot{Z}_i,F_{Bri}) \\ \ddot{\Theta}_i &= f_\theta(R_i,\Theta_i,Z_i,\dot{R}_i,\dot{\Theta}_i,\dot{Z}_i,F_{B\theta i}) \\ \ddot{Z}_i &= f_z(R_i,\Theta_i,Z_i,\dot{R}_i,\dot{\Theta}_i,\dot{Z}_i,F_{Bzi}) \end{aligned}\right\} \quad (20)$$

where the Basset terms can be evaluated from the integration of equation (12) on the assumption that the accelerations of water and the bubble remain unaltered during each small time interval. Thus, the Basset term can be obtained by

$$\mathbf{F}_{Bi} = -18m_i\sqrt{\frac{\nu}{\pi}}\sum_{j=1}^{i}\left(\frac{D\mathbf{W}_{j-1}}{Dt} - \frac{D\mathbf{V}_{j-1}}{Dt}\right)(\sqrt{t-(j-1)\Delta t}-\sqrt{t-(j\Delta t)})/d_i \quad (21)$$

The new position of the bubble after a short time of Δt can be computed by

$$\left.\begin{aligned} R_{i+1} &= R_i+\dot{R}_i\cdot\Delta t+\ddot{R}_i\cdot(\Delta t)^2/2 \\ \Theta_{i+1} &= \Theta_i+\dot{\Theta}_i\cdot\Delta t+\ddot{\Theta}_i\cdot(\Delta t)^2/2 \\ Z_{i+1} &= Z_i+\dot{Z}_i\cdot\Delta t+\ddot{Z}_i\cdot(\Delta t)^2/2 \end{aligned}\right\} \quad (22)$$

and its velocity components in the new position are

$$\left.\begin{aligned} \dot{R}_{i+1} &= \dot{R}_i+\ddot{R}_i\Delta t \\ \dot{\Theta}_{i+1} &= \dot{\Theta}_i+\ddot{\Theta}_i\Delta t \\ \dot{Z}_{i+1} &= \dot{Z}_i+\ddot{Z}_i\Delta t \end{aligned}\right\} \quad (23)$$

Error included in equation (22) is of the order of $(\Delta t)^3$, while that in equation (23) is of the order of $(\Delta t)^2$, which is greater than the former. Thus, the velocity components given by equation (23) can be taken as the first approximation, and these values are substituted in equation (20) to obtain the acceleration components after the time interval Δt. With these acceleration components, the second approximation of velocity components after the time Δt may be calculated by the second order Runge-Kutta method as follows:

$$\left.\begin{aligned} \dot{R}_{i+1} &= \dot{R}_i+(\ddot{R}_i+\ddot{R}_{i+1})\Delta t/2 \\ \dot{\Theta}_{i+1} &= \dot{\Theta}_i+(\ddot{\Theta}_i+\ddot{\Theta}_{\theta+1})\Delta t/2 \\ \dot{Z}_{i+1} &= \dot{Z}_i+(\ddot{Z}_i+\ddot{Z}_{i+1})\Delta t/2 \end{aligned}\right\} \quad (24)$$

These processes are repeated for every successive time interval Δt until the bubble leaves the region of the impeller. With this every step of the trajectory, the velocity of the bubble, and also the magnitude of the forces acting on the bubble are known.

If the bubble has a chance to hit the surface of an impeller blade, the time interval necessary for the bubble to just hit the wall Δt_i and its velocity component tangential to the surface at the collision are obtained. Since the bubble may travel along the surface with this velocity component, the travelling distance just after the collision in the rest time interval $(\Delta t-\Delta t_i)$ is also obtained.

If the above numerical integration is carried out for the differential equations given by equation (17), the computational accuracy will depend on the time interval adapted. In order to obtain the optimum time step Δt, the numerical solution of equation (17) is calculated for a hypothetical particle having a small diameter of the order of $d = 0.2$ mm and the same density as water. The difference between the trajectory of the hypothetical particle and the path of water obtained from the definite method is made small to coincide sufficiently by decreasing the time step Δt.

4 Experimental Apparatus and Sample Data for Numerical Analysis

In order to confirm this numerical analysis, an experiment was made with a centrifugal pump having a transparent casing and tubing. The pump is of a radial-flow and low-specific speed type [specific speed: 180 (m, rpm, m^3/min), capacity: 0.90 m^3/min, head: 19 m, rotating speed: 1750 rpm, number of blades: 5]. A meridian section of the pump is shown in Fig. 2 (right), and the flow in the impeller may be considered to be two-dimensional. When the pump is operated near optimum capacity, the streamlines in the impeller will lie substantially in the radial direction. To calculate the flow in the pump, the flow region can be divided into two successive parts; one is the impeller eye region ($r-z$ planes) and the other is the region in the impeller ($m-\Theta$ planes). For both regions, a two-dimensional calculation can be applied (see Fig. 1). In the impeller eye region, the bubbles which were entrained from some upstream sections gather inside part of the inlet bend, and the bubbles are drawn partially into the impeller. Thus, the bubble motion in the impeller should be treated along the impeller shroud. In calculation, twenty-one meridian streamlines were taken in the meridian section and, in the impeller region, the shroud surface and the third streamline nearest to it were chosen so as to constitute a partial flow channel, the center line of which is given by the second streamline from the shroud. Movement of the bubble was investigated in the blade-to-blade surface as explained above.

The behavior of bubbles in the pump impeller was observed at the optimum point discharge ($\phi = 0.08$) at the normal rotating speed of 1750 rpm, when the suction pressure was

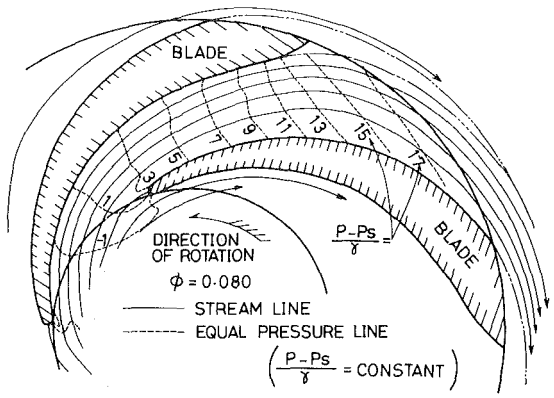

Fig. 3 Streamlines of water in the impeller

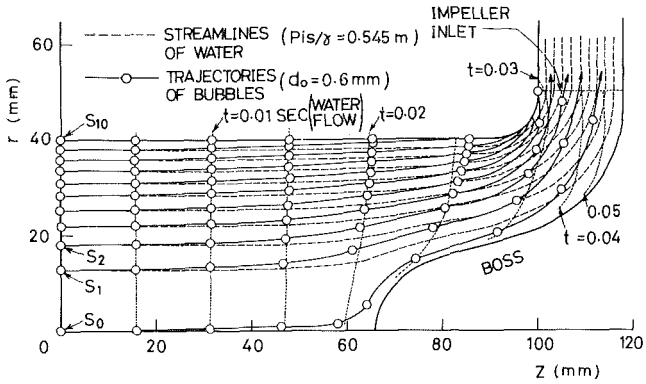

Fig. 4 Trajectories of air bubbles and streamlines of water in impeller eye region

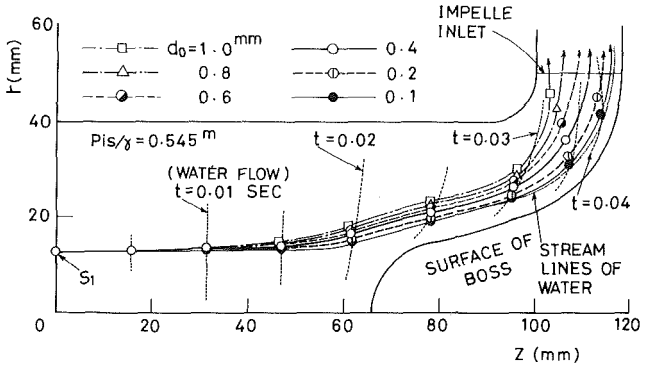

Fig. 5 Effects of bubble diameter on its trajectory

maintained high enough to prevent cavitation (p_{is}/γ = 5.45 m). In this case, the water in the impeller eye flows uniformly without prerotation and enters the impeller channel at a right angle. Then, the water leaves it at an angle of 85.1 deg[1], which was assumed from the measured results of Pitot tube mounted at a point $r = 1.07\ r_2$ behind the impeller. The leakage flow through the running clearance between the impeller blades and the casing wall was so small that its effect on the main flow could be neglected.

The blade-to-blade streamlines obtained numerically[2] from the above procedure are shown in Fig. 3. The results obtained are substantially consistent with the experimental results of visualization by a tuft method, as is described later. Consequently, the flow pattern in Fig. 3 will be available as a basis for calculations of the bubble motion. For reference, the lines of equal pressure $\{(p-p_s)/\gamma = \text{constant}\}$ are also drawn in Fig. 3, where p_s is the static pressure referred to the height of pump inlet.

When a pump is operated near its optimum discharge, the water flows, in general, at a considerably high velocity in the suction pipe. In this condition, if a small quantity of air, usually less than 7 percent in the volumetric ratio of air to water in the inlet condition, is admitted to the suction pipe, the air is dispersed in a bubbly form and flows down to the pump inlet, the diameter of each bubble being less than 3 mm [1]. On entering the impeller passage of the pump, these bubbles are crushed into finer and more uniform size of spheres and flow through the impeller [1, 2]. Diameter of air bubbles in the impeller is generally less than 0.6 mm, and it decreases as the pump speed and the number of the impeller blades increase and also as the quantity of air decreases [2, 4]. When the pump with five impeller blades was operated at its normal speed (1750 rpm) and capacity (0.90 m^3/min), the size was approximately 0.25 mm [1].

The trajectories of air bubbles in the impeller passage were also traced experimentally by means of a high speed motion picture. 16 mm films taken at 3000 frames per second were projected on a screen of 1.3 m × 1.0 m in size, and trajectories of air bubbles were traced firstly on this screen in the stationary coordinate system, and then, the results were reduced to the rotating coordinate system, In this photographing only, pump speed was selected to be 1300 rpm lower than the normal because of the limitation of luminous intensity. And air was admitted at the rate of 1.5 percent in volumetric ratio through the section $13D$ (D: diameter of suction pipe) ahead of the impeller, when the water flow rate was ϕ = 0.08, corresponding to the maximum efficiency point.

5 Results of Calculations and Discussions

5.1 Movement of Air Bubbles in Impeller Eye Region. Trajectories of air bubbles calculated by the method described earlier are shown in Fig. 4, where it is assumed that bubbles with a diameter of 0.6 mm have the same velocity as water at the initial section ($z_0 = 0$, $\varphi_0 = 90$ deg) located 100 mm ahead of the impeller. In the same figure, the paths of water particles are also shown by broken lines.

The positions of the bubbles at every 0.005 seconds are shown with circular marks. As the bubbles flow down, the trajectories of bubbles begin to deviate gradually from the streamlines of water toward the inside of the inlet curvature of the passage, and hence it follows that the bubbles enter the impeller through the crowded region of air. The deviation will depend on the bubble size. Effects of the diameter on this deviation are shown in Fig. 5, where the initial position of bubble motion is taken to be the section S_1 as in Fig. 4. The deviation tends to be less as the bubble diameter decreases.

The above numerical solutions are based on the spherical shape of a bubble. According to the past investigations on the behavior of a bubble, the bubble keeps a spherical shape when the Reynolds number Re defined by equation (7) is lower than 500 ~ 700. However, if Re is increased beyond this limit, the bubble takes an ellipsoidal shape, and then finally, a spherical cap shape when Re exceeds 4000 ~ 5000. In course of motion, the bubble changes its size according to the pressure in the flow field. Change in the bubble diameter experienced in Fig. 5 is illustrated in the above half of the Fig. 6, where d_0 is the bubble diameter at the initial section ($z=0$). The change is appreciable only in the range near the impeller. A noticeable difference in the diametrical ratio in the region, $z>90$ mm,

[1] Uncertainty: ± 0.5 deg

[2] In this calculation, square mesh is constructed in the pump inlet with twelve grids in the radial direction (space: 10/3 mm) and rectangular mesh in the cascade with twenty-one grids in the meridial direction (space: 3.33 mm) and thirty in the circumferential direction (space: 0.419 rad).

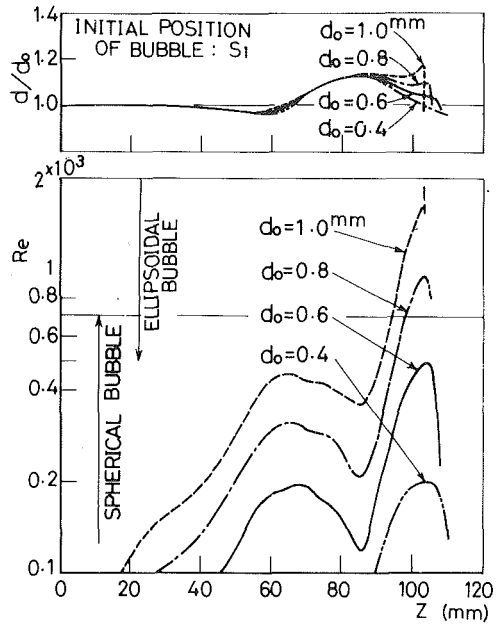

Fig. 6 Change in diameter and Reynolds number of bubble in impeller eye region

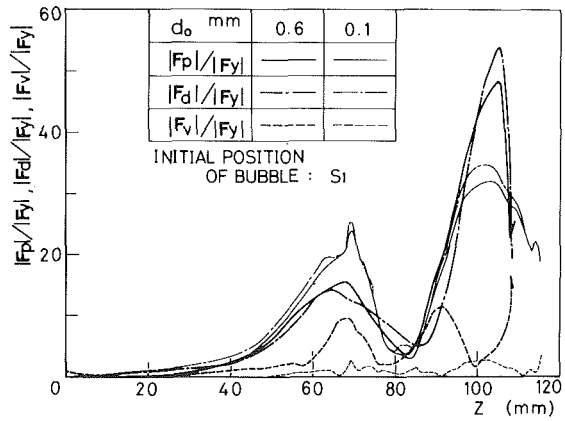

Fig. 7 Change in component forces acting on a bubble in impeller eye region

will result from the difference in travelling course of each individual bubble caused by a transverse pressure gradient in the flow field. Change in the Reynolds number of bubble based on the bubble diameter and its velocity relative to the surrounding water is shown in Fig. 6 below. The value of Re varies remarkably as the location of the bubbles, z, changes. Increase of Re in the range of 50 mm $\leqq z \leqq$ 80 mm is due to a reduction of the flow passage area and that in the range of $z \geqq$ 90 mm is due to the passage curvature. Within the range of $z >$ 100 mm, namely the region just before the impeller inlet, a rapid drop of Re which resulted probably from a rise of pressure in the field can be seen.

The smaller the bubble diameter d, the smaller the Reynolds number. If d is decreased below 0.6 mm, the bubble retains a spherical shape throughout the motion. But if d is increased beyond 0.8 mm, the bubble assumes an ellipsoidal shape when it is in the range of Reynolds numbers corresponding to the flow in the curved passage just ahead of the impeller. The results in Fig. 6 are obtained on the assumption that the bubble maintains a spherical shape, though an ellipsoidal shape is partially included in it.

A bubble in motion is affected by various external forces as is seen in equaton (5). Since the mass of a small bubble is

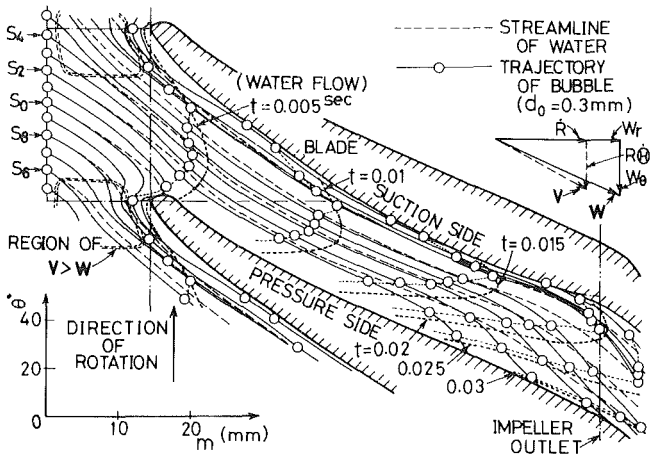

Fig. 8 Trajectories of air bubbles on a blade-to-blade surface of revolution

extremely small, the inertial force can be taken substantially to be zero, and the motion is nearly in a steady state and the hysteresis force known as the Basset term can also be neglected. The buoyancy due to the difference in densities of the bubble and the surrounding water keeps nearly a constant value throughout the flow field.

Component forces acting on a bubble are shown dimensionlessly against the distance from the initial position z in Fig. 7, where $\mathbf{F}_p$ is the force caused by pressure gradient, $\mathbf{F}_d$ the drag force, $\mathbf{F}_v$ the force relating to the virtual mass, and $\mathbf{F}_y$ the buoyancy due to the difference of the fluid densities. In the area near the inlet ($z \leqq 40$ mm), the motion of the bubble is decided substantially by buoyancy and drag force, since the bubble motion is nearly rectilinear in this area and the pressure gradient along the motion is only slight. While in the areas of converging flow sections (60 mm $\leqq z \leqq$ 80 mm) and of the curved flow sections (90 mm $\leqq z \leqq$ 100 mm), the pressure gradient along the flow or normal to it grows to an appreciable amount and the force $|\mathbf{F}_p|/|\mathbf{F}_y|$ increases to a comparable order to the force $|\mathbf{F}_d|/|\mathbf{F}_y|$. In this area the inertia force expressing the virtual mass effect, $|\mathbf{F}_v|/|\mathbf{F}_y|$, is also increased. The results obtained for bubbles with different diameters are also compared in Fig. 7. The smaller the bubble diameter d, the smaller the virtual mass effect, and finally, the motion of the bubble is decided by the two forces of pressure gradient and flow resistance.

5.2 Movement of Bubbles in Impeller. Trajectories of air bubbles starting from the points on different streamlines are calculated by the above numerical integration and the results are plotted in Fig. 8, when the bubble diameter at the initial section is assumed to be 0.3 mm as usually observed in pump impellers. The initial section is located at 15 mm ahead of the impeller and velocities of bubbles at this section are taken to be the same as the water. The bubble trajectories are seen to coincide approximately with the streamlines of water in the inlet region, but as the bubbles flow down, they begin to deviate from the streamlines of water toward the pressure side of impeller blades.

The motion of bubbles in the impeller is chiefly governed by the drag force due to the resistance of flowing water and the force due to pressure gradient in the flow field which will be described in more detail in the later part of this section (Fig. 11). The difference between pressures on both sides of impeller blades will disappear at the outlet ends, and the change of pressure in the circumferential direction or the corresponding change of relative velocities lessens, and $R\dot{\theta} \approx W_\theta$. The existence of impeller blades, however, does

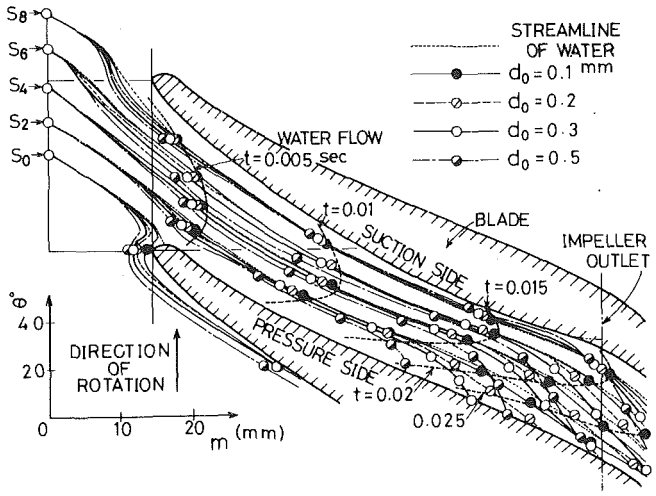

Fig. 9 Effects of bubble diameter on its trajectory in impeller

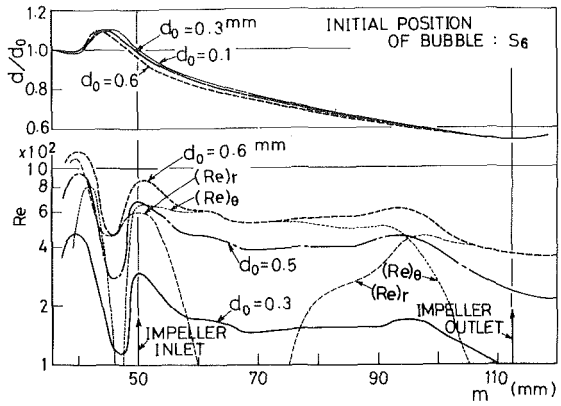

Fig. 10 Change in diameter and Reynolds number of bubble

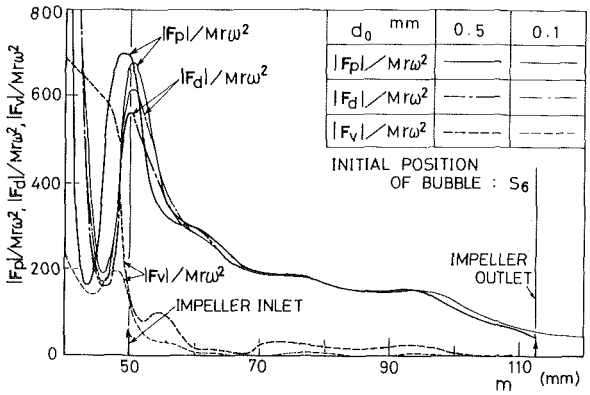

Fig. 11 Change in component forces acting on a bubble in impeller

not exert any substantial effect on the change of pressure in the radial direction and there prevails a positive pressure gradient in that direction. Thus, the radial component of the bubble velocity is less than that of water and $\dot{R} < W_r$. In this circumstance, the bubble trajectories will deviate from the streamlines of water toward the pressure side of impeller blades, as is seen from the velocity triangle in the inset in Fig. 8. A similar trend can be seen in the region just before the impeller inlet, where the section of flow passages is expanded radially (Fig. 4), but it remains almost unaltered circumferentially. Thus, it follows that the field pressure in the inlet region changes more slowly in the circumferential direction than in the radial one.

The time of elapse required for the bubbles to flow down the impeller passage from a given section is also shown in Fig. 8, where positions of the bubbles at every 0.005 seconds are denoted by the thin dotted lines passing through the circular marks, and the corresponding positions of water particles are expressed by the thick dotted lines. Water and air bubbles on the suction side of the impeller blades move faster than those on the pressure side. Only in a particular region enclosed doubly by the broken lines just before the impeller inlet, where a negative pressure gradient dominates locally (Fig. 3), the bubbles move faster than water. If the accelerated bubbles enter the impeller in which a positive pressure gradient prevails, the bubbles receive a retarding force and gather closely. Thus, in this region, the chance of unification of bubbles by collision will be increased and fairly large bubbles will be expected there, when volumetric ratio of air to water is increased over 3 percent.

Trajectories of the bubbles with different diameters are compared in Fig. 9. Deviation of bubble trajectories from the streamlines of water increases with increase of bubble diameter d. For reference, the positions of an individual bubble and water particle at each time interval are shown in the same figure. Difference in the travelling distances of bubbles and water particles at each time interval increases with the bubble diameter d_0, and the time required for a bubble to pass through the impeller passage becomes longer for larger bubbles. Consequently, larger bubbles have larger velocities relative to water, and experience a greater hydraulic resistance which causes much hydraulic loss in a pump.

According to the field pressure, the bubbles change their size as is shown in Fig. 10 above, where it is assumed that the bubbles started from the point S_6 as shown in Fig. 9 and they flow down through the central zone of the impeller passage. Within the region of $m > 50$ mm corresponding to the impeller region, all of the bubbles contract their diametrical ratio (d/d_0) in the same rate toward the impeller outlet.

The Reynolds numbers of bubbles corresponding to this change are shown in the lower part of Fig. 10. The larger the bubble diameter d_0, the greater the Reynolds numbers become, but the individual Reynolds numbers remain unaltered within the impeller passage.

In order to examine the change of relative velocities of bubbles in meridian- and peripheral-directions, the values of Reynolds numbers in m- and θ-directions, namely, $(\mathrm{Re})_m$ and $(\mathrm{Re})_\theta$ are also plotted in Fig. 10, when $d_0 = 0.6$ mm. Both of the Reynolds numbers reach their maximum at the impeller inlet. The peripheral Reynolds number $(\mathrm{Re})_\theta$ remains unchanged in m-direction, while the meridian Reynolds number $(\mathrm{Re})_m$ shows maximum values at the inlet and outlet of the impeller, and takes a fairly small value in the middle of the impeller. In this part, equi-pressure lines stretch nearly radially as is seen in Fig. 2, and the pressure gradient in that direction will be small.

The magnitude of component forces acting on an air bubble will be briefly explained below. Since the inertia force, the buoyancy, and the hysteresis force acting on a bubble are negligibly small, these values are excluded from the following discussion. The changes in the force caused by pressure gradient $\mathbf{F}_p$, the drag force $\mathbf{F}_d$, and the virtual mass force $\mathbf{F}_v$ are plotted in Fig. 11, where all of the forces are expressed dimensionlessly by use of a centrifugal force $Mr\omega^2$. The value of $|\mathbf{F}_v|/Mr\omega^2$ is fairly small, and the forces that governs the bubble motion are $\mathbf{F}_d$ and $\mathbf{F}_p$. This relation is not affected by the size of bubble, d_0.

7 Observation of Air Bubbles in Impeller

A general photographic view of the flow in an impeller

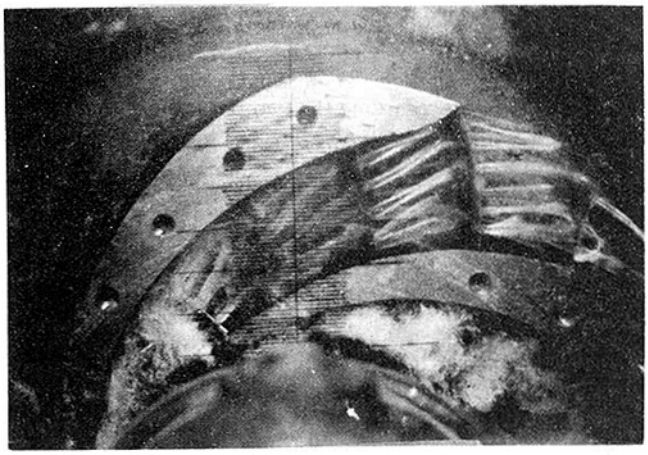

Fig. 12 Flow of water and air bubbles in impeller channel (1750 ± 2 rpm, $\phi = 0.085 \pm 0.0005$)

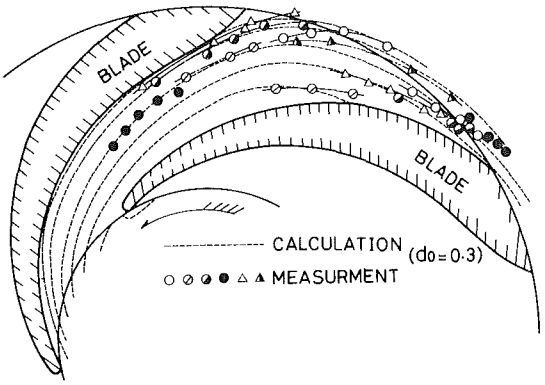

Fig. 13 Trajectories of air bubbles measured by use of a high speed camera (1300 ± 2 rpm, $\phi = 0.080 \pm 0.0005$)

Uncertainty interval for measured coordinates(R_θ,)

Uncertainty interval mm	Uncertainty at radius R_{mm}		
±3.0	R =	112.5 ± 3.0	
	θ =	± 1.5°	(Impeller outlet)
	R =	50.0 ± 3.0	
	θ =	±3.4°	(Impeller inlet)

(Absolute values: 20:1 odds)

channel is shown in Fig. 12, when the pump was operated near normal discharge (ϕ = 0.085) at normal speed and with volumetric ratio of air to water of 0.017 percent. The white lines in the impeller passage are silk threads exhibiting the streamlines of water. Judging from the movement of these threads, the streamlines of water lie parallel to the surfaces of impeller blades as is seen in Fig. 3. Since the air bubbles move substantially along the streamlines of water as in Fig. 8, a uniformly distributed flow of air can be expected in the impeller.

In order to verify this flow, the motion of air bubbles in the impeller was traced experimentally by use of a high speed camera when the pump speed was 1300 rpm, and then the motion was analyzed on the films by projecting the pictures on a screen. The results are shown in Fig. 13. Examinations of the bubble motion were limited only to the regions near the impeller blades, because a high concentration of air bubbles in the central zone of the passage prevented a precise examination.

Diameter of air bubbles inside the impeller was measured on the photographs by referring to a scale marked on the inner wall of pump casing, the division of which was 1 mm. The size of bubbles measured in the region of the impeller inlet was nearly uniform and about 0.3 mm in diameter.

8 Conclusions

Equations of motion for air bubbles in a centrifugal pump impeller were obtained and solved for a special case of flow in a radial-flow impeller of a low specific speed pump, and the results were compared with experiments.

The results are summarized as follows:

(1) Governing factors for the motion of bubbles are the force caused by the pressure gradient in the flow field, the drag force due to the surrounding flow resistance, and the inertia force due to a virtual mass of the liquid.

(2) As the diameter of bubbles decreases, effect of the inertia force on the motion also decreases, and the trajectories of the bubbles in the impeller tend to approach to the path of water. When the diameter is of order of 0.1 mm, the trajectories coincide substantially with the loci of water particles.

(3) Due to a positive pressure gradient, the air bubbles move slower than the water in the impeller channel. But in the suction side region of the impeller inlet, where a negative pressure gradient prevails, the bubbles move faster than the water. Thus, in the space just after this region the bubbles gather closely and accumulate there easily.

(4) Velocities of the bubbles relative to the water increase with the bubble size. The diametrical range in which the bubbles take a spherical shape is $d_0 \leqq 0.6$ mm in impeller eye region and $d_0 \leqq 0.4$ mm in the impeller channel.

References

1 Murakami, M., and Minemura, K., "Effects of Entrained Air on the Performance of Centrifugal Pump (1st Report, Performance and Flow conditions)," *Bulletin of the JSME,* Vol. 17, No. 110, 1974, p. 1047.

2 Murakami, M., and Minemura, K., "Effects of Entrained Air on the Performance of Centrifugal Pumps (2nd Report, Effects of Number of Blades)," *Bulletin of the JSME,* Vol. 17, No. 112, 1974, p. 1286.

3 Murakami, M., and Minemura, K., "Effects of Running Clearance of Semi-Open Impeller Pumps under Air Admitting Conditions," *Bulletin of the JSME,* Vol. 19, No. 136, 1976, p. 1141.

4 Murakami, M., and Minemura, K., "Effects of Entrained Air on the Performance of a Horizontal Axial-Flow Pump," *Proceedings of the Symposium on Polyphase Flow in Turbomachinery,* ASME, 1978, p. 79.

6 Schrage, D. L., and Perkins, Jr., H. C., "Isothermal Bubble Motion Through a Rotating Liquid," ASME *Journal of Basic Engineering,* Vol. 94, No. 1, 1972, p. 187.

7 Siekmann, J., and Dittrich, K., "Über die Bewegung von Gasblasen in einem rotierenden Medium," *Ingenieur-Archiv,* Vol. 44, No. 3, 1975, p. 10.

8 Truman, C. R., Rice, W., and Jankowski, D. F., "Laminar Throughflow of Varying-Quality Steam Between Corotating Disks," ASME JOURNAL OF FLUIDS ENGINEERING, Vol. 100, No. 2, June 1978, p. 194.

9 Vavra, M. H., *Aero-Thermodynamics and Flow in Turbomachines,* Wiley, 1960, p. 304,

10 Katsanis, T., "Computer Program for Calculating Velocities and Streamlines on a Blade-to-Blade Stream Surface of a Turbomachine," NASA TN D-4525, 1968.

11 Katsanis, T., "Use of Arbitrary Quasi-Orthogonals for Calculating Flow Distribution in a Turbomachine," ASME *Journal of Engineering for Power,* Vol. 88, No. 2, 1966, p. 197.

12 Soo, S. L., *Fluid Dynamics of Multiphase Systems, Blaisdell Publishing Co., 1967, p. 31.*

13 Kubota, M., et al., *"The Behavior of Single Air Bubbles in Liquids of Small Viscosity," (in Japanese), Chemical Engineers,* Japan, Vol. 31, No. 11, 1967, p. 1074.

14 Wallis, G. B., *One-Dimensional Two-phase Flow,* 1969, McGraw-Hill, p. 178.

15 Pfleiderer, C., *Die Kreiselpumpen,* 5-Aufl., Springer-Verlag, 1961, p. 225.

DISCUSSION

C. Randall Truman[3]

The authors have presented a simple, approximate analysis of an interesting and significant turbomachinery problem. Presentation of experimental data for the problem is limited to a single flow rate and bubble concentration for comparison with the analysis. Publication of additional data by the authors would be a useful contribution to the literature.

Several questions arise concerning the approximate analysis.

1. Bubbles are assumed to retain a spherical shape even though at high Reynolds numbers the bubbles take on an ellipsoidal shape (Figs. 6, 10). How significant might the effect be if the nonspherical bubble shape were accounted for in the drag force (see Boothroyd [16])? Can this effect be observed experimentally in the regions of high Reynolds number near the impeller inlet?

2. The inviscid solution for the liquid flow field neglects effects of the boundary layers which form on the passage surfaces. In reality, as bubbles near a wall they encounter a small liquid velocity, directly affecting the drag force upon the bubble. Can this effect upon bubbles approaching a surface (e.g., impeller blade) be seen in the photographs? Further, what assumptions were made in determining how a bubble traveled along a surface after collision?

3. In computing the bubble flow field, liquid velocity and pressure were obtained by linear interpolation from the inviscid solution. Thus, the accuracy of the bubble calculation depends on the grid sizes used in the inviscid solution. What was the "optimum" Δt determined to be, and what is the relationship between Δt for the bubble solution and the grid for the inviscid liquid solution? For example, approximately how many grid points does a bubble traverse in each Δt?

Several studies have examined the flow of fluids containing droplets or solid particles in conventional [17, 18] and multiple-disk [8, 19, 20] turbomachines. Truman, Rice, and Jankowski [8, 20] presented two-phase analyses in which local flow fields for the particle/droplet field and viscous field are computed simultaneously. Do the authors consider a similar solution for the present problem (gas bubble in liquid) feasible?

Additional References

16 Boothroyd, R.G., *Flowing Gas-Solids Suspensions,* Chapman and Hall Ltd., London, 1971, pp. 11-12.

17 Gyarmathy, G., "Foundations of a Theory of the Wet Steam Turbine," Juris-Verlag, Zurich, 1962. Translation available as FTD-TT-63-785, Air Force System Command, Foreign Technology Division, Wright-Patterson AFB, Ohio Aug. 1966.

18 Kirillov, I.I., and Yablonik, R.M., "Fundamentals of the Theory of Turbines Operating on Wet Steam," Leningrad, 1968. Translation available as NASA TT F-611.

19 Rice, W., Jankowski, D.F., and Truman, C. R., "Bulk-Parameter Analysis for Two-Phase Throughflow Between Parallel Corotating Disks," *Proceedings,* Heat Transfer and Fluid Mechanics Institute, University of California, Davis, Calif., June 1976, pp. 77-91.

20 Truman, C. R., Rice, W., and Jankowski, D. F., "Laminar Throughflow of a Fluid Containing Particles Between Corotating Disks," ASME JOURNAL OF FLUIDS ENGINEERING, Vol. 101, No. 1, Mar. 1979, pp. 87-92.

[3] Faculty Associate, Mechanical & Energy Systems Engineering, Arizona State University, Tempe, Ariz. 85281.

P. W. Runstadler Jr.[4]

It would certainly be of interest to workers in this field to know the authors' thoughts about what conclusions this study might lead them to regarding the two-phase flow and bubble dynamics within the pump and hence the anticipated effects on performance. They might want to consider such in their summary discussions. Also, what would they expect to happen differently if the pump is operated off the "design" flow studied in the paper?

[4] Creare, Inc., Hanover, N. H. 03755.

Authors' Closure

The authors express their gratitude to Dr. Runstadler and Dr. Truman for their valuable comments.

When the volumetric ratio of air to water is less than 0.04, the size of air bubbles in a pump impeller is so small that the bubbles move approximately along the streamlines of water, and hence, an observation of the air bubble motion in the pump impeller can be a simple visualization method for the flow pattern investigation.

With aid of the calculation described in this paper, the motions of air bubbles and water particles in the impeller can be assumed. The magnitude of the local velocities of air bubbles relative to the surrounding water and the places where the bubbles gather closely can also be estimated for a given pump impeller of radial flow type.

This calculation can be applied not only to the flow in the design condition but also to that in an off-design condition, when the flow rate is not less than one half of the design flow rate. By use of this method, the motion of cavitation vapor bubbles in a pump impeller can also be predicted.

For a more precise calculation, non-spherical shape of a bubble, which will be observed in a high Reynolds number, should be taken into account in the calculation. Parameters expressing the ellipticity of the bubble will be necessary but the calculation in this case will be a rather troublesome work. In the range of Reynolds numbers, $Re \geqq 500 \sim 700$, the air bubble receives a large drag force and the bubble takes a spheroidal shape. The bubble moves in the direction of its minor axis and the area projected in that direction by the spheroidal bubble becomes larger than that projected by the equivalent sphere with the same volume, and hence, a greater resistance than that assumed in the present analysis will be met by the actual bubble. In pump impellers air bubbles are fairly small, as described in the paper, and the shape can be assumed with a sufficient accuracy to be spherical, and the calculation based on this assumption will give a sufficiently valid results.

Air bubbles in pump impeller generally lag behind the flowing water due to the adverse pressure gradient in that field, and the velocity of the bubbles relative to the water in the boundary layer becomes smaller in the region near the impeller wall. This velocity defect calls forth the Magnus effect on the bubbles and they follow a very complicated path, which is far beyond the application of the present theory. Any inaccuracies which may arise from the non-inclusion of the boundary layer could not be detected from the observation of the films.

If an air bubble has a chance to hit the surface of a blade in a time interval of Δt, the location of the bubble after Δt is described as in the paper. In the interval after the collision, the acceleration and velocity of the bubble can be calculated

on the basis of the new field flow pattern, and if the new position after the next interval Δt is situated inside the impeller blade, then the bubble moves along the blade surface with the tangential components of its acceleration and velocity.

The procedure to estimate the optimum time interval Δt is described in the paper. The time interval Δt and the grid size Δl should be selected so as to satisfy the following relationships

$$\Delta t < \Delta l_r / \dot{R}, \Delta l_\theta / R\dot{\Theta}, \Delta l_z / \dot{Z}$$

The present analysis, in which the effect of air bubble existence on the flow pattern of water is neglected, can be applied only to a flow containing a relatively small number of air bubbles. When the number of air bubbles is increased, the existance of the bubbles will affect the flow field and in this case the method developed by Truman and his co-workers seems to be more superior. They determined simultaneously the flow field of vapor and droplet motion between co-rotating disks. But for the motion of bubbles in a rotating impeller, as treated in this paper, this method does not show any merit because of the following reasons. (*a*) The Reynolds number of the fluid flow in an impeller passage is generally so large that the flow is always turbulent and the flow pattern resembles that of an inviscid flow rather than that of a laminar viscous flow seen in their work. (*b*) As is seen from geometry of impeller blades, the boundary conditions will be so complex that much labor will be necessary to obtain a new computer program. The method adopted in this paper, however, has the considerable advantage that calculations are easily performed by a step by step method already developed for turbomachinery calculations. The computer program is available for the motions of particles in the fluid irrespective of particle density.

J.H.G. Howard
Professor,
Mechanical Engineering Department,
University of Waterloo,
Waterloo, Ontario, Canada

S.V. Patankar
Professor,
Mechanical Engineering Department,
University of Minnesota,
Minneapolis, Minn.

R.M. Bordynuik
Former Research Assistant,
University of Waterloo,
now with Ontario Hydro,
Toronto, Ontario, Canada

Flow Prediction in Rotating Ducts Using Coriolis-Modified Turbulence Models

A parabolic numerical analysis procedure has been used to predict the flow in a straight, radial rotating channel of rectangular cross-section, chosen as a simple model of an impeller passage. A two equation turbulence model was employed, with alternative modifications, to include the influence of Coriolis force on turbulent kinetic energy. Alternative Coriolis force terms were evaluated by comparisons in a high-aspect-ratio duct with measured velocity, wall shear stress and turbulent viscosity. Secondary velocity predictions were checked with data from a low-aspect-ratio duct where the Coriolis modification of turbulence was found less influential than the secondary flow in the modification of side wall shear stress.

Introduction

The flow in a centrifugal impeller passage is one of the most complex encountered in engineering fluid mechanics. It can be strongly three-dimensional in character due to passage curvature and rotational effects. These factors also have a considerable influence on the turbulent shear flow in the diffusing impeller passages of a centrifugal compressor. The most commonly used internal flow analysis methods are, however, based on inviscid analysis and are termed quasi-three-dimensional since they presume that, in the blade-to-blade plane, stream surfaces lie along surfaces of revolution. Thus, neither the three-dimensionality nor the viscous nature of the flow is accounted for, although simple flow models may account for certain of the missing effects, for example, the jet-wake model included by Howard and Osborne [1].

The effect of Coriolis force on the structure of turbulence in a rotating radial channel has been well studied by Johnston, et al. [2]. Increased stability is observed toward the suction side of the channel and the decreased momentum transfer is believed to be a principal cause of observed separation phenomena and the formation of a low velocity (or "wake") region in the portion of a diffusing impeller channel. The formation of strong secondary flows in the channel, while strongly modified by tip clearance effects, as shown by Howard and Kittmer [3], also follows from the Coriolis force and tends to sweep low momentum fluid from hub or shroud to the suction surface where it can enhance the tendancy toward separation or join an already-formed wake region.

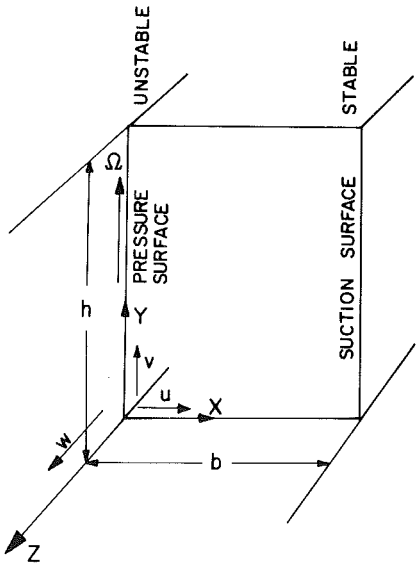

Fig. 1 Coordinate system and passage cross-section looking upstream

A solution procedure which was parabolic in the principal flow direction was used by Majumdar, Pratap, and Spalding [4] to carry out a three-dimensional viscous flow analysis in a rotating channel. The partially-parabolic procedure of Majumdar and Spalding [5] allowed the pressure field calculated at one iteration to be the basis for the streamwise pressure gradient at the next iteration. In this way, pressure distributions at a downstream boundary could influence the flow field prediction. Coriolis and centrifugal forces were included in the momentum equations but not in the two closure equations, for the turbulent energy k and dissipation rate ϵ.

In the present study, a parabolic finite-difference solution

Contributed by the Fluids Engineering Division and presented at the Winter Annual Meeting, Chicago, Ill., November 16–21, 1980, of THE AMERICAN SOCIETY OF MECHANICAL ENGINEERS. Manuscript received by the Fluids Engineering Division, March 26, 1979. Paper No. 80-WA/FE-1.

procedure similar to [4] was applied to flow in straight, radial, rotating channels with rectangular cross-section. Three turbulence models were tested which included effects of Coriolis force on the turbulent energy and dissipation rate. Comparisons are made with velocity profiles, turbulent viscosity and wall shear stresses for a high aspect ratio rotating duct tested by Johnson [2] and for a low aspect ratio duct investigated by Wagner and Velkoff [6].

Fundamental Equations

Following [4], the basic equations are expressed for the coordinate system and channel cross-section of Fig. 1. Thus the continuity equation is

$$\frac{\partial}{\partial x}(\rho u)+\frac{\partial}{\partial y}(\rho v)+\frac{\partial}{\partial z}(\rho w)=0 \tag{1}$$

The momentum equations are

$$\frac{\partial}{\partial x}(\rho uu)+\frac{\partial}{\partial y}(\rho uv)+\frac{\partial}{\partial z}(\rho uw)$$

$$=-\frac{\partial p^*}{\partial x}+\frac{\partial}{\partial x}(\tau_{u,x})+\frac{\partial}{\partial y}(\tau_{u,y})-2\rho\Omega w \tag{2}$$

$$\frac{\partial}{\partial x}(\rho uv)+\frac{\partial}{\partial y}(\rho vv)+\frac{\partial}{\partial z}(\rho vw)$$

$$=-\frac{\partial p^*}{\partial y}+\frac{\partial}{\partial x}(\tau_{v,x})+\frac{\partial}{\partial y}(\tau_{v,y}) \tag{3}$$

$$\frac{\partial}{\partial x}(\rho uw)+\frac{\partial}{\partial y}(\rho vw)+\frac{\partial}{\partial z}(\rho ww)$$

$$=-\frac{\partial \bar{p}^*}{\partial z}+\frac{\partial}{\partial x}(\tau_{w,x})+\frac{\partial}{\partial y}(\tau_{w,y})+2\rho\Omega u \tag{4}$$

where $\tau_{u,x}=2\mu_e\frac{\partial u}{\partial x}$ $\quad\tau_{v,y}=2\mu_e\frac{\partial v}{\partial y}$

$$\tau_{u,y}=\tau_{v,x}=\mu_e\left\{\frac{\partial v}{\partial x}+\frac{\partial u}{\partial y}\right\}$$

$$\tau_{w,x}=\mu_e\frac{\partial w}{\partial x} \qquad \tau_{w,y}=\mu_e\frac{\partial w}{\partial y}$$

The Coriolis forces appear in the last terms of the x and z momentum equations, while the centrifugal force, for a radial channel, is included in the "reduced" pressure

$$p^*=p-\frac{1}{2}\rho\Omega^2 z^2 \tag{5}$$

The cross-channel average pressure $\bar{p}$ is employed in the z equation to allow a z-direction marching solution while the x and y pressure gradients are determined by the solution of the elliptic equations on that plane.

As described in [7], the effective viscosity is modelled as

$$\mu_e=\mu+C_\mu\rho k^2/\epsilon=\mu+\mu_t \tag{6}$$

and the k, ϵ equations are

$$\frac{\partial}{\partial x}(\rho uk)+\frac{\partial}{\partial y}(\rho vk)+\frac{\partial}{\partial z}(\rho wk)=\frac{\partial}{\partial x}\left(\frac{\mu_t}{\sigma_k}\frac{\partial k}{\partial x}\right)$$

$$+\frac{\partial}{\partial y}\left(\frac{\mu_t}{\sigma_k}\frac{\partial k}{\partial y}\right)+G-\rho\epsilon+G_c \tag{7}$$

$$\frac{\partial}{\partial x}(\rho u\epsilon)+\frac{\partial}{\partial y}(\rho v\epsilon)+\frac{\partial}{\partial z}(\rho w\epsilon)=\frac{\partial}{\partial x}\left(\frac{\mu_t}{\sigma_\epsilon}\frac{\partial \epsilon}{\partial x}\right)$$

$$+\frac{\partial}{\partial y}\left(\frac{\mu_t}{\sigma_\epsilon}\frac{\partial \epsilon}{\partial y}\right)+C_1\epsilon G/k-C_2(1+C_c)\rho\epsilon^2/k+G_c\epsilon/k \tag{8}$$

where the terms C_c and G_c in equations (7) and (8) have been added to account for Coriolis effects and

$$G=\mu_t\left\{2\left[\left(\frac{\partial u}{\partial x}\right)^2+\left(\frac{\partial v}{\partial y}\right)^2\right]+\left(\frac{\partial u}{\partial y}+\frac{\partial v}{\partial x}\right)^2\right.$$

$$\left.+\left(\frac{\partial w}{\partial y}\right)^2+\left(\frac{\partial w}{\partial x}\right)^2\right\}$$

Following [6], the values chosen for the constants C_μ, C_1, C_2, σ_k, and σ_ϵ were 0.09, 1.44, 1.92, 1.0, and 1.3.

The value of μ_t at a wall was set by the wall function method of [7]. The turbulence generation term G for a location adjacent to a wall became $\tau_0(\partial w/\partial x)$ or $\tau_0(\partial w/\partial y)$ where the wall shear stress τ_0 was determined using equation (2.3-1) of [7]. The wall shear velocity, $\sqrt{(\tau_0/\rho)}$, was based on the same equation. Wilcox [8] has proposed a Coriolis modification to the law of the wall. Incorporation of this modification in the wall function method failed to improve predictions as discussed later.

Alternative Models for Coriolis Modification of Turbulence

Three alternative models were tested to allow for the effect of the Coriolis force on the turbulence and hence on μ_t. In all cases, the models had been proposed in similar form elsewhere for two-dimensional boundary layers. They are here applied to three-dimensional duct flow analysis in a form that is limited to radial channels such that the Coriolis effect is confined to the side wall boundary layers.

The first model was developed by Wilcox and Chambers [8, 9], by considering that the k equation is an equation in turbulent mixing energy which should be proportional to the fluctuating velocity normal to the wall (in this case $<u'^2>$). The equation for this turbulence correlation is, see [2], where $<>$ refers to a time average,

$$\frac{D<u'^2>}{dt}=<-w'u'>4\Omega+\text{ other terms.} \tag{9}$$

Nomenclature

b = channel width
C_μ, C_1, C_2 = constants
k = turbulent kinetic energy
h = channel height
p = pressure
p^* = "reduced" pressure, (equation (5))
Ri_t = turbulent Richardson number (equation (10))
Ro = rotation number (= $\Omega b / w_m$)
u, v, w = velocity components in x, y, z directions
w_m = mean passage velocity
x, y, z = coordinates (in directions of width, height and length)
ϵ = dissipation rate
μ = laminar viscosity
μ_t = turbulent viscosity
μ_e = effective viscosity
ρ = density
$\sigma_k, \sigma_\epsilon$ = constants
τ = shear stress
Ω = angular rotation about axis
ω = "pseudovorticity" used in Wilcox-Traci model

Superscripts

$\bar{}$ = average over passage
$'$ = fluctuating component

Since it has been observed near the wall that the proportion of the turbulence correlations (see Hinze [10], p 639) is (for a side wall layer)

$$<w'^2>:<u'^2>:<v'^2> = 4:2:3$$

the value of k is $9/4\ <u'^2>$. Since $<-w'\,u'>$ is $\mu_t\ \partial w/\partial x$ the Coriolis term in the k equation (G_c) will be $9\Omega\ \mu_t\ \partial w/\partial x$. The remaining production terms have been left unchanged from the usual form for the k equation by Chambers and Wilcox [8] and this model is followed for the duct equation (7). This should result in appropriate turbulence production levels on the top and bottom duct walls.

Wilcox used a $k - \omega$ equation model where ω (sometimes termed "pseudovorticity") is described in [8] as "dissipation rate." No Coriolis effect was found for the ω equation, but since $\epsilon = C_\mu k\omega$, the term G_c will be reflected in the ϵ equation (8) as $G_c\ \epsilon/k$ (see [8]).

Summary *Model I* $\quad C_c = 0, G_c = 9\,\Omega\,\mu_t \dfrac{\partial w}{\partial x}$

The second and third models for Coriolis effects are based on a study of curved boundary layers by Launder, et al. [11]. The k equation was maintained in its usual form, where Coriolis terms will cancel out, thus $G_c = 0$ in (7) and (8). In the ϵ equation, "on the grounds of seeking the simplest possible form," they chose to accommodate curvature effects by making the value of C_2 depend on a turbulent curvature Richardson number (Ri_t). Thus C_2 was multiplied by $(1 - 0.2\ \mathrm{Ri}_t)$. The constant 0.2 was found to be optimum after extensive explorations. For the rotating duct case, two forms of Richardson number are considered, in [2] and elsewhere. They are

$$\text{(i)}\ \mathrm{Ri} = \frac{-2\Omega\left(\dfrac{\partial w}{\partial x} - 2\Omega\right)}{\left(\dfrac{\partial w}{\partial x}\right)^2}$$

and

$$\text{(ii)}\ \mathrm{Ri} = -2\Omega/\left(\frac{\partial w}{\partial x}\right)$$

Following the practise of Launder, et al. [11], turbulent Richardson numbers are formed by replacing the mean flow time-scale represented by the denominator $(\partial w/\partial x)^2$ with a turbulence time scale (k/ϵ). Thus the models are

$$\text{(i)}\ \mathrm{Ri}_t = -2\Omega(k/\epsilon)^2\left(\frac{\partial w}{\partial x} - 2\Omega\right) \qquad (10)$$

and

$$\text{(ii)}\ \mathrm{Ri}_t = -2\Omega(k/\epsilon)^2\frac{\partial w}{\partial x}$$

These models may be incorporated in equations (7) and (8)

Summary $\quad$ *Model II* $G_c = 0, C_c = 0.2\,(k/\epsilon)^2 2\Omega\left(\dfrac{\partial w}{\partial x} - 2\Omega\right)$

$$\textit{Model III}\ G_c = 0, C_c = 0.2\,(k/\epsilon)^2 2\Omega\frac{\partial w}{\partial x}$$

also without Coriolis $G_c = 0, \mathrm{C_c} = 0$.

A further model for turbulence modification is described in [14].

Solution Procedure

The governing differential equations (1) to (4) and (7) and (8) were solved by the finite-difference procedure described by Patankar and Spalding [12]. This is a marching procedure for three-dimensional parabolic flows, in which the finite-difference equations are formed by integrating the differential equations over a control volume surrounding each grid point. The forward marching is performed via a fully implicit method. The linkage between the momentum and continuity equations is handled through a pressure-correction equation. Further details of the solution procedure are given in [12] and [13].

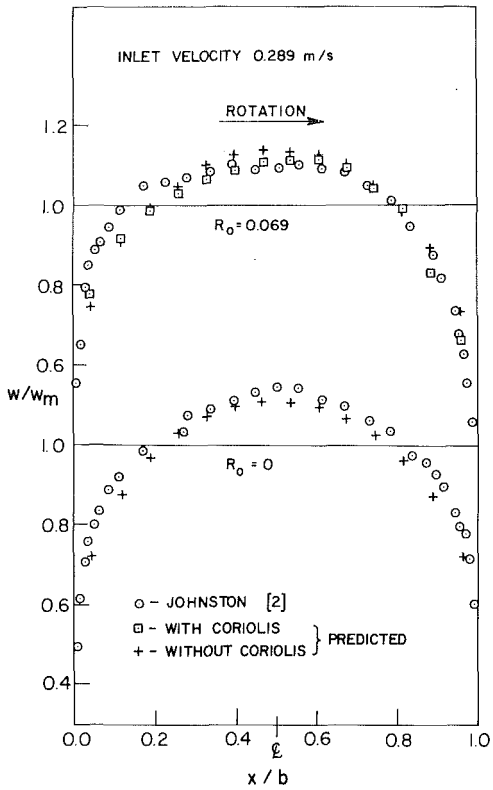

Fig. 2 Velocity profile – comparison of prediction with Johnston's data Re (= $w_m b/\nu$) = 11500; R_o = 0 and R_o = 0.069 with and without Coriolis-modified turbulence

Comparisons With Experimental Data

The Johnston High Aspect Ratio Duct. Johnston, et al. [2] conducted experiments on water flowing in a rotating channel flow apparatus. The radial channel had a rectangular cross-section with height (h) of 279 mm (11 in.) and width (b) of 39 mm (1.54 in.). This high aspect ratio channel reduced the effects of the secondary flow on the mainstream velocity profile in order to isolate other effects of rotation.

In the test region of the channel, 1.04 m to 1.23 m (41 to 48.5 in.) from the entrance, fully developed flow was indicated by the measurements. The velocity profiles were measured at the channel center plane, ($y = h/2$), where the flow was observed to be two-dimensional.

Johnston used an inlet plenum and honeycomb to straighten the flow at the channel entrance but he did not make any measurements of the inlet velocity profiles. Therefore, for computational purposes, the inlet mainstream velocity was assumed to be uniform and was calculated from the total flow Q; the cross-stream flows were set to zero. The number of grid lines employed for this analysis was 16 for the width and 12 for the channel height. The spacing of computation planes in the z direction was 21 mm (.07 ft) with reduced spacing for the initial few steps.

Figures 2 and 3 compare the experimental and computed mainstream (w) velocity profiles at $y = h/2$. As the rotation speed is increased a strengthening difference in velocity

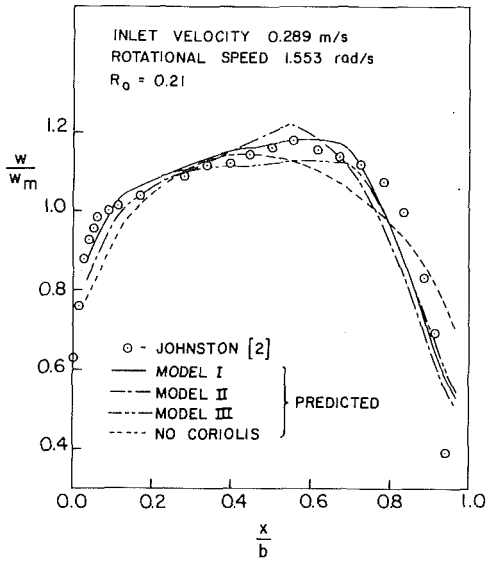

Fig. 3 Velocity profile – comparison of predictions with and without Coriolis modified turbulence models, with Johnston's data – Re = 11500, R_o = 0.21.

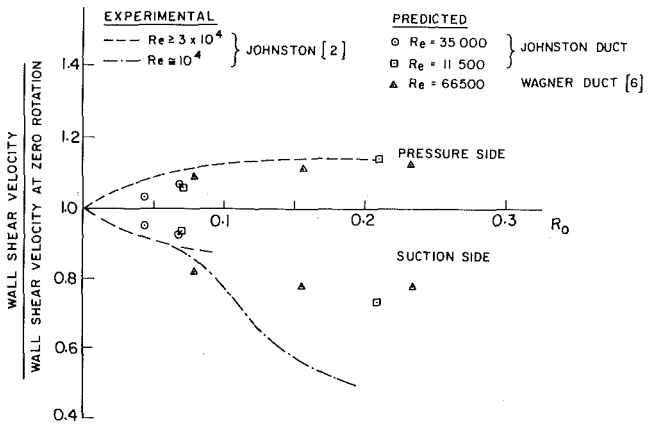

Fig. 4 Predicted and measured wall shear velocity ratios – measured data from [2] – predictions use Coriolis-modified turbulence model I

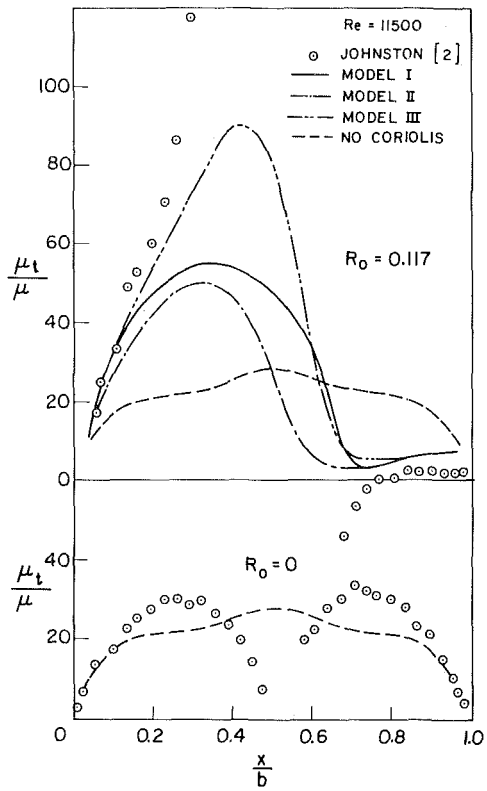

Fig. 5 Comparison of predicted turbulent viscosity with measured data [2] – Re = 11500, R_o = 0 and 0.117.

profile is noted when the Coriolis terms are included. Only the Model I is shown in Fig. 2, as velocity differences between models are minor. Figure 3 shows the highest rotation number ($R_o = \Omega b/w_m$) for which data were presented in [2]. In this case, Johnston observed a significant laminar region near the suction (stable) side of the passage. No model fitted this case exactly, but across most of the profile, the inclusion of Coriolis turbulence effects is seen to be needed.

For R_o = 0.21 (Fig. 3), the inclusion of a Coriolis modification, from [8], to the wall function method resulted in a markedly poorer fit with the measured velocity profile. This is thought to be due to the value of $x\sqrt{\tau_0}\sqrt{\rho}/\mu$ for the first grid line spacing from the wall which was between 15 and 30. Measurements [15] illustrate that the unmodified law of the wall fits well in this region. The wall law-modification proposed by [15] was judged to be too specific to its test case to be applied in this analysis.

In Figure 4, the ratio of the wall shear velocity to the same value at zero rotation is shown as a function of rotation number. All three turbulence models gave indistinguishable results. The comparison with Johnston's data [2] shows good agreement with the modifying effect on the pressure side of the passage but indicates a lesser effect on the suction side. When the computation is carried out without the Coriolis effect on the turbulence model, the difference in wall shear velocities on the two channel sides becomes almost negligible.

In [2], Johnston presents the distribution of eddy viscosity (μ_t/ρ) calculated from measured velocity profiles, measured wall shear velocities and the linear shear stress distribution across the channel associated with fully-developed flow. Figure 5 compares the data to present predictions. Johnston cautions that data in the range $0.3 < x/b < 0.7$ have high uncertainty. The distribution of μ_t at zero rotation is moderately well predicted. The highest Ro at which Johnston could determine μ_t in this fashion was Ro = 0.117 where μ_t becomes zero near the stable wall. At this rotation, none of the models achieve a prediction of zero eddy viscosity, but they are differentiated largely by the mid-passage distributions of μ_t. Numerical computations at higher rotation (e.g. Ro = 0.42), lead to instabilities with Model III.

In an impeller passage, rotation number should be based on boundary layer thickness rather than passage width. Nevertheless, a rotation number of 0.2 or more may be found in a radial impeller. This comparison with a two-dimensional flow field provides a useful, but incomplete, test for the capabilities of a duct analysis method.

Low Aspect Ratio Channel Test. Wagner and Velkoff [6] designed their experimental rig to study the secondary flows in a rotating radial channel. The duct, using air as the working fluid, was 864 mm (34 in.) in length with a nozzle at the duct exit. The rectangular cross-section had a height (h) of 44.5 mm (1.75 in.) and a width (b) of 121 mm (4.75 in.).

The data are compared at 610 mm from the entrance with predicted cross-velocities in Fig. 6 and with mainstream velocities in Fig. 7. The points shown on Figs. 6 and 8 from the Wagner and Velkoff [6] data are transcribed from curves passed through the measured data. The predictions are satisfactory for the 200 and 300 rpm conditions, but at lower rotation the predicted boundary layer growth and some of the secondary velocities are high.

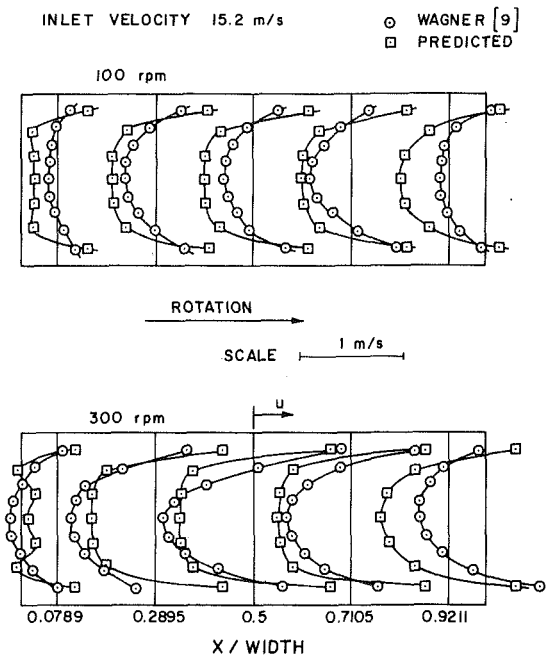

Fig. 6 Cross-passage velocity profiles – comparison of predictions with data by Wagner and Velkoff [6] – Re = 66500 based on passage hydraulic diameter – 100 rpm and 300 rpm.

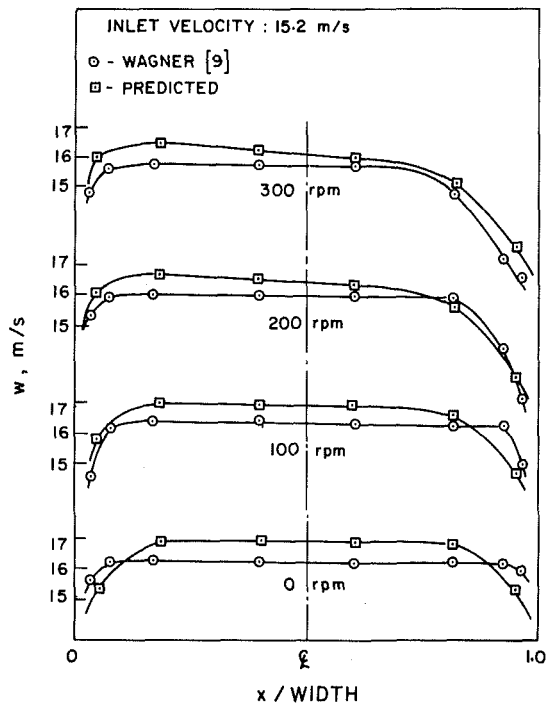

Fig. 7 Mainstream velocity profiles – comparison of predictions with data by Wagner and Velkoff [6]

Comparisons between Wagner's experimental data, Majumdar and Spalding's [5] calculation and the present program calculation for two cases (100 and 300 rpm) are shown in Fig. 8. Majumdar and Spalding used a partially-parabolic procedure, with no Coriolis effects added to the turbulence equations, on a 10×10 grid pattern in the cross-stream direction and 24 steps in the downstream direction starting from a cross-section 8 in. (203 mm) from the entrance with its measured velocities. The present program is a wholly parabolic calculation with Coriolis effects added to the

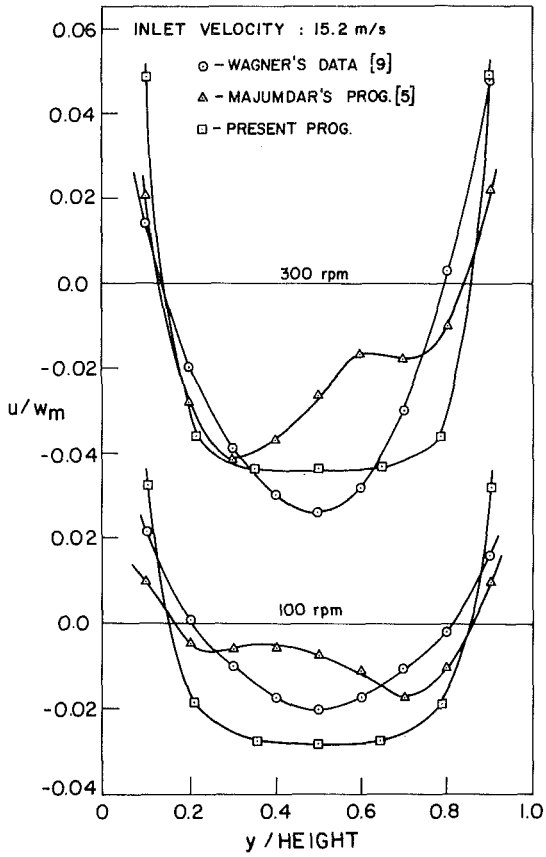

Fig. 8 Cross-passage velocity profiles at passage centerline – comparison of present prediction with prediction by Majumdar [5] and data by Wagner [6] – 100 rpm and 300 rpm.

turbulence equations. It employed a 10×11 grid with 14 steps downstream starting from the duct entrance where a uniform mainstream velocity was assumed with no secondary velocities. Although neither method gives exact agreement with the experimental data, the present predictions can be seen to produce the correct shape of the secondary velocity distribution without the kink predicted by [5].

The ratios of wall shear velocities were also calculated for the Wagner duct and are shown in Fig. 4. A closer correspondance to Johnston data would result if boundary layer thickness were used for R_o calculation. The removal of Coriolis effect on turbulence reduced the deviation of the ratio from unity by less than one quarter. Thus the presence of strong secondary flows in this duct appears from the prediction to be the principal source of the modified wall shear stress.

Concluding Remarks

A fully parabolic solution procedure has been applied to the flow in a rotating rectangular duct. The $k - \epsilon$ model was used to obtain the turbulent viscosity. Three models for the Coriolis modification of turbulence were evaluated by comparison with velocity and turbulent viscosity profiles at mid-height of a high-aspect-ratio rotating channel. Despite a complex derivation, Model I from Wilcox and Chambers [8, 9] gave the most satisfactory prediction while containing no empirical coefficient and maintaining numerical stability at high Ro. Model III, adapted from [11], was also satisfactory at moderate Ro. The need for inclusion of a Coriolis model for turbulence modification was confirmed.

Moderate agreement was also achieved in the prediction of secondary velocities in a low aspect ratio rotating duct,

comparable to other predictions. These velocities are driven by Coriolis forces in the momentum equation and have little sensitivity to Coriolis turbulence modification. In this case, the variation in side wall shear stress appeared to arise more from the strong secondary flows than from the Coriolis turbulence modification.

References

1 Howard, J.H.G., and Osborne, C., "A Centrifugal Compressor Flow Analysis Employing a Jet-Wake Passage Flow Model," ASME JOURNAL OF FLUIDS ENGINEERING, Mar. 1977, pp. 141–147.

2 Johnston, J.P., Halleen, R.M. and Lezius, D.K., "Effects of Spanwise Rotation on the Structure of Two-Dimensional Fully Developed Turbulent Channel Flow," *J. of Fluid Mechanics,* 1972, Vol. 56, Part 3, pp 533–557.

3 Howard, J.H.G., and Kittmer, C.W., "Measured Passage Velocities in Radial Impeller with Shrouded and Unshrouded Configurations," ASME *Journal of Eng. for Power,* Apr. 1975, pp. 207–213.

4 Majumdar, A.K., Pratap, V.S., and Spalding, D.B., "Numerical Computation of Flow in Rotating Ducts," ASME JOURNAL OF FLUIDS ENGINEERING, Mar. 1977, pp. 148–153.

5 Majumdar, A.K. and Spalding, D.B., "A Numerical Investigation of Three-Dimensional Flows in a Rotating Duct by a Partially-Parabolic Procedure," ASME Paper 77-WA/FE-7, 1977.

6 Wagner, R.E., and Velkoff, H.R., "Measurement of Secondary Flows in a Rotating Duct," ASME *Journal of Engineering for Power,* Vol. 94, pp. 261–270.

7 Launder, B.E., and Spalding, D.B., "The Numerical Computation of Turbulent Flows," *Computer Methods in Applied Mechanics and Engineering,* Vol. 3, 1974. pp. 269–289.

8 Wilcox, D.C., and Chambers, T.L., "Streamline Curvature Effects on Turbulent Boundary Layers," *AIAA Jnl.,* Vol. 15, No. 4, Apr. 1977.

9 Chambers, T.L., and Wilcox, D.C., "Critical Examination of Two-Equation Turbulence Closure Models for Boundary Layers," *AIAA Jnl.,* Vol. 15, No. 6, June 1977, pp 821–828.

10 Hinze, J.O., *Turbulence,* McGraw-Hill, 1975.

11 Launder, B.E., Priddin, C.H., and Sharma, B.I., "The Calculation of Turbulent Boundary Layers on Spinning and Curved Surfaces," ASME JOURNAL OF FLUIDS ENGINEERING, Mar. 1977, pp. 231–239.

12 Patankar, S.V., and Spalding, D.B., "A Calculation Procedure for Heat, Mass and Momentum Transfer in Three-Dimensional Parabolic Flows," *Int. J. of Heat Mass Transfer,* 1972, Vol. 15, pp. 1787–1806.

13 Bordynuik, R.M., "A Finite Difference Analysis of Parabolic Flows in Rotating Rectangular Passages," M.A.Sc. thesis, University of Waterloo, 1978.

14 So, R.M.C., "A Turbulence Velocity Scale for Curved Flows," *J. Fluid Mech.,* Vol. 70, Part 1, 1975, pp. 37–57.

15 Koyama, H., Masuda, S., Ariga, I. and Watanabe, I., "Stabilizing and Destabilizing Effects of Coriolis Force on Two-Dimensional Laminar and Turbulent Boundary Layers," ASME *Journal of Eng. for Power,* Vol. 101, No. 1, Jan. 1979, pp. 23–31.

Numerical Analysis of Turbulent Wakes of Turbomachinery Rotor Blades

C. Hah
Research Associate
in Aerospace Engineering,

B. Lakshminarayana
Director of Computational
Fluid Dynamics Program
and Professor of Aerospace Engineering.

The Pennsylvania State University.
University Park, Pa. 16802

The wakes of turbomachinery rotor blades are turbulent, three-dimensional, and are subjected to curvature and rotation effects. The objective of this study is to predict the development of such wakes and compare the predictions with the existing data. A finite difference procedure is employed in the numerical analysis of the wake utilizing the continuity, momentum, and turbulence closure equations in the rotating curvilinear and non-orthogonal coordinate system. The turbulence closure is affected by the modified Reynolds stress model. The effects of curvature and rotation on the turbulence structure are accounted for with this turbulence closure model. The pedictions from the present turbulence model agree well with the mean velocity and the turbulence wake data.

1. Introduction

Both the fluid dynamic properties of a turbomachinery rotor (e.g., compressor, propeller, helicopter, turbine, etc.), governing efficiency and performance, and the acoustical properties, governing the radiated noise, are dependent upon the characteristics of the wake behind the rotor. The flow is three-dimensional and usually turbulent. Many attempts have been made recently to measure the turbulent rotor wake. Raj and Lakshminarayana [1], Reynolds, Lakshminarayana and Ravindranath [2] and Ravindranath and Lakshminarayana [3] used tri-axial hot-wire probes to measure both the mean velocity and the Reynolds stresses in the wake of a compressor rotor.

Very few attempts have been made to predict the rotor wakes. A simplified analytical approach to predict qualitative flow characteristics was developed by Raj and Lakshminarayana [1]. Lakshminarayana [4] applied the momentum integral technique and predicted the wake decay rate away from the blade trailing edge region. None of these methods are capable of predicting the local flow properties such as mean velocity and turbulence characteristics in the near wake, where the effects of curvature and rotation are substantial. No attempts have been made so far to predict the three-dimensional turbulent rotor wakes numerically or otherwise. Even in the two-dimensional case, only symmetrical wakes (flat plate) have been successfully predicted. Launder, Reece, and Rodi [5] and Pope and Whitelaw [6] calculated the turbulent symmetrical wake of a flat plate using various turbulent closure models. Recently, Hah and Lakshminarayana [7] have measured the asymmetrical turbulent wakes of a single airfoil at various incidences and concluded that the turbulence structure in this case is quite different from the symmetrical wake and that the effect of streamline curvature is substantial in the near wake region.

To predict the development of the rotor wake, which is asymmetrical and under the influence of machine rotation, the effects of streamline curvature and rotation should be properly incorporated in the turbulence closure model. Several attempts have been made to include the effects of streamline curvature in the turbulence closure models. Bradshaw [8] incorporated the effects of streamline curvature by using the mixing length concept and the analogy between buoyancy and curvature effects. Launder, Pridden and Sharma [9] modified the two-equation turbulence closure model for the effects of streamline curvature. These modifications are based on experimental results. The validity of universal constants that represent the effects of curvature is uncertain.

The literature on the flow that is affected by rotation has been reviewed by Johnston [10]. Very few theoretical investigations have been made that fully account the flow situation and the effects of rotation. Recently, Majumdar, Pratrap and Spalding [11] have applied the finite-difference procedure with the two-equation turbulence closure model (valid for non-rotating flow) for the calculation of flows in rotating ducts and have reported that the results were less satisfactory at large rotational speed. Although the rotation does not change the total turbulence kinetic energy, it affects the components of kinetic energy through the rotation-related terms in the Reynolds stress equation. A qualitative analysis on this effect is carried out by Lakshminarayana and Reynolds [12]. Many experimental studies (Raj and Lakshminarayana, [1]; Reynolds, Lakshminarayana and Ravindranath, [2]; and Ravindranath and Lakshminarayana, [3])

Contributed by the Fluids Engineering Division and presented at the ASME-CSME Fluids Engineering, Applied Mechanics, Bioengineering Conference, Niagara Falls, N.Y., June 18–20, 1979. Manuscript received by the Fluids Engineering Division, September 17, 1979.

show that the decay rate of the rotor wake is higher than that of a cascade or a single airfoil wake. The difference is believed to be partly due to the effects of rotation.

In the present study, the effects of machine curvature and rotation in an axial flow turbomachinery blade are accounted for by utilizing the transport equations of Reynolds stresses in curvilinear coordinates fixed to the rotor blade. The results are compared with those based on conventional turbulence closure models. The analysis is for incompressible, turbulent flow.

2. Coordinate System and Governing Equations

2.1 Coordinate System. In the numerical analysis of complex flow problems, the judicious choice of the coordinate system and simplification of the governing equations are prerequisite for successful results. The rotor wake develops between the annulus and hub walls, which are concentric cylinders for the present study. The fluid particle from the trailing edge of the rotor blade moves approximately in a helical path whose angle varies radially. To make the governing equations simple, the streamwise direction (s) is chosen as one of the coordinates. Because the hub and annulus walls form the boundary surface, the radial direction (r) is also chosen as one of the coordinates. The third coordinate direction is chosen normal to the streamwise direction (n) on the cylindrical surface (constant radius). This physical coordinate system fixed to the rotor blade is shown in Fig. 1.

This coordinate system is non-orthogonal (between s and r directions and between n and r directions) and provides simplicity in describing governing equations and boundary conditions. The coordinate s is along the streamwise direction at the wake center line and n is along the principal normal and perpendicular to s. r is along the blade trailing edge initially and follows the wake surface downstream. r is not perpendicular to s or n. The angle β between the streamwise direction and the machine axis varies radially. It is assumed to be constant in the s and n directions and, hence, the subsequent curvature effects are absent in this analysis. To get the metric tensor of this coordinate system, the corresponding Cartesian coordinates system is introduced at the axis of the rotor shown in Fig. 1. The y direction coincides with the axial direction of the rotor and the z direction coincides with the radial direction of the rotor. Any arbitrary point p can be represented both in Cartesian coordinates (x, y, z) and in the curvilinear coordinates (s, n, r). The components of (s, n, r) and (x, y, z) are related as follows,

$$x=-r\ \sin\left(\frac{s\ \sin\beta+n\ \cos\beta}{r}\right) \tag{1}$$

$$y=s\cos\beta-n\sin\beta \tag{2}$$

$$z=r\ \cos\left(\frac{s\ \sin\beta+n\ \cos\beta}{r}\right) \tag{3}$$

where s, n, r are streamwise, principal normal, and radial directions, respectively. The resulting metric tensor and Christoffel functions for this coordinate system are given in Appendix A.

2.2 Governing Equations in Rotating Coordinate System. The equations governing the incompressible, fully turbulent flow relative to a coordinate system rotating with angular velocity, Ω_i, is introduced in generalized tensor form and in the curvilinear coordinates described in the previous section.

The continuity equation for incompressible flow is,

$$U^i{}_{,i}=0 \quad , \quad u^i{}_{,i}=0 \tag{4}$$

or

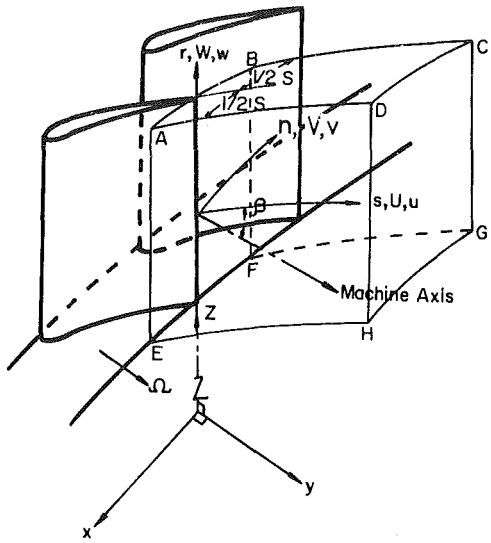

Fig. 1 Coordinate system and calculation domain (only two blades are shown for clarity)

$$\frac{\partial U^i}{\partial x^i}+\Gamma^i_{il}U^l=0 \quad , \quad \frac{\partial u^i}{\partial x^i}+\Gamma^i_{il}u^l=0$$

where U^i, u^i are mean and fluctuating contravariant velocity components. Using Christoffel symbols in equation (A5), in Appendix A,

$$\frac{\partial U^i}{\partial x^i}=0 \quad , \quad \frac{\partial u^i}{\partial x^i}=0 \tag{5}$$

In the present coordinate system,

$$\frac{\partial U}{\partial s}+\frac{\partial V}{\partial n}+\frac{\partial W}{\partial r}=0 \quad , \quad \frac{\partial u}{\partial s}+\frac{\partial v}{\partial n}+\frac{\partial w}{\partial r}=0 \tag{6}$$

The momentum equations for free turbulent shear flow at high Reynolds number are given by

$$U^j U^i{}_{,j}+\overline{u^j u^i}_{,j}+2\epsilon^{ijk}\Omega_j U_k=-\frac{g^{ij}}{\rho}\frac{\partial p}{\partial x^j} \tag{7}$$

and

$$\overline{u^j u^i}_{,j}=u^j\frac{\partial u^i}{\partial x^j}+\overline{u^j u^k}\Gamma^i_{jk}=\frac{\partial \overline{u^i u^j}}{\partial x^j}+\overline{u^j u^k}\Gamma^i_{jk} \tag{8}$$

where ϵ^{ijk} is the alternating tensor, Ω_j is the angular velocity of the rotor, ρ is the fluid density, p is the static pressure. For thin shear flow in turbomachinery blade wakes

$$V<<U \quad , \quad W<U \tag{9}$$

Then the components of equation (7) in the curvilinear coodinate system (Fig. 1) are as follows (neglecting lower order convection terms in mean velocity and all the small curvature terms in Reynolds stresses)

$$\begin{aligned} U\frac{\partial U}{\partial s} &+ V\frac{\partial U}{\partial n}+W\frac{\partial U}{\partial r}+U^2\ \Gamma^1_{11}+W^2\ \Gamma^1_{33} \\ &+ 2UW\ \Gamma^1_{13}+V^2\Gamma^1_{22}+2UV\ \Gamma^1_{12} \\ &+ 2VW\ \Gamma^1_{23}-2\Omega W^*\sin\beta=-\frac{1}{\rho}\left[g^{11}\frac{\partial P}{\partial s}+g^{12}\frac{\partial P}{\partial n}\right. \\ &\left.+g^{13}\frac{\partial P}{\partial r}\right]-\frac{\partial}{\partial s}\overline{u^2}-\frac{\partial}{\partial n}\overline{uv}-\frac{\partial}{\partial r}\overline{uw} \end{aligned} \tag{10}$$

$$U\frac{\partial V}{\partial s} + V\frac{\partial V}{\partial n}+W\frac{\partial V}{\partial r}+U^2\ \Gamma^2_{11}+W^2\ \Gamma^2_{33}$$

$$+ 2UW\ \Gamma^2_{13} + V^2\ \Gamma^2_{22} + 2UV\ \Gamma^2_{12}$$

$$+ 2VW\ \Gamma^2_{23} - 2\Omega W^* \cos\beta =$$

$$- \frac{1}{\rho}\left[g^{21}\frac{\partial P}{\partial s} + g^{22}\frac{\partial P}{\partial n} + g^{23}\frac{\partial P}{\partial r}\right]$$

$$- \frac{\partial}{\partial s}\overline{uv} - \frac{\partial}{\partial n}\overline{v^2} - \frac{\partial}{\partial r}\overline{vw} \qquad (11)$$

$$U\frac{\partial W}{\partial s} + V\frac{\partial W}{\partial n} + W\frac{\partial W}{\partial r} + 2\Omega V^* \cos\beta + 2\Omega U^* \sin\beta$$

$$+ W^2\ \Gamma^3_{33} + 2UW\ \Gamma^3_{13} + V^2\ \Gamma^3_{22}$$

$$+ 2UV\ \Gamma^3_{12} + 2VW\ \Gamma^3_{23} + U^2\ \Gamma^3_{11} = -\frac{1}{\rho}\left[g^{31}\frac{\partial P}{\partial s}\right.$$

$$\left. + g^{32}\frac{\partial P}{\partial n} + g^{33}\frac{\partial P}{\partial r}\right]$$

$$- \frac{\partial}{\partial s}\overline{uw} - \frac{\partial}{\partial n}\overline{vw} - \frac{\partial}{\partial r}\overline{w^2} - \overline{u^2}\Gamma^3_{11} - \overline{uv}\Gamma^3_{12} \qquad (12)$$

where U^*, V^*, W^* are covariant components of mean velocity and U, V, W are contravariant components of mean velocity. The solution of these equations gives the contravariant components of mean velocity which can be transformed to physical ones.

The physical components of velocity in k direction are given by $U^k\sqrt{g_{kk}}$ (no summation convention).

3. Modelling for Turbulence and Closure Equations

Various turbulence closure models have been proposed to simulate the behavior of real turbulent flows. The common feature of a good turbulence model is its universality to a wide range of flows and simplicity in its use. Two relatively complex turbulence closure models are utilized for the calculation of the rotor wake which develops under the influence of curvature and rotation. A two equation turbulence closure model, which adopts two transport equations of turbulence characteristic quantities, has been proposed by Daly and Harlow [13] and Launder and Spalding [14]. Launder, Pridden, and Sharma [9] extended this model to include the effects of curvature by modifying the primary decay term in the equation for the rate of dissipation. This modification is based on the experimental data and approximately represents the effect of curvature.

To include the effects of curvature and rotation, the Reynolds stress model is used in the present analysis. The Reynolds stress model, which utilizes approximate transport equations of Reynolds stresses, has been proposed by Rotta [15] and Hanjalic and Launder [16].

The transport equation of Reynolds stress in rotating curvilinear coordinate system is given by Raj and Lakshminarayana [17]

$$U_j\overline{u^iu^k}_{,j} + \overline{u^ku_j}U^i{}_{,j} + \overline{u^iu_j}U^k{}_{,j}$$

$$+ \overline{u^iu^k}u_{j,j} + 2\Omega_l\epsilon^{ilm}\overline{u_mu^k}$$

$$+ 2\Omega_l\epsilon^{klm}\overline{u_mu^i} = -\frac{1}{\rho}\left(\overline{u^kp'}_{,i} + \overline{u^ip'}_{,k}\right)$$

$$+ \nu g_{lj}\left(\overline{u^ku^i}_{,lj} + \overline{u^iu^k}_{,lj}\right) \qquad (13)$$

where p' is the fluctuating static pressure and ν is the kinematic viscosity.

To get closure, several authors have suggested a modelled form of the above equation. All the models proposed hitherto are for the non-rotating case. Most calculations for thin shear flow assume that the convection term and diffusion term in equation (13) are equal. So [18] applied this assumption for the calculation of two-dimensional curved flow.

For the rotor wake, the flow is asymmetric and the turbulence structure is influenced by the effects of streamline curvature and rotation. Therefore, the balance between the convection and the diffusion is hardly attained. The individual effects of convection and diffusion can be included if additional six transport equations are solved for the Reynolds stresses. However, this increases the computing time and computer storage significantly and often it causes numerical instability reported by Pope and Whitelaw [6]. For the present analysis, the convection and diffusion terms are considered collectively. The combined effect of the two terms are assumed to be related to the production term and one variable C_1 is introduced at each point to represent the total effect of convection and diffusion through the production term. The variable C_1 is updated at each point during iteration. Numerical solutions show that the value of C_1 becomes zero in the far wake where the wake becomes symmetric and almost two-dimensional. The modeling of the pressure-strain correlation is based on the work of Rotta [15] and Naot, Shavit, and Wolfshtein [19]. The pressure-strain correlation has two parts, one from the interaction of the mean strain rate with the turbulence and the other from the mutual interaction between the fluctuating components. The effect of rotation on the pressure-strain correlation can be incorporated through the first part in higher order modeling, but the present model adopts simple equation for the rate of energy dissipation. Consequently, the effect of rotation on pressure-strain correlation is not investigated here. For simplicity, the rate of turbulence energy production, which appears in the modeling for the mean-strain effects in the pressure-strain correlation, is replaced with the rate of dissipation. The effect due to the difference between the rates of production and dissipation is corrected through the variable C_1 during the calculation. Also, a high local turbulence Reynolds number is assumed and the scalar representation of dissipation (the contraction of dissipation tensor) is introduced for the dissipation terms of equation (13). The exact transport equation of the dissipation rate in the rotating coordinate system indicates that the rotation affects the dissipation rate when the turbulence is non-isotropic. However, these effects are significant only in the higher order modeling and is not considered in the present model. With these models, the equation (13) reduces to

$$0 = (1 + C_1)(-\overline{u_ku^i}U^i{}_{,k} - \overline{u_ku^i}U^j{}_{,k})(1-\gamma)$$

$$- 2(\epsilon^{ilm}\Omega_l\overline{u_mu^j} + \epsilon^{jlm}\Omega_l\overline{u_mu^i})$$

$$- \frac{2}{3}g^{ij}\epsilon(1-\gamma) - C_{\phi 1}\frac{\epsilon}{k}\left(\overline{u^iu^j} - \frac{2}{3}g^{ij}k\right) \qquad (14)$$

where $k = (1/2)\, g_{ij}\, \overline{u^iu^j}$, $\epsilon =$ the rate of energy dissipation (last term in equation 13) and $C_{\phi 1,\gamma}$ are constants. C_1 is variable whose values are evaluated using the upstream flow condition and updated during the iteration.

These equations are still intractable unless some realistic and practical assumptions are made. Using the assumptions utilized for the simplification of the mean momentum equations, the component form of equation (14) can be expressed as follows for the coordinate system of Fig. 1.

$\overline{u^2}$:

$$0=2(1+C_1)(1-\gamma)\left\{\left[-\overline{uv}-\overline{uw}\left(-\frac{s}{r}\sin\beta\cos\beta+s\frac{d\beta}{dr}\right)\right]\left(\frac{\partial U}{\partial n}+U\Gamma^1_{12}+W\Gamma^1_{23}\right)+\left[-\overline{u^2}+\overline{uw}\left(\frac{s}{r}\sin^2\beta\right)\right]\left(\frac{\partial U}{\partial s}+U\,\Gamma^1_{11}+W\,\Gamma^1_{13}\right)\right\}-4\Omega_n\left[-\overline{u^2}\frac{s}{r}\sin^2\beta+\overline{uv}\left(-\frac{s}{r}\sin\beta\cos\beta+s\frac{d\beta}{dr}\right)+\overline{uw}\left(1+\frac{s^2}{r^2}\sin^2\beta-\frac{2s^2}{r}\frac{d\beta}{dr}\sin\beta\cos\beta\right)\right]-\frac{2}{3}\left(1+\frac{s^2}{r^2}\sin^4\beta\right)\epsilon(1-\gamma)-C_{\phi 1}\frac{\epsilon}{k}\left[\overline{u^2}-\frac{2}{3}\left(1+\frac{s^2}{r^2}\sin^4\beta\right)k\right] \quad (15)$$

$\overline{v^2}$:

$$0=2(1+C_1)(1-\gamma)\left[-\overline{v^2}-\overline{vw}\left(-\frac{s}{r}\sin\beta\cos\beta+s\frac{d\beta}{dr}\right)\right]\left(\frac{\partial V}{\partial n}+U\Gamma^2_{12}+W\Gamma^2_{23}\right)+4\Omega_s\left[\overline{uv}\left(-\frac{s}{r}\sin^2\beta\right)+\overline{v^2}\left(-\frac{s}{r}\sin\beta\cos\beta+s\frac{d\beta}{dr}\right)+\overline{vw}\left(1+\frac{s^2}{r^2}\sin^2\beta-2\frac{s^2}{r}\frac{d\beta}{dr}\sin\beta\cos\beta\right)\right]-\frac{2}{3}\left(1+\frac{s^2}{r^2}\sin^2\beta\cos^2\beta-\frac{2s^2}{r}\frac{d\beta}{dr}\sin\beta\cos\beta\right)\epsilon(1-\gamma)-C_{\phi 1}\frac{\epsilon}{k}\left[\overline{v^2}-\frac{2}{3}\left(1+\frac{s^2}{r^2}\sin^2\beta\cos^2\beta-\frac{2s^2}{r}\frac{d\beta}{dr}\sin\beta\cos\beta\right)\right] \quad (16)$$

$\overline{w^2}$:

$$0=2(1+C_1)(1-\gamma)\left\{\left[-\overline{vw}-\overline{w^2}\left(-\frac{s}{r}\sin\beta\cos\beta+s\frac{d\beta}{dr}\right)\right]\left(\frac{\partial W}{\partial n}+U\,\Gamma^3_{12}+W\Gamma^3_{23}\right)+\left(-\overline{uw}+\overline{w^2}\frac{s}{r}\sin^2\beta\right)\left(\frac{\partial W}{\partial s}+U\,\Gamma^3_{11}=W\Gamma^3_{13}\right)\right\}-4\Omega_s\left[\overline{vw}+\overline{w^2}\left(-\frac{2}{r}\sin\beta\cos\beta+s\frac{d\beta}{dr}\right)\right]+4\Omega_n\left(\overline{uw}-\overline{w^2}\frac{s}{r}\sin^2\beta\right)-\frac{2}{3}\epsilon(1-\gamma)-C_{\phi 1}\frac{\epsilon}{k}\left(\overline{w^2}-\frac{2}{3}k\right) \quad (17)$$

$\overline{uv}$:

$$0=(1+C_1)(1-\gamma)\left\{\left[-\overline{v^2}-\overline{vw}\left(-\frac{s}{r}\sin\beta\cos\beta+s\frac{d\beta}{dr}\right)\right]\left(\frac{\partial U}{\partial n}+U\,\Gamma^1_{12}+W\,\Gamma^1_{23}\right)+\left(-\overline{uv}+\overline{vw}\frac{s}{r}\sin^2\beta\right)\left(\frac{\partial U}{\partial s}+U\,\Gamma^1_{11}+W\,\Gamma^1_{13}\right)+\left[-\overline{uv}-\overline{uw}\left(-\frac{s}{r}\sin\beta\cos\beta+s\frac{d\beta}{dr}\right)\right]\left(\frac{\partial V}{\partial n}+U\,\Gamma^2_{12}\right)\right\}-2\left\{\Omega_n\left[-\overline{uv}\frac{s}{r}\sin^2\beta+\overline{v^2}\left(-\frac{s}{r}\sin\beta\cos\beta+s\frac{d\beta}{dr}\right)+\overline{vw}\left(1+\frac{s^2}{r^2}\sin^2\beta-\frac{2s^2}{r}\frac{d\beta}{dr}\sin\beta\cos\beta\right)\right]-\Omega_s\left[-\overline{u^2}\frac{s}{r}\sin^2\beta+\overline{uv}\left(-\frac{s}{r}\sin\beta\cos\beta+s\frac{d\beta}{dr}\right)+\overline{uw}\left(1+\frac{s^2}{r^2}\sin^2\beta-\frac{2s^2}{r}\frac{d\beta}{dr}\sin\beta\cos\beta\right)\right]\right\}-\frac{2}{3}\left(\frac{s^2}{r^2}\sin^3\beta\cos\beta-\frac{s^2}{r}\frac{d\beta}{dr}\sin^2\beta\right)\epsilon(1-\gamma)-C_{\phi 1}\frac{\epsilon}{k}\left[\overline{uv}-\frac{2}{3}\left(\frac{s^2}{r^2}\sin^3\beta\cos\beta-\frac{s^2}{r}\frac{d\beta}{dr}\sin^2\beta\right)k\right] \quad (18)$$

$\overline{vw}$:

$$0=(1+C_1)(1-\gamma)\left\{\left[-\overline{v^2}-\overline{vw}\left(-\frac{s}{r}\sin\beta\cos\beta+s\frac{d\beta}{dr}\right)\right]\left(\frac{\partial W}{\partial n}+U\,\Gamma^3_{12}+W\,\Gamma^3_{23}\right)+\left(-\overline{uv}+\overline{vw}\frac{s}{r}\sin^2\beta\right)\left(\frac{\partial W}{\partial s}+U\,\Gamma^3_{11}+W\,\Gamma^3_{13}\right)+\left[-\overline{vw}-\overline{w^2}\left(-\frac{s}{r}\sin\beta\cos\beta+s\frac{d\beta}{dr}\right)\right]\left(\frac{\partial V}{\partial n}+U\,\Gamma^2_{12}\right)\right\}-2\left\{\Omega_s\left[\overline{v^2}+\overline{vw}+\left(-\frac{s}{r}\sin\beta\cos\beta+s\frac{d\beta}{dr}\right)\right]-\Omega_n\left(\overline{uv}-\overline{vw}\frac{s}{r}\sin^2\beta\right)-\Omega_s\left[-\overline{uw}\frac{s}{r}\sin^2\beta+\overline{vw}\left(-\frac{s}{r}\sin\beta\cos\beta+s\frac{d\beta}{dr}\right)+\overline{w^2}\left(1+\frac{s^2}{r^2}\sin^2\beta-\frac{2s^2}{r}\frac{d\beta}{dr}\sin\beta\cos\beta\right)\right]\right\}$$

$$- \frac{2}{3}\left(\frac{s}{r}\sin\beta\cos\beta - s\frac{d\beta}{dr}\right)\epsilon(1-\gamma)$$

$$- C_{\phi 1}\frac{\epsilon}{k}\left[\overline{vw} - \frac{2}{3}\left(\frac{s}{r}\sin\beta\cos\beta - s\frac{d\beta}{dr}\right)k\right] \quad (19)$$

$\overline{uw}$:

$$\begin{aligned}
0 = (1 &+ C_1)(1-\gamma)\Big\{\Big[-\overline{vw} - \overline{w^2}\left(-\frac{s}{r}\sin\beta\cos\beta\right. \\
&\left. + s\frac{d\beta}{dr}\right)\Big]\left(\frac{\partial U}{\partial n} + U\,\Gamma^1_{12} + W\,\Gamma^1_{23}\right) \\
&+ \left[-\overline{uw} + \overline{w^2}\frac{s}{r}\sin^2\beta\right)\left(\frac{\partial U}{\partial s} + U\,\Gamma^1_{11} + W\,\Gamma^1_{13}\right) \\
&+ \Big[-\overline{uv} - \overline{uw}\left(-\frac{s}{r}\sin\beta\cos\beta\right. \\
&\left. + s\frac{d\beta}{dr}\right)\Big]\left(\frac{\partial W}{\partial n} + U\,\Gamma^3_{12} + W\,\Gamma^3_{23}\right) \\
&+ \left(-\overline{u^2} + \overline{uw}\frac{s}{r}\sin^2\beta\right)\left(\frac{\partial W}{\partial s} + U\,\Gamma^3_{11} + W\,\Gamma^3_{13}\right)\Big\} \\
&- 2\Big\{\Omega_s\Big[\overline{uv} + \overline{uw}\left(-\frac{s}{r}\sin\beta\cos\beta + s\frac{d\beta}{dr}\right)\Big] \\
&- \Omega_n\Big[\overline{u^2} - \overline{vw}\left(-\frac{s}{r}\sin\beta\cos\beta\right. \\
&\left. + s\frac{d\beta}{dr}\right) - \overline{w^2}\left(1 + \frac{s^2}{r^2}\sin^2\beta - \frac{2s^2}{r}\frac{d\beta}{dr}\sin\beta\cos\beta\right)\Big]\Big\} \\
&+ \frac{2}{3}\frac{s}{r}(\sin^2\beta)\epsilon(1-\gamma) \\
&- C_{\phi 1}\frac{\epsilon}{k}\left(\overline{uw} + \frac{2}{3}k\frac{s}{r}\sin^2\beta\right) \quad (20)
\end{aligned}$$

where U, V, W, u, v, w are mean and fluctuating velocity components in s, n, r (Fig. 1) directions. Ω_s, Ω_n are the components of angular velocity in s and r directions.

4. Effects of Rotation and Curvature on the Turbulence Structure – A Qualitative Discussion

The effects of rotation on the turbulence structure can be qualitatively analyzed employing equations (15)–(20) and neglecting the curvature terms. A detailed discussion of this is given in reference [12].

For the coordinate system shown in Fig. 1, $\Omega_s = \Omega\cos\beta$, $\Omega_n = -\Omega\sin\beta$, the effect of rotation is to decrease $\overline{u^2}$ and increase $\overline{w^2}$ for negative values of $\overline{uw}$, while the negative value of $\overline{vw}$ increases the radial component of intensity ($\overline{w^2}$) and decreases normal component of intensity ($\overline{v^2}$). These effects are reversed when the correlations are positive. The wake measurements reported by Lakshminarayana and Reynolds [12] indicate that $\overline{uw}$ is negative. Thus the overall effect of rotation is to increase the radial intensity and decrease the streamwise intensity in a compressor rotor wake. Similar comments can be made with regard to shear stresses. Negative values of $\overline{uw}$ and $\overline{vw}$ increase the streamwise shear stress ($-\overline{uv}$) through the rotation. The radial shear stress ($-\overline{vw}$) increases when $\overline{u^2} > \overline{w^2}$ and when $\overline{uv}$ is positive. Comparison of the data for isolated airfoil (Hah and Lakshminarayana, [7]), cascade (Raj and Lakshminarayana, [20]), and rotor wake (Lakshminarayana and Reynolds, [2]) provide a confirmation of the trends predicted by this qualitative argument.

No attempt is made in this paper to evaluate the curvature effects for several reasons. The curvature terms in the Reynolds stress equation are many and involve production, pressure-strain and dissipation terms. Also the effects of curvature depend on β and $d\beta/dr$. For rotors with large hub radius compared to blade chord, the effects of curvature can be neglected in the near wake region.

5. Closure of Turbulence for the Numerical Analysis

In the preceding section, the effect of rotation was examined with the simplified form of the transport equation of Reynolds stress. In the numerical analysis, the transport equations of turbulence kinetic energy and the rate of turbulence dissipation were solved together with equations (15)–(20). The latter equations were employed to derive the components of Reynolds stress and turbulence intensities.

The two transport equations are as follows (Hanjalic and Launder, 1974)

$$U^k\frac{\partial\epsilon}{\partial x^k} = C_{\epsilon 1}\frac{\epsilon}{k}P - C_{\epsilon 2}\frac{\epsilon^2}{k} + C_\epsilon\left(\frac{k}{\epsilon}\overline{u^k u^l}\frac{\partial\epsilon}{\partial x^l}\right)_{,k} \quad (21)$$

$$U^k\frac{\partial k}{\partial x^k} = P - \epsilon + C_s\left(\frac{k}{\epsilon}\overline{u^k u^l}\frac{\partial k}{\partial x^l}\right)_{,k} \quad (22)$$

where $P = -\overline{u_i u_j}U^i{}_{,j}$; $C_{\epsilon 1}$, $C_{\epsilon 2}$, C_ϵ, C_s are constants.

The present turbulence closure model solves two transport equations for the turbulence kinetic energy (equation (21)), the rate of turbulence dissipation (equation (22)), and the mean momentum and continuity equations (6), (10)–(12) simultaneously. The Reynolds shear stresses and the components of intensity are calculated through the modelled form of the transport equation of Reynolds stress (equations (15–20)). This procedure thus leads to simultaneous solution of U, V, W, p, k and ϵ from a coupled set of equations. The components of stresses ($\overline{u^2}$, $\overline{v^2}$, $\overline{w^2}$, $\overline{uv}$, $\overline{vw}$, $\overline{uw}$) are derived from the Reynolds stress equations (uncoupled from the main program, equations (15)–(20). Though this model does not include the individual effects of convection and diffusion, the effects of rotation and curvature are fully accounted. Also the consistency of this turbulence closure model is achieved through the variable C_1 in equation (14). Therefore, this model is efficient for the calculation of thin shear flow under strong effects of rotation and curvature with considerably less computation time and computer storage compared to the full Reynolds stress model. The numerical values for the universal constants used in this analysis are given below (Launder, et al, [5], and Pope and Whitelaw, [6]). A slightly higher value of $C_{\epsilon 1}$ resulted in a better prediction in the mean velocity as well as the turbulence quantity.

C_s	$C_{\phi 1}$	C_ϵ	$C_{\epsilon 1}$	$C_{\epsilon 2}$	γ
0.1	1.5	0.15	1.45	1.9	0.6

6. Solution Algorithm

The continuity equation and the time-mean momentum equation (6), (10)–(12) along with turbulence model equations were solved elliptically. At the near wake region, the streamwise velocity gradient is of the same order of magnitude as the normal velocity gradient, hence the conventional boundary layer calculation cannot predict this region well. According to experimental data by Raj and Lakshminarayana [1], Reynolds, Lakshminarayana, and Ravindranath [2], and Ravindranath and Lakshminarayana [2], the Reynolds stresses acting on the nr plane are of comparable magnitude to those on the sn and sr plane. This

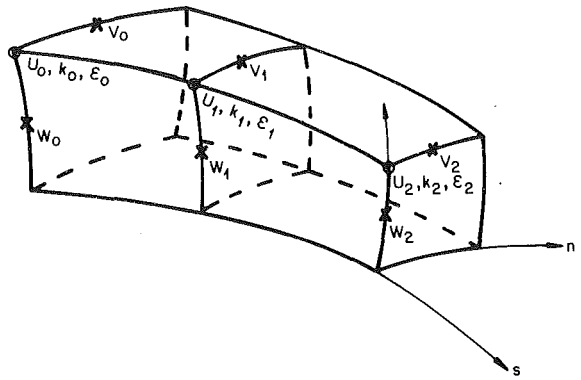

Fig. 2 Typical three-dimensional grid

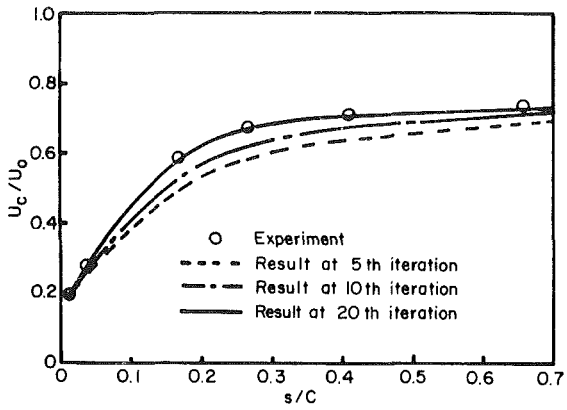

Fig. 3 Wake center velocity prediction at different iterations. Experimental data by Ravindranath and Lakshminarayana [3].

may be due to the effects of rotation and curvature. Hence the parabolic marching technique can not be used. Such strong elliptic effects in rotating flow was also pointed out by Majumdar, Pratrap, and Spalding [11].

As the calculation procedure solves the governing equations in elliptic form, boundary conditions on the whole perimeter of the domain is needed. The experimental data hardly provides all this information, thus some extrapolation of data for the unknown boundary was inevitable. Fine mesh was used in the wake center region and no "wall function" was utilized. A typical mesh is shown in Fig. 2. The staggered grid was used for the convenience of calculation. At every nodal point, the Reynolds stresses ($\overline{u^i u^j}$) were computed using equations (15)–(20) with the calculated values of U, V, W, p, ϵ, k at previous iteration. These Reynolds stresses were utilized in solving the momentum and the turbulence closure equations for the new value of U, V, W, p, ϵ, k.

To handle the pressure term explicitly, a poisson equation for the pressure was obtained by combining the continuity equation and the divergence of the mean momentum equation. The detailed derivation of this equation for the present coordinate system is given by Hah [21]. As the pressure field was stored three-dimensionally, the pressure equation was solved in elliptic form and updated continuously.

The major difference between the present numerical scheme and partially-parabolic scheme is that the downstream effects are not confined only to pressure field and downstream unknown variables are included in the finite-difference equations and the equations are solved iteratively. The computing domain extended from hub to tip, one complete passage and several chords downstream of the trailing edge. Due to the nature of the rotor wake, the flow field is periodic in circumferential direction with the periodicity S in Fig. 1. The unknown variables on the boundary plane ADHE and BCGF were set equal between corresponding points (at the same radial and axial stations).

For most of the calculation, 10 stations in the radial direction and 40 stations each for the normal and streamwise directions were used. For the initial condition in the elliptic calculation, the effect of downstream flow on upstream flow was neglected. About 15 to 20 iterations were necessary for reasonable convergency. In Fig. 3, the calculated decay rates at wake center are shown at various iterations for the data of Ravindranath and Lakshminarayana [3]. In Fig. 3, U_c represents the velocity in the stream-wise direction at the center of the wake, U_0 is the corresponding free stream velocity and C is the chord length. The computing time was up to 30 minutes for the 40 × 10 × 40 nodal points using the IBM 370/3033 at The Pennsylvania State University.

7. Comparison With Experimental Data

Comparison between the theory and experiment is made using the compressor rotor wake data which provide both the mean velocity and turbulence quantity. Some relevant data on the compressor and the operating conditions are given in Table 1.

The domain of calculation is shown in Fig. 1. A, B, C and D

Table 1

	Raj and Lakshminarayana [1]	Reynolds, et al. [2]	Ravindranath and Lakshminarayana [3]
hub/tip	0.44	0.44	0.5
rpm	1010	1010	1066
number of blade	12	12	21
blade shape	symmetric	symmetric	cambered
ratio of blade chord (c) to spacing (s) at mid-radius	1.47	1.47	1.35
tip radius	0.27 m	0.27 m	0.46 m
incidence at mid-radius	0°	10°	7°
stagger angle at mid-radius	45°	45°	30°
drag coefficient (C_D) at mid-radius	0.0055	0.011	0.0116
lift coefficient (C_L) at mid-radius	0.028	0.3	0.6

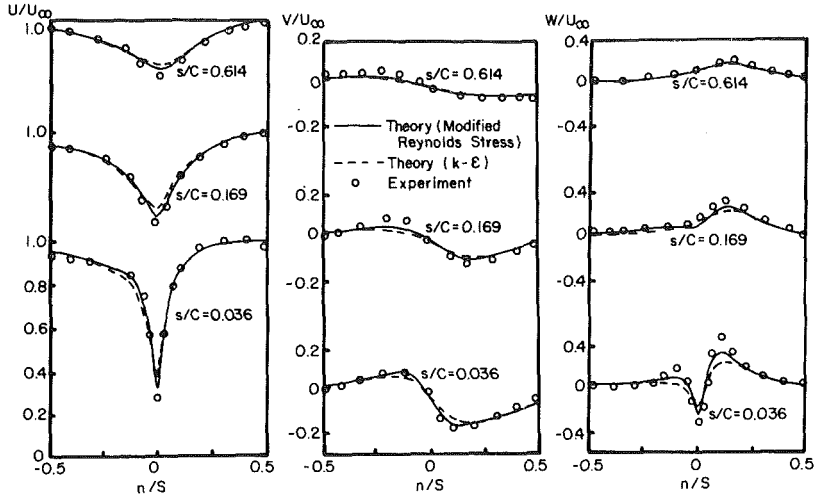

Fig. 4 Profiles of mean velocity components at r/r_t = 0.58. Experimental data by Raj and Lakshminarayana [1].

lie on the cylindrical surface formed by the annulus wall and E, F, G and H lie on the cylindrical surface formed by the hub wall. For elliptic calculation, the initial condition was specified on ABFE (this was mainly based on experimental data), boundary condition on ABCD, EFGH and outflow condition on DCGH. The surface DCHG was located two chords downstream from the trailing edge and both the mean flow and the turbulence do not fully decay on this surface. Since the governing differential equations are solved in elliptic form, correct boundary condition at outflow is required for unique solution. The boundary condition on the surface DCGH was obtained using the empirical decay laws which was based on experimental data and given in references [1, 2, 3]. However, if the outflow boundary is located far downstream, boundary condition based on the assumption that the wake is fully developed into uniform flow can be applied. As the experimental data provides boundary condition only on the limited number of points on the boundary surface, power laws were used between these points to get the proper boundary condition for the finite difference calculation. The periodic boundary condition was specified between the surfaces ADHE and BCGF.

The universal constants in the turbulence closure model, suggested by Launder, Reece, and Rodi [5] were used.

The comparison of prediction and measurement is made at r/r_t = 0.58 for the data by Raj and Lakshminarayana [3]. Comparison between the predictions and the experimental data for all the three velocity components are shown in Fig. 4. The streamwise velocity U, normal velocity V, and radial velocity W, are normalized by U_0. The intensity and Reynolds stresses are plotted in Fig. 5. In these figures s is the distance from trailing edge and n is the distance from wake center. n = s = 0 represents the blade trailing edge and S is the blade spacing. The prediction is quite accurate for streamwise and radial components of mean velocity. The discrepancy in normal velocity components may be due to inaccurate information on boundary condition or scatter in the experimental data. The prediction for Reynolds stresses is quite satisfactory considering the complexity of the flow field.

The second set of data used for the comparison is due to Reynolds, et al. [2]. They measured the wake in the same compressor as Raj and Lakshminarayana [1], but the rotor was tested with a higher blade loading. Comparisons of the mean velocity, normal stress and shear stress at various profiles inside the wake at r/r_t = 0.72 (ratio of local to tip radius) are shown in Figs. 6 and 7. Here again the prediction is

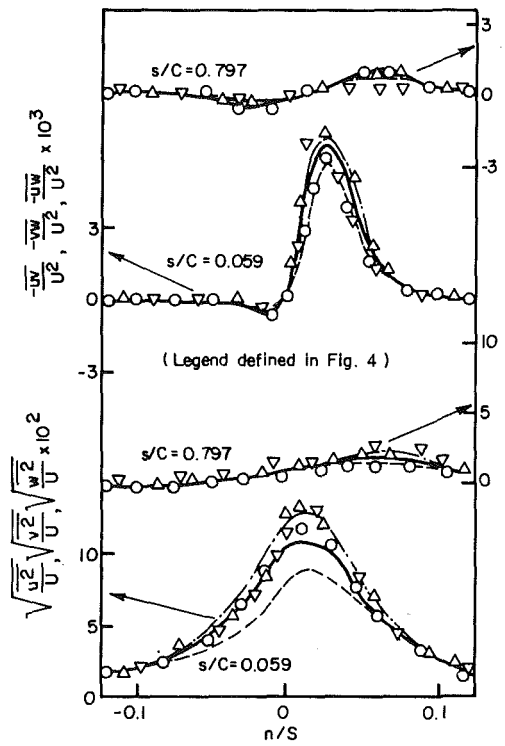

Fig. 5 Profiles of Reynolds stresses at r/r_t = 0.58. Experimental data by Raj and Lakshminarayana [1].

accurate for the mean velocity component as well as Reynolds stresses. For this case, the effects of rotation and streamwise curvature are substantial compared to the first example. The agreement between prediction and data for both the far and near wake is remarkably good, considering the difficulty in predicting such complex flow phenomena. The radial intensity is nearly equal to the streamwise intensity and the trend is predicted well. Therefore, the present method can fully account for the rotation effect through the modelling of the Reynolds stress equation in the curvilinear, rotating coordinates.

The final set of data used for the comparison is due to Ravindranath and Lakshminarayana [3]. The experiment was done in a single stage compressor (Table 1). The blade was

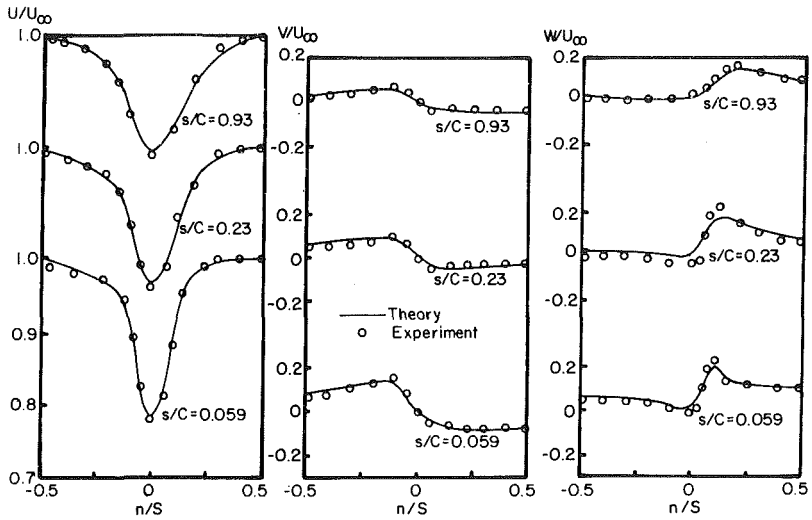

Fig. 6 Profiles of mean velocity components at r/r_t = 0.72. Experimental data by Reynolds, et al. [2]

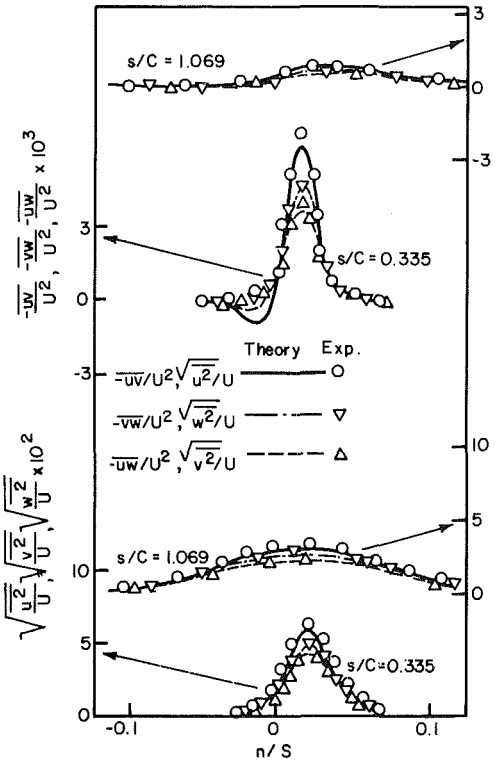

Fig. 7 Profiles of Reynolds stresses at r/r_t = 0.72. Experimental data by Reynolds, et al. [2]

moderately loaded. For this last example, the conventional k−ϵ model by Launder and Spalding [14] was also used and the results were compared with the present model. The transport equations which appear in $k-\epsilon$ model were written in (s,n,r) coordinates (Fig. 1). The details of this procedure are given by Hah [21]. The comparison of mean velocity is given in Fig. 8. The agreement between the theory and data is good, especially for the authors' method. It should be mentioned here that the conventional $k-\epsilon$ model will not predict the shear stress or intensity components satisfactorily. The authors' method can provide this information accurately. The comparison of Reynolds stresses are given in Fig. 9. The present turbulence closure model shows substantial improvements in prediction of mean velocity as well as turbulent quantity.

As explained earlier, the effect of rotation is to reduce the streamwise intensity and increase the radial component of turbulence intensity. The authors' model, which includes this effect correctly predict the trend (Fig. 9). The radial component of intensities predicted by the $k-\epsilon$ model is much lower than the measured data (Fig. 9), while the authors prediction comes closer to the data.

The $k-\epsilon$ model predicts higher values of shear stresses in the pressure side of the wake (Fig. 9). The mean strain rates are very high in the pressure side of the wake and this results in higher shear stresses when $k-\epsilon$ model is used for turbulence closure.

The decay of streamwise and radial velocity components is compared in Fig. 10, where U_0 is the streamwise velocity component in the free stream and U_c, W_c are the streamwise and the radial velocity components at the center of the wake. Also the decay of Reynolds stresses is given in Figs. 11 and 12 where subscript m indicates the maximum value in the wake at that streamwise station. The agreements between predictions and experimental data are excellent though some minor deviations are observed at very near wake region.

These comparisons seem to indicate that the turbulence models employed in this paper correctly model the rotation and curvature effects, through the Reynolds stress transport equation.

8. Conclusions

The method presented in this paper solves the continuity and momentum equations in a curvilinear coordinate system rotating with the rotor. The turbulence closure model utilizes the transport equations for kinetic energy and the dissipation rate. The components of Reynolds stress are calculated using a modelled Reynolds stress equation which includes all the dominant rotation and curvature terms.

The numerical results show excellent agreement with wake data from different blade geometries. All the components of the mean velocity profile, as well as the turbulence intensity and stress profiles, are predicted accurately. Future investigations should concentrate on the development of a boundary layer calculation scheme, output of which can be utilized as the initial condition for the wake program.

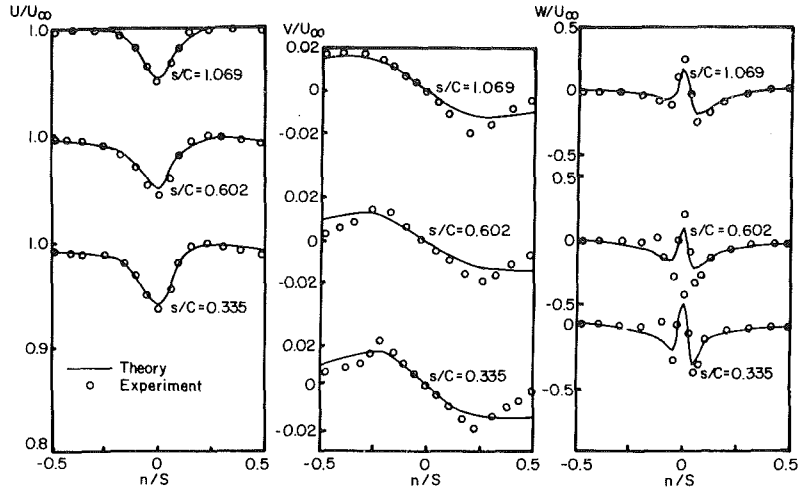

Fig. 8 Profiles of mean velocity components at r/r_t = 0.8. Experimental data by Ravindranath and Lakshminarayana [3].

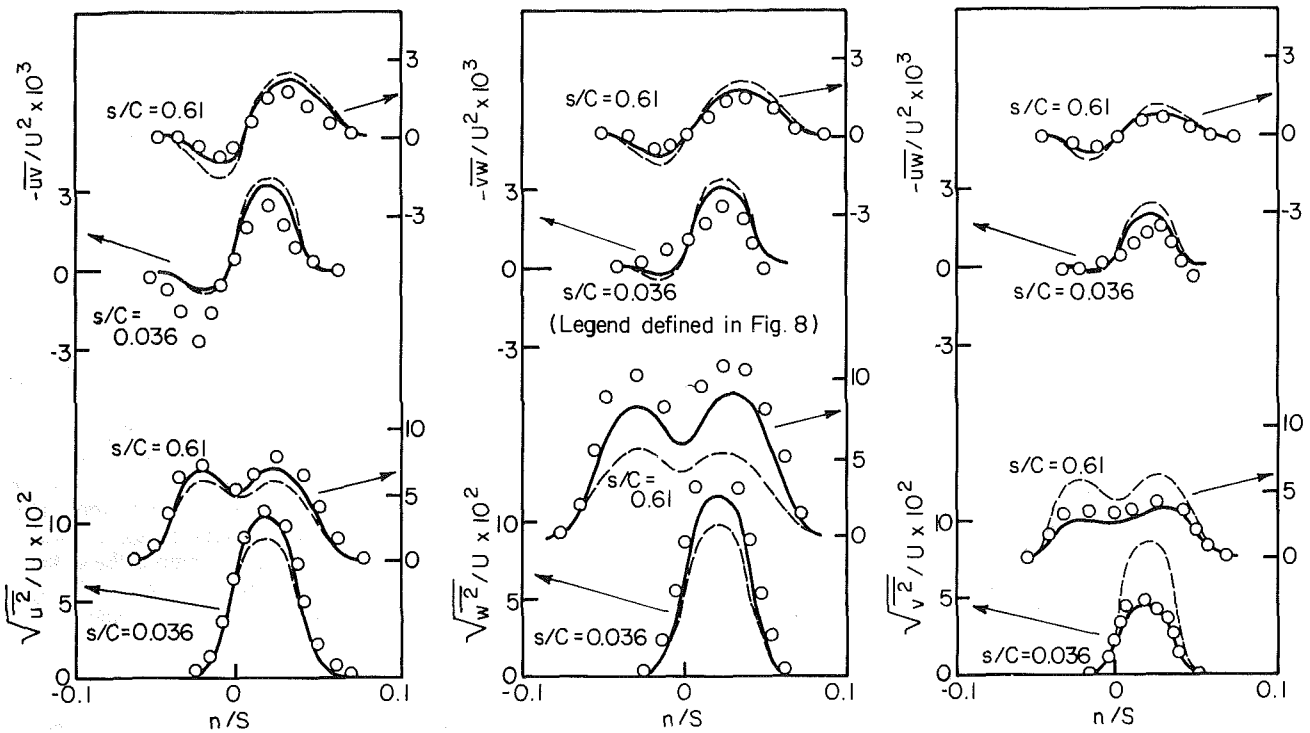

Fig. 9 Profiles of Reynolds stresses at r/r_t = 0.8. Experimental data by Ravindranath and Lakshminarayana [3].

Acknowledgments

This work was supported by the National Aeronautics and Space Administration through grant NsG 3012, with M. F. Heidmann as the technical monitor. The authors wish to thank A. Ravindranath and B. Reynolds for providing the experimental data utilized in this paper.

References

1 Raj, R., and Lakshminarayana, B., "Three-Dimensional Characteristics of Turbulent Wakes Behind Rotors of Axial-Flow Turbomachinery," *Journal of Engineering for Power,* Vol. 98, 1976, pp. 218-228.

2 Reynolds, B., Lakshminarayana, B., and Ravindranath, A., "Characteristics of the Near-Wake of a Compressor or Fan Rotor Blade," *AIAA J.,* Vol. 17, No. 9, Sept. 1979.

3 Ravindranath, A., and Lakshminarayana, B., "Mean Velocity and Decay Characteristics of the Wake of a Compressor Blade With Moderate Loading," ASME *Journal of Engineering for Power,* Vol. 102, 1980, pp. 535-548.

4 Lakshminarayana, B., "The Nature of Flow Distortions by Rotor Blade Wakes," AGARD CP 177, 1976.

5 Launder, B. E., Reece, G. J. and Rodi, W., "Progress in the Development of a Reynolds-Stress Turbulence Closure," *J. Fluid Mech.,* Vol. 68, Part 3, 1975, pp. 537-566.

6 Pope, S. B., and Whitelaw, J. H., "The Calculation of Near-Wake Flows," *J. Fluid Mech.,* Vol. 73, Part 1, 1976, pp. 9-32.

7 Hah, C., and Lakshminarayana, B., "Experimental and Numerical Study of Asymmetrical Wakes of a Single Airfoil," (in preparation) 1980.

8 Bradshaw, P., "The Analogy Between Streamline Curvature and Buoyancy in Turbulent Shear Flow," *J. Fluid Mech.,* Vol. 36, Part 4, 1971, p. 1007.

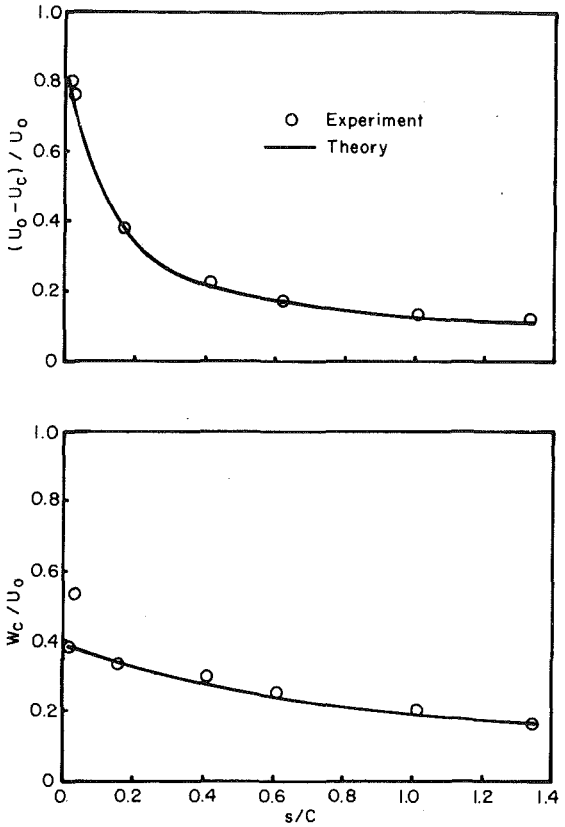

Fig. 10 Decay of wake center velocity defects. Experimental data by Ravindranath and Lakshminarayana [3].

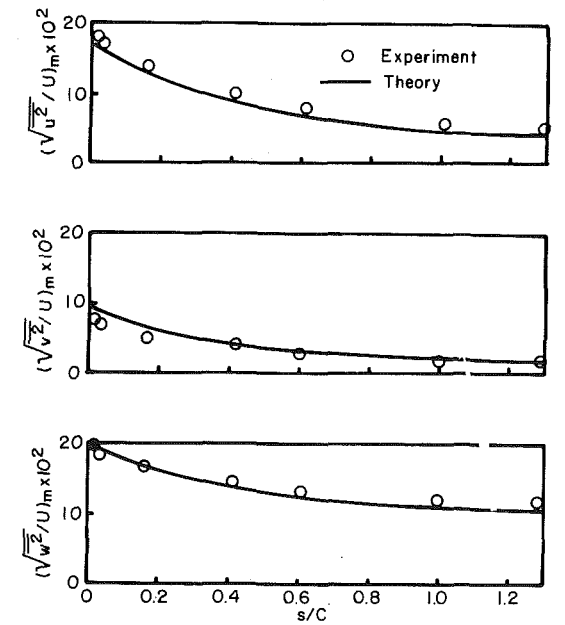

Fig. 11 Decay of maximum turbulence intensity. Experimental data by Ravindranath and Lakshminarayana [3].

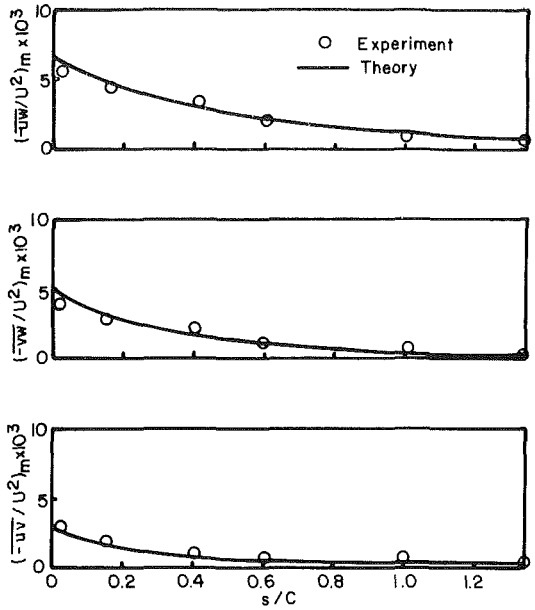

Fig. 12 Decay of maximum shear stress. Experimental data by Ravindranath and Lakshminarayana [3].

9 Launder, B. E., Pridden, C. H., and Sharma, B. I., "The Calculation of Turbulent Boundary Layers on Spinning and Curved Surfaces," ASME JOURNAL OF FLUIDS ENGINEERING, 1977, pp. 231-239.

10 Johnston, J. P., "The Effects of Rotation on Boundary Layers in Turbomachine Rotors," NASA S-204, edited by B. Lakshminarayana, et al., 1974.

11 Majumdar, A. K., Pratrap, V. S., and Spalding, D. B., "Numerical *Computation of Flows in Rotating Ducts*," ASME JOURNAL OF FLUIDS ENGINEERING, 1977, pp. 148-153.

12 Lakshminarayana, B., and Reynolds, B., "Turbulence Characteristics in the Near Wake of a Compressor Rotor Blade," *AIAA Journal,* Nov. 1980.

13 Daly, B. J. and Harlow, F. H., "Transport Equations of Turbulence," *Phys. of Fluids,* Vol. 13, 1970, p. 2634.

14 Launder, B. E. and Spalding, D. B., "The Numerical Computation of Turbulent Flows," *Numerical Methods in Applied Mechanics and Engineering,* Vol. 3, 1974, pp. 269-289.

15 Rotta, J. C., "Statische thorie nichthomogener turbulenz," *J. Physics,* Vol. 129, No. 19, 1951, p. 547.

16 Hanjalic, K., and Launder, B. E., "A Reynolds Stress Model of Turbulence and its Application to Thin Shear Flows," *J. Fluid Mech.,* Vol. 52, Part 4, 1972, pp. 609-638.

17 Raj, R., and Lakshminarayana, B., "On the Investigation of Cascade and Turbomachinery Rotor Wake Characteristics," NASA Rept. No. CR 134680, 1974.

18 So, R. M. S., "A Turbulent Velocity Scale for Curved Shear Flows," *J. Fluid Mech.,* Vol. 70, Part 1, 1975, pp. 37-58.

19 Naot, D., Shavit, A., and Wolfshtein, M., "Interactions Between Components of the Turbulent Velocity Correlation Tensor," *Israel J. of Tech.,* 1970, p. 259.

20 Raj, R. and Lakshminarayana, B., "Characteristics of the Wake Behind a Cascade of Airfoils," *J. Fluid Mech.,* Vol. 61, Part 4, 1973, pp. 707-730.

21 Hah, C., "A numerical and Experimental Study of the Turbulent Wakes of Turbomachinery Rotor Blades, Isolated Airfoils, and a Cascade of Airfoils," Ph.D. thesis, Department of Aerospace Engineering, The Pennsylvania State University, Mar. 1980.

APPENDIX A

Metric Tensor and Christoffel Function for the Rotor s, n, r System

The resulting metric tensor (g_{ij}) is in covariant components,

$$g_{11} = 1, g_{12} = g_{21} = 0, g_{22} = 1$$

$$g_{13} = g_{31} = -\frac{s \sin^2\beta + n \sin\beta\cos\beta}{r} - n\frac{d\beta}{dr}$$

$$g_{23} = g_{32} = -\frac{s \sin\beta\cos\beta + n \cos^2\beta}{r} + s\frac{d\beta}{dr}$$

$$g_{33} = 1+\frac{s^2}{r^2}\sin^2\beta-\frac{2s^2}{r}\sin\beta\cos\beta\frac{d\beta}{dr} +s^2\left(\frac{d\beta}{dr}\right)^2+\frac{2sn}{r^2}\sin\beta\cos\beta +\frac{n^2}{r^2}\cos^2\beta+\left(\frac{2n^2}{r}\cos\beta\sin\beta-\frac{2ns}{r}\cos^2\beta +\frac{2ns}{r}\sin^2\beta\right)\frac{d\beta}{dr}+n^2\left(\frac{d\beta}{dr}\right)^2 \quad \text{(A-1)}$$

For thin shear flow

$$n<<s,r \quad \text{(A-2)}$$

Also the terms containing $(d\beta/dr)^2$ is negligibly small for most rotors, with these assumptions the metric tensor reduces to,

$$g_{ij}=\begin{bmatrix} 1, & 0, & -\frac{s}{r}\sin^2\beta \\ 0, & 1, & \left(-\frac{s}{r}\sin\beta\cos\beta+s\frac{d\beta}{dr}\right) \\ -\frac{s}{r}\sin^2\beta, & \left(-\frac{s}{r}\sin\beta\cos\beta+s\frac{d\beta}{dr}\right), & \left(1+\frac{s^2}{r^2}\sin^2\beta-\frac{2s^2}{r}\frac{d\beta}{dr}\sin\beta\cos\beta\right) \end{bmatrix} \quad \text{(A-3)}$$

$$g^{ij}=\begin{bmatrix} \left(1+\frac{s^2}{r^2}\sin^4\beta\right), & \left(\frac{s^2}{r^2}\sin^3\beta\cos\beta-\frac{s^2}{r}\frac{d\beta}{dr}\sin^2\beta\right), & \frac{s}{r}\sin^2\beta \\ \left(\frac{s^2}{r^2}\sin^3\beta\cos\beta-\frac{s^2}{r}\frac{d\beta}{dr}\sin^2\beta\right), & 1+\frac{s^2}{r^2}\sin^2\beta\cos^2\beta-\frac{2s^2}{r}\frac{d\beta}{dr}\sin\beta\cos\beta & \left(\frac{s}{r}\sin\beta\cos\beta-s\frac{d\beta}{dr}\right) \\ \frac{s}{r}\sin^2\beta, & \left(\frac{s}{r}\sin\beta\cos\beta-s\frac{d\beta}{dr}\right), & 1 \end{bmatrix} \quad \text{(A-4)}$$

The Christoffel functions of the first kind, Γ_{ijk}, and the second kind, Γ^i_{jk}, are calculated from equations (A-1) and (A-2). The expressions for Γ^i_{jk} are as follows:

$$\Gamma^1_{11} = -\frac{s}{r^2}\sin^4\beta$$

$$\Gamma^1_{12} = -\frac{s}{2r^2}\sin^3\beta\cos\beta+\frac{s}{2r}\frac{d\beta}{dr}\sin^2\beta$$

$$\Gamma^1_{22} = 0$$

$$\Gamma^1_{13} = \frac{s^2}{2r^3}(2\sin^4\beta-\cos^2\beta)-\frac{s^2}{r^2}\frac{d\beta}{dr}\sin^3\beta\cos\beta$$

$$\Gamma^1_{23} = \frac{1}{2r}\sin\beta\cos\beta+\frac{s^2}{2r^3}\sin^5\beta\cos\beta -\frac{1}{2}\frac{d\beta}{dr}-\frac{s^2}{2r^2}\frac{d\beta}{dr}\sin^4\beta$$

$$\Gamma^1_{33} = -\frac{s^3}{r^4}\sin^6\beta+\frac{2s^3}{r^3}\frac{d\beta}{dr}\sin^5\beta\cos\beta$$

$$\Gamma^2_{11} = -\frac{s}{r^2}\sin^3\beta\cos\beta+\frac{s}{r}\frac{d\beta}{dr}\sin^2\beta$$

$$\Gamma^2_{22} = 0$$

$$\Gamma^2_{12} = -\frac{s}{2r^2}\sin^2\beta\cos^2\beta+\frac{s}{r}\frac{d\beta}{dr}\sin\beta\cos\beta$$

$$\Gamma^2_{13} = -\frac{1}{2r}\sin\beta\cos\beta-\frac{s^2}{2r^3}\sin^3\beta\cos^3\beta +\frac{s^2}{r^3}\sin^3\beta\cos\beta+\frac{s^2}{2r^2}\frac{d\beta}{dr}\sin^2\beta\cos^2\beta +\frac{1}{2}\frac{d\beta}{dr}-\frac{s^2}{r^2}\frac{d\beta}{dr}\sin^2\beta(2\cos^2\beta+1)$$

$$\Gamma^2_{23} = \frac{s^2}{2r^3}\sin^4\beta\cos^2\beta-\frac{s^2}{r^2}\frac{d\beta}{dr}\sin^3\beta\cos\beta$$

$$\Gamma^2_{33} = \frac{s}{r^2}\sin\beta\cos\beta-\frac{s^3}{r^4}\sin^5\beta\cos\beta +\frac{s^3}{r^3}\frac{d\beta}{dr}[\sin^2\beta\cos^2\beta(2-\cos^2\beta+\sin^2\beta) +2\sin^2\beta-\cos^2\beta]$$

$$\Gamma^3_{11} = -\frac{\sin^2\beta}{r}$$

$$\Gamma^3_{21} = \left(-\frac{1}{2r}\sin\beta\cos\beta+\frac{1}{2}\frac{d\beta}{dr}\right)$$

$$\Gamma^3_{22} = 0$$

$$\Gamma^3_{13} = \frac{s}{r^2}\sin^2\beta\left(1-\frac{\cos^2\beta}{2}\right)-\frac{s}{r}\frac{d\beta}{dr}\sin\beta\cos\beta$$

$$\Gamma^3_{23} = \frac{s}{2r^2}\sin^3\beta\cos\beta-\frac{s}{2r}\frac{d\beta}{dr}\sin^2\beta$$

$$\Gamma^3_{33} = -\frac{s^2}{r^3}\sin^4\beta+\frac{2s^2}{r^2}\frac{d\beta}{dr}\sin^3\beta\cos\beta \quad \text{(A-5)}$$

Rotational Inviscid Flow in a Variable Area Annulus, Pipe or Channel

B. R. Munson

Department of Engineering Science and Mechanics, Engineering Research Institute, Iowa State University, Ames, Iowa 50011

Theoretical and experimental results concerning rotational inviscid flow in an annulus, pipe or channel of variable cross-section are given. Vorticity and continuity considerations are used to determine the velocity profile downstream from the variable area portion in terms of the velocity profile upstream. The lengthening or shortening of vortex lines alters the vorticity in the flow. Regimes of possible reverse flow and flow separation are obtained. The agreement between the theory and experiment is good.

Introduction

One of the important consequences of Helmholtz's equation of vorticity is that for an inviscid fluid of constant density, the stretching (or shortening) of vortex lines increases (or decreases) the strength of the vorticity of the fluid. For inviscid two-dimensional flows the vorticity of a fluid particle remains constant because the length of vortex lines remains constant. For axisymmetric flow, however, the vortex lines may change length as the fluid particles move away from or toward the axis of symmetry. This principle, combined with continuity considerations, is used here to predict the velocity profiles in a variable area annulus, pipe or channel.

The simple theory used is based on the fact that inviscid effects are not important in the flow field. Obviously, for the internal flows considered here this assumption may seem unreasonable. The boundary layers near the walls of the channel, pipe or annulus will produce vorticity that will eventually diffuse throughout the flow field. Experimental results are presented that indicate that in spite of the seemingly severe assumptions used to obtain the theoretical results, the theory and experiment do compare quite well. The ideas discussed provide further insight into the mechanisms of separation and reverse flow.

Theoretical Results

We consider first the axisymmetric, steady, inviscid incompressible flow in an annulus whose cross-sectional area changes along the axis of symmetry, as shown in Fig. 1. Upstream from the contraction or expansion section of the annulus, the annulus cross-section is constant and the velocity, assumed independent of x, is given by $U(R)\mathbf{i}$. The object of this theoretical consideration is to determine the velocity downstream from the variable area portion, where it is again assumed that the velocity is independent of x and given by $u(r)\mathbf{i}$.

Even though the fluid is assumed to be inviscid, the velocity profile upstream need not be irrotational. Vorticity may have been imparted to the fluid by a variety of means (obstructions, filters, etc.). Once this vorticity has been produced, it is assumed that further viscous effects are confined to thin boundary layers on the annulus walls that are neglected for this study.

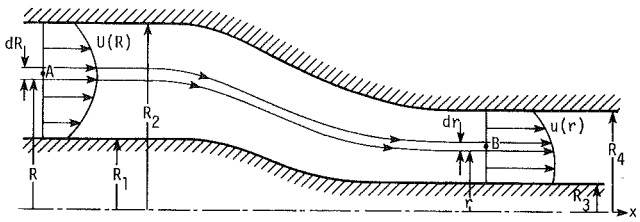

Fig. 1 Flow geometry

Vortex lines are circles centered about the axis of symmetry, with dU/dR and du/dr being the upstream and downstream vorticity, respectively. According to Helmholtz's theorem, for any fluid particle the vorticity divided by the distance from the axis of symmetry must remain constant [1]. Thus, if a fluid particle flows from A to B as shown in Fig. 1, it follows that

$$\dot{U}/R = u'/r \tag{1}$$

where $(\dot{})$ and $(')$ denote differentiation with respect to R and r, respectively.

Continuity considerations for the fluid between neighboring streamlines a distance dR apart upstream and dr apart downstream imply that $2\pi RUdR = 2\pi rudr$. Thus,

$$\frac{dR}{dr} = ru/RU \tag{2}$$

Differentiation of (1) produces $dR/dr = (u''/r - u'/r^2)/(\ddot{U}/R - \dot{U}/R^2)$, which, when combined with (1) and (2), gives

$$u'' = \frac{1}{r}u' = \left[\left(\ddot{U} - \frac{u'}{r}\right)/U\dot{U}^2\right]u(u')^2 \tag{3}$$

The boundary conditions for this equation are obtained by assuming that particles on the inner and outer cylinders remain on those cylinders. Thus, from (1) we obtain

Contributed by the Fluids Engineering Division and presented at the Winter Annual Meeting, Chicago, Ill., November 16-21, 1980, of The American Society of Mechanical Engineers. Manuscript received by the Fluids Engineering Department, March 9, 1979. Paper No. 80-WA/FE-14.

$$u' = \frac{R_4}{R_2}\dot{U}\Big|_{R=R_2} \quad \text{for } r=R_4 \text{ and } u' = \frac{R_3}{R_1}\dot{U}\Big|_{R=R_1} \quad \text{for } r=R_3 \qquad (4)$$

For a given upstream profile, $U = U(R)$, it is necessary to eliminate R from (3) (it appears in U, $\dot{U}$ and $\ddot{U}$) by using (1). The result is a second order nonlinear boundary value problem for $u = u(r)$ that can be solved by quadrature. To this end we let $v = u'/r$ and note that (3) can be written as

$$v' = [(\ddot{U} - v/)\, U\dot{U}^2]vuu' \qquad (5)$$

Now $vR = \dot{U}$ in which $\dot{U}$ is a known function of R. Thus, this relationship can be solved for R as a function of v to give $R = R(v)$. This can then be used to eliminate R and write U, $\dot{U}$ and $\ddot{U}$ as functions of v alone. Hence (5) can be integrated to give

$$\int F(v)\,dv = \frac{1}{2}u^2 + c_1, \text{ where } F(v) = U\dot{U}^2/[v(\ddot{U} - v)]$$

is a known function of v and c_1 is a constant. After integration this result may be solved for v and written as $v = 2/G(u^2)$, where $G(u^2)$ is a known function. Thus, $u'/r = 2/G(u^2)$, which can be integrated to give

$$r^2 + c_2 = \int G(u^2)du, \text{ where } c_2 \text{ is a constant.}$$

The ease with which the various steps can be carried out depends upon the particular upstream profile assumed. Power law upstream profiles, $U = A(R/R_4)^n$, where A and n are constants, produce relatively easy to obtain results that illustrate many of the important principles involved. These results are presented below.

In dimensionless form we replace R by R/R_4, r by r/R_4, let $f = u/A$ and let $v = f'/r$. For power law upstream profiles we obtain $R = (v/n)^{1/(n-2)}$ and $F(v) = 1/(n-2)(v/n)^{(n+2)/(n-2)}$, which can be integrated and inverted to give $G(f^2) = 2/n\,[f^2 + c_1]^{(2-n)/2n}$ provided $n \neq 0$ or $n \neq 2$. The boundary conditions on f' can be written as boundary conditions on f by noting that

$$\frac{f'}{r} = 2/G = n(f^2 + c_1)^{\frac{n-2}{2n}}, \text{ or } f = \left[\left(\frac{f'}{rn}\right)^{\frac{2n}{n-2}} - c_1\right]^{\frac{1}{2}}$$

Thus in dimensionless form we obtain the solution as $u(r) = Af(r)$, where

$$r^2 = \frac{2}{n}\int (f^2 + c_1)^{\frac{2-n}{2n}}df - c_2 \text{ for } \eta_3 \le r \le 1 \text{ with} \qquad (6)$$

boundary conditions $f = \sqrt{\eta_1^{2n} - c_1}$ for $r = \eta_3$ and

$$f = \sqrt{\eta_2^{2n} - c_1} \text{ for } r = 1$$

Here the radius ratios are defined as $\eta_1 = R_1/R_4$, $\eta_2 = R_2/R_4$ and $\eta_3 = R_3/R_4$.

The special cases of $n = 0$ and $n = 2$ are easily handled as follows. For $n = 0$, U is a constant; there is no vorticity upstream and thus no vorticity downstream. Thus, if U is constant, u is a constant determined by continuity considerations requiring that the upstream and downstream flow rates are equal. If $n = 2$, then $U = AR^2$ so that $\dot{U}/R = 2A$. Thus from (1), recalling that $u = Af$, we obtain $f'/r = 2$, or $f = r^2 + c_3$, where $c_3 = (\eta_2^2 + \eta_3^2 - \eta_1^2 - 1)/[2(1 - \eta_3^2)]$ as determined from continuity considerations. The fact that $\dot{U}/R$ is a constant means that regardless of the location of point B relative to point A (see Fig. 1), the value of u'/r is the same. Thus, it is not necessary to use the more general analysis leading to the derivation and solution of (3).

Specific results with $n = -1$, 0, 1 and 2 are presented to illustrate the physics of the problem. Thus, for $n = 1$ (linear profile upstream) we integrate (6) and apply the boundary conditions to obtain

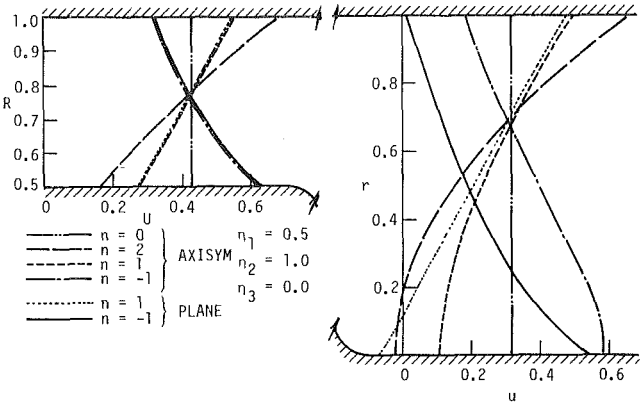

Fig. 2 Shortening of vortex lines

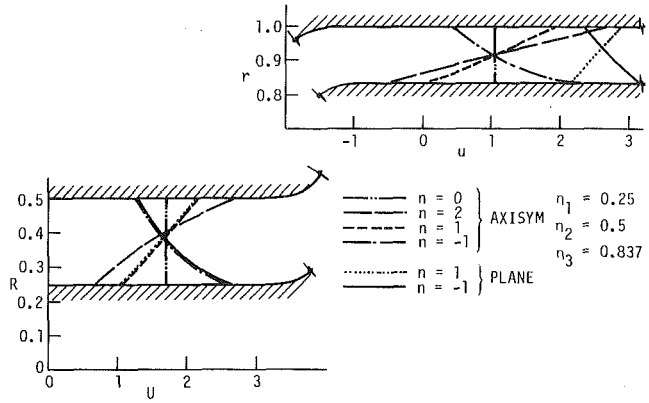

Fig. 3 Lengthening of vortex lines

$$r^2 = f\sqrt{f^2 + c_1} + c_1 \ln\left[\frac{f + \sqrt{f^2 + c_1}}{\eta_2 + \sqrt{\eta_2^2 - c_1}}\right] + 1 - \eta_2\sqrt{\eta_2^2 - c_1} \qquad (7)$$

where c_1 is obtained from

$$\eta_2\sqrt{\eta_2^2 - c_1} - \eta_1\sqrt{\eta_1^2 - c_1} + c_1 \ln\left[\frac{\sqrt{\eta_2^2 - c_1} + \eta_2}{\sqrt{\eta_1^2 - c_1} + \eta_1}\right] = 1 - \eta_3^2$$

Similarly, for $n = -1$ we obtain

$$r^2 = -2f/(c_1\sqrt{f^2 + c_1}) + 2\sqrt{1 - \eta_2^2 c_1}/c_1 + 1 \qquad (8)$$

where c_1 is obtained from

$$c_1(\eta_3^2 - 1) = 2\sqrt{1 - \eta_2^2 c_1} - 2\sqrt{1 - \eta_1^2 c_1}$$

These axisymmetric flow solutions, along with the special cases of $n = 0$ and $n = 2$, are plotted in Figs. 2-4 for various values of η_1, η_2 and η_3. In each case the magnitude of the upstream velocity has been adjusted to give a dimensionless flow rate of 1. That is,

$$2\pi\int_{\eta_1}^{\eta_2} U(R)\,RdR = 1; \text{ or } A = (n+2)/\left[2\pi\left(\eta_2^{n+2} - \eta_1^{n+2}\right)\right]$$

It is noted that flow in a variable area pipe is obtained by setting $\eta_1 = \eta_3 = 0$. Similar results for channel flow (two-

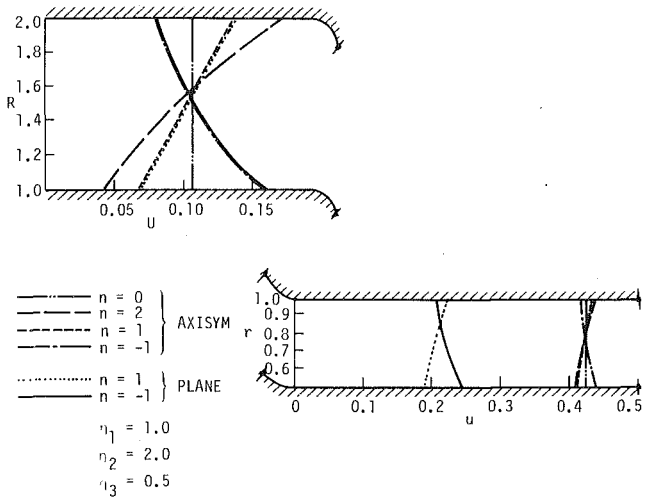

Fig. 4 Generation of nearly uniform flow

dimensional) are also indicated in the figures and discussed below.

A typical case in which the vortex lines are shortened, thus reducing the vorticity, is shown in Fig. 2 where $\eta_1 = 0.5$, $\eta_2 = 1.0$ and $\eta_3 = 0$. The fact that $\eta_3 = 0$ means that the inner cylinder of the annulus has shrunk to zero radius. Thus as $r \to 0$ it follows that $u' \to 0$, so that the vorticity vanishes on the axis and is negligibly small in the neighborhood of the axis. Since $\eta_2 = 1.0$, the radius of the outer cylinder of the annulus remains constnat so that the slopes of the upstream and downstream velocity profiles are the same for $R = 1$ and $r = 1$. As with any of the power law upstream profiles, there is no point at which $\dot{U} = 0$. This means that there can be no relative minimum or maximum for the downstream profiles. Thus, the magnitude of u is bounded by its values on the inner and outer cylinders.

A typical case in which the vortex lines are lengthened, thus increasing the vorticity, is shown in Fig. 3 where $\eta_1 = 0.25$, $\eta_2 = 0.5$ and $\eta_3 = 0.837$. In all cases except the vorticity-free uniform upstream profile, the magnitude of the vorticity is increased. It is of interest to note that the profile with $n = 1.0$ gives $u = 0$ at the inner cylinder, $r = \eta_3$. For the given $\eta_1 = 0.25$ and $\eta_2 = 0.5$, it can be shown that $u > 0$ for $r = \eta_3$ if $\eta_3 > 0.837$. If $\eta_3 < 0.837$, there is no real solution for c_1 from (7) and it is not possible to obtain the downstream profile from the consideration described here. Physically, the reason for this breakdown is that the stretching of vortex lines of fluid particles on the inner and outer cylinders specifies the slope of the velocity profile at these points. In addition, the area change from upstream to downstream is tied to the magnitude of the velocity. The net result for $\eta_3 < 0.837$ is that to satisfy both vorticity and continuity constraints, the velocity near the inner cylinder must be negative ($u < 0$ for $r \approx \eta_3$).This possibility was not allowed when we derived the governing equation. That is, if point A (see Fig. 1) is on the inner cylinder, it is assumed that point B, which came with A, is also on the inner cylinder.

Thus, under certain conditions it is possible to obtain "separation" (or reverse flow) for inviscid rotational flow in an annulus. This can be seen in the special case of $n = 2$ for which it was not necessary to use equation (3) and its boundary conditions to obtain the downstream profile. Thus, regions of reverse flow near the inner cylinder are indicated in Figs. 2 and 3 when $n = 2$. In either case it is noted that the total downstream flow area is larger than the upstream flow area. Thus, such inviscid separation occurs under the same general conditions for which boundary layer separation may occur—flow in a diverging annulus. The nature of the separation region in the variable area portion of the annulus, while not within the scope of this present work, is of considerable interest.

Another situation involving separation of an inviscid rotational flow occurs for flow in a two-dimensional channel or a circular tube with a sink on the axis of symmetry at the closed end [2]. If the flow upstream is irrotational no separation occurs, but if the flow upstream is rotational, corner eddies near the closed end occur even if viscous effects are neglected. Thus in both this situation and the annulus flow presented here, it is the vorticity far upstream that causes separation even in the absence of viscosity.

It should be noted that for situations in which separation occurs, the fluid in the reverse flow region does not originate far upstream and thus does not necessarily have the vorticity given by the above analysis [3]. Thus the theoretical profiles discussed here may be expected to be valid only for the region outside of the reverse flow region. The experimental results described below confirm this fact.

The final axisymmetric example concerns what happens if the radius of the annulus walls is reduced considerably, thus greatly shortening the vortex lines. That is, we assume that $\eta_1 = \beta/\epsilon$, $\eta_2 = 1/\epsilon$ and $\eta_3 = \alpha$, where α and β are constants, and consider the limit $\epsilon \to 0$. It can be shown that as $\epsilon \to 0$, the magnitude of c_1 becomes very large and the velocity profile becomes nearly uniform. For example, with $n = 1$ it can be shown from (7) that $c_1 \to -4(1 - \beta^3)^2/[9\epsilon^6(1 - \alpha^2)^2]$, while for $n = -1$ it can be shown from (8) that $c_1 \to -4(1 - \beta)^2/[\epsilon^2(1 - \alpha^2)^2]$. In either case f varies between its value at $r = \eta_3$ and $r = 1$ which, for small ϵ, are essentially the same. Thus, for small ϵ, $f \approx \sqrt{-c_1}$ for $\eta_3 \leq r \leq 1$. That is, the flow is uniform flow in the limit of $\epsilon \to 0$. This limiting characteristic is shown in Fig. 4 where $\eta_1 = 1.0$, $\eta_2 = 2.0$ and $\eta_3 = 0.5$, that is $\alpha = 0.5$, $\beta = 0.5$ and $\epsilon = 0.5$. It is noted that even though ϵ is not very small, the uniform flow limit valid for $\epsilon \to 0$ is a reasonable approximation to the profiles shown.

Results for two-dimensional channel flow rather than axisymmetric annulus flow can be easily obtained by using the same methods discussed above. Thus for channel flow we replace R and r in Fig. 1 by Y and y and use vorticity and continuity considerations in the form $\dot{U} = u'$ and $UdY = udy$. These equations can be combined and integrated to give

$$U^2(Y) = u^2(y) + c_1 \tag{9}$$

For a given upstream flow, the vorticity relationship $\dot{U}(Y) = u'$ can be inverted to give Y as a function of u'. Thus (9) can be written as $u' = 1/\tilde{G}(u^2)$, where $\tilde{G}(u^2)$ is a known function. A second integration gives $y + c_2 = \int \tilde{G}(u^2)du$, where c_2 is a constant.

As with the axisymmetric case, power law upstream profiles provide easy-to-obtain solutions. Thus with $U = AY^n$ and $u = Af$ we obtain $y = 1/n\int(f^2 + c_1)^{(1-n)/2n}\, df - c_2$ for $\eta_3 \leq r \leq 1$, provided $n \neq 0$ or $n \neq 1$. The constants c_1 and c_2 are determined by assuming that fluid particles on the channel walls remain on the walls. That is, $f' = n{\eta_1}^{n-1}$ and $f' = n{\eta_2}^{n-1}$ at $y = \eta_3$ and $y = 1$, respectively. As before, these give $f = \sqrt{{\eta_1}^{2n} - c_1}$ at $y = \eta_3$ and $f = \sqrt{{\eta_2}^{2n} - c_1}$ at $y = 1$. For the special cases of n = 0 (uniform flow) and n = 1 (uniform vorticity) we obtain $f = (\eta_2 - \eta_1)/(1 - \eta_3)$ and $f = y + ({\eta^2}_2 + {\eta^2}_3 - {\eta_1}^2 - 1)/[2(1 - \eta_3)]$, respectively.

Typical channel flow results for $n = 1$ and -1 are shown in Figs. 2-4. For these plane cases the upstream profile is the same as for the axisymmetric cases. Thus the flow rate does not equal one. The fact that the vorticity is "frozen" for a given particle in two-dimensional flow but varies due to the shortening or lengthening of vortex lines in axisymmetric flow is clearly evident.

It has been shown that the theoretical velocity profile downstream from the expansion or contraction portion of an

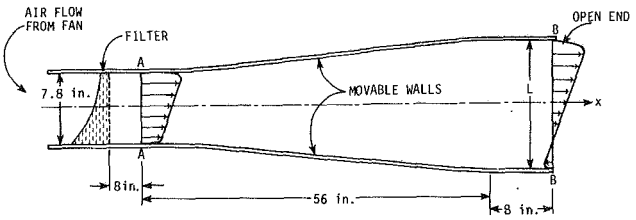

Fig. 5 Schematic diagram of variable area channel. Channel width is 9 in.

annulus, pipe or channel can be relatively easily obtained from the velocity profile upstream of the variable area portion by using simple vorticity and continuity considerations, provided viscous effects are not important. The shortening or lengthening of vortex lines can make the profile tend to either a more or less nearly uniform flow profile. In some cases regions of reverse flow are predicted due to the area change of the annulus and the vorticity in the upstream flow.

Experimental Results

As mentioned above, the basis of the theoretical results presented is that viscous effects are unimportant in the flow field (except in thin boundary layers near the walls). Thus Helmholtz's vorticity equation is assumed valid. The validity of the solutions obtained, therefore, is dependent on whether this quite strict assumption is reasonable for such internal flows considered. A result of a set of experiments conducted to test these theoretical results is presented below.

The experimental apparatus used consisted of a two-dimensional channel as shown in Fig. 5. Air flowed through a series of filters so that the desired velocity profile was obtained at the upstream end of the variable are portion of the channel.

The walls of the channel were movable so that various downstream channel widths could be investigated. The results shown in Fig. 6 are for a constant upstream width of 7.8 in. expanded into downstream widths of 11.7, 15.5, and 17.5 in., respectively. The velocity profiles at section A and B were measured by use of Pitot-static tube and an electronic pressure transducer.

By placing appropriate filters across the channel upstream from its expansion section, it was possible to obtain a nearly linear velocity profile at section A. This profile, shown in Fig. 6(*a*), corresponds to the theoretical profile with $n = 1$ in Fig. 2. It is seen that the boundary layers at this section of the flow are quite thin and that nearly all of the fluid has essentially constant vorticity.

If viscous effects are not important the theoretical results presented above predict the theoretical velocity profiles shown in Fig. 6(*b*), (*c*), and (*d*). Since this is two-dimensional flow, the vorticity remains constant and the velocity gradient across the channel, du/dy, is the same for any expansion ratio of the channel. If the expansion ratio becomes too large, continuity considerations imply that separation and reverse flow are to be expected in the channel.

The experimental results shown indicate a remarkably good agreement with the theory. The obvious difference between the theoretical and experimental results is the presence of a boundary layer, particularly noticeable on the upper wall of the channel. Outside of this boundary layer the upstream vorticity is indeed conserved as the fluid flows from A to B. In addition, the region of backflow, as predicted by the theory, does occur as shown in Fig. 6(*d*). The flow in this separated region is quite unsteady, with almost periodic bursts of alternating backflow and foward flow. This characteristic was easily observed by use of smoke injection and by use of small wool tufts suspended in the flow field. Because of this un-

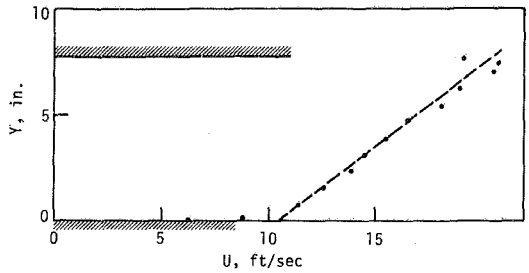

Fig. 6(*a*) upstream profile

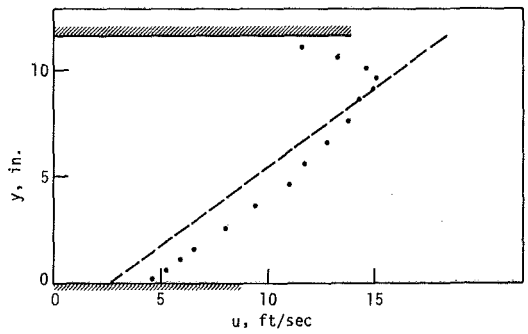

Fig. 6(*b*) downstream profile, small expansion, $L = 11.7$ in.

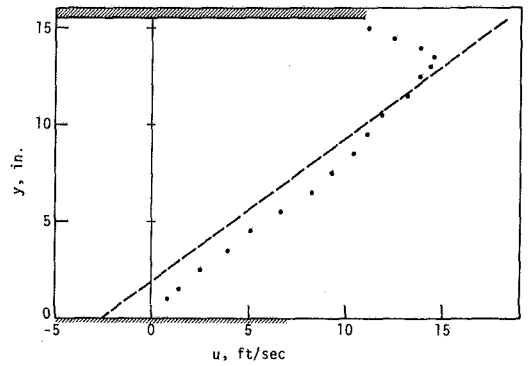

Fig. 6(*c*) downstream profile, moderate expansion, $L = 15.5$ in.

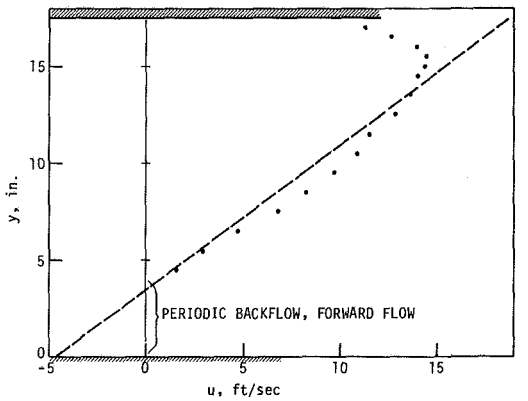

Fig. 6(*d*) downstream profile, larger expansion, $L = 17.5$ in.

Fig. 6 Experimental velocity profiles (• • •); theoretical velocity profile (— —). (uncertainty estimates: $y \pm 0.1$ in., $u \pm 1$ ft/s)

steadiness the velocity profile in the separated region is not plotted on the graph. In spite of this unsteadiness in the separated region, the flow across the remainder of the channel was steady.

It should be noted that experiments performed with uniform upstream velocity profiles showed that the divergence angle of the diffuser was small enough in all cases so that separation did not occur. Hence it can be concluded that it is the imposed vorticity in the main portion of the flow that causes the separation, rather than the customary boundary layer effects that produce separation in otherwise uniform flows.

It is clear that the above good agreement between inviscid theory and experiment is not expected to be valid if the length of the variable area portion of the channel is long enough to cause considerable boundary layer growth. Indeed, fully developed symmetric flow is to be expected if the velocity profile is measured far downstream from point B.

The use of simple vorticity and continuity considerations shows that it is possible, based on the upstream velocity profile, to obtain flow separation in a variable area channel for situations which would not produce separation if the flow were uniform upstream. The experimental results verify this theory. Although similar experiments have not been performed for rotational flow in a variable area annulus, it is expected that a similar agreement between theory and experiment would be obtained.

Acknowledgment

This research was supported by the Engineering Research Institute of Iowa State University.

References

1 Batchelor, G. K., *An Introduction to Fluid Dynamics,* Cambridge University Press, 1967.

2 Yih, C. S., "Two Solutions for Inviscid Rotational Flow with Corner Eddies," *J. Fluid Mech.*, Vol. 5, Part 1, 1959, p. 36.

3 Batchelor, G. K., "On Steady Laminar Flow with Closed Streamlines at Large Reynolds Number," *J. Fluid Mech.*, Vol. 1, 1956, p. 117.

A. Morse

J.H. Whitelaw

M. Yianneskis

Imperial College of Science and Technology,
Department of Mechanical Engineering,
Fluids Section,
London SW7 2BX.

The Influence of Swirl on the Flow Characteristics of a Reciprocating Piston-Cylinder Assembly

Measurements of three orthogonal components of mean velocity and the rms values of the corresponding velocity fluctuations have been obtained by laser-Doppler anemometry in the axisymmetric swirling flow in a motored piston-cylinder assembly. The crank was rotated at 200 rpm and the inlet arrangement, a simulated open valve inclined at 60 deg to the cylinder head, provided swirl numbers at entry of approximately 0.45 and 1.20. There was no significant compression. The present results and previous results without swirl are compared.

1. Introduction

In a previous paper [1], the large influence of the inlet geometry on the flow in a motored, piston-cylinder assembly was demonstrated and quantified. These results related to flows with no tangential velocity component and the present work carries the investigation of flow patterns closer to engine practice by determining the influence of a swirl velocity imposed at the inlet valve.

The general philosophy of the research was stated and discussed in references [2 and 3] and required that measurements of the components of local velocity and the corresponding Reynolds stresses be obtained in motored reciprocating assemblies for a variety of engine speeds and geometrical arrangements. The results are intended to guide the development of corresponding calculation methods (see references [2 and 4]) and to improve understanding and intuitive grasp of the relationship between the flow and geometrical boundary conditions and details of the in-cylinder flow behavior. Subsequently, the investigation will be extended to include compression and combustion.

The flow configurations and instrumentation used for the present work are similar to those of references [1-3] and, apart from new features, are described only briefly in the following section. The results are presented in the third section and related to previous work in the Discussion.

2. Flow Configuration and Instrumentation

The idealized flow configuration entailed axial symmetry, fixed valve lift and neither compression nor combustion. The cylinder was fabricated from plexiglass, and the 75 mm diameter flat-headed piston driven in simple harmonic motion with a stroke of 60 mm. The ratio of swept-to-clearance volume was 2.0. The rotational speed was 200 rpm which, on the basis of previous work, implies fully turbulent flow in the cylinder.

The geometry of the "valve" arrangement can be seen by reference to Figs. 1-3, and corresponds to one of the configurations investigated in reference [1] but with the addition of swirl vanes located around the valve stem. The angle of the valve entry was 30 degrees to the axis[1] and the width of the parallel section 4 mm, measured in the radial direction. Two sets of measurements were made, corresponding to swirl vanes inclined at 15 and 30 degrees to the cylinder axis[2]. The inlet arrangement was connected to a large polythene bag which was filled with air seeded with atomised silicone oil in order to provide a reasonable data rate for the laser-Doppler anemometer.

2.1 Optical Arrangement. The optical arrangement comprised a conventional forward-scatter laser-Doppler anemometer system utilizing a 5 mW helium-neon laser and a rotating diffraction grating to provide a frequency shift of ± 1.5 MHz between the first-order beams. The model engine was mounted with the axis of the cylinder horizontal. The optical arrangement could be traversed across two orthogonal diameters and parallel to the cylinder axis.

2.2 Data Acquisition and Processing. Doppler signals from the photomultiplier were amplified and band-pass filtered to remove low frequency pedestal-and high frequency electronic-noise and then passed to an oscilloscope to be displayed, and to the input of a Hewlett Packard model 5360A frequency counter. The filter had a flat response between 0.5 MHz and 3.5 MHz, corresponding to the range of velocities encountered. The triggering mechanism of the oscilloscope was used to accept Doppler signals above a certain threshold level, and for each corresponding burst, an arming pulse was sent from the oscilloscope to the measuring

Contributed by the Fluids Engineering Division and presented at the Winter Annual Meeting, Chicago, Ill., November 16-21, 1980 of THE AMERICAN SOCIETY OF MECHANICAL ENGINEERS. Manuscript received by the Fluids Engineering Division, March 9, 1979. Revised manuscript received at ASME Headquarters August 25, 1980. Paper No. 80-WA/FE-8.

[1] Incorrectly quoted in reference [1] as 30 degrees to the plane of the cylinder head.

[2] Only the 30 degree-results are presented here.

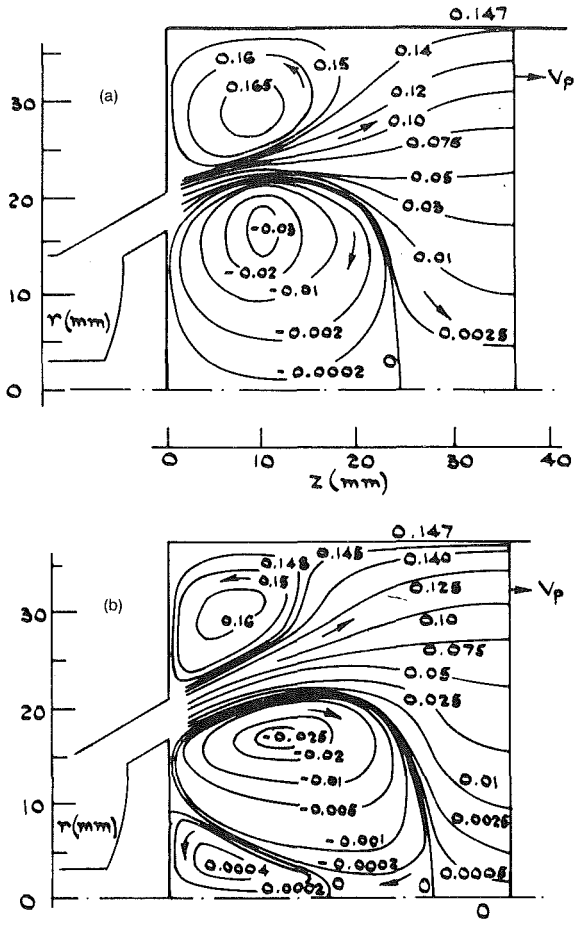

Fig. 1 Streamlines at 36°ATDC. *(a)* zero swirl case, *(b)* 30 deg vanes (S = 1.20)

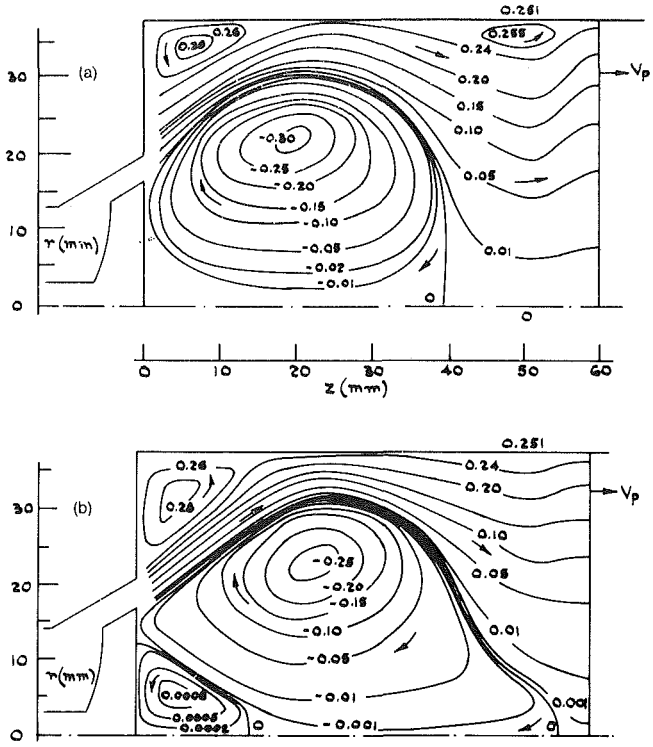

Fig. 2 Streamlines at 90° ATDC. *(a)* zero swirl case, *(b)* 30 deg vanes (S = 1.20)

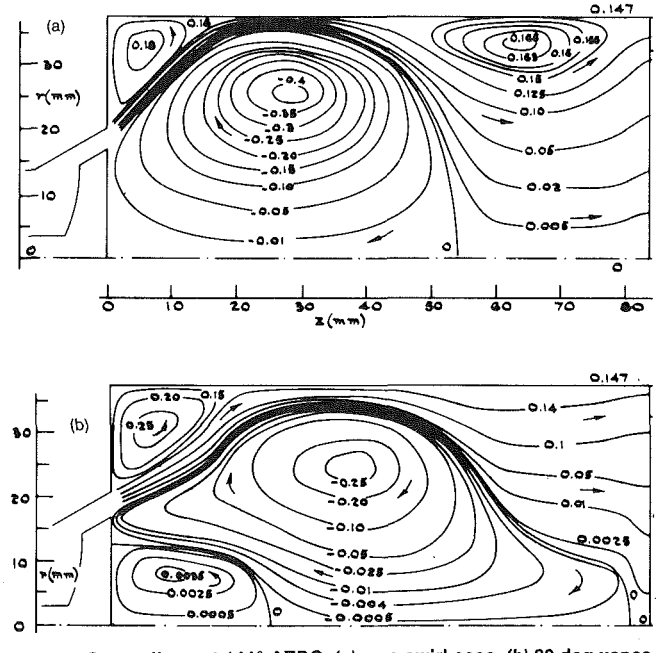

Fig. 3 Streamlines at 144° ATDC. *(a)* zero swirl case, *(b)* 30 deg vanes (S = 1.20)

time input of the counter. The arming pulses were also sent to a "gating" circuit, which received a train of pulses from an optical shaft encoder coupled to the engine drive shaft and synchronized with its rotation. The Doppler frequency from the counter and the encoder pulse at which the signal occurred were stored in digital buffers and read through corresponding interfaces to the memory of a Digital PDP 8/e minicomputer. The computer software was programmed in PAL III coding.

When the frequencies and crank angle locations corresponding to 8,000 signals had been recorded in the memory of the computer, the information was passed through an interface and a format unit and written on magnetic tape (Racal model number 7000). This process was successively repeated until sufficient measurements had been obtained at each axial station. After each set of measurements had been completed, the magnetic tape was decoded on a CDC 6400 computer, programmed in Fortran IV, which evaluated the mean and rms velocities for the crank angles of interest.

In order to increase the sample size for each selected crank angle (θ_c), signals were accepted from the range $\theta_c - \Delta\theta/_2 \leq \theta \leq \theta_c + \Delta\theta/_2$, where $\Delta\theta$ denotes the crank-angle window. In the present work, a choice of $\Delta\theta$ = 10 deg was made (as suggested by the results of reference [1]) as a compromise between sample size and precision. Typical sample sizes for this window were in the range of 150–800 depending on the point in the cycle and the location inside the cylinder at which the measurements were made. The data rate over the whole cycle was typically 50/s for signal-to-noise ratios of the order of 25:1 (28dB), thus requiring a measurement time at each point of around 150 s.

2.3 Precision. Possible sources of uncertainty have been considered in detail in reference 5 with the conclusion that the mean velocity values are subject to uncertainties of not more than 3 percent except at the lowest velocities and highest rms levels. Confirmation was provided by evaluating the net mass flow rates from measured velocity profiles.

3. Results. Data were obtained as a continuous function of crank angle and the contours of Figs. 1 to 3 correspond to 36, 90 and 144 degrees ATDC to allow comparison with the

results of reference [1]. Results at 270 degrees on the exhaust stroke are not presented since they have been considered in reference [6]. The outline of the cylinder, valve inlet and piston are shown in cross-section with the piston head in the correct position for the crank angle.

The streamline patterns at 36 degrees ATDC are shown for zero swirl and a swirl number (defined as the ratio of the angular-to-axial momentum fluxes at entry divided by the width of the port of 1.20). For the nonswirling case and for $z > 10$ mm, the jet is drawn mainly in the axial direction whereas, with the addition of swirl, it is increasingly directed towards the wall. The jet does not actually reach the wall at this early part of the cycle but spreads around the primary vortex and onto the piston face. Comparison of Figs. 1(*a*) and 1(*b*) shows that swirl increases the rate of spread of the jet and causes a slight contraction of the secondary vortex in the centre between the wall and the cylinder head with corresponding lengthening of the primary vortex. As a consequency of the latter, the stagnation point on the axis (indicated by the dividing streamline) moves nearer to the piston face and the curvature of the flow in this region is increased. The primary vortex is elongated by the appearance of a weak third vortex near the cylinder axis and is evidenced by the presence of forward axial velocities up to a distance of 10 mm from the cylinder head.

By mid-stroke, the angle of trajectory of the indrawn jet relative to the cylinder head has decreased to about 50 deg, with the result that the flow is strongly directed towards the wall. The actual point of contact moves slightly closer to the head with increasing swirl number - from about $z = 25$ mm for the zero swirl case (Fig. 2(*a*)) to $z = 23$ mm at $S = 0.45$ and $z = 20$ mm at $S = 1.20$ (Fig. 2(*b*)). In all three flows, the primary vortex has grown considerably from $\theta = 36°$, extending from the axis to within 5 mm of the wall and recirculating in each case approximately 100 percent of the net mass flow rate. For the swirl cases, the vortex reaches considerably nearer to the piston and the stagnation point on the center-line is situated at about $z = 56$ mm compared to $z = 40$ mm in the absence of swirl; its center of rotation has also moved perceptibly away from the axis and the cylinder head. In the region near the wall, the addition of swirl causes suppression of the vortex which forms close to the piston face, although the slight curvature of the streamlines beyond $r = 25$ mm suggests that a vortex of very small size and intensity may be present. Due to the change in the angle of entry, the vortex in the corner between the wall and cylinder head has decreased in size since $\theta = 36°$, but less so for the swirl case. As at $\theta = 36°$, the weak vortex near the cylinder axis is only present for the higher swirl number flow. As a result of the reduction in flow velocities past mid-stroke, the trajectory angle of the jet relative to the cylinder head begins to increase, reaching a value at $\theta = 144°$ of about 60 deg. This allows the secondary vortex in the corner between the head and the cylinder wall to recover in size after the contraction experienced during the first half of the stroke. Although only slightly larger for the two swirling flows, the vortex is much stronger, recirculating about 70 percent of the net mass flux, as against 25 percent for the case with zero swirl. In spite of the increase in the angle of entry, the jet reaches the wall at roughly the same downstream distances as those recorded at $\theta = 90°$ - due to the increased strength of the secondary vortex and the expansion of the primary vortex, the incoming jet is subjected to a sudden change in direction at about $z = 12.5$ mm and $r = 25$ mm and is sharply deflected toward the wall. The primary vortex now encroaches to within 2.5 mm of the wall, and is somewhat stronger for zero swirl, recirculating about 275 percent of the net mass flow rate, compared with 200 percent for $S = 0.45$ and 170 percent for $S = 1.20$. The elongation of this vortex increases with swirl number, the stagnation point on the center-line shifting from $z = 55$ mm at $S = 0$ to $z = 81$ mm (within 3 mm of the piston face) at $S = 1.20$.

4. Discussion

One purpose of the present investigation was to provide information which would allow those seeking to calculate flow characteristics to assess their methods and the present work was carried out in conjunction with calculations performed by Johns [7]. These calculations, based on finite-difference representations of the axisymmetric form of the continuity and momentum equations with turbulence characteristics represented by the Prandtl-Kolmogorov eddy-viscosity hypothesis, have been shown to describe satisfactorily all the main features of the present flow. This may be regarded as slightly fortuitous in view of the use of an isotropic viscosity hypothesis for a swirling flow and it is likely that discrepancies will increase with the swirl number. Similarly, the problems associated with squish and its calculation may represent future sources of uncertainty and require investigation.

Acknowledgments

The authors gratefully acknowledge financial support from the Science Research Council, the Atomic Energy Research Establishment (A.E.R.E.), Harwell, the U.S. Army Research Office and the U.S. Department of Energy.

References

1 Morse, A., Whitelaw, J.H., and Yianneskis, M., "Turbulent Flow Measurements by Laser-Doppler Anemometry in Motored Piston Cylinder Assemblies," ASME JOURNAL OF FLUIDS ENGINEERING, Vol. 101, 1979, p. 208.

2 Gosman, A.D., Melling, A., Watkins, A.P., and Whitelaw, J.H., "Axisymmetric Flow in a Motored Reciprocating Engine," *Proc. I. Mech. E.*, Vol. 192, 1978, p. 213.

3 Hutchinson, P., Morse, A., and Whitelaw, J.H., "Velocity Measurements in Motored Engines: Experience and Prognosis," S.A.E. Paper 780061, 1978.

4 Gosman, A.D., Johns, R.J.R., and Watkins, A.P., "Assessment of a Prediction Method for In-Cylinder Processes in Reciprocating Engines," *Proc. General Motors Symp.*, Detroit, 1978.

5 Morse, A., Whitelaw, J.H., and Yianneskis, M., "The Influence of Swirl on the Flow Characteristics of a Reciprocating Piston-Cylinder Assembly," Imperial College, Mech. Eng. Dept, Report FS/78/41, 1978. See also, in reduced form, ASME Paper 79-WA/FE-1.

6 Bicen, A., Vlachos, N.S., and Whitelaw, J.H., "The Creation and Destruction of Vortices in Unsteady Flows," Letters in *Heat and Mass Transfer*, Vol. 7, 1980, p. 77.

7 Johns, R.J.R., "Prediction of Flow in Diesel Engine Cylinders," Ph. D. thesis, University of London (1980).

Two Aspects of Cavitation Damage in the Incubation Zone: Scaling by Energy Considerations and Leading Edge Damage

D. R. Stinebring

J. William Holl

Applied Research Laboratory,
The Pennsylvania State University,
State College, Pa. 16801

Roger E. A. Arndt

Saint Anthony Falls
Hydraulic Laboratory,
Minneapolis, Minn. 55414

This study focused on two aspects of the cavitation damage problem, namely an energy approach to the scaling of cavitation damage in the incubation zone and damage near the leading edge of a test model. The damage to the surface of the models was in the form of small indentations in which no material was removed. For a wide range of velocities namely 14.9 to 59.3 m/s the rate of pit formation per unit area in the maximum damage zone increased by the sixth power of velocity. Furthermore it is shown that the damage rate versus velocity data are in good agreement with three other investigations. The volumes of the pits were found to increase by the fifth power of velocity. A relationship between the volume of a pit and the cavitation bubble collapse energy absorbed was developed. The damage to the leading edge was felt to be due to the reentrant jet striking the leading edge of the cavity creating a short term pressure rise causing the collapse of any cavitation bubbles in this area.

Introduction

Cavitation and the damage caused by cavitation have been studied for over half a century. Vast amounts of literature have been published dealing with this very practical problem in all areas of hydraulics research. However, the prediction of prototype cavitation damage from model data is an unsolved problem.

Research in this field has followed along many lines. Theoretical studies dealing with bubble dynamics have provided insight as to the possible mechanisms of damage. Another major area of interest has been the relative resistance of various materials to cavitation damage. These investigations have usually made use of a test instrument called a magnetostrictive device, which only vaguely approximates conditions in a flowing system. In cases where the studies have been conducted in a flowing system, the damage has usually been assessed as a weight loss due to cavitation. However, there is a problem with attempting to develop scaling relationships in the weight loss regime. The weight loss to the model surface can be due to the collapse of a single cavitation bubble, a fatigue failure caused by the collapse of many cavitation bubbles, a cavitation corrosion interaction, or combinations of these factors.

The approach of this investigation was to look at the initial stages of cavitation damage in a flowing system, i.e., the incubation zone, in which weight loss has not yet occurred. The models were 0.635 cm diameter zero-caliber ogives constructed of pure annealed aluminum. Damage to the model was in the form of small indentations in the surface with no material removal. Knapp [1] in his classic study of cavitation damage showed that, for damage in the incubation zone, each indentation was produced by the collapse of a single cavitation bubble. This is probably the most important characteristic of the incubation zone, since there is a one-to-one correspondence between the observed damage in the form of individual pits and the cavitation bubble collapse. By observing the damage to the surface, much can be learned about the hydrodynamic aspects of the cavity flow.

There were two test facilities utilized during the course of the investigation. The primary test facility was the ultra-high-speed water tunnel capable of velocities over 92 m/s in a 3.8 cm diameter test section. Preliminary tests were conducted in a tunnel with a 30.5 cm diameter test section and a maximum velocity of 21.3 m/s. The effects of velocity, cavity length and air content were studied in order to develop scaling relationships. For this paper, only two aspects of the investigation will be discussed, namely the energy approach to scaling, and the damage near the leading edge of the models. Other work is reported in references [2] and [3].

An Energy Approach to the Scaling of Cavitation Damage in the Incubation Zone

An energy approach to the problem of scaling of cavitation damage has been proposed by a number of investigators [4], [5], and [6]. From a set of simplifying assumptions, Kato [4]

Contributed by the Fluids Engineering Division for publication in the JOURNAL OF FLUIDS ENGINEERING. Manuscript received by the Fluids Engineering Division, November 22, 1979.

derives the dependence of the mean depth of deformation rate on the flow velocity, characteristic length, material hardness and ultimate resilence. Hammitt [5] postulated that there is a statistical distribution of bubble energies that varies with the degree of cavitation. The approach presented by Thiruvengadam [6] suggests that the strain energy of a material is a good correlating parameter with the relative resistance of materials to cavitation erosion.

The majority of investigations in this field have been conducted in regimes where significant material is removed so that cavitation damage is measured by the weight loss. As stated previously the weight loss may be due to a number of factors such as material removal due to a single bubble collapse, fatigue failure caused by repetative loading, or cavitation-corrosion interactions. Thus, developing scaling relationships in the weight loss regime can present many problems, and consequently this study was conducted in the incubation zone.

The cavitation damage problem can be divided into two general areas namely, (1) the hydrodynamic aspects of the cavity flow and (2) the response of the material to the impulsive loading caused by the cavitation bubble collapse. This investigation focused on the hydrodynamic aspects of the problem. A very soft ductile material (1100-0 aluminum) was used as a recording medium to register the collapse of the cavitation bubbles. By utilizing a very soft material even bubbles with a relatively low collapse energy would produce an indentation in the model surface. In another phase of the investigation [2] employing a scanning electron microscope, it was shown that there was no material removal during the formation of the pits. The cavitation test models were 0.635 cm diameter zero-caliber ogives, which are axisymmetric blunt-nosed bodies.

The number of pits produced on a model's surface can be used as a measure of the damage. However, the size of the individual pits should also be considered. The volume of each indentation in the surface is proportional to the cavitation bubble collapse energy absorbed by the material. A method was developed for measuring the volumes of the individual cavitation pits. As an approximation, the damage pits were assumed to be spherical segments. A single pit was magnified by a factor of 100 with a microscope and illuminated with a collimated light beam. The angle of the collimated light beam was varied until there was no shadow visible in the pit. At this angle the light beam is tangent to the side of the pit at the rim. The volume can be calculated by knowing the lighting angle, the pit diameter, and the approximation to a spherical segment. Further details of this procedure, the test results, and the equation for calculating the pit volume can be found in references [2] and [3]. By recording both numbers and volumes of the identations, a measure of the total absorbed collapse energy may be determined. A relationship between the pit volume and the energy absorbed by the material was also developed. A dynamic hardness test was devised which measures the surface hardness of the material at a high strain rate. Most hardness tests are conducted at very small strain rates, but in the formation of a cavitation pit the strain rates are very high. To account for this fact, a surface hardness measurement at a high strain rate is required. It is assumed that the dynamic hardness of the aluminum is independent of the loading rate. A range of impact energies of over seven to one in the dynamic hardness test produced no observable effect of the loading rate upon the results. This in effect, removes the material response as a factor in the scaling relationship to be developed.

From the distribution of pit volumes for a given flow condition a plot of the distribution of absorbed bubble collapse energies can be obtained. The absorbed energy though is not the total cavitation bubble collapse energy. The total energy, E_T, is

$$E_T = E_A + E_E + E_R \ , \tag{1}$$

where

E_A = the absorbed collapse energy
E_E = the elastic energy due to the recovery of the surface after the collapse
E_R = the energy remaining in the bubble after the initial collapse, i.e., the energy of the rebounding bubble(s).

The absorbed energy, as stated previously, is calculated from measurements of the pit volume. After the cavitation bubble collapse there is some recovery of the surface due to elasticity of the material. This elastic recovery produces an acoustic wave that propagates through the fluid. An expression for estimating the magnitude of the elastic energy will be presented shortly. It will be assumed that the energy remaining in the bubble after the initial collapse is small and can be neglected. Thus, the total energy of the cavitation bubble collapse can be estimated for a given flow condition. This is significant because it allows the scaling of the total collapse energy with various flow parameters. For this study only the velocity was considered.

For a range of test velocities from 14.9 to 59.3 m/s the pitting rate per unit area in the maximum damage zone increases by the sixth power of velocity, [2], [3]. (The maximum damage zone lies within the region about the maximum point on the model where the pitting density decreases to 25 percent of the maximum.)

The velocity also had a marked effect upon the size of the individual pits. As shown in Fig. 1, the average volume per pit or average absorbed bubble collapse energy increases by the fifth power of velocity. Since the number of pits increase by the sixth power of velocity and the average energy per pit by

Nomenclature

a = radius of a cavitation damage pit
D = model diameter
E_A = absorbed cavitation bubble collapse energy
E_E = elastic energy
E_M = modulus of elasticity
E_R = energy in a cavitation bubble after the initial collapse
E_T = total cavitation bubble energy
f = cavity cycling frequency
F = total force
F_I = instantaneous force
h = depth of a cavitation damage pit
ppm = parts per million
P_D = dynamic hardness expressed as a mean dynamic pressure
r_1 = radius of a sphere used for the calculation of the elastic energy
r_2 = radius of curvature of a cavitation damage pit
S = Strouhal number
V_p = volume of a cavitation pit
V_∞ = free stream velocity
z = vertical distance
α = air content
α_I = instantaneous radius of the area of contact between the sphere of radius, r_1, and the cavitation pit
σ = cavitation number
ν_M = Poisson's ratio of the model material

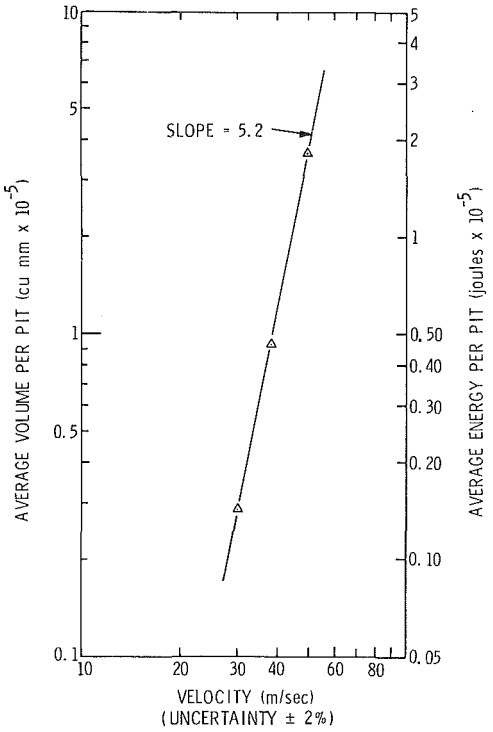

Fig. 1

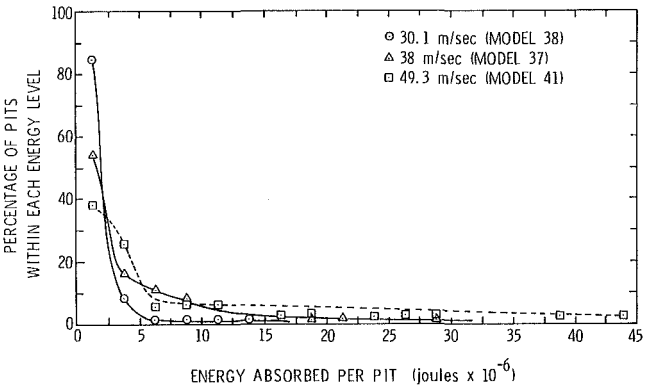

Fig. 2

the fifth power, the total cavitation bubble collapse energy absorbed by the material increases by approximately the eleventh power of velocity. The distribution of bubble collapse energies is shown in Fig. 2 for three test velocities. This plot was generated by multiplying the distribution of pit volumes by the measured dynamic hardness namely 0.5 J/mm^3. Although the statistical sample is relatively small the graph demonstrates the relative distribution of energy. For the lowest velocity there is a large percentage of bubbles collapsing with relatively little damage to the boundary. As the velocity increases, there is a greater percentage of pits formed by a much higher collapse energy.

The energy parameter presented in Figs. 1 and 2 is the bubble collapse energy absorbed by the material. The elastic energy due to recovery of the surface after loading should also be considered. The total bubble collapse energy available at the surface is then the sum of the two. If the elastic energy is a sizable percentage of the total energy and this percentage is also a function of velocity there could be a significant change in the shape of the curves in Figs. 1 and 2. A rough analysis was performed to show that for all the test data, the elastic

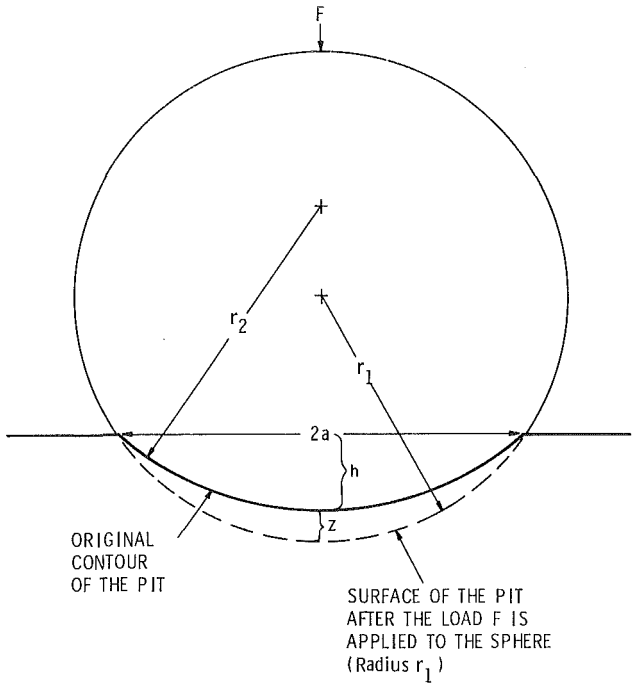

Fig. 3

energy was a relatively small percentage of the total. The analysis is similar to that developed for the dynamic hardness test presented by Tabor [7] and also included in Reference [2]. The pits are assumed to be spherical segments with a diameter, $2a$, and a radius of curvature, r_2, as shown in Fig. 3. It is further assumed that the maximum elastic recovery occurs at the center of the pit, i.e., the point of highest strain, and negligible elastic recovery at the outer circumference where there is no plastic deformation.

A sphere of radius r_1 ($r_1 < r_2$) is placed in contact with the pit. A force is applied to the sphere until the limit of elastic deformation occurs at the center of the pit. The radius, r_1, is chosen such that when this limit is attained the sphere is in contact with the sides of the pit as illustrated in Fig. 3. At this point the force on the sphere is, F. The relationship between r_1, r_2 and F can be found from Hertz's equation

$$2a = \left[\frac{6F\ r_1 r_2}{r_1 - r_2} f(E)\right]^{1/3}. \tag{2}$$

For the case of the sphere being undeformed by the application of the force

$$f(E) = \frac{1 - \nu_M{}^2}{E_M}, \tag{3}$$

where ν_M is Poisson's ratio, and E_M is the modulus of elasticity of the test material. At any point during the deformation the force on the sphere is given by

$$F_I = F\frac{\alpha_I{}^3}{a^3} \tag{4}$$

where $2\alpha_I$ is the diameter of the region of contact and as stated previously, F, is the force when there is full contact with the sides of the pit. As the force increases to the maximum value the sphere will sink a distance z given by

$$z = \frac{3F\ \alpha_I{}^2}{4a^3} f(E). \tag{5}$$

The total elastic energy E_E is the integral of $F_I\ dz$ from $\alpha_I = 0$ to $\alpha_I =$ a given by

$$E_E = \int_0^a \frac{3}{2}\frac{F^2}{a^6} f(E)\,\alpha_I{}^4\, d\alpha_I = \frac{3}{10}\frac{F^2}{a} f(E). \tag{6}$$

By the definition of the dynamic hardness,

$$F = P_D \ \pi \ a^2, \tag{7}$$

where P_D is the dynamic hardness expressed as a mean dynamic pressure. The dynamic hardness was used for this instance to more closely approximate the conditions of the high loading rate that occurs during the formation of a cavitation pit. Thus the elastic energy is, after substitution,

$$E_E = \frac{3}{10} P_D{}^2 \pi^2 a^3 f(E). \tag{8}$$

The plastic energy or absorbed energy is the dynamic hardness multiplied by the original volume of the pit. To a first approximation

$$V_p = \frac{\pi \ a^4}{4 \ r_2}. \tag{9}$$

where V_p is the pit volume. The plastic energy is then,

$$E_A = \frac{P_D \pi a^4}{4 r_2}. \tag{10}$$

The elastic energy expressed as a fraction of the total energy is,

$$\frac{E_E}{E_E + E_A} = \frac{1}{1 + \frac{5}{6}\left[\frac{a}{r_2 P_D \pi f(E)}\right]}. \tag{11}$$

For 1100-0 aluminum as a test material equation (10) reduces to,

$$\frac{E_E}{E_E + E_A} = \frac{1}{1 + \frac{a}{r_2}(41.16)}. \tag{12}$$

From the geometry of the problem, a/r_2, can be expressed as

$$a/r_2 = \sin(\pi - 2 \ \tan^{-1} \ a/h). \tag{13}$$

It follows then that,

$$\frac{E_E}{E_E + E_A} = \frac{1}{1 + 41.14\{\sin[\pi - 2 \ \tan^{-1}(a/h)]\}}. \tag{14}$$

The result is that the percentage of elastic energy is only a function of the diameter to depth ratio of the pit. As $2a/h$ increases, the pit becomes more shallow and the percentage of elastic energy increases. For all the pits measured during the course of the investigation (approximately 150) the greatest diameter to depth ratio ($2a/h$) was 29.6. This corresponds to the elastic energy being 15.3% of the total. The lowest percentage was 3.9 percent ($2a/h = 6.0$). During the dynamic hardness test the total and elastic energy of the spherical indenter were measured. For one test point chosen at random the measured elastic energy was 16.8 percent of the total energy. From the geometry of the pit and the preceeding relationships, the calculated value was 20.1 percent of the total. For the dynamic hardness test there is good agreement between the measured elastic energy and the theoretical estimate.

These findings show that within the limitation of the simple theory the slope of the curve presented in Fig. 1 would only be changed slightly if the elastic recovery energy for each pit was added to the absorbed energy.

Leading Edge Pitting

During the initial phase of the invetigation pitting was observed near the leading edge of the test models. According to classical theories of cavitation erosion one would expect the damage to occur in the vicinity of the trailing edge of the cavity. The distribution of the cavitation damage pits for one model is shown in Fig. 4. The two peaks in the distribution of

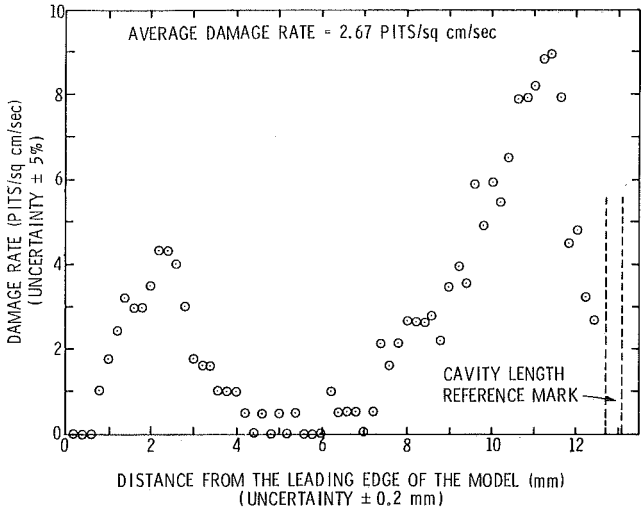

Fig. 4

damage along the model are apparent. The larger peak corresponds to the point of cavity closure on the model while the smaller peak is located near the leading edge of the cavity.

Damage near the leading edge of a cavity on a hemispherical nosed body has been recently reported by Sato, et al. [8]. They feel that the observed pitting may be a result of the collision of small metal particles contained in the test water with the model. For the case of a zero-caliber ogive this explanation for the damage is highly unlikely due to the nature of the flow field about the body. In addition, if the pits were a result of abrasion caused by contaminants in the test fluid, they would be irregular in shape, and elongated in the direction of the flow. However, the leading edge pits observed during this investigation were round, smooth, shallow indentations in the surface and had the same appearance as the pits at other points on the model surface. A high speed photographic study was undertaken to determine the characteristics of the cavitation in order to assist in explaining the leading edge pitting. Movies at a framing rate of 5000 frames per second proved adequate to observe the cavity behavior. A Redlake Hycam camera and an EG&G Type 501 strobe unit were used for all sequences.

Upon examination of the movies it was found that the cavity would periodically break off from the model. Upon closer examination, it was revealed that the cavity cycling was due to a reentrant jet striking the leading edge of the cavity and thereby causing the cavity to break up. When striking the leading edge of the cavity the reentrant jet could cause a substantial short-term pressure rise. This pressure rise in turn would initiate the collapse of any cavitation bubbles in this area and cause damage.

Examination of the films for a range of test conditions showed that cycling of the cavity occurred over a narrow range of cavity lengths. For very short cavities there is no well defined cavity and the bubbles grow and collapse in the free stream. For longer cavity lengths the reentrant jet lacks the momentum to reach the leading edge. Between these two extremes there is a regular cycling of the cavity. For the short and long cavity lengths where no cycling occurred there was no pitting near the leading edge of the test models. Nearly all models tested in the cavity cycling regime had leading edge damage. This evidence further supports the conclusion that the reentrant jet behavior is responsible for the observed pitting.

Upon examination of the movie segments it was observed that the frequency of the cavity cycling was a function of the flow conditions. Figure 5 is a plot of the Strouhal number, S,

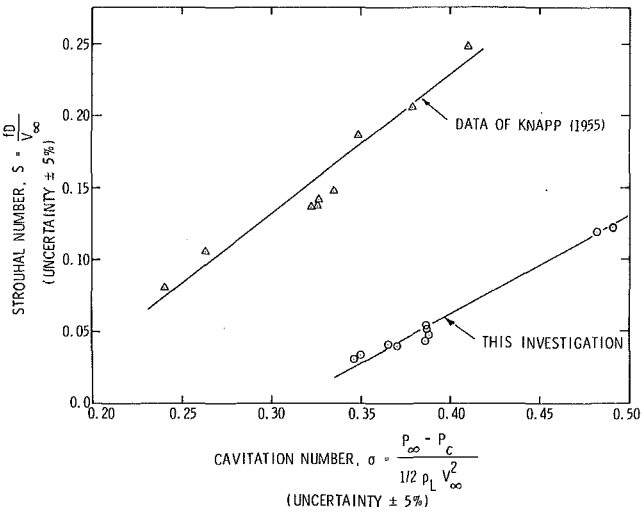

Fig. 5

as a function of cavitation number, σ. The Strouhal number is defined as

$$S = \frac{fD}{V_\infty}, \tag{15}$$

where f is the frequency of the cavity oscillation, D is the model diameter, and V_∞ is the free stream velocity. It can be seen that the Strouhal number increases with cavitation number. The data of Knapp [1] for a number of hemispherical nosed bodies is plotted on the same figure. It is noted that the magnitude of the Strouhal number of Knapp's stucy of the hemispherical nose is significantly greater than recorded for the zero-caliber ogive. The same general trend in the data was found for both investigations, i.e., S increases with σ.

The Importance of the Incubation Zone for Cavitation Damage Testing

Two aspects of a study of cavitation damage in the incubation zone were discussed, namely an energy approach to scaling of cavitation damage and cavitation damage observations near the leading edge of a zero-caliber ogive.

A very important aspect of this study was that the damage, in the form of individual pits, had a one-to-one correspondence with the cavitation bubble collapse. Thus by observing the damage an estimation of the total cavitation bubble collapse energy and the change of this energy with velocity can be found. This investigation is not attempting to predict the damage in the form of weight loss on a prototype but only to measure some scale effects on the hydrodynamics of the problem. Extension of these results to weight loss on different materials is a separate and difficult problem since, as previously stated, the weight loss can be due to a number of causes. To support the rationale for conducting the investigation in the incubation zone, the information in Figure 6 is presented. Cavitation damage data for four investigations are shown in this figure. In all cases, the tests were conducted in the incubation zone where the damage was assessed by measuring the pitting on an aluminum body. However, the size and/or flow geometry were different for each investigation. The data were corrected only for air content according to a hyperbolic relationship, i.e. if the air content is

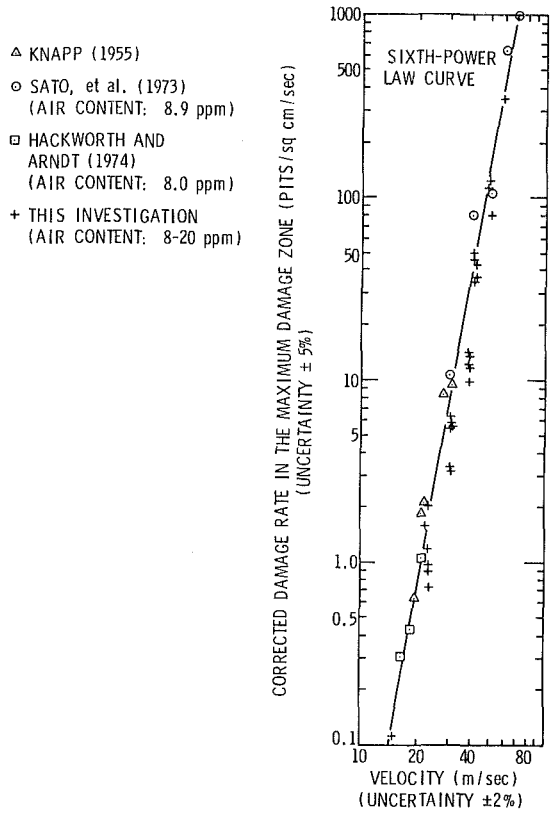

Fig. 6

doubled the damage rate will decrease by a factor of two, which was developed as another phase of this investigation [2] and [3]. By correcting the data to an air content of 8.9 ppm the data for all investigations over a 10,000 to 1 range in damage rates shows remarkable agreement. This result indicates that further emphasis should be placed on investigations of cavitation damage in the incubation zone.

Acknowledgments

The investigation was conducted at the Garfield Thomas Water Tunnel of the Applied Research Laboratory at The Pennsylvania State University under the sponsorship of E/F Research Project 6114. The authors wish to acknowledge the helpful suggestions of M. T. Pigott, who was the monitor of this grant for the sponsor.

References

1 Knapp, R. T., "Recent Investigations of Cavitation and Cavitation Damage," *Trans. ASME,* Vol. 77, 1955, pp. 1045-1054.

2 Stinebring, D. R., "Scaling of Cavitation Damage," M.S. thesis, The Pennsylvania State University, Aug. 1976.

3 Stinebring, D. R., Arndt, R. E. A., and Holl, J. W., "Scaling of Cavitation Damage," *J. of Hydronautics,* Vol. 11, No. 3, July 1977, pp. 67-73.

4 Kato, H., "A Consideration of Scaling Laws of Cavitation Erosion," International Shipbuilding Progress, Vol. 22, Sept. 1975, pp. 305-327.

5 Hammitt, F. G., "Observation on Cavitation Damage in a Flowing System," ASME *Journal of Basic Eng.,* Sept. 1963, pp. 347-367.

6 Thiruvengadam, A., "The Concept of Erosion Strength," Hydronautics, Inc., Tech. Report, pp. 233-239, Dec. 1965.

7 Tabor, D., *The Hardness of Metals,* Oxford, 1951, pp. 115-140.

8 Sato, R., Kato, H., and Tamiya, S., "Study on Cavitation Erosion," *J. Soc. Nav. Archit.,* Japan, Nov. 1973 (in Japanese), pp. 43-63.

Y. Yoshinaga
Mechanical Engineering Research Laboratory, Hitachi, Ltd., Tsuchiura, 300 Japan

I. Gyobu
Tsuchiura Works, Hitachi, Ltd., Tsuchiura, 300 Japan

H. Mishina

F. Koseki

H. Nishida

Mechanical Engineering Research Laboratory, Hitachi, Ltd., Tsuchiura, 300 Japan

Aerodynamic Performance of a Centrifugal Compressor With Vaned Diffusers

An experimental investigation to improve the stage efficiency through the use of vaned diffusers is presented. Sixteen different vaned diffusers were tested on a model compressor rig. The results showed that the pressure recovery of the vaned diffuser increased up to the critical diffusion ratio, which was shown to be approximately 0.5. The measured pressure distribution around vanes of the well-designed diffusers which had the fair diffusion ratios, were found to agree well with the potential flow solutions. Finally, the importance of the diffuser inlet configuration to the improvement of the stage efficiency is discussed.

Introduction

Improvement in the performance of large capacity centrifugal compressors has been required, in order to increase the efficiency of industrial plants. The authors have made a series of studies on the performance of centrifugal compressors with the pressure ratios from 1.5 to 2.0 for several years [1].

Currently impeller efficiencies on the order of 90 percent are attainable in modern compressor designs. On the other hand, the design method of the diffuser section has not been well established, and the improvement of diffuser performance is necessary in order to increase the compressor stage efficiency.

The present work is aimed at improving the efficiency of a centrifugal compressor stage through the use of vaned diffusers.

There are two existing methods used to design vaned diffusers: (1) design on the basis of an equivalent channel flow, (2) design by application of cascade technology.

In the former, the chief aerodynamic principle is to limit the rate of area change of a two-dimensional straight channel diffuser having some prescribed distribution of divergence angle. There have been many extensive experimental investigations of two-dimensional diffusers [2,3,4], and clear accounts have been given on the effects of inlet boundary layer thickness, inlet Mach number, and inlet flow distortion. Only a few applications of those data, however, have been made to the vaned diffuser design. It is difficult for designers to predict precisely the performance of a vaned diffuser using the experimental results on two-dimensional diffusers.

Although the latter has been considered to be rational for vaned diffuser design, only a few works have been published concerning this subjects [4,5,6]. At present, it is not possible to apply conventional cascade data directly to the vaned diffusers whose cascades have small aspect ratios and large area ratios. The analytical procedure, such as incompressible potential flow analyses, alone can be used in vaned diffuser design only to a limited extent.

The experimental investigations were made with radial aerofoil cascades on a model compressor rig in order to improve diffuser efficiency as well as to obtain basic design data. Principal dimensions of the radial cascades, such as radius ratio, number of vanes, and vane camber, were varied.

The experimental results showed that a critical diffusion ratio was approximately 0.5, and the diffuser pressure recovery was reduced below this range.

The pressure recoveries of vaned diffusers were compared with those of two-dimensional channel diffusers, and their respective maxima merely were found to be obtained at the same divergence angle.

Pressure distributions around diffuser vanes were measured, and compared with the results of potential flow analyses. Both were shown to be in a qualitative agreement to each other in the case of well-designed diffusers.

Other experiments were made with the intention of investigating the effect of diffuser inlet configuration. The results seemed to show the importance of its effect on the performance of a centrifugal compressor stage.

Experimental Procedure

Experimental Apparatus. The experiments were made with a centrifugal compressor test system, consisting of a single stage compressor, a torque meter, a d-c motor with built-in gears, an air cooler, and flow piping. A closed loop of air piping made use of varying suction pressure and temperature to control the inlet conditions of the compressor.

Contributed by the Fluids Engineering Division for publication in the JOURNAL OF FLUIDS ENGINEERING. Manuscript received by the Fluids Engineering Division, April 16, 1979.

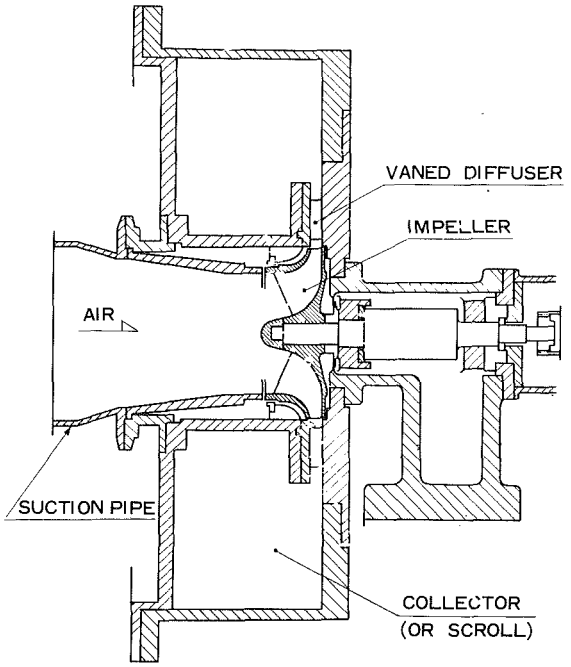

Fig. 1 Sectional view of a model compressor rig

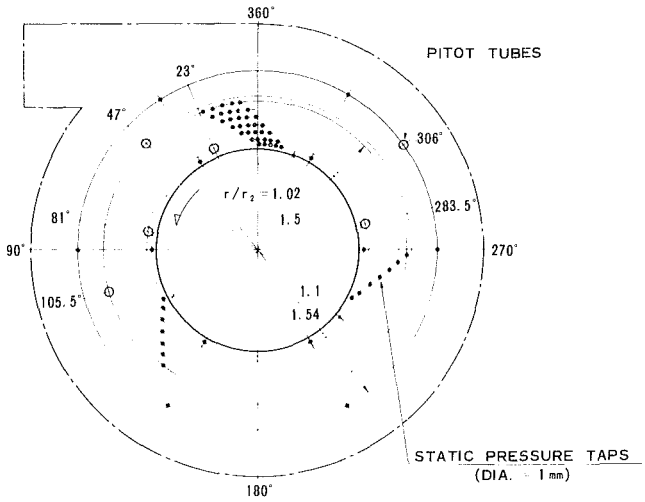

Fig. 2 Locations of pitot tube traversing points and static pressure taps

Figure 1 shows a cross-sectional view of the centrifugal compressor. Two types of high specific speed impellers were used in this experiment, and both of them had the same diameter (250 mm), the same exit angle (50 deg), and the same number of blades (18). The specific speed of them were 0.36. Only their tip circumferential speeds were slightly different, one was 307 m/s the other was 300 m/s.

Diffusers and a collector (or a scroll) were set down stream of an impeller.

A vaneless diffuser as reference and sixteen different vaned diffusers were tested on this test rig. The compressor casing was covered with insulating materials to eliminate the heat leakage effect on the total temperature measurement.

Measuring Method. The total pressure and the total temperature at the suction and discharge sections, were measured with Kiel type probes and total temperature probes consisting of copper-constantan thermocouples.

The performance of the compressor stage was evaluated on the basis of the total-to-total rating. The flow rate was controlled with a valve at the discharge side and was measured with an orifice type flow meter in the suction pipe.

The total pressure, velocity and flow angle were measured at three circumferential positions of the vaneless diffuser with use of Cobra type yaw probes. Figure 2 shows locations of the probe traversing point and static pressure taps.

The pressure recovery factor of the vaned diffuser was

Nomenclature

A = cross-sectional area
A_B = blockaged area, $1 - A_E$
A_E = effective area, $\int_A \frac{c}{c_{\max}} dA$
B = blockage factor, A_B/A
B_f = impeller blockage factor, $1 - \bar{c}_m/\bar{c}_{mm}$
b = height of diffuser vane
C_p = static pressure recovery coefficient, $\frac{P_{s4} - P_{s3}}{P_{t3} - P_{s3}}$
C_{pi} = ideal pressure recovery coefficient
c = absolute velocity
c_m = radial fraction of absolute velocity
$\bar{c}_m$ = area-averaged radial velocity, $\frac{\int_A \rho c_m dA}{\rho A}$
$\bar{c}_{mm}$ = mass-averaged radial velocity, $\frac{\int_A \rho c_m^2 dA}{\int_A \rho c_m dA}$
D = diameter
i = incidence angle, $\alpha_3 - \beta_3$
L = chord length
n_s = specific speed, $\phi 1/2/\psi 3/4$
p = pressure
Q = flow rate
r = radius
u = peripheral velocity
W = equivalent width of vaned diffuser, $2\pi r \sin\beta/Z$
X = distance from leading edge along chord
Z = number of vanes
α = flow angle measured from circumferential direction
β = vane angle measured from circumferential direction
δ = deviation angle
δ^* = boundary layer displacement thickness
ϵ = effectivenss of diffuser, C_p/C_{pi}
2θ = diffuser divergence angle, $2\tan^{-1}\left(\frac{W_4 - W_3}{2L}\right)$
σ = chord/pitch ratio of equivalent rectangular cascade, the pitch is defined at the inlet radius
ϕ = flow coefficient, $4Q/\pi D_2{}^2 u_2$
ψ = isentropic head coefficient relative to $u_2{}^2/2g$

Subscript

0 = suction
1 = impeller inlet
2 = impeller exit
3 = diffuser vane inlet
4 = diffuser vane exit
des = design point
m = meridional
t = total state
s = static state
max = refers to maximum value

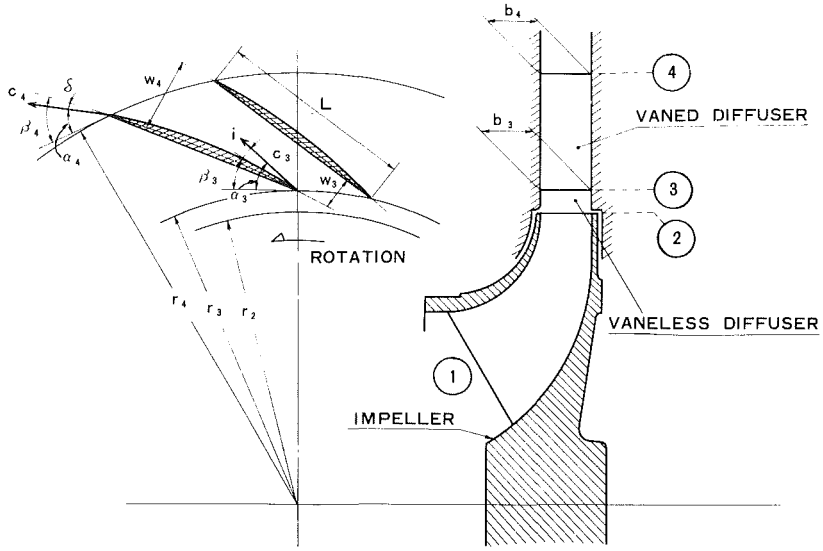

Fig. 3 Notation of a vaned diffuser

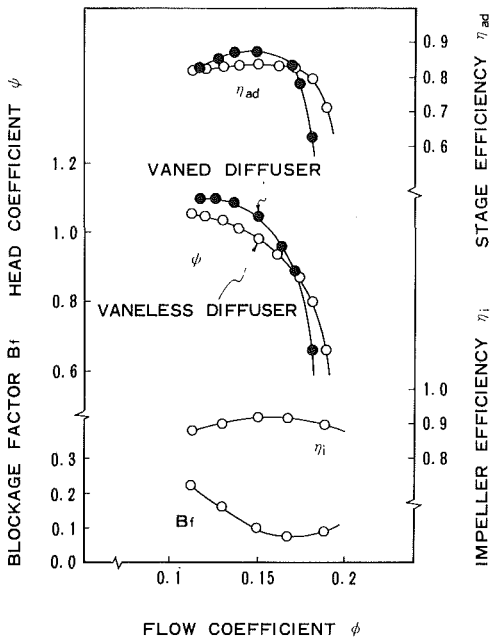

Fig. 4 Performance characteristics of vaneless and vaned diffuser

data	uncertainty
ϕ	±0.01
ψ	±0.002
B_f	±0.025
η_{ad}	±0.004
η_i	±0.01

a least-square averaging of the data was used

rated on the basis of the reference dynamic pressure measured at the impeller exit on the vaneless diffuser stage.

Vaned Diffusers. Figure 3 shows the notation of a vaned diffuser. Table 1 shows principal specifications of the vaned diffusers for this investigation in the terms of a cascade and an equivalent two-dimensional channel diffuser.

The radius ratios of the short vaneless diffusers located between the impeller exit and the vaned diffuser inlet, were all 1.1 except VD-10 and VD-11 diffusers which have the ratios of 1.06. The height ratios of diffusers and impeller, b_3/b_2 and b_4/b_2, were equal to 1.0. Their incidence angles of vanes were all −1 deg except VD-2 (+1 deg), VD-3 (−3 deg), and VD-12 (0 deg).

The same basic thickness form, NACA66-006, was used in the design of vane shapes.

The diffusers from VD-1 to VD-11 inclusive were designed for the impeller which had the 307 m/s tip circumferential speed, and the diffusers from VD-12 to VD-16 inclusive were designed for the 300 m/s impeller. The reference vaneless diffuser had a diameter equal to 1.5 times impeller tip diameter, and constant width along the radial direction.

Experimental Results and Discussion

Flow Conditions at the Impeller. Figure 4 shows an example of aerodynamic performance of a vaneless diffuser stage and a vaned diffuser stage. The vaned diffuser stage which had the same radius ratio of the vaneless diffuser stage, showed about 4 percent higher efficiency than the vaneless diffuser stage. This was due to the higher pressure recovery of the vaned diffuser.

The impeller efficiency which was measured with the vaneless diffuser stage is also shown in Fig. 4. The blockage factor B_f shown in Fig. 4 indicates the rate of distortion of impeller exit flow profile.

The details of the impeller exit flow which were measured at the radius of $r/r_2 = 1.1$ are shown in Fig. 5. The total pressure was higher at the hub side than at shroud side, and the absolute velocity distribution across the impeller exit width was similar to the total pressure distribution. The flow angle at the shroud was extremely small as shown in Fig. 5(*c*), in other words, the impeller exit flow was directed towards a circumferential direction at the shroud side.

These figures clearly show that the flow at the impeller exit is extremely distorted. The blockage factor B, at the diffuser inlet is approximately 15 percent at the design flow rate, based on calculations commonly used in the two-dimensional diffuser investigations. This distortion can not be avoided easily and this fact must be kept in mind to improve the performance of diffusers for centrifugal compressors.

Diffusion Ratio and Pressure Recovery. It is desirable in the actual centrifugal compressor design to attain higher pressure recovery, with small diffuser radius, and with a small number of vanes. Generally speaking, however, there is an optimum chord/pitch ratio of a cascade for a given pressure recovery. In order to attain high pressure recovery, a high chord/pitch ratio cascade is usually required.

Table 1 Vaned diffuser specifications

	r_4/r_3	σ	b_3/L	2θ (deg)	W_4/W_3	L/W_3	b_3/W_3	c_4/c_3
VD-1	1.35	2.39	0.25	5.12	1.54	6.05	1.51	0.64
2	1.35	2.30	0.26	8.08	1.77	5.43	1.42	0.58
3	1.35	2.26	0.26	8.52	1.92	6.15	1.62	0.54
4	1.35	1.53	0.27	13.03	1.89	3.88	1.03	0.53
5	1.35	1.89	0.27	10.56	1.89	4.79	1.27	0.53
6	1.35	2.26	0.27	8.88	1.89	5.70	1.51	0.53
7	1.35	2.16	0.28	11.13	2.07	5.48	1.51	0.48
8	1.35	1.70	0.30	15.48	2.17	4.31	1.27	0.44
9	1.35	2.02	0.30	11.04	2.17	5.14	1.51	0.44
10	1.42	2.39	0.26	9.74	2.18	6.14	1.42	0.45
11	1.42	1.95	0.26	13.09	2.05	5.16	1.32	0.43
12	1.35	2.14	0.28	8.84	1.79	5.12	1.45	0.58
13	1.45	2.75	0.21	7.29	1.89	7.03	1.50	0.53
14	1.45	2.50	0.23	10.43	2.17	6.43	1.50	0.46
15	1.60	3.31	0.17	7.69	2.19	8.88	1.50	0.45
16	1.60	3.12	0.18	9.51	2.40	8.43	1.50	0.41

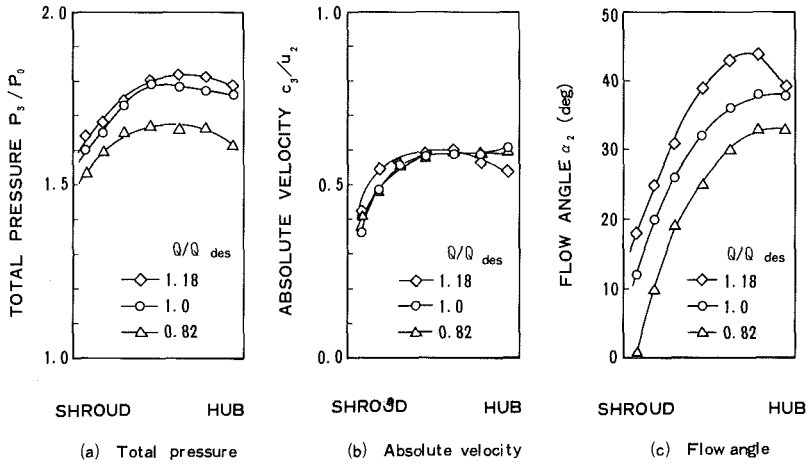

Fig. 5 Flow distribution at impeller exit

data	uncertainty
P_3/P_0	±0.001
C_3/u_2	±0.04
α_2	±2.0 deg
Q/Q_{des}	±0.01

a least-square averaging of the data was used

(a) Total pressure
(b) Absolute velocity
(c) Flow angle

In the case of a vaned diffuser, the method to increase the chord/pitch ratio is as follows:

(1) increase the number of vanes as the radius ratio is kept constant,

(2) increase the radius ratio as the number of vanes is kept constant.

It is undesirable to increase the number of vanes because it usually moves the surge limit of a centrifugal compressor to a higher flow rate. In the present investigation, therefore, the maximum number of vanes was limited to 27, and the radius ratios of the vaned diffusers were varied in the range between 1.35 and 1.60. In other words, the chord/pitch ratios of the vaned diffusers were varied between 1.5 and 3.3, as shown in Table 1.

In the following, the pressure recovery factor C_p, and the effectiveness ϵ, at the design flow rate, were used to evaluate the performance of a vaned diffuser.

Figure 6 shows the pressure recovery of the vaned diffusers with different diffusion ratios. The curve of C_{pi} shows the ideal pressure recovery for an inlet Mach number equal to 0.5. The curve of C_p shown with a broken line indicates the pressure recovery assuming that the effectiveness of the vaned diffuser is given by the following equation.

$$\epsilon = \frac{C_p}{C_{pi}} = \left(\frac{c_4}{c_3}\right)^{0.15} \tag{1}$$

The pressure recovery of the well-designed diffusers which had the diffusion ratios numerically greater than or equal to 0.5, showed a good agreement with the predicted values by equation (1). On the contrary, all the diffusers which were designed to attain the greater diffusion of the flow showed poor pressure recoveries compared with the predicted values by equation (1).

The above results seem to indicate that the critical diffusion ratio is around 0.5, on the condition that the radius ratio is smaller than 1.6 and the maximum number of vanes is 27.

Comparison With Two-Dimensional Channel Diffuser. It is convenient to apply the results for two-dimensional diffusers to the design of vaned diffusers for centrifugal compressors.

As mentioned previously, precise performance maps of

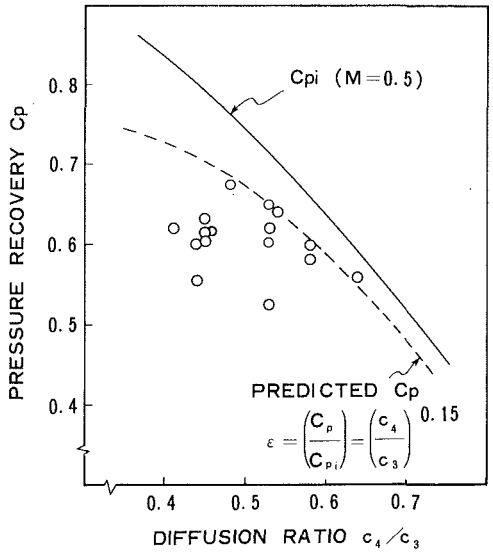

Fig. 6 Pressure recovery of vaned diffusers versus diffusion ratio

data	uncertainty
Cp	±0.03

a least-square averaging of the data was used

The uncertainty of C_p in the following figures is same as shown above.

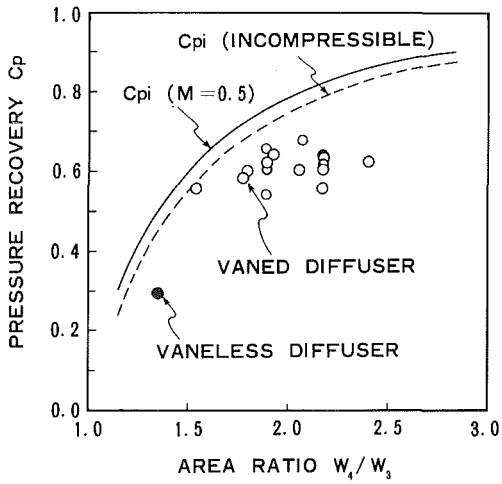

Fig. 7 Pressure recovery of vaneless and vaned diffusers versus area-ratio

two-dimensional diffusers have been given as a funcion of the important variables. They would give a convenient method for determining the principal dimensions of vaned diffusers, and predicting the performance of a vaned diffuser at the design flow rate, if more information on the correlation between both performances were aquired.

Figure 7 shows the correlation of the equivalent area ratio vs. the pressure recovery of the vaned diffusers. The curve with a broken line indicates an ideal pressure-recovery for incompressible flow, and it is given by equation (2):

$$C_{pi}\,(\text{incompressible}) = 1 - \left(\frac{W_3}{W_4}\right)^2 \qquad (2)$$

The curve with a solid line indicates an ideal pressure recovery for compressible flow for an inlet Mach number equal to 0.5.

The pressure recovery of the vaneless diffuser is also shown in Fig. 7. As the area ratios of vaned diffusers were larger than that of the vaneless diffuser, pressure recoveries of the

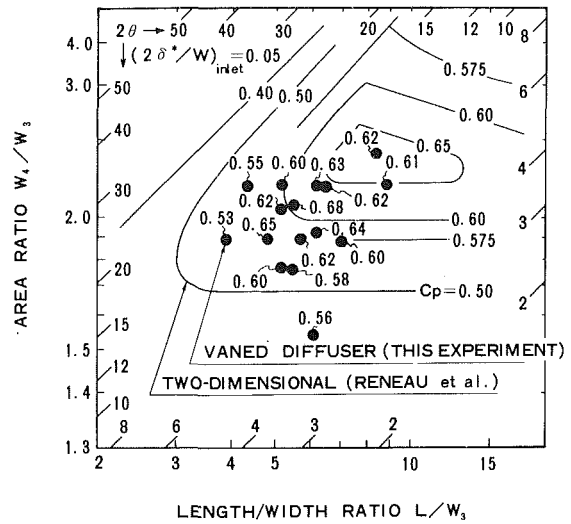

Fig. 8 Comparison of pressure recovery between vaned diffusers and two-dimensional diffusers

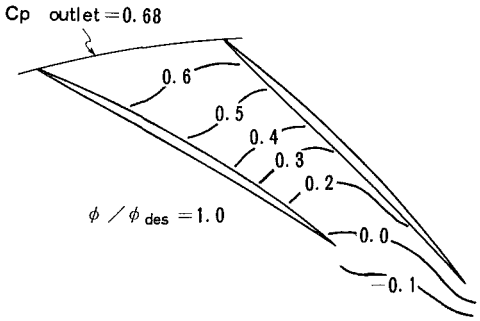

Fig. 9 Pressure distribution of VD-7 vaned diffuser

vaned diffusers were higher than that of vaneless diffuser. As the area ratio of the vaned diffuser became greater than 2.0, the effectiveness and the pressure recovery of the vaned diffuser decreased.

Figure 8 shows the results of the vaned diffuser pressure recovery compared with the data on the two-dimensional diffuser, for incompressible flow, with the inlet blockage, $2\delta^*/W=0.05$ (by Reneau, et al. [2]). As the present investigation was made at the diffuser inlet Mach number 0.5, the comparison should be made with the results which considered the inlet Mach number effect, e.g. by Runstadler and Dean [3]. Their experiments were made, however, in the range of larger length/width ratio than in the present work. The direct comparison of those data may not be appropriate.

Considering the difference of the inlet condition, such as inlet Mach number and inlet blockage, the comparison shown in Fig. 8 is not complete. It should be noted that the following discussion is intended to convey a qualitative interpretation only.

In Fig. 8, the equivalent dimensions of the vaned diffusers were plotted with symbols (●). Numbers next for the plotted points indicate the pressure recovery of the vaned diffuser at the design flow rate.

The following may be concluded from Fig. 8:

(1) The peak pressure recovery of the vaned diffuser was attained when the length/width ratio was around 5.5 and the area ratio was around 2.

(2) The area ratio and the length/width ratio which gave the peak pressure recovery were smaller than those of the two-dimensional diffuser.

(3) In spite of the difference of inlet flow conditions and

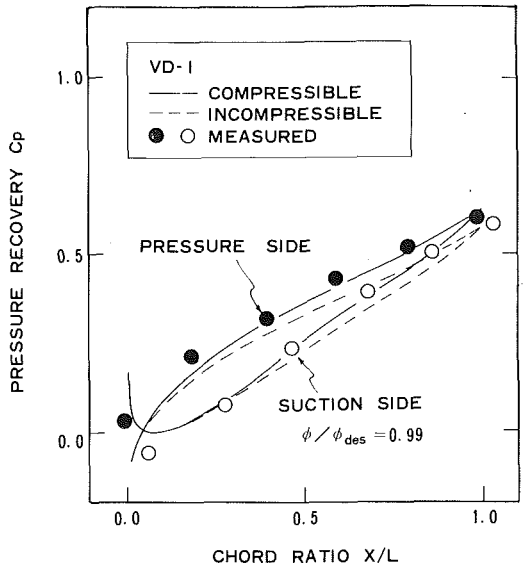

Fig. 10(a) VD-1 ($c_4/c_3 = 0.64$)

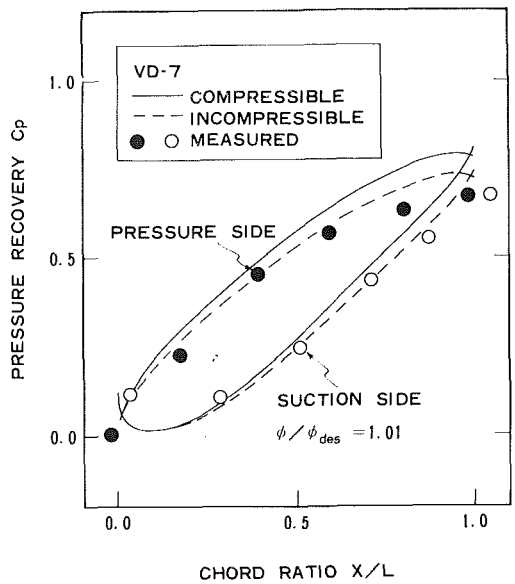

Fig. 10(b) VD-7 ($c_4/c_3 = 0.48$)

Fig. 10 Comparison of pressure distribution around a vane between measured data and potential flow solutions (in the case of diffusers designed for fair pressure recovery)

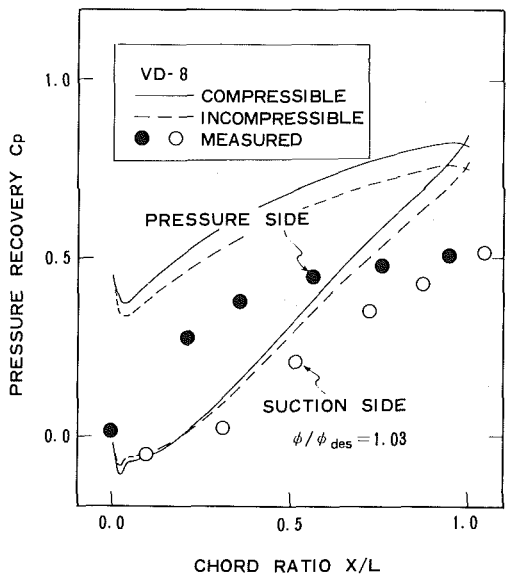

Fig. 11(a) VD-8 ($c_4/c_3 = 0.44$)

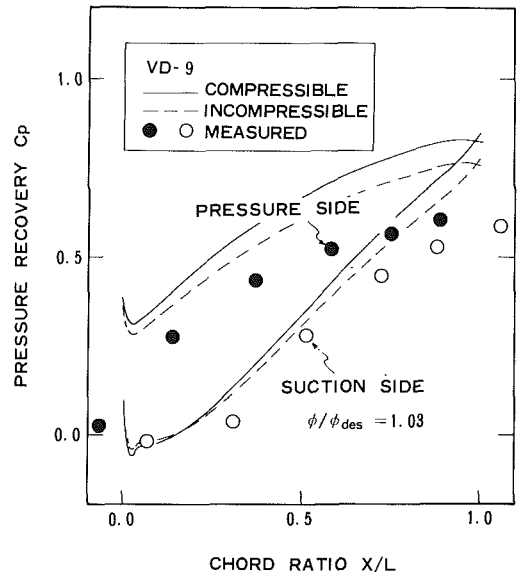

Fig. 11(b) VD-9 ($c_4/c_3 = 0.44$)

Fig. 11 Comparison of pressure distribution around a vane between measured data and potential flow solutions (in the case of diffusers designed for higher pressure recovery)

their configurations, the optimum equivalent divergence angle was approximately 10 deg similar to that of the two-dimensional diffuser.

Although the comparison discussed above could not cover the scope of both characteristics, the performance map of the two-dimensional diffuser seems to be useful for determining the principal dimensions of a vaned diffuser and for predicting roughly the pressure recovery.

Pressure Distribution Around a Vane. Figure 9 shows a pressure distribution between vanes which was measured with static pressure taps on the wall. This pressure distribution was transcribed to a pressure distribution around a vane, assuming that the vane-to-vane flow distribution shows the same pattern in each radial plane.

The experimental result was compared with a potential flow solution. In order to analyze the potential flow around a vane, a conformal transformation to a rectangular cascade was performed, and the Schlichting's method [8] was applied.

Figure 10(*a, b*) shows the comparison between the experimental results and the potential flow solutions in the case of well-designed diffusers (VD-1 and VD-7). The curves with

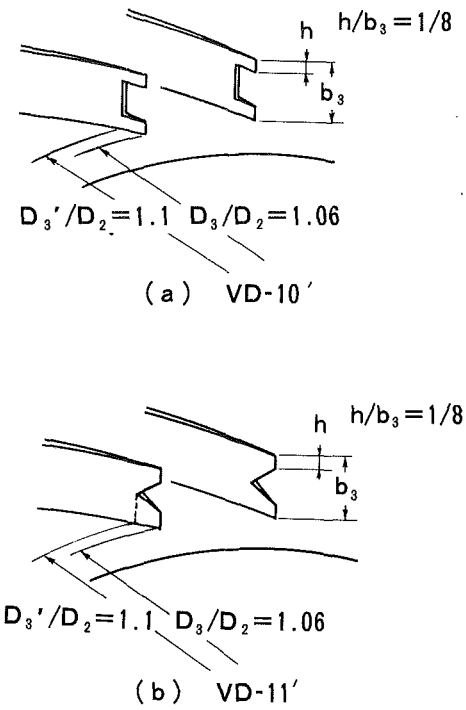

Fig. 12 Leading edge shapes of vanes VD-10′ and VD-11′

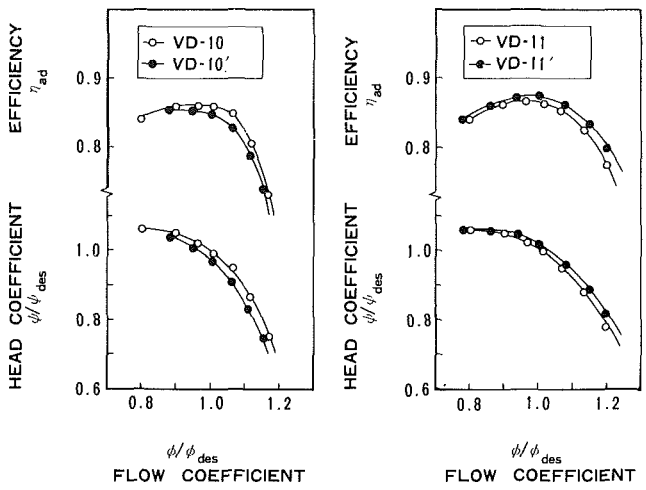

Fig. 13 Effect of leading edge shapes of vanes on the stage efficiency

data	uncertainty
ϕ/ϕ_{des}	±0.01
η_{ad}	±0.004
ψ/ψ_{des}	±0.002

a least-square averaging of the data was used

(a) VD-10′
(b) VD-11′

broken lines indicate the solution for incompressible flow, and the curves with solid lines indicate the solution for compressible flow corrected by the Karman-Tsien's method. Experimental results agreed well with the calculations in this case.

Figure 11(*a,b*) shows the similar comparison in the case of the diffusers (VD-8 and VD-9) which were designed to attain the greater diffusion of the flow. VD-8 and VD-9 had the same high camber of 20 degrees, and their diffusion ratios were 0.44. This value was smaller than the critical one as shown in Fig. 6.

In the case of VD-8 and VD-9, the experimental results were far from the potential flow situations. This difference was more intense in VD-8 than in VD-9. This seems to be due to the vane loading difference, i.e., the vane loading in VD-8 was greater than in VD-9. In these diffusers the effect of wall boundary layer was extremely high, and the separation of the boundary layer seemed to have occured.

These results show that the Schlichting's potential flow analysis is useful to calculate the flow field in the radial cascade consisting of thin aerofoil vanes as in this experiment, and the limit of the diffusion ratio shown in Fig. 6 is supposed to be due to the boundary layer separation near the diffuser inlet.

The Effect of Leading Edge Shapes of Vanes. As the impeller exit flow is distorted extremely as shown in Fig. 5, it is difficult to match a vane inlet angle with a flow angle across the vane height. Several reports (e.g. [9]) pointed out previously that the knowledge about the complicated flow at the impeller exit would be necessary in order to improve the performance of centrifugal compressors.

An approach to investigate the effect of the leading edge shapes of vanes on the diffuser performance is described below. For this purpose, the leading edges of VD-10 and VD-11 were cut out to the desired configurations as shown in Fig. 12(a,b).

Figure 13(*a,b*) shows the effect of the leading edge shapes on the stage efficiencies. The stage with VD-10′ showed the lower efficiency than the original stage with VD-10. On the other hand, the stage with VD-11′ showed the stage efficiency rise of more than 0.5 percent compared with its original stage with VD-11 at the design point.

It seems evident that the leading edge shapes of vanes have considerable influences on the performance of diffusers and therefore of their centrifugal compressor stages.

Conclusion

Experiments were made with sixteen different vaned diffusers on a model compressor rig in order to improve the efficiency of a centrifugal compressor stage.

(1) Pressure recovery of vaned diffusers was increased until their design diffusion ratios reached a critical value. The critical diffusion ratio was approximately 0.5, on the basis of present investigation, where the maximum number of vanes was 27, and the radius ratios of vaned diffusers were between 1.35 to 1.60.

(2) Performance maps of the pressure recovery which have been used commonly in two-dimensional channel diffusers, are found to be convenient to determine the principal dimensions of vaned diffusers.

(3) Potential flow analysis is useful for estimating the flow field around the diffuser vanes. The experimental results on the well-designed diffusers were found to be in a qualitative agreement with potential flow solutions.

(4) The leading edge shapes of vanes have considerable influence on the performance of the diffusers and the attendant centrifugal compressors.

Acknowledgments

The authors wish to express their appreciation to Dr. K. Morita, Dr. S. Ueda, Mr. K. Naya of the Mechanical Engineering Research Laboratory, and Mr. E. Yokoyama, and Mr. Y. Kanekiyo of Tsuchiura Works for their suggestions and helpful discussions at various stages of this investigations.

References

1 Mishina, H., and Gyobu, I., "Performance Investigation of Large Capacity Centrifugal Compressors," ASME Paper No. 78-GT-3, 1978.

2 Reneau, L.R., Johnston, J.P., and Kline, S.J., "Performance and Design of Straight, Two-Dimensional Diffusers," ASME *Journal of Basic Engineering,* Vol. 89, No.1, Mar. 1967.

3 Runstadler, P.W. Jr., and Dean, R.C. Jr., "Straight Channel Diffuser Performance at High Inlet Mach Numbers, ASME *Journal of Basic Engineering,* Vol. 91, No. 3, Sept. 1969.

4 Wolf, S., and Johnston, J.P., "Effects of Non-uniform Inlet Velocity Profiles on Flow Regimes and Performance in Two-Dimensional Diffusers," ASME *Journal of Basic Engineering,* Vol. 91, No. 3, Sept. 1969.

5 Faulders, C.R., "Aerodynamic Design of Vaned Diffusers for Centrifugal Compressors," ASME Paper No. 56-A-213, July 1956.

6 Smith, V.J., "A Review of the Design Practice and Technology of Radial Compressor Diffusers," ASME Paper No. 70-GT-116, May 1970.

7 Pampreen, R.C., "The Use of Cascade Technology in Centrifugal Compressor Vaned Diffuser Design," ASME *Journal of Engineering for Power,* Vol. 94, No. 3, July 1972.

8 Schlichting, H., "Berechnung der reibungslosen inkompressiblen Strömung für ein vorgegebenes ebenes Shaufelgitter," VDI-Forschungsheft 447, Ausgabe B, Band 21, 1955.

9 Dean, R.C. Jr., "The Fluid Dynamic Design of Advanced Centrifugal Compressors," Creare TN-185, July 1974.

Leading Edge Separation From a Blunt Plate at Low Reynolds Number

J. C. Lane

R. I. Loehrke

Mechanical Engineering Department,
Colorado State University,
Fort Collins, Colo. 80523

The flow over a blunt plate aligned parallel to the stream was visualized using dye tracers. A leading edge separation bubble was observed to form at a Reynolds number based on plate thickness of 100. The steady, laminar separation bubble on a long plate, $L/t \geq 8$, grows in size with increasing Reynolds number reaching a maximum streamwise length at $Re_t = 325$. The separated shear layer becomes unsteady and the bubble shrinks in size with further increases in Reynolds number. The leading and trailing edge separation zones on short plates, $L/t \leq 4$, may combine to form a large recirculation pocket.

Introduction

The flat plate is a prototype for many heat transfer surfaces. In particular, some heat exchanger surfaces may consist, in part, of an array of plate segments aligned parallel to the flow. As a first step toward understanding the complex fluid flow and heat transfer processes occuring in heat exchanger cores it is helpful to identify flow modules [1] or flow structures which may affect the performance of this type of equipment.

One such flow module which can be important is the separation bubble which may form at the leading edge of a blunt plate as shown schematically in Fig. 1. Ota and his coworkers [2,3] have observed the character of the leading edge flow at high Reynolds number. They report that the turbulent separated layer reattaches to the plate at a distance of four times the plate thickness from the leading edge and that this reattachment location is independent of Reynolds number over the range $2720 \leq Re_t \leq 17900$.

The range of interest in many heat exchanger applications extends to much lower Reynolds number. Ghia and Davis [4] have predicted that the size of the laminar bubble which will form at low Reynolds number should depend on Reynolds number and that it may extend for well over twenty plate thicknesses downstream from the leading edge. The experiments reported here were performed to provide a direct check of these predictions and to fill the gap between laminar theory and turbulent measurements.

The Experiment

The flow over plates placed in a water channel was visualized using dye injection. The water channel is an open, Plexiglas flume 2.5 m long with a 7.6 cm square cross section. The test plates were mounted vertically in the channel, positioned and supported on the bottom by slots milled into the floor of the channel. A top view of the test section and the geometric nomenclature are shown in Fig. 1.

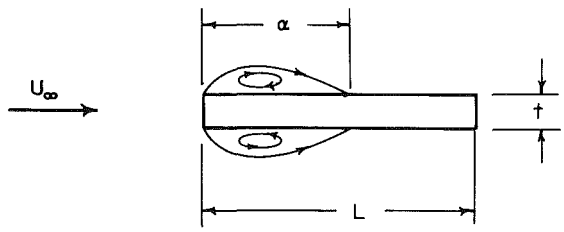

Fig. 1 Test section schematic

Water enters the flume through a bed of marbles and then passes through a series of honeycomb before arriving at the test section. The mean velocity in the test section is essentially uniform in the horizontal plane over the central 85 percent of the test section and vertically from the free surface down to about 95 percent of the channel depth. The turbulence intensity in the test section is on the order of 0.1 percent. The mean velocity for these experiments was determined by measuring the time of flight of a dye tracer down the center of the empty test section over a prescribed distance.

The leading and trailing edges of the Plexiglas plates used in the experiments were milled to form flat faces perpendicular to the sides. The plates extend 6 cm up from the floor of the water channel so that the upper surface of the plates is just below the surface of the water. Plates of different thickness and length were used to cover a range of L/t and Reynolds number. A summary of the plate geometries is contained in Table 1.

The principal quantitative measurement obtained was the downstream extent of the recirculating region along the side of a plate. This position was determined by injecting a dye tracer (methyl blue or methyl orange solution) into the flow near the surface of the plate at mid-height in the channel through a hypodermic probe having an outside diameter of

Contributed by the Fluids Engineering Division for publication in the JOURNAL OF FLUIDS ENGINEERING. Manuscript received by the Fluids Engineering Division, March 15, 1979.

Table 1 Plate dimensions

L/t	t(mm)	L(mm)
2.0	6.35	12.7
4.0	6.35	25.4
8.0	6.35	50.0
10.0	6.35	63.5
16.0	1.59	25.4

0.75 mm. The probe was bent 90 degrees so that the aperture was 1.5 cm upstream from the vertical stem. As the point of dye injection was moved upstream from behind the plate a location would be reached at which some of the dye was carried upstream. The recirculation length α is defined as the maximum distance downstream from the leading edge of the plate at which any of the dye moved in an upstream direction along the side of the plate. In order to assess the influence of the dye probe on the flow a different technique was also used for some of the runs. Dye was introduced into the boundary layer through 0.5 mm diameter holes drilled in the side of the plate and spaced 1.5 mm apart in the mean flow direction. The results from the two techniques are in good agreement.

Results

The flow along the sides of all plates with $L/t \geq 8$ is quantitatively similar. Recirculation is first observed, as the channel velocity is increased from near zero, at a Reynolds number based on plate thickness of about 100. When first detectable this separation bubble begins at a point $t/4$ downstream from the leading edge and extends to a distance $\alpha = t/2$. As the Reynolds number is increased the bubble grows in both upstream and downstream extent. The leading edge of the bubble reaches the front of the plate at $Re_t = 125$ and no subsequent changes in its location are observed. The trailing edge continues to move downstream with increasing Reynolds number. Photographs of the dye marked flow along one side of the plate are shown in Fig. 2. At $Re_t = 260$, Fig. 2(a), the recirculating flow is steady and extends just beyond $\alpha/t = 4.0$. In these experiments a maximum, steady recirculation length of $\alpha/t = 6.5$ was obtained at $Re_t = 325$.

At higher Reynolds number the separated shear layer becomes unsteady as evidenced in Fig. 2(b). The reattachment point is no longer stationary and α may be correlated with the maximum downstream reattachment location. The dye for this photograph, as well as the previous one, was injected into the flow near the surface of the plate, travelled upstream to the leading edge and was then swept downstream. The dye probe was removed before the picture was taken.

The regular, two-dimensional rolls formed in the separated shear layer are transformed into a more three-dimensional, random structure as the Reynolds number is further increased. For the flow shown in Fig. 2c the residence time of dye introduced into the recirculating region was too small to permit probe removal prior to picture taking. Instead a dye streakline was formed far upstream of the plate. Slight waves in the streakline introduced at the dye injection point are deformed near the plate stagnation point to give an exaggerated impression of unsteadiness upstream of the plate. The increased momentum transfer associated with the unsteady flow causes the separation bubble to shrink. A plot of α/t versus Reynolds number for experiments on three different long plates is shown in Fig. 3. For Reynolds number

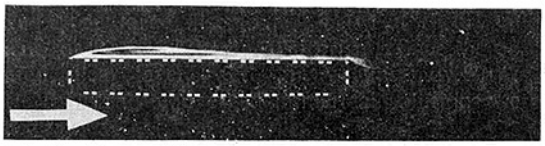

Fig. 2a $Re_t = 260.$

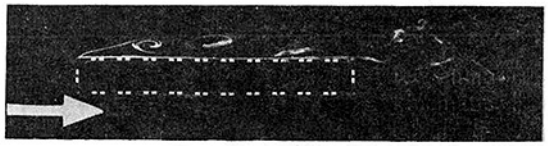

Fig. 2b $Re_t = 380.$

Fig. 2c $Re_t = 490$

Fig. 2 The separation bubble at the leading edge of a plate, $L/t = 8$.

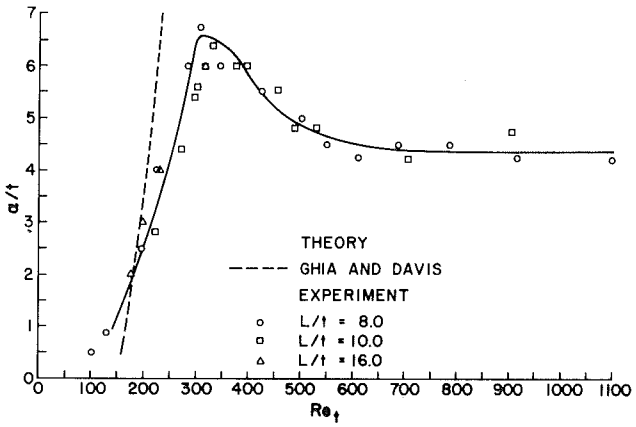

Fig. 3 Recirculation length for long plates

greater than 500 the recirculation length α/t changes very little and is in good agreement with values reported by Ota and Kon [2] and Ota and Itasaka [3] for the turbulent reattachment point at high Reynolds number. The maximum Reynolds number which could be obtained with the thin plate, $L/t = 16$, was limited by the maximum attainable channel velocity. The solid line in Fig. 3 is faired through the data and the broken line is interpolated from numerical solutions to the steady flow Navier-Stokes equation obtained by Ghia and Davis [4]. The agreement between experiment and theory is good at low Reynolds number. At high Reynolds number the theory predicts separation bubbles much larger than those observed. The large discrepancy between theory and experiment for $Re_t > 325$ is not surprising since the observed separated shear layers were always unsteady. It is also possible that truly converged numerical solutions were not obtained [5].

Nomenclature

L = plate length
Re_t = Reynolds number $U_\infty t/\nu$
t = plate thickness
U_∞ = freestream velocity
α = recirculation length
ν = kinematic viscosity

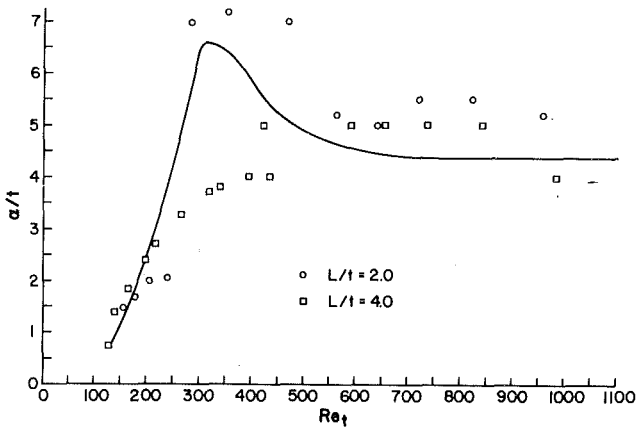

Fig. 4 Recirculation length for short plates

For the short plates, $L/t = 2$ and 4, the onset of leading edge separation mimics that of the long plates. The change in size of the bubble differs, however, as is shown in Fig. 4. The solid line through the long plate data (Fig. 3) is included in this figure for reference. The bubble on the short plates tends to be smaller and the reattachment point sticks to the trailing edge as the Reynolds number is increased. At a sufficiently high Reynolds number the forward and aft separated regions merge to form a pocket in which fluid from far downstream of the plate trailing edge may recirculate to the leading edge of the plate. The flow in the wake of the plates is unsteady for Reynolds number greater than approximately 100 and so is the recirculating flow after the merger of the separated regions.

Experimental Uncertainty

The uncertainty in the measurements which were made leads to the following estimates for uncertainty in the data. The possible Reynolds number error, which is influenced chiefly by the resolution of the velocity measurement, ranges from 5 percent at low Reynolds number to 15% at the highest Reynolds number. The uncertainty in determining the extent of the backflow region ranges from 1 mm for a steady separation bubble to 2.5 mm for an unsteady separation pocket.

The Plexiglas plates which were used in these experiments were cut to length on a milling machine. Faint tool marks are visible on the leading surfaces of some of the plates while others appear smooth to the naked eye. The side surfaces on all the plates are polished. The corners are sharp to the touch. The corner radius, which varies slightly from plate to plate, is on the order of 1 percent of the plate thickness. Neither the morphology of the flow nor the length of the recirculation region was sensitive to the small geometric differences among the plates tested. The grooves in the bottom of the water channel which supported the plates were machined parallel to the channel side walls so that the plate alignment with the flow is well controlled. This is verified by the symmetry which was always observed between the laminar separation bubbles on either side of the plate. No effect of the side walls could be detected in these tests. The results for laminar recirculation length measured using plates of two different thickness agree with each other and the measured recirculation length at high Reynolds number agrees with measurements by other observers. The principal results do not appear to be overly sensitive to the facility. Zelenka and Loehrke [6] detected the onset of transition in the separation bubble on a high aspect ratio plate in a low turbulence wind tunnel at a Reynolds number of 300 using a hot-wire anemometer. One should, however, be cautious about applying the results of shear layer transition measurements to situations where the freestream turbulence conditions are orders-of-magnitude different than those under which the measurements were made.

Discussion

These direct observations of recirculation length show that a laminar separation bubble forms at a Reynolds number of 100 and grows rapidly with increasing Reynolds number. On long plates, $L/t \geq 8$, the bubble reaches a maximum length of 6.5 times the plate thickness at a Reynolds number of 325. At this Reynolds number unstable oscillations begin in the separated shear layer. Further increases in Reynolds number result in a transition to turbulence in the separated shear layer and in a reduction of the recirculation length to an asymptotic value of four times the plate thickness. These observations compare well with theory [4] at low Reynolds number and other direct observations [2,3] at high Reynolds number.

Estimates of the size of the separation bubble have been made by several authors on the basis of local, time-averaged, mass transfer measurements. Sorensen [7] observed a local maximum in the mass transfer coefficient on the side of a flat plate just downstream from the blunt leading edge for $Re_t > 245$. The location of this maximum moved from a downstream position of about 5.8 times the plate thickness toward the leading edge as the Reynolds number was increased. Kottke, et al [8], obtained similar results using a different mass transfer technique. They identified a first critical Reynolds number of 380 at which the local maximum first appears. A second critical Reynolds number at 2200 was inferred, based on further changes in the shape of the local mass transfer rate profile, to indicate the onset of votex shedding in the separated region. The results of the present experiments would indicate that first observations of mass transfer maxima are more closely correlated with the onset of unsteady flow in the separated layer than with the first appearance of the laminar, steady bubble.

Zelenka and Loehrke [6] show that the effects of leading edge separation on transport rate may be clearly seen when the average transport coefficient for a blunt plate of $L/t \approx 10$ is compared with the prediction of laminar theory for unseparated flow. Heat and mass transfer data are correlated which show the insulating effect of a large laminar bubble and transition from laminar-like behavior at Reynolds numbers based on plate thickness greater than approximately 400.

Acknowledgment

This research was supported by NSF through Grant ENG 74-03338.

References

1 Morkovin, M. V., "An Approach to Flow Engineering Via Functional Flow Modules," *Deutsche Luft-und Raumfahrt Forschungsbericht*, Vol. 72-27, May 1972.

2 Ota, T., and Kon, N., "Heat Transfer in the Separated and Reattached Flow on a Blunt Flat Plate," ASME *Journal of Heat Transfer*, Vol. 96, No. 4, Nov. 1974, pp. 459–462.

3 Ota, T., and Itasaka, M., "A Separated and Reattached Flow on a Blunt Flat Plate," ASME JOURNAL OF FLUIDS ENGINEERING, Vol. 98, No. 1, Mar. 1976, pp. 79–86.

4 Ghia, U., and Davis, R. T., "Navier-Stokes Solutions for Flow Past a Class of Two-Dimensional Semi-Infinite Bodies," *AIAA J.*, Vol. 12, No. 12, Dec. 1974, pp. 1659–1665.

5 Ghia, U., Personal communication.

6 Zelenka, R. L., and Loehrke, R. I., "Heat Transfer From Interrupted Plates," *Advances in Enhanced Heat Transfer*, ASME Symposium Volume, 1979.

7 Sorensen, A., "Mass Transfer Coefficients on Truncated Slabs," *Chem. Engr. Sc.*, Vol. 12, 1969, pp. 1445–1460.

8 Kottke, V., Blenke, H., and Schmidt, K. G., "Einfluss von Anströmprofil und Turbulenzintensität auf die Unströmung längsangeströmter Platten endlicher Dicke," *Warme-und Stoffübertragung*, Vol. 10, 1977, pp. 159–174.

S. D. Savkar
Mechanical Systems and Technology Laboratory, General Electric Co., Schenectady, N.Y. 12301

Derivation of Kline Line a-a for Straight Walled Diffusers From Stratford's Separation Criterion

Introduction

The basis of much diffuser design is the use of the so-called Kline plot [1], and variations thereof, coupled with some trial and error. However, the work of Kline and his associates has largely been based on empirical, experimentally arrived at data. For diffusers of simple design, these plots have proved invaluable. The procedure, however, becomes much more complicated when diffusers of complex contours are involved. In 1973, the author was faced with one such group of problems of high Mach number inlet, the so-called accelerating inlet, design [2].

The central issues of that paper were acoustic, and the critically important concern of the inlet diffuser design was mentioned only in passing. Nevertheless, the feasibility of the accelerating inlets hinged crucially on the ability to minimize the total pressure recovery penalty for inlets constrained to an $L/d \leq 1$. This in effect forced a fix on the overall diffuser length. In order to get around the problem, the author devised an inverse design procedure based on the Stratford separation criterion [3]. This was done by rewriting the pressure coefficient in terms of the local one-dimensional Mach number and the local area ratio, and carrying out the indicated integration to deduce an approximation to the wall coordinates. these coordinates were then used to generate the inviscid flow and pressure field. The inverted Stratford criterion thus yielded a good first approximation from which within several iterations the desired wall contour was derived. The results of the calculations were verified by a detailed boundary layer calculation (using the Mellor-Herring model). This procedure allowed an almost "tailored" axial Mach number distribution.

To illustrate the procedure, in this note, it is shown that the classical line a-a of the Kline plot [1] is well bracketed for a flat, straight walled channel diffuser using Stratford's criterion.

Prediction of Kline Line a-a

Stratford employed a modified form of the matched asymptotic expansion technique to the turbulent flow in the vicinity of separation. The inner solution, corresponding to the region adjacent to the wall, was obtained assuming zero skin friction and assuming a direct balance between pressure forces and gradient in the shear force. The beauty of the analysis is the simplicity of the resulting separation criterion.

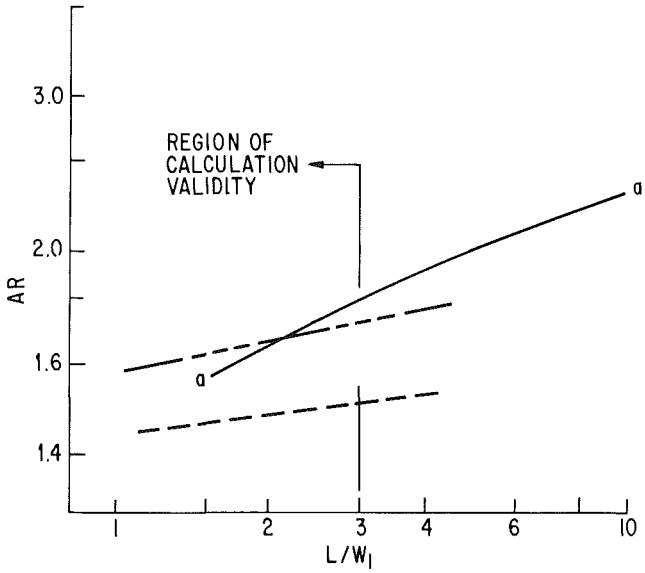

Fig. 1 Diffuser flow regime according to the Kline plot and verification based on Stratford separation model; ___ Kline line a-a; _ _ _ Inverted Stratford calculation ($U_0\ W_1/\nu = 10^6$; ___ _ _ ___ Inverted Stratford calculation ($U_0\ W_1/\nu = 10^7$)

Stratford criterion can be used for diffusers without any entry length into the throat, by writing (for the case $d^2P/dx^2 < 0$)

$$C_p \left[x \frac{dC_p}{dx} \right]^{1/2} = .35 \left[\frac{Ux}{\nu} / 10^6 \right]^{0.1} \tag{1}$$

Assuming one-dimensional incompressible flow in a straight walled diffuser, velocity U at a given axial station x is given as

$$\frac{U}{U_0} = 1 - (1 - 1/AR)\, x/L \tag{2}$$

substituting the above and $C_p = 1 - (U/U_0)^2$, obtain

$$\left[\frac{(AR^2 - 1\sqrt{(AR-1)}}{0.0622\ AR^{2.9}} \right]^{10} \left[\frac{L}{W_1} \right]^{-1} = \frac{U_0 W_1}{\nu} \tag{3}$$

Now, Stratford developed his theory for a Reynolds number of 10^6; however, the resultant separation criterion being a weak function of Reynolds number has been verified to work well for Reynolds numbers up to 10^7 and somewhat less than

Contributed by the Fluids Engineering Division for publication in the JOURNAL OF FLUIDS ENGINEERING. Manuscript received by the Fluids Engineering Division, January 10, 1980.

10^6. For diffusers of aspect ratios order 1 and no entry length, this means that $U_0\ W_1/\nu$ is of order 10^6 to 10^7. Using these two limits, one can calculate a band on the Kline plot equivalent to line a-a, below which the diffuser does not stall. This is illustrated in Fig. 1. Considering the simplicity of verification, the agreement, in the range of applicability ($L/W_1 \sim 0(1)$) based on the applicability of Stratford's criterion up to C_p of 0.625, is acceptable. It should be noted that the Stratford predictions are extrapolated to high values of L/W_1 only to illustrate the predicted trend. The range of applicability of the Stratford formula is perhaps $L/W_1 < 3$. Finally, the Stratford criterion can be easily corrected for non-zero inlet length or the effect of non-zero initial displacement thickness. If such a correction is made and a more accurate description of the diffusing velocity profiles included, the accuracy of the prediction will be enhanced.

References

1 Reneau, L. R., Johnston, J. P., and Kline, S. J., "Performance and Design of Straight Two-Dimensional Diffusers," Stanford University Thermosciences Division Report PD-8, Sept. 1964.

2 Savkar, S. D., and Kazin, S. B., "Some Aspects of Fan Noise Suppression Using High Mach Number Inlets," *AIAA J. of Aircraft,* Vol. 12, No. 5, May 1975, pp. 487–493. See also the Errata published in Vol. 13, No. 1, Jan. 1976, p. 64.

3 Stratford, B. S., "The Prediction of Separation of the Turbulent Boundary Layer," *J. Fluid Mechanics,* Vol. 5, Part 1, Jan. 1959, pp. 1–35.

Nomenclature

AR = area ratio
C_p = pressure coefficient
L = diffuser axial length
U_0 = diffuser throat velocity
W_1 = diffuser throat width
x = axial coordinate
ν = kinematic viscosity

A Device for Measuring Very Low Pressure Differences

Takeo Nakagawa
Department of Civil Engineering,
Nagoya University,
Furo-cho, Chikusa-ku,
Nagoya 464 Japan

A new technique is proposed for measuring very low pressure differences between two points in a fluid. The device combines an optical velocity measurement with the Hagen-Poiseuille relation to infer the pressure drop. A prototype model has been constructed which measures pressure differences in the range 3.07×10^{-5} to 1.59×10^{-3} cm H_2O. The estimated uncertainty of this technique is approximately 4 percent. However, no accurate, independent calibration of this device has yet been achieved.

1. Concept

The Hagen-Poiseuille equation is valid for fully-developed laminar flow in a straight pipe with constant pressure gradient. The relation for pressure drop between two points 1 and 2 in the pipe is

$$\Delta p = p_1 - p_2 = 4\mu L u_m / R^2 \qquad (1)$$

where μ is the fluid viscosity, L the pipe length between 1 and 2, u_m is the maximum (center line) velocity, and R the pipe radius. Assuming that μ, L, and R are known, measurement of u_m allows the computation of pressure difference. In the proposed device u_m has been determined photographically with tracer particles.

2. Design of the Device

Principle of Operation. A sketch of the proposed device is shown in Fig. 1. The pipe is filled with water containing neutrally buoyant particles. When a pressure difference exists between taps 1 and 2, the water begins to flow and the particles rapidly accelerate up to the water velocity. To measure the maximum velocity, a thin central fluid plane through the pipe axis is illuminated by parallel light passing through a narrow slit. The camera viewing direction is carefully set to be normal to this illuminated plane. A streak photograph is taken with exposure time Δt. Each photograph has a scale and a central arrow to mark the center line of the fluid plane. Then, if L_s is the length of a center line streak, the desired maximum velocity is $u_m = L_s/\Delta t$.

With u_m known, if minor losses between 1 and 2 are negligible compared to the Poiseuille straight-pipe loss, Equation (1) may be used to compute the desired pressure drop between the taps.

Details of the Construction. A prototype model has been constructed with parameters whose mean values and uncertainties are listed in Table 1. The three primary components are the pipe, the water-filled box, and the tracer particles.

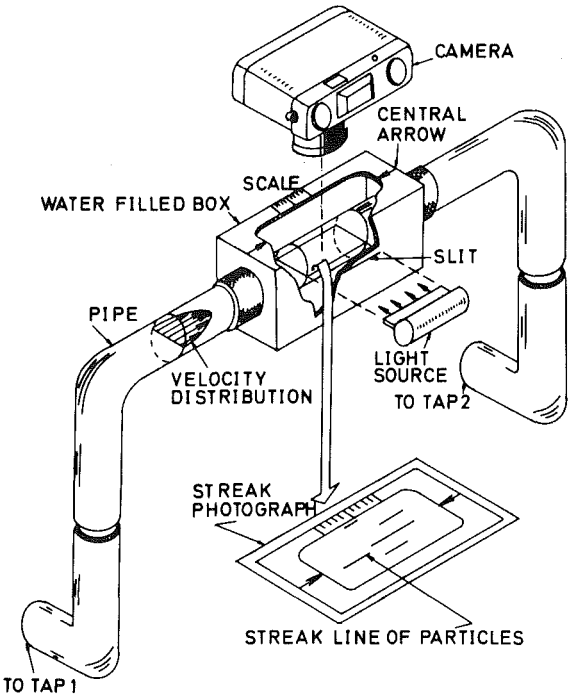

Fig. 1 Sketch of the proposed low pressure measurement device

The pipe is precision-bored glass, of radius 0.45 cm, with two vinyl tubes, 10 cm long, attached to each end. To reduce inlet and exit losses, each end is cut smoothly to form a well-rounded shape. The horizontal part of the pipe is 26 cm long.

A water-filled box 9 cm long, 2 cm wide, and 3 cm deep was placed around the middle of the horizontal part of the pipe. The box is covered with black rubber and has a thin slit 1 mm wide and 3 cm long, as shown in Fig. 1. Since the viscosity of water is a strong function of temperature, the water-filled box

Contributed by the Fluids Engineering Division for publication in the JOURNAL OF FLUIDS ENGINEERING. Manuscript received by the Fluids Engineers Division, February 9, 1979.

Table 1 Mean values and uncertainty intervals of variables with odds 13:1

Variable				Mean	Uncertainty interval
dynamic viscosity	μ	(g/cm.s)		1.056×10^{-2}	$\pm\ 0.027\times10^{-2}$
length of pipe	L	(cm)		174.90	$\pm$ 0.01
Streak length of tracer particle on film	L_s	(cm)	maximum	0.80	$\pm$ 0.01
			minimum	0.20	$\pm$ 0.01
exposure time of camera	Δt	(s)		1.00	$\pm$ 0.01
length of reference scale on film	L_r	(cm)		3.00	$\pm$ 0.01
radius of pipe	R	(cm)		0.45	$\pm$ 0.005

served to keep the pipe water temperature constant to within 1°C. The box also reduced the reflection of light from the surface of the pipe.

Tracer particles are used to measure the water velocity. For an ideal measurement, the particle slip velocity should be negligible, which requires that the particles be nearly neutrally buoyant, very small, and of total volume small compared to the fluid volume. The prototype model used spherical Timica particles in the size range 15-40 μm, mixed with the water in a very dilute mixture of 1 part solid to 10^5 parts liquid by volume. Under these conditions it is believed that the particles do not alter the flow pattern and that slip losses are negligible, as discussed in the next section.

Development of this device was stimulated by the need to measure pressure drops in flow past a small obstacle mounted on a plate, as shown in Fig. 2. Used in these circumstances, no standard pressure devices gave any noticeable readings. The proposed device was mounted as shown in Fig. 2, with dimensions in mm. Pressure drops were measured with the tap plate moving at speeds in the range 0.05 to 2.67 cm/s. At each speed, 13 photographs were taken of the Timica particles. In this way, pressure differences in the range 3.07×10^{-5} to 1.59×10^{-3} cm H_2O were successfully measured.

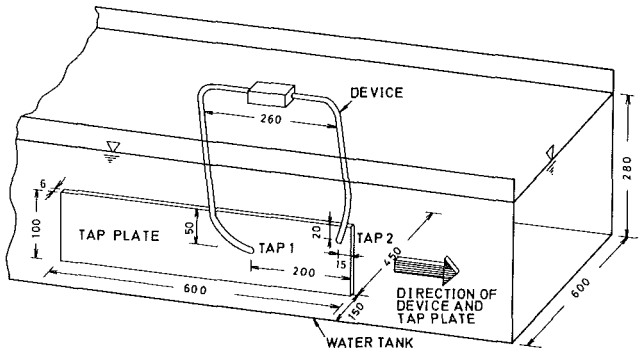

Fig. 2 Schematic diagram of a measurement of the pressure difference between two taps. (Dimensions in mm)

3 Error Analysis

At present it has not yet been possible to calibrate this new device with an independent pressure measurement. However, one can make an error analysis based upon 1) uncertainties in the measurement variables; and 2) possible deviations from the Poiseuille relation, equation (1).

Uncertainty in Measured Variables. The total uncertainty is computed here by the method of Kline and McClintock [1]. If $F = F(v_1, v_2,...,v_n)$ is the quantity to be measured and δv_i is the uncertainty in any specified variable v_i, then the total uncertainty δF in the measurement is given by

$$\delta F=\left[\sum_{i=1}^{n}\left(\frac{\partial F}{\partial v_i}\delta v_i\right)^2\right]^{1/2} \tag{2}$$

assuming that each of the variables is normally distributed. Each of the uncertainties should be quoted at the same odds.

Since the photographs are developed at more than full scale, the maximum velocity of the Timica particles is computed from

$$u_m = C\ L_s/(\Delta t\ L_r) \tag{3}$$

where $C = 0.23$ cm is the actual length of the reference scale and L_r is the length of the reference scale on the photograph. Substitution into Equation (1) gives the relation between pressure drop and the measured variables:

$$\Delta p=\frac{4\ C\ \mu\ L\ L_s}{\Delta t\ L_r\ R^2} \tag{4}$$

Then, assuming that each variable in equation (4) has an independent uncertainty, the total relative uncertainty in pressure drop is given by

$$\frac{\delta(\Delta p)}{\Delta p}=\left[\left(\frac{\delta\mu}{\mu}\right)^2+\left(\frac{\delta L}{L}\right)^2+\left(\frac{\delta L_s}{L_s}\right)^2+\left(\frac{\delta\Delta t}{\Delta t}\right)^2+\left(\frac{\delta L_r}{L_r}\right)^2+\left(\frac{2\delta R}{R}\right)^2\right]^{1/2} \tag{5}$$

It is sufficient to compute the uncertainties at the minimum and maximum pressure differences measured. When the variable uncertainties from Table 1 are substituted into equation (5), the relative uncertainty for the maximum pressure difference is found to be

$$\frac{\delta(\Delta p)}{\Delta p_{\max}}=[6.54\times10^{-4}+3.26\times10^{-9}+1.56\times10^{-4}+1.00\times10^{-4}+1.11\times10^{-5}+4.94\times10^{-4}]^{1/2}=3.76\ \% \tag{6}$$

It is seen that uncertainty in viscosity and pipe radius are the primary causes of measurement uncertainty. Tracer streak

Nomenclature

a = acceleration
C = length of reference scale
g = gravitational acceleration
L = Length of pipe
L_r = length of reference scale on film
L_s = streak length of tracer particle on film
p_1 = pressure at tap 1
p_2 = pressure at tap 2
R = radius of pipe
R_p = radius of tracer particle
Δu = slip velocity
Δt = exposure time of camera
u_m = maximum velocity in pipe
ρ = density
ρ_p = particle density
μ = kinematic viscosity of fluid
ν = dynamic viscosity of fluid

length and camera exposure time have a moderate effect, while pipe length and reference scale length errors have a negligible effect.

Similarly, the uncertainty in the minimum pressure difference is computed to be

$$\frac{\delta(\Delta p)}{\Delta p_{\min}} = 6.13\% \tag{7}$$

Again the major contribution is from viscosity and pipe radius uncertainty.

Error Analysis for the Technique. In addition to uncertainty in the test variables, there are possible errors due to 1) deviations from the Hagen-Poiseuille equation; 2) slip losses; and 3) minor losses in the pipe system.

The flow must be laminar for equation (1) to be valid. For the prototype experiments u_m was in the range 8.2×10^{-4} to 4.3×10^{-2} cm/s, which corresponds to a pipe Reynolds number $\mathrm{Re}_D = 1.83$ at most. This is clearly much less than the transition Reynolds number of 2300. At such low Reynolds numbers, the accepted formula for entrance development length x in the pipe is equation (4-247a) of White [2]:

$$x \doteq 0.32 u_m R^2/\nu + 1.4R \tag{8}$$

Substituting from the test variables in Table 1, we find that the entrance length x varies from 0.63 to 0.76 cm, which is negligible compared to the pipe length. It is expected that the secondary flow decay distance downstream of the pipe bends is of the same order as this entrance length. Hence the test conditions appear to justify the use of the fully-developed Hagen-Poiseuille equation.

Particle slip losses tend to decay with time in a steady viscous flow. At the test velocities and sizes the Reynolds number of the particles is of order 10^{-3} or less, so that the Stokes drag relation should hold:

$$D = 6\ \pi\ \mu\ R_p \Delta u \tag{9}$$

where Δu is the relative or slip velocity between the particle and the water. Also, one would expect a lift force if the particle is off the centerline in the region of velocity shear. However, the computed lift was found to be only 2 percent or less of the drag and was neglected.

Utilizing equation (9) for the drag and assuming the particle is in rectilinear motion, its equation of motion is

$$\rho_p a_p - \rho a = (\rho_p - \rho) g - 4.5\mu\ \Delta u/R_p^2 \tag{10}$$

where subscript p denotes the particle. If $\Delta u = u_p$-u and the particle is neutrally buoyant, $\rho_p = \rho$, equation (10) becomes

$$\frac{d(\Delta u)}{dt} = -4.5\ \nu\ \Delta u/R_p^2 \tag{11}$$

which has the solution

$$\Delta u = \Delta u_0\ \exp(-4.5\ \nu t/R_p^2) \tag{12}$$

Thus the slip velocity Δu decays in a time of order R_p^2/ν, which is of the order of a microsecond for the Timica particles. To illustrate that these particles are nearly neutrally buoyant, when dropped in still water they take over 30 minutes to sink 10 cm. Hence it is believed that particle slip is not a problem in the proposed device.

The piping system suffers additional minor pressure losses due to the entrance, the exit, pipe bends, and the junctions with the vinyl tubes. Using the loss coefficient estimates of Streeter [3], it was determined that the total of all these minor losses is less than 1 percent of the Hagen-Poiseuille loss from equation (1).

Summarizing these sources of possible error, it is felt that the proposed device does not have any significant discrepancies due to development, slip, or minor loss effects.

4 Recommendations for Further Work

Recommendations for further work are twofold; (*a*) to suggest possible calibration methods for this new technique, and (*b*) to develop a more refined device than the present version.

No calibration of the device with different instruments such as a piezometer is given here, because they are usually calibrated by a reference manometer that is not suitable for the measurement of the small pressure difference as the present case. It may be, however, possible that a calibration of this device could be provided by determining the pressure difference between the two tap positions using standard manometer techniques. Alternative calibration could be given by using two overflowing reservoirs at a small elevation difference, which provides a reference pressure difference between the two ends of a horizontal pipe.

This device is an explanatory version to determine its potential for the measurement of an extremely low pressure difference. As demonstrated in Section 3, the uncertainty of the result is primarily caused by the process of determining the maximum velocity in the pipe with the tracer particles. Thus, if there is an alternative way to determine the maximum velocity without using tracer particles, significant improvement of this device could be obtained. It is suggested here that such a method is to incorporate a laser Doppler flow meter into this device. Goldstein and Kreid [4] have shown that near the axis of a square duct, measured velocities with a laser meter are within about 0.1 percent error. Such high performance of the laser Doppler flow meter could be essential to obtain a very accurate low pressure difference in terms of this new technique.

5 Conclusions

It has been verified experimentally that the measurement concept for very low pressure differences work satisfactorily. It must be emphasized that any device constructed from the proposed concept has no limitation in the rage of pressure differences to be measured, but future versions of this device should minimize uncertainty intervals of the variables by incorporating advanced techniques.

This prototype device is capable of measuring the pressure difference 3.07×10^{-5} to 1.59×10^{-3} cm H_2O, and the estimated relative uncertainty interval of the pressure difference between the taps is 3.76 percent for the maximum pressure difference and 6.13 percent for the minimum pressure difference with 13:1 odds.

Considering its ability to measure extremely low pressure difference, it is believed that this new technique could be useful for both fundamental and practical fluid mechanic research.

6 Acknowledgments

The author gratefully acknowledges Drs. A. D. McEwan of C.S.I.R.O., T. H. Nguyen of Monash University, and B. B. Sharp of the University of Melbourne in Australia for stimulating discussions. The author would like to express his thanks to Professor F. Takagi of Nagoya University for his critical comments and discussion. The author is grateful to the Technical Editor, Professor F. M. White for his substantial improvement of the final manuscript.

References

1 Kline, S. J., and McClintock, F. A., "The Description of Uncertainties in Single Sample Experiments," *Mechanical Engineering,* Jan. 1953, p. 3.

2 White, F. M., *Viscous Fluid Flow,* McGraw-Hill, New York, 1974, p. 338.

3 Streeter, V. L., *Handbook of Fluid Dynamics,* McGraw-Hill, New York, 1961, p. 3-20.

4 Goldstein, R. J., and Kreid, D. K., "Measurement of Laminar Flow Development in a Square Duct using a Laser - Doppler Flowmeter," ASME *Journal of Applied Mechanics,* Dec. 1967, p. 813.

The Linear Instability Due to the Compressible Crossflow on a Swept Wing

S. G. Lekoudis
Assistant Professor,
School of Aerospace Engineering,
Georgia Institute of Technology
Atlanta, Ga. 30332

The problem of the propagation of three-dimensional laminar instabilities, due to crossflow, in a three-dimensional compressible boundary layer, is examined using linear theory. The theory is applied to the case of a transonic swept wing. It is shown that compressibility has a mild stabilizing effect in the regions where the crossflow is strong. The problem of defining the direction of propagation of the disturbances is discussed.

1 Introduction

High fuel prices force the designers of future transport airplanes to be very conscious about drag reduction. Skin friction contributes a large portion to the drag; therefore, if reduced, it can provide large fuel savings. Currently, a promising way to reduce skin friction drag is laminar flow control.

Laminar flow control uses wall suction which changes the stability characteristics of the laminar boundary layer and prevents transition to turbulent flow. Because the suction system needs power, it is desirable to find the minimum suction that will keep the flow laminar, over a particular configuration. To do this analytically, one has to use stability theory. Before stability theory can determine the minimum suction required, the following items need attention. First, the stability characteristics of the three-dimensional boundary layer have to be known. And second, transition to turbulent flow has somehow to be related to these stability characteristics.

The most widely accepted way to predict boundary layer transition on two-dimensional configurations is the e^N method [1]. The method uses an integral of the amplification rates of Tollmien-Schlichting waves computed from linear stability theory. Hence, the natural way of extending the method to three-dimensional configurations is by computing integrals of amplification rates. However, there is one parameter, nonexistent in the two-dimensional case, that complicates the problem. This parameter is the direction of propagation of the disturbance. Next, previous work on the three-dimensional problem is outlined.

The stability characteristics of a three-dimensional boundary layer flow were investigated by Gregory, Stuart, and Walker [2]. They examined the flow over a rotating disk and they reduced the problem to a series of two-dimensional problems. They explained the nature of cross-flow instability and concentrated on the unstable stationary disturbance. Mack [3] examined the complete three-dimensional problem. He used as the direction of growth a vector defined by the real parts of the group velocity vector and examined the Blasius layer and the flow over a rotating disk. Srokowski and Orszag [4] examined flows over wings and developed a user-oriented computer program, SALLY. SALLY uses incompressible stability theory to compute the maximum temporal amplification rate for a constant frequency. It then uses the direction formed from the real parts of the group velocity and calculates N factors. Other options are also available [1,4]. It was found that the fore and aft parts of the wings with laminar flow control were dominated by instability due to crossflow. Mack [5] used incompressible flow theory and examined the characteristics of crossflow instability and the instability due to both crossflow and Reynolds number. Nayfeh and Padhye [6] derived a transformation that relates the temporal to spatial growth along a prescribed direction without relying on conservative wave theory. They could also transform the growth from one direction to a different direction using the spatial stability theory.

The effects of compressibility on the stability of the three-dimensional boundary layer on the same swept wing have been examined by Mack [7] and Lekoudis [8]. They found that compressibility has a strong stabilizing effect for instabilities due to Reynolds number, but it has a mild stabilizing effect on instabilities due to crossflow. The solution techniques and certain results from reference [8] are repeated in the present paper. Runyan, et al, [9,10] performed incompressible and compressible stability calculations and correlated growth factors with experimental data on transition on swept and unswept wings. Correlations with a variety of experimental data, for swept wings and a comprehensive review of the state of the art are given by Hefner and Bushnell [1].

In all the work discussed above, the fundamental problem of how one defines the direction of propagation of three-dimensional waves in a three-dimensional boundary layer has been treated with ad-hoc procedures. Nayfeh [11], and Cebeci and Stewartson [12], defined this direction as given by the real

Contributed by the Fluids Engineering Division for publication in the JOURNAL OF FLUIDS ENGINEERING. Manuscript received by the Fluids Engineering Division, March 7, 1980.

ratio of the complex group velocities in the plane of the boundary layer flow. This condition holds for monochromatic waves. Lekoudis [13] used this condition for the case of a transonic swept wing with wall cooling. Some of the results of reference [13] are repeated in this paper.

The purpose of this paper is to describe a method, based on linear theory, that examines the stability of the three-dimensional compressible boundary layer. The method is described in section 2. The developed computer program is described in section 3. Results and the problem of defining the direction of propagation are discussed in section 4. The effects of compressibility are illustrated by examining the flow over an infinite swept supercritical wing with suction. In section 5 the work is summarized.

2 Formulation of the Problem

We consider the stability of a three-dimensional laminar, compressible, boundary layer over a supercritical wing with laminar flow control. The wing is of infinite span, 35° sweep, and has a streamwise chord of 2.46 m. The freestream Mach number is M = 0.891. The wing is defined in a Cartesian coordinate system shown in Fig. 1. The wing is defined in a Cartesian coordinate system shown in Fig. 1. The x-axis is in the direction of the normal chord, the y-axis is normal to the surface and the z-axis is along the span. To nondimensionalize the Navier-Stokes equations, we use the local incompressible displacement thickness in the x-direction δ^*, the local boundary layer edge velocity in the x-direction $U_e{}^*$ and the local freestream temperature $T_e{}^*$. The same wing has been used befoe the stability calculations on a swept wing [4,7,8,13] and details about the boundary layer that develops on its upper surface can be found in reference [7].

We assume locally parallel flow and sinusoidal disturbances in the form of travelling waves

$$d_i(x,y,z,t) = j_i(y)\exp(\alpha x+\beta z-\omega t) \tag{1}$$

where ω is the frequency, α and β are the wavenumbers in the x and z directions respectively, t is the time, $j_i(y)$ is the distribution of the disturbance amplitude and phase across the boundary layer (eigenfunction) and d_i stands for the disturbance quantities. The d_i are

$$\begin{aligned} d_1 &= u & d_5 &= s \\ d_2 &= \partial u/\partial y & d_6 &= \partial s/\partial y \\ d_3 &= v & d_7 &= w \\ d_4 &= p & d_8 &= \partial w/\partial y \end{aligned} \tag{2}$$

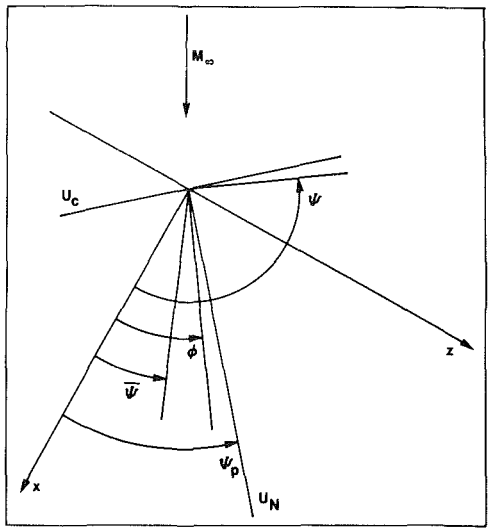

Fig. 1 The coordinate system

where u, v and w are the disturbance velocities in the x, y, and z directions respectively, p is the disturbance pressure and s is the disturbance temperature.

By substituting in the Navier-Stokes equations and by keeping only linear terms in the disturbance quantities, one can obtain a system of eight ordinary differential equations in the y-variable. These equations are contained in reference 14 where they were used to study the temporal growth of three-dimensional disturbances in a compressible Blasius boundary layer, and were rederived and verified for use in the present study.

The boundary conditions are that u, v, w and $\partial s/\partial y$ vanish at the wall and that all the disturbance quantities vanish away from the wall. Becuase these conditions are homogeneous, the boundary value problem becomes an eigenvalue problem. The distinction between temporal theory and spatial theory for three-dimensional flows is discussed in reference [6]. In what follows it is assumed that when temporal theory is used, ω_r and ω_i are the real and imaginary parts respectively of the eigenvalue, and α and β are the real wavenumbers. When spatial theory is used, σ is the growth rate along a direction $\bar{\psi}$, and α_r and β_r are the real parts of α and β that form the wavenumber vector k in the direction ψ. Also, α_i and β_i are

Nomenclature

a = coefficient
C = wing streamwise chord
C_p = pressure coefficient
c = phase speed in the x-direction
d = disturbance quantity
f = frequency in Hz
g = eigensolution of the sixth order system
$\tilde{g}$ = eigensolution of the adjoint sixth order system
H = coefficient
h = coefficient
i = imaginary unit = $\sqrt{-1}$
j = eigensolution of the eighth order system
k = magnitude of the real wavenumber vector
M = Mach number
N = integral of amplification rates
p = disturbance pressure
Pr = Prandtl number
q = coefficient
Q = incoming freestream velocity
R = Reynolds number = $\dfrac{U_{e\delta}{}^*}{\nu_e}$
r = coefficient
s = disturbance temperature
T = mean temperature
t = time
U = mean velocity in x-direction
U_c = mean velocity in the crossflow direction
U_N = mean velocity in the direction of the external streamline
u = disturbance velocity in x-direction
V_α, V_ρ = group velocities in x and z-direction
v = disturbance velocity in the y-direction
W = mean velocity in the z-direction
w = disturbance velocity in the z-direction
x,y,z = Cartesian coordinate system
α = wavenumber in the x-direction

the imaginary parts of α and β, and F is the input real frequency in Hz. Hence,

$$\psi = \tan^{-1}(\beta_r/\alpha_r) \qquad k = (\alpha_r{}^2 + \beta_r{}^2)^{1/2}$$
$$\psi = \tan^{-1}(\beta_i/\alpha_i) \qquad \sigma = (\alpha_i{}^2 + \beta_i{}^2)^{1/2} \tag{3}$$

The group velocities in the x and z directions, respectively, are

$$V_\alpha = \partial\omega/\partial\alpha, V_\beta = \partial\omega/\partial\beta \tag{4}$$

and their ratio defines the complex (in general) quantity

$$\phi = \tan^{-1}(V_\beta/V_\alpha) \tag{5}$$

The angles ψ, $\bar{\psi}$, ϕ (if real) and ψ_p, which is the angle of the local potential streamline with respect to the x-axis, are shown in Fig. 1. The angles are measured positive in the counterclockwise direction.

In the case of incompressible flow, the three-dimensional problem can be transformed into a two-dimensional problem [2,5]. However, this is not possible when the flow is compressible, unless the velocity fluctuation along the constant phase line (in the temporal theory) can be neglected in the energy equation [14]. Then the order of the system is reduced from eight to six. For the transonic range of speeds of interest, the difference between the results of the eighth order system and the sixth order system is small [7]. To use the sixth order system, we use the coordinates

$$\begin{aligned} \tilde{x} &= x\cos\bar{\phi} + z\sin\bar{\phi} \\ \tilde{y} &= y \\ \tilde{z} &= -x\sin\bar{\phi} + z\cos\bar{\phi} \\ \tilde{t} &= t\cos\bar{\phi} \end{aligned} \tag{6}$$

where

$$\tan\bar{\phi} = \beta/\alpha. \tag{7}$$

Then

$$\alpha x + \beta z - \omega t = \tilde{\alpha}(\tilde{x} - c\,\tilde{t}) \tag{8}$$

where

$$\begin{aligned} \tilde{\alpha} &= (\alpha^2 + \beta^2)^{1/2} \\ c &= \omega/\alpha. \end{aligned} \tag{9}$$

Notice that in the spatial theory, ϕ loses the identity of an angle and the transformation becomes a computational tool. The system of equations in the $\tilde{x},\tilde{y},\tilde{z}$ coordinates is

$$\frac{\partial g_i}{\partial y} - \sum_{j=1}^{6} a_{ij} g_j = 0, i = 1,\ldots 6 \tag{10}$$

where the a_{ij} are functions of the mean flow quantities [14]. The boundary conditions require that g_1, g_3, g_5 vanish at the wall and all g's decay away from the wall.

2.1 Calculation of the Group Velocity. A technique of calculating the group velocity without resorting to numerical differentiation [6] is applied to the compressible case with the rotated coordinate system. The system [10] gives

$$\frac{\partial}{\partial y}\left(\frac{\partial g_i}{\partial \tilde{\alpha}}\right) - \sum_{j=1}^{6} a_{ij}\frac{\partial g_j}{\partial \tilde{\alpha}} = \sum_{j=1}^{6}\frac{\partial a_{ij}}{\partial \tilde{\alpha}} g_j \, i = 1,\ldots 6 \tag{11}$$

We multiply (11) by $\bar{g}_i$ where

$$\frac{\partial \bar{g}_i}{\partial y} + \sum_{j=1}^{6} a_{ji}\bar{g}_j = 0, i = 1,\ldots 6 \tag{12}$$

all $\bar{g}$'s vanish away from the wall and g_2, g_4, and g_6 vanish at the wall. Then (11) becomes

$$\frac{\partial}{\partial y}\left(\bar{g}_i\frac{\partial g_i}{\partial \tilde{\alpha}}\right) - \frac{\partial g_i}{\partial \tilde{\alpha}}\frac{\partial \bar{g}_i}{\partial y} - \left[\sum_{j=1}^{6} a_{ij}\frac{\partial g_i}{\partial \tilde{\alpha}}\right]\bar{g}_i = \left[\sum_{j=1}^{6}\frac{\partial a_{ij}}{\partial \tilde{\alpha}} g_j\right]\bar{g}_i \, i = 1,\ldots 6 \tag{13}$$

Adding the six equations (13), using the definition of the adjoint (12), integrating the resulting equation from $y = 0$ to $y = \infty$, and using the boundary conditions results

$$\sum_{i=1}^{6}\sum_{j=1}^{6}\int_0^\infty \frac{\partial a_{ij}}{\partial \alpha} g_j \bar{g}_i \, dy = 0. \tag{14}$$

Also

$$\frac{\partial a_{ij}}{\partial \tilde{\alpha}} = q_{ij} + r_{ij}\frac{\partial c}{\partial \tilde{\alpha}} \tag{15}$$

where the q's and r's are defined in the Appendix A. Substituting equation (15) into (14) gives an equation for $\partial c/\partial\tilde{\alpha}$. Finally the group velocities in x and z directions are calculated from

$$V_\alpha = \frac{\partial\omega}{\partial\alpha} = c + \frac{\alpha^2}{\tilde{\alpha}}\frac{\partial c}{\partial \tilde{\alpha}}\bigg|_\beta \tag{16}$$

$$V_\beta = \frac{\partial\omega}{\partial\beta} = \frac{\partial\beta}{\tilde{\alpha}}\frac{\partial c}{\partial \tilde{\alpha}}\bigg|_\alpha \tag{17}$$

Nomenclature (cont.)

β = wavenumber in the z-direction
γ = gas constant, ratio of specific heats
δ^* = incompressible displacement thickness in the x-direction - $\int_0^\infty \left(1 - \frac{U}{U_e}\right) dy^*$
κ = ratio of the second viscosity coefficient to the first viscosity coefficient
μ = molecular viscosity
ν = kinematic viscosity
ρ = mean density
σ = spatial growth rate
$\bar{\phi}$ = rotation angle that trans-forms $\tilde{x}\ \tilde{y}\ \tilde{z}$ coordinate system
ϕ = angle formed from the real ratio the complex group velocities
ψ = angle of the wavenumber vector with the x-direction
$\bar{\psi}$ = angle of the direction of growth with the x-direction
ψ_p = angle of the external streamline with the x-direction
ω = angular frequency
ω_i = temporal amplification rate

Subscripts

c = normalized with the wing streamwise chord
e = boundary layer edge conditions
∞ = incoming freestream conditions
i,j = indices
w = wall conditions
ϕ = in the direction of ϕ

Superscripts

$*$ = dimensional quantity
$\sim$ = quantity in the $\tilde{x}\ \tilde{y}\ \tilde{z}$ system

Table 1 Comparison of temporal amplification rates, $\omega_i \times 10^3$

Frequency	x/C	α	β	"SALLY"	Present Method
500 Hz	.00186	.269470	−.254191	6.269	6.182
	.00352	.234390	−.288615	5.707	5.637
	.00580	.212152	−.305274	4.586	4.534
	.00869	.200906	−.324088	4.145	4.121
	.01222	.195498	−.342586	3.967	3.932
1,000 Hz	.00186	.271303	−.254393	6.212	6.124
	.00352	.236102	−.289126	5.668	5.598
	.00580	.213884	−.306022	4.557	4.505
	.00869	.202829	−.325181	4.116	4.075
	.01222	.197747	−.344211	3.932	3.898
5,000 Hz	.00186	.28680	−.256911	5.691	5.603
	.00352	.250604	−.294332	5.298	5.228
	.00580	.228775	−.313647	4.258	4.202
	.00869	.219546	−.336306	3.801	3.755
	.01222	.217546	−.360763	3.552	3.512

In equation (16), $\partial c/\partial\tilde{\alpha}|_\beta$ is obtained with β held constant and in equation (17), $\partial c/\partial\tilde{\alpha}|_\alpha$ is obtained with α held constant. The effect of these conditions on the calculations of g's and r's is discussed in Appendix B.

3 Computational Procedure

The computer program that solves the systems of equation (10) and (12) is coupled with a boundary layer program [4]. The boundary layer program provides information about velocities in x and z directions, and their first and second derivatives in the y-direction and the distribution of the temperature across the boundary layer with its first and second derivative. The solution of the systems (10) and (12) uses an orthonormalization scheme. The number of orthonormalizations is calculated as a linear function of the Reynolds number with the constants of proportionality controlled from the input. A Newton-Raphson iteration scheme converges to the eigenvalue. The iteration scheme of Mueller did not provide any advantage. The Prandtl number is kept constant, equal to the one in the boundary layer program. We used Sutherland's law to relate the viscosity to the temperature. The ratio of the second viscosity coefficient to the first viscosity coefficient is kept equal to $\kappa = 0.8$.

4 Results and Discussion

To test the validity of the method that was developed and to examine previous work, we compare results from the present study with existing calculations of the stability of the three-dimensional boundary layer. An available method is the program SALLY [4]. Because SALLY uses incompressible theory, the present method was applied with a Mach number of .01 and a uniform temperature distribution $T = 1$, for all y. Table 1 shows the temporal amplification rates ω_i obtained from the two programs for three frequencies 500, 1,000, and 5,000 Hz and for five x/C positions that are close to the leading edge. The wavenumbers α and β are shown, which correspond to unstable waves with phase velocities directed inboard. The amplification rates are the same to within approximately 1 percent.

We next examine the stability of crossflow disturbances over the different regions of the wing. Crossflow is defined as the boundary layer velocity profile normal to the local potential streamline. Figure 2 shows the velocity profiles in the direction of the external streamline and in the direction of crossflow for the five x/C positions. The amount of the crossflow decreases around the midchord and increases again towards the rear end of the airfoil.

The region close to the leading edge is investigated first. The instability is due to crossflow. Figure 3 shows the temporal amplification rate ω_i for a constant magnitude of the wavenumber k. The compressibility stabilizes the disturbance but its effect on the amplification rate does not exceed 10 percent around the maximum ω_i. The unstable waves have their phases oriented in a narrow band of angles ψ about 90 ° away from the direction ψ_p of the external streamline. Waves that travel in both positive and negative x-directions are unstable. The maximum amplified wave travels upstream. Keeping the wavenumber positive, the waves that travel in the negative x-direction have negative frequencies. The range of unstable frequencies is large. If the temporal amplification rate ω_i is plotted versus the magnitude of the wavenumber k, for a constant frequency f, a clear maximum exists, as shown in Fig. 4. This maximum was used to develop the envelope method [4].

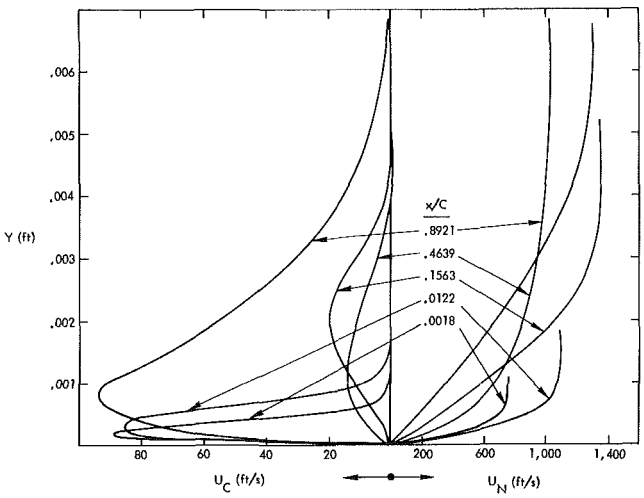

Fig. 2 The velocity profiles in the direction of the potential flow, U_N, and in the crossflow direction, U_C

The same behavior of the instabilities due to crossflow is shown in Figs. 5 and 6 for a station close to the trailing edge of the wing where the crossflow is strong. However, the range of unstable frequencies is much smaller. Although the Reynolds number based on the streamwise chord is about 14 million, the boundary layer is assumed laminar because of the imposed suction. For more details about this particular wing and about the stability of the boundary layer in the mid-chord region, the reader should consult references [7 and 8].

From the above results it is clear that when temporal stability theory is used, there is no ambiguity about defining a maximum amplification rate for a particular unstable frequency. This maximum can be captured with search techniques, as has been shown in reference [4]. However, this

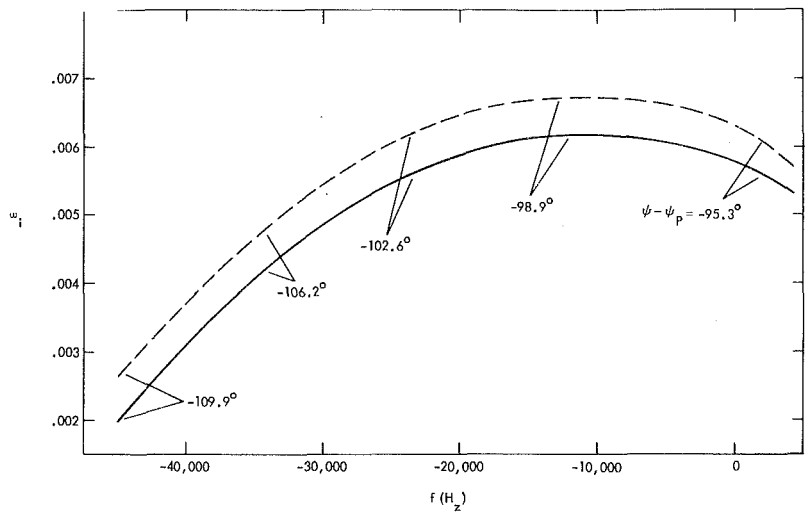

Fig. 3 The variation of the temporal amplification rate ω_i with the frequency *f*. x C = 0.00186, *k* = 0.4, compressible theory (____), incompressible theory (. . .).

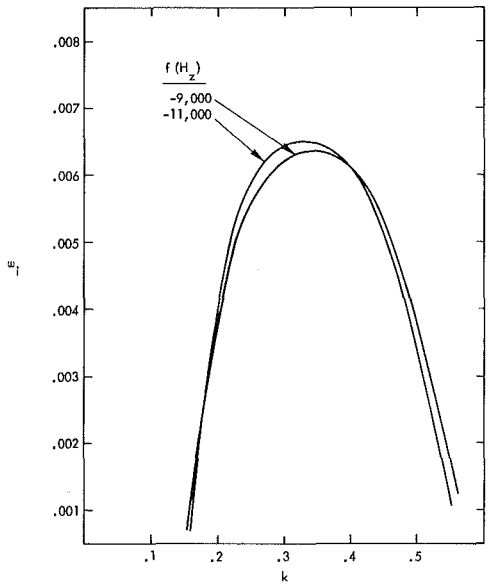

Fig. 4 The variation of the temporal amplification rate ω_i with the wavenumber *k*, x/C = 0.00186, compressible theory

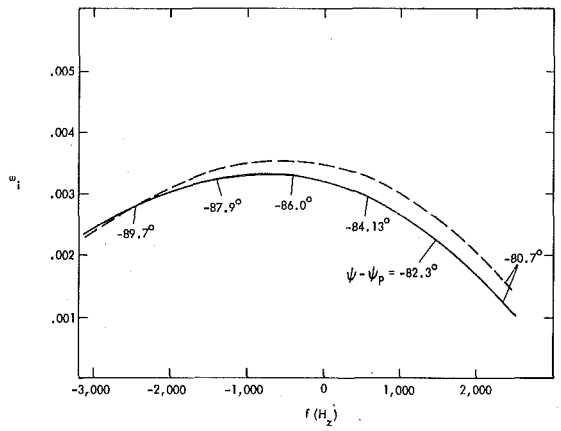

Fig. 5 The variation of the temporal amplification rate ω_i with the frequency *f*, x/C = 0.8921, *k* = 0.36, compressible theory (____), incompressible theory (---).

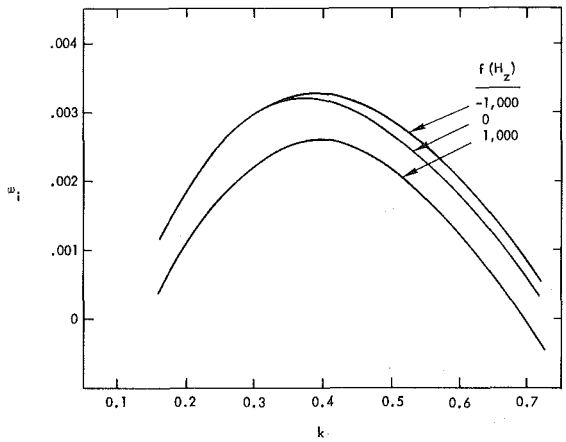

Fig. 6 The variation of the temporal amplification rate ω_i with the wavenumber *k*. x/C = 0.8921, compressible theory.

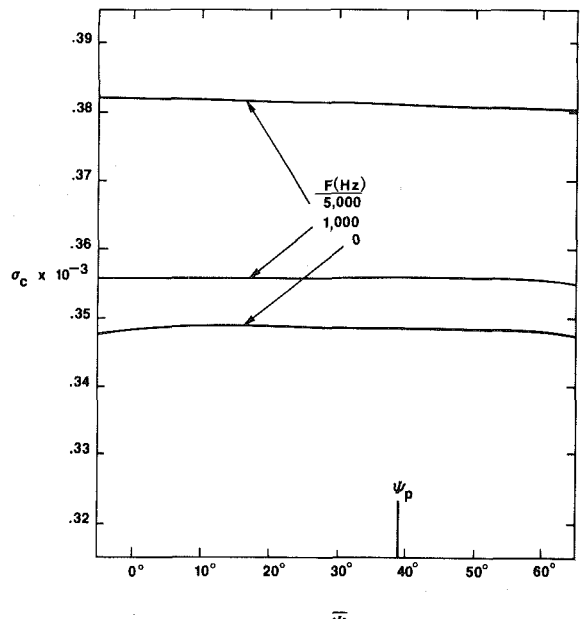

Fig. 7 The variation of the growth rate σ_c with the growth direction $\bar{\psi}$ at x/C = .0058

is not so when the spatial theory is used. Both analytical and numerical difficulties exist, as will be shown next.

To integrate the local amplification rate and to obtain total growth estimates, called N factor [1], one needs to know the direction of the propagation of the disturbances. In three-dimensional flows this direction does not have to coincide with the direction of growth, given by the solution of the eigenvalue problem, if one uses spatial stability theory. For conservative wave systems, the direction is defined by the real group velocity vector, for the particular component of the spectrum. For nonconservative systems, the group velocity is a complex vector. Nayfeh [11] and Cebeci and Stewartson [12] proposed that the eigenvalue problem should be solved so that the complex components of the group velocity vector define a real physical direction. This direction is the direction of propagation. This means that the ratio V_β/V_α is a real number.

The condition described in the previous paragraph does not fully resolve the problem of calculating N factors. Since the group velocities are obtained from a local calculation, this condition applies strictly to homogeneous systems. An example of a homogeneous system is fully developed pipe flow. The growing boundary layer is a nonhomogeneous system. Also, the requirement that the ratio of the group velocities be real, still leaves one degree of freedom for the spatial problem unspecified [13]. That is, one can compute different eigenvalues that have real ϕ, by choosing $\bar{\psi}$, or β_r, as an independent variable. In reference [12], ϕ was kept constant and equal to the value computed at neutral stability.

In the temporal problem, if one insists on keeping ω_r constant and V_β/V_α real, then the eigenvalue problem is determined uniquely. Locally, for constant frequency ω_r,

$$d\omega_r = \frac{\partial \omega_r}{\partial \alpha} d\alpha + \frac{\partial \omega_r}{\partial \beta} d\beta = 0 \tag{18}$$

Because V_β/V_α is real,

$$\frac{\partial \omega_r/\partial \alpha}{\partial \omega_r/\partial \beta} = \frac{\partial \omega_i/\partial \alpha}{\partial \omega_i/\partial \beta} \tag{19}$$

Equations (18) and (19), together with $\omega_i = \omega_i\ (\alpha,\beta)$ give

$$d\omega_i = 0 \tag{20}$$

which means that ω_i is at an extremum. In reference [4], this extremum was found to be a maximum. This fact is used in references [1 and 4] to calculate N factors when the "envelope" method of computation is selected. To the author's knowledge, no other extremum has been calculated that satisfies both equations (18) and (20).

If spatial stability theory is used, however, things are more complicated. The reason is that there is more than one way to satisfy the condition that the angle ϕ, defined in equation (5), is real. Because this is so one would like to select the wave that, locally, is most amplified in the direction of propagation. That is, the quantity

$$\sigma_\phi = -\alpha_i \cos\phi - \beta_i \sin\phi \tag{21}$$

must be a maximum.

In the computational procedure, $\bar{\psi}$ was chosen as a parameter and k updated so that ϕ was real. Figure 7 shows the resulting growth rate

$$\sigma_c = -\alpha_i - \beta_i \tan\phi \tag{22}$$

normalized with the wing chord C, for frequencies of 0, 1 and 5 kHz and for a station close to the leading edge. Similar results were obtained for other stations close to the leading edge of the wing.

In these calculations, the value of σ_c is almost constant, independent of the angle $\bar{\psi}$. The resulting group velocities have almost identical ϕ.

The range of the resulting wavenumber k is very narrow, but this range varies significantly with the chordwise coordinate x/C. Hence, in order to compute N factors, one can choose any of these waves with very small error. For the cases examined the error is always less than $\sim .3$ percent.

These computations were restricted to crossflow instabilities. The wavenumber k was oriented in a direction ψ close to the crossflow direction. The resulting range of ψ is very small, as found before [5,6,8]. Based on these results, N factors should be computed using $\bar{\psi} = \psi_p$ and V_β/V_α real, because the waves with real ϕ result in growth rates in the direction ϕ which are almost identical.

When the angle $|\bar{\psi} - \psi_p|$ was increased beyond $\sim 40°$, the iteration scheme used failed to converge to an eigenvalue. Hence, it was not possible to produce growth rates with ϕ real. Thus, the conclusions are valid for the limited range of $\bar{\psi}$, for which eigenvalue convergence was obtained.

In summary, the problem of the propagation of laminar instabilities due to crossflow on a swept wing has been examined using linear theory and the following points have been noted.

1. When the crossflow is strong, the effect of compressibility on the amplification rates is small and stabilizing.
2. The crossflow instability has a large band of unstable frequencies close to the leading edge of a transonic swept wing.
3. When the condition of real ϕ (equation (15)) is applied to monochromatic waves with temporal stability, it results in a single eigenvalue with maximum amplification rate. When applied with spatial stability, the growth in the direction of propagation is independent of the direction of the wave growth $\bar{\psi}$. The direction of propagation, ϕ, remains almost constant. The variation of the wavenumber vector ϕ an its direction ψ is very small. These results are valid only for the cases where eigenvalue convergence is possible.

Acknowledgment

The work was supported by Lockheed-Georgia's IR & D program.

References

1 Hefner, J. N., and Bushnell, D. M., "Application of Stability Theory to Laminar Flow Control," AIAA Paper No. 79-1493.

2 Gregory, N., Stuart, J. T., and Walker, W. S., "On the Stability of Three-Dimensional Boundary Layers with Application to the Flow Due to a Rotating Disk," *Phil. Trans. Roy. Soc., London*, Vol. A248, 1955, p. 155.

3 Mack, L. M. "Transition Prediction and Linear Stability Theory," in Laminar-Turbulent Transition, AGARD Conference Proceedings No. 224, 1977, pp. 1-1 to 1-22.

4 Srokowski, A. J., and Orszag, S. A., "Mass Flow Requirements for LFC Wing Design," AIAA Paper No. 77-1222.

5 Mack, L. M., "Three-Dimensional Effects in Boundary Layer Stability," in Proceedings of 12th Symposium on Naval Hydrodynamics, June 5-9, 1978.

6 Nayfeh, A. H., and Padhye, A., "The Relation Between Temporal and Spatial Stability in Three-Dimensional Flows," *AIAA Journal*, Vol. 17, No. 10, 1978, pp. 1084, 1090.

7 Mack, L. M., "On the Stability of the Boundary Layer on a Transonic Swept Wing," AIAA Paper No. 79-0264.

8 Lekoudis, S. G., "Stability of Three-Dimensional Compressible Boundary Layers Over Wings with Suction," AIAA Paper No. 79-0265.

9 Runyan, L. J., and George-Falvy, D., "Amplification Factors at Transition on an Unswept Wing in Free Flight and on a Swept Wing in Wind Tunnel," AIAA Paper No. 79-0267.

10 Runyan, L. J., and Steers, L. L., "Boundary Layer Stability Analysis of a Natural Laminar Flow Above on the F-III Tact Airplane," LTV Conference in Drag Reduction, Dallas, Texas, 1979.

11 Nayfeh, A. H., "Stability of Three-Dimensional Boundary Layers," *AIAA Journal*, Vol. 18, No. 4, 1980, pp. 406, 416.

12 Cebeci, T., and Stewartson, K., "On Stability and Transition in Three-Dimensional Flows," *AIAA Journal*, Vol. 18, No. 4, 1980, pp. 398, 405.

13 Lekoudis, S. G., "The Stability of the Boundary Layer on a Swept Wing with Wall Cooling," *AIAA Journal*, Vol. 18, No. 9, 1980, pp. 1029-1035.
14 Mack, L. M., "Boundary-Layer Stability Theory," Report 900-277, Rev. A, Jet Propulsion Laboratory, Pasadena, Calif., Nov. 1969.

APPENDIX A

$$h_1 = \frac{1}{\alpha\tilde{\mu}}\left(-\frac{\tilde{R}}{\tilde{\alpha}} + \frac{\partial\tilde{R}}{\partial\tilde{\alpha}}\right) + \frac{2(2+\kappa)}{3} i\gamma\left[2(\tilde{U}-c)\tilde{M}\frac{\partial\tilde{M}}{\partial\tilde{\alpha}} + \tilde{M}^2\frac{\partial\tilde{U}}{\partial\tilde{\alpha}}\right] \quad \text{(A-1)}$$

$$h_2 = -\frac{2(2+\kappa)}{3} i\gamma\,\tilde{M}^2 \quad \text{(A-2)}$$

$$H = \frac{\tilde{R}}{\tilde{\alpha}\mu} + \frac{2(2+\kappa)}{3} i\gamma\,\tilde{M}^2(\tilde{U}-c) \quad \text{(A-3)}$$

$$q_{21} = 2\tilde{\alpha} + i\left(\tilde{R} + \tilde{\alpha}\frac{\partial\tilde{R}}{\partial\tilde{\alpha}}\right)\left(\frac{\tilde{U}-c}{\mu T}\right) + \frac{i\tilde{\alpha}\tilde{R}}{\mu T}\frac{\partial\tilde{U}}{\partial\tilde{\alpha}} \quad \text{(A-4)}$$

$$q_{23} = \left(\tilde{R}\tilde{U}' + \tilde{\alpha}\tilde{U}'\frac{\partial\tilde{R}}{\partial\tilde{\alpha}} + \tilde{\alpha}\tilde{R}\frac{\partial\tilde{U}'}{\partial\tilde{\alpha}}\right)/(\mu T) - 2\mathrm{i}\alpha\left[\frac{1}{\mu}\frac{d\mu}{dT} + \frac{(1+2\kappa)}{3T}\right]T' \quad \text{(A-5)}$$

$$q_{24} = \mathrm{i}\left(\tilde{R} + \tilde{\alpha}\frac{\partial\tilde{R}}{\partial\tilde{\alpha}}\right)/\mu - \frac{(1+2\kappa)\gamma}{3}\left[2\tilde{\alpha}\tilde{M}^2(\tilde{U}-c) + 2\tilde{M}\tilde{\alpha}^2(\tilde{U}-c)\frac{\partial\tilde{M}}{\partial\tilde{\alpha}} + \tilde{\alpha}^2\tilde{M}^2\frac{\partial\tilde{U}}{\partial\tilde{\alpha}}\right] \quad \text{(A-6)}$$

$$q_{25} = (1+2\kappa)\left[2\tilde{\alpha}(\tilde{U}-c) + \tilde{\alpha}^2\frac{\partial\tilde{U}}{\partial\tilde{\alpha}}\right]/(3\mathrm{T}) - \frac{1}{\mu}\frac{d}{dT}\frac{\partial\tilde{U}''}{\partial\tilde{\alpha}} - \frac{T'}{\mu}\frac{d^2\mu}{dT^2}\frac{\partial\tilde{U}'}{\partial} \quad \text{(A-7)}$$

$$q_{26} = \frac{1}{\mu}\frac{d\mu}{dT}\frac{\partial\tilde{U}'}{\partial\tilde{\alpha}} \quad \text{(A-8)}$$

$$q_{34} = -\mathrm{i}\gamma\left[2\tilde{M}(\tilde{U}-c)\frac{\partial\tilde{M}}{\partial\tilde{\alpha}} + \tilde{M}^2\frac{\partial\tilde{U}}{\partial\tilde{\alpha}}\right] \quad \text{(A-9)}$$

$$q_{35} = \frac{i}{T}\frac{\partial\tilde{U}}{\partial\tilde{\alpha}} \quad \text{(A-10)}$$

$$q_{41} = -\frac{a_{41}h_1}{H} \quad \text{(A-11)}$$

$$q_{42} = -\frac{ih_1}{H^2} \quad \text{(A-12)}$$

$$q_{43} = \left[-a_{43}h_1 - 2\tilde{\alpha} - i\left(\frac{\tilde{U}-c}{\mu T}\right)\left(\tilde{R} + \tilde{\alpha}\frac{\partial\tilde{R}}{\partial\tilde{\alpha}}\right) - \frac{i\tilde{\alpha}\tilde{R}}{\mu T}\frac{\partial\tilde{U}}{\partial\tilde{\alpha}}\right]/H \quad \text{(A-13)}$$

$$q_{44} = \frac{a_{44}h_1}{H} + \frac{2a_{44}}{M}\frac{\partial\tilde{M}}{\partial\tilde{\alpha}} - \frac{2\mathrm{i}(2+\kappa)}{3H}\gamma\tilde{M}^2 \times\left(\frac{T'}{T}\frac{d\mu}{dT}\frac{\partial\tilde{U}}{\partial\tilde{\alpha}} + \frac{\partial\tilde{U}'}{\partial\tilde{\alpha}}\frac{T'}{T}\frac{\partial\tilde{U}}{\partial\tilde{\alpha}}\right) \quad \text{(A-14)}$$

$$q_{45} = -\frac{a_{45}h_1}{H} + \frac{i}{H}\left(\frac{1}{\mu}\frac{d\mu}{dT} + \frac{2(2+\kappa)}{3T}\right)\frac{\partial\tilde{U}'}{\partial\tilde{\alpha}} + \frac{2(2+\kappa)}{3\mu T}\frac{T'}{\mu T}\frac{d\mu}{dT}\frac{\partial\tilde{U}}{\partial\tilde{\alpha}} \quad \text{(A-15)}$$

$$q_{46} = \frac{1}{H}\left(-a_{46}h_1 + \frac{2(2+\kappa)}{3T}\frac{\partial\tilde{U}}{\partial\tilde{\alpha}}\right) \quad \text{(A-16)}$$

$$q_{63} = \frac{\mathrm{Pr}T'}{\mu T}\left(\tilde{R} + \tilde{\alpha}\frac{\partial\tilde{R}}{\partial\tilde{\alpha}}\right) - 2i\mathrm{Pr}(\gamma-1)\left(\tilde{\alpha}^2\tilde{M}^2\frac{\partial\tilde{U}'}{\partial\tilde{\alpha}} + 2\tilde{\alpha}\tilde{U}'\tilde{M}^2 + 2\tilde{M}\tilde{U}'\tilde{\alpha}^2\frac{\partial\tilde{M}}{\partial\tilde{\alpha}}\right) \quad \text{(A-17)}$$

$$q_{64} = -\frac{\mathrm{i}(\gamma-1)\mathrm{Pr}}{\mu}\left\{\tilde{\alpha}\tilde{R}\tilde{M}^2\frac{\partial\tilde{U}}{\partial\tilde{\alpha}} + (\tilde{U}-c)\left[\left(\tilde{R} + \tilde{\alpha}\frac{\partial\tilde{R}}{\partial\tilde{\alpha}}\right)M^2 + 2\tilde{M}\tilde{\alpha}\tilde{R}\frac{\partial\tilde{M}}{\partial\tilde{\alpha}}\right]\right\} \quad \text{(A-18)}$$

$$q_{65} = \frac{i\mathrm{Pr}}{\mu T}\left[(\tilde{U}-c)\left(\tilde{R} + \tilde{\alpha}\frac{\partial\tilde{R}}{\partial\tilde{\alpha}}\right) + \tilde{\alpha}\tilde{R}\frac{\partial\tilde{U}}{\partial\tilde{\alpha}}\right] + 2\tilde{\alpha} - 2\mathrm{Pr}(\gamma-1)\frac{1}{\mu}\frac{d\mu}{dT}\left[\left(\tilde{U}'\frac{\partial\tilde{U}'}{\partial\tilde{\alpha}} + \tilde{W}'\frac{\partial\tilde{W}'}{\partial\tilde{\alpha}}\right)M^2 + (\tilde{U}'^2 + \tilde{W}'^2)\tilde{M}\frac{\partial\tilde{M}}{\partial\tilde{\alpha}}\right] \quad \text{(A-19)}$$

$$r_{21} = -\frac{i\tilde{\alpha}\tilde{R}}{\mu T} \quad \text{(A-20)}$$

$$r_{24} = (1+2\kappa)\gamma\tilde{M}^2\tilde{\alpha}^2/3 \quad \text{(A-21)}$$

$$r_{25} = -(1+2\kappa)\tilde{\alpha}^2/(3T) \quad \text{(A-22)}$$

$$r_{34} = -\mathrm{i}\gamma\tilde{M}^2 \quad \text{(A-23)}$$

$$r_{35} = -\frac{i}{T} \quad \text{(A-24)}$$

$$r_{41} = -\frac{h_2 a_{41}}{H} \quad \text{(A-25)}$$

$$r_{42} = -\frac{ih_2}{H^2} \quad \text{(A-26)}$$

$$r_{43} = \left(-a_{43}h_2 + \frac{\mathrm{i}\tilde{\alpha}\tilde{R}}{\mu T}\right)/H \quad \text{(A-27)}$$

$$r_{44} = -\frac{a_{44}}{H}h_2 + \frac{2i}{3H}(2+\kappa)\gamma\tilde{M}^2\left(\frac{T'}{\mu}\frac{d\mu}{dT} + \frac{T'}{T}\right) \quad \text{(A-28)}$$

$$r_{45} = -\frac{a_{45}h_1}{H} - \frac{2\mathrm{i}(2+\kappa)}{3\mu\mathrm{T}H}T'\frac{d\mu}{dT} \quad \text{(A-29)}$$

$$r_{46} = \frac{1}{H}\left(-a_{46}h_2 - \frac{2(2+\kappa)}{3T}\right) \quad \text{(A-30)}$$

$$r_{64} = i(\gamma-1)\mathrm{Pr}\tilde{\alpha}\tilde{R}\tilde{M}^2/\mu \quad \text{(A-31)}$$

$$r_{65} = -\frac{\mathrm{i}\tilde{\alpha}\tilde{R}\mathrm{Pr}}{\mu T} \quad \text{(A-32)}$$

All the rest of q_{ij} and r_{ij} are zero.

APPENDIX B

When α is held constant,

$$\frac{\partial \tilde{R}}{\partial \tilde{\alpha}} = -\frac{\tilde{R}}{\tilde{\alpha}} \tag{B-1}$$

$$\frac{\partial \tilde{M}}{\partial \tilde{\alpha}} = -\frac{\tilde{M}}{\tilde{\alpha}} \tag{B-2}$$

$$\frac{\partial \tilde{U}}{\partial \tilde{\alpha}} = \frac{\tilde{q}}{\alpha\beta} W \tag{B-3}$$

$$\frac{\partial \tilde{U}'}{\partial \tilde{\alpha}} = \frac{\tilde{\alpha}}{\alpha\beta} W' \tag{B-4}$$

$$\frac{\partial \tilde{U}''}{\partial \tilde{\alpha}} = \frac{\tilde{\alpha}}{\alpha\beta} W'' \tag{B-5}$$

$$\frac{\partial \tilde{W}'}{\partial \tilde{\alpha}} = -\frac{\tilde{\alpha}}{\alpha\beta} U' \tag{B-6}$$

When β is held constant,

$$\frac{\partial \tilde{R}}{\partial \tilde{\alpha}} = \frac{R}{\alpha} - \frac{\tilde{R}}{\tilde{\alpha}} \tag{B-7}$$

$$\frac{\partial \tilde{M}}{\partial \tilde{} } = \frac{M}{\alpha} - \frac{\tilde{M}}{\tilde{\alpha}} \tag{B-8}$$

$$\frac{\partial \tilde{U}}{\partial \tilde{\alpha}} = -\frac{\tilde{\alpha}\beta}{\alpha^3} W \tag{B-9}$$

$$\frac{\partial \tilde{U}'}{\partial \tilde{\alpha}} = -\frac{\tilde{\alpha}\beta}{\alpha^3} W' \tag{B-10}$$

$$\frac{\partial \tilde{U}''}{\partial \tilde{\alpha}} = -\frac{\tilde{\alpha}\beta}{\alpha^3} W'' \tag{B-11}$$

$$\frac{\partial \tilde{W}'}{\partial \tilde{\alpha}} = \frac{\tilde{\alpha}\beta}{\alpha^3} U'' \tag{B-12}$$

The $U(y)$ and $W(y)$ are the boundary layer velocity components in the x and z directions, respectively, and

$$R = \frac{U_e{}^* \delta^*}{\nu e^*} \tag{B-13}$$

$$M = U_e{}^* / \gamma R T_e{}^* \tag{B-14}$$

$$\tilde{R} = \frac{R\alpha}{\tilde{\alpha}} \tag{B-15}$$

$$\tilde{M} = \frac{M\alpha}{\tilde{\alpha}} \tag{B-16}$$

$$\tilde{U} = U + \frac{\beta}{\alpha} W \tag{B-17}$$

$$\tilde{W} = -\frac{\beta}{\alpha} U + W \tag{B-18}$$

The definition of a_{ij} is contained in reference [14].

A Theoretical Model for the Transverse Impingement of Free Jets at Low Reynolds Numbers

R. Winton
Structural Dynamics Research Corporation, Toronto, Canada.

H.R. Martin
University of Waterloo, Ontario, Canada

There are many applications in industrial fluid mechanics and fluidic technology where jets of fluid interact. This paper examines the interaction of two liquid laminar free jets under low Reynolds number conditions and particularly highlights the phenomenon of the inwards deflecting jet. A potential flow solution is developed for the modelling of the control jet flow in the vicinity of the control nozzle exit plane, which demonstrates the presence of a net suction force modifying the momentum interaction of the two orthogonal jets under these low Reynolds number conditions.

1. Introduction

The objective of this particular study is to develop a generalized mathematical model which adequately describes the resultant deflection of two free Newtonian liquid laminar jets which impinge at right angles, especially under very low Reynolds number conditions. An example of the application of this model is the development of the liquid jet amplifier described in [1].

Consider in the first instance a free laminar jet of Newtonian fluid issuing from a vertical nozzle downwards through an essentially inviscid medium such as air and in the absence of a deflecting body. Middleman and Gavis [2] have shown that such jets contract or expand depending on the conditions of ejection and fluid properties. Ignoring gravitational effects, jets with Re $>$ 16 are found to contract and such contraction is influenced by viscous dissipation due to relaxation of the velocity profile downstream of the nozzle exit [3].

One important consequence of the contraction of the capillary jet is the direct reduction of surface energy with surface area per unit length. The mutual attraction between liquid molecules near a surface creates a surface tension so that the liquid surface behaves like a stretched membrane. With the reduction of jet diameter there is a simultaneous increase in internal pressure which is given by the familiar pipe tension equation

$$P = 2\sigma/d \tag{1}$$

The existence of a surface tension stress within the free surface of capillary jets allows one to visualize such jets as consisting of a "fluid membrane" enclosing a column of liquid at a pressure greater than the surrounding atmosphere. When a transverse laminar jet is now allowed to impinge on such a vertical jet of much higher kinetic energy, three different effects have been observed experimentally [4], Fig. 1 (*a*), (*b*), (*c*).

(*a*) In Fig. 1(*a*) an extremely low transverse jet flow is applied. Under these conditions the vertical jet behaves very much like a wall since the kinetic energy of the transverse jet is insufficient to penetrate the "fluid membrane."

(*b*) Fig. 1(*b*) shows the much more common situation of two impacting jets where the resultant deflection is away from the transverse jet.

(*c*) Fig. 1(*c*) shows an unusual phenomena of the inward deflecting jet used to develop the fluidic amplifier described in [1]. The vertical jet Reynolds number is in the range 2000 $>$ Re_j $>$ 1000 and for the transverse control jet 800 $>$ Re_c $>$ 300.

2 The Inward Deflected Jet

The photographs shown above were the result of introducing a fluorescent tracer dye into the transverse nozzle upstream of the flow exit. Fig. 1(*c*) shows quite clearly, that the two jets, after impact, essentially retain their original integrities for at least four to five nozzle diameters downstream of the interaction zone. Thus observation infers that there is virtually no mixing between the vertical and horizontal streams, except possibly for a very limited amount of laminar diffusion at the interfacial stream surface where the action of viscous shear establishes a thin vortex street.

The argument can now be presented that, in the case of inwardly deflected jets, the net transverse kinetic energy of the control flow is sufficient to penetrate the so called "fluid membrane" of the vertical jet, yet insufficient to directly disturb the fluid particles at the centre. Coalescence of the two streams, after interaction into a single jet of circular cross section can be shown to minimize the total surface energy of the system [13].

An understanding of the process causing the inward

Contributed by the Fluids Engineering Division for publication in the JOURNAL OF FLUIDS ENGINEERING. Manuscript received by the Fluids Engineering Division, April 27, 1979.

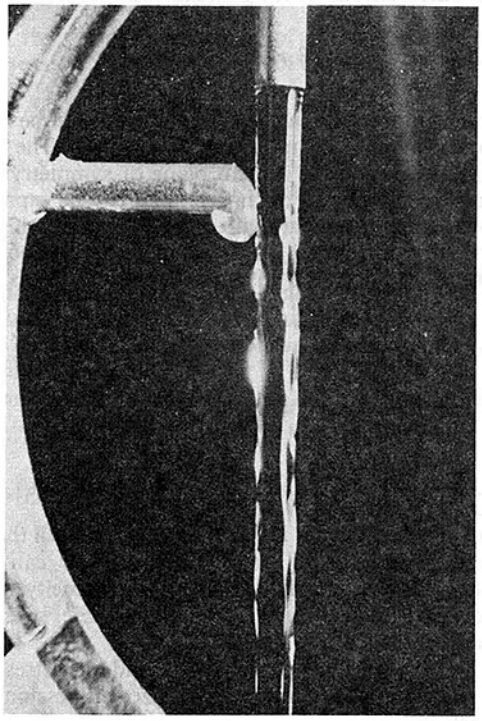

Fig. 1(*a*) Operating conditions: $Re_c = 500$, $Re_j = 1600$ $d_c = d_j = 3.303$ mm
tracer dye: Fluorescien.

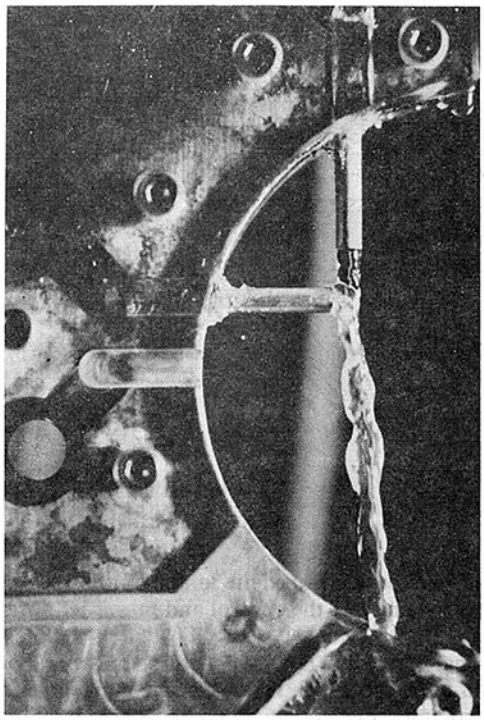

Fig. 1(*b*) Operating conditions: $Re_c = 50$, Re_j 1600 $d_c = d_j = 3.303$ mm

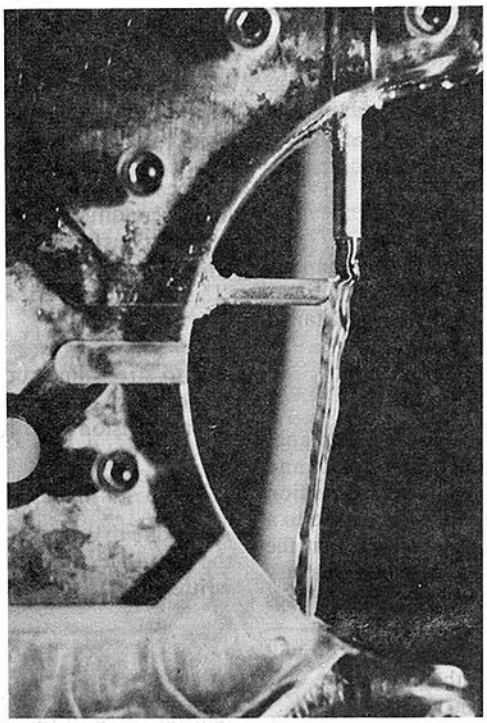

Fig. 1(*c*) Operating conditions: $Re_c = 800$, $Re_j = 1600$ $d_c = d_j = 3.303$ mm

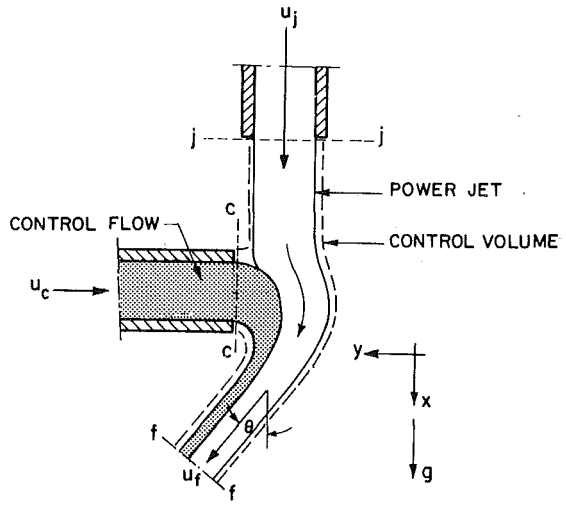

Fig. 2 The control volume

deflection can be developed in terms of the local velocity fields in the vicinity of the control and power jet nozzle exits. Friedman and Martin [1] show through a simple control volume analysis of the impacting flows, that for the inward deflection to be sustained, the net momentum fluxes over the control volume, Fig. 2, must be balanced by a resultant transverse suction force acting at the control nozzle exit area. It has been shown by Malcolm [5], that surface tension effects alone are insufficient to account for this force.

The existence of an effective suction pressure at the control nozzle exit plane can be accounted for, based on potential flow considerations.

The solution of impacting jets in the case where the kinetic energy is large enough to deflect the main jet away from the control jet has been treated by many investigators. At such high Reynolds numbers, where the inertia forces dominate all other effects, the control flow is capable of fully penetrating the main jet and individual integrities of the two jets is lost.

Potential flow solutions and vectorial momentum solutions both show the resultant angle of deflection to be away from the control jet, Fig. 1(b) which can be described by the following model:

$$\theta = \tan^{-1}\left(-\frac{\mathrm{Re}_c^2}{\mathrm{Re}_j^2}\right) \tag{2}$$

The inward deflecting jet, Fig. 1(*c*) is a more complex relationship involving, Reynolds number, Weber number, Froude number and nozzle geometry, requiring a detailed combined control volume and potential flow solution.

3 Control Volume Equations

The selected control volume is shown in Fig. 2. The planes *j-j* and c-c are chosen to cut the exits of the power nozzle and the control nozzle respectively. Downstream of the interaction zone where the combined jets are assumed to have relaxed to a uniform velocity profile, the plane *f-f* is chosen such that the normal to this surface is co-linear with the mean velocity vector $\bar{U}_f$. The remainder of the control volume just encloses the free streamline of both jets.

The velocity profile at the control volume surface *j-j* will depend on the upstream conditions of the main jet. The momentum flux across the surface *j-j* can be written as:

$$J_j = 2\pi \int_0^{d_j/2} \rho . U_j^2 . r . dr \tag{3}$$

With the assumption of a uniform velocity profile at the plane *f-f*, the momentum flux cutting this surface is:

$$J_f = 2\pi \int_0^{d_f/2} \rho . U_f^2 . r . dr = \frac{\pi}{4} . \rho . d_f^2 . \bar{U}_f^2 \tag{4}$$

The momentum flux cutting the plane *c-c* can be resolved into two orthogonal components, J_{cn} and J_{ct}. The velocity field in this region has a vertical plane of symmetry passing through the centreline of the nozzle, and can be expressed in terms of a component parallel to the normal of this plane, U_{cn}, and one tangential, U_{ct}. Hence, the component of momentum flux normal to this plane can be written as

$$J_{cn} = \iint_{A_c} \rho . U_{cn}{}^2 . dA_c \tag{5}$$

and the tangential component as:

$$J_{ct} = \iint_{A_c} \rho . U_{cn} . U_{ct} . dA_c \tag{6}$$

Since the velocity profiles are non-uniform at both the power and control nozzle exits, Stoke's viscosity law can be employed to relate the normal stresses to the velocity field. By virtue of the accepted sign convention these stresses are considered tensile.

For a Newtonian fluid of viscosity μ and bulk stress $\tilde{\sigma}$, one arbitrary component of Stoke's generalized expression may be written as:

$$\sigma_{xx} = \mu\left(2\frac{dVx}{dx} - \frac{2}{3}\,\mathrm{div}\ V\right) + \tilde{\sigma} \tag{7}$$

Conditions of incompressible flow require that in the above expression div $V = 0$ and $\tilde{\sigma} = -P$, where P denotes the thermodynamic pressure. Specifically then for each of the three planes:

$$\sigma_{jj} = 2\,\mu\left(\frac{\partial U_j}{\partial x}\right)_j - P_j \tag{8}$$

$$\sigma_{cc} = 2\,\mu\left(\frac{\partial U_c}{\partial y}\right)_c - P_c \tag{9}$$

$$\sigma_{ff} = -P_f \tag{10}$$

Since the flow from the power nozzle exits into atmosphere under conditions of axial symmetry, the only pressure P_j acting at surface *j-j* will be that due to surface tension, thus from (1):

$$P_j = \frac{2\sigma}{d_j} \tag{11}$$

Due to streamline curvature effects at the control nozzle exit plane, there will be an additional term $P_c{}^*$ to that of the surface tension pressure at *c-c*:

$$P_c = P_c{}^* + \frac{2\sigma}{d_c} \tag{12}$$

Also, due to assumed axial symmetry and capillary effects at the plane *f-f*, the pressure P_f, relative to atmosphere may be written as:

$$P_f = \frac{2\sigma}{d_f} \tag{13}$$

The solid boundary of the power nozzle exerts a surface tension force in the negative X direction on the fluid in the Control Volume, thus:

$$F_j = \pi d_j \sigma \tag{14}$$

A similar force exists at the control exit:

$$F_c = \pi d_c \sigma \tag{15}$$

Finally, the fluid downstream of the section *f-f* exerts a surface tension force on the control volume in the direction of flow:

$$F_f = \pi d_f \sigma \tag{16}$$

Newton's viscosity law may be used to compute the shear stresses τ_{yx_c} acting on the face of the plane *c-c*;

$$\tau_{yx_c} = \mu(\partial U_{ct}/\partial y)_c \tag{17}$$

Equations (3) through (17), together with the external gravitational force, allow a complete momentum flux balance to be written for the control volume shown in Fig. 2. All stresses have been assumed relative to atmosphere which is arbitrarily set to zero.

The complete momentum flux balanced by external forces in the X direction can be written as:

$$2\pi\int_0^{d_j/2}(\rho.U_j^2 - \sigma_{jj}).r.dr + \iint_{A_c}(\rho.U_{ct}.U_{cn} - \tau_{yx_c})dA_c$$

$$-\frac{\pi d_f^2}{4}\cos\theta\left(\rho.\bar{U}_f^2 + \frac{2\sigma}{d_f}\right) = \pi d_j.\sigma - \pi d_f\sigma\cos\theta - L_\rho'\frac{g.\pi d_j^2.\rho}{4} \tag{18}$$

where the last term on the right-hand side of equation (18) is the gravitational force acting on the control volume. The effective volume of this term is the product of the cross-sectional area of the main jet times a representative length, L'.

A similar momentum flux balance for the Y direction yields:

$$\iint_{A_c}(\rho U_{cn}^2 - \sigma_{cc}).dA_c + \left(\rho.\bar{U}_f^2 + \frac{2\sigma}{d_f}\right).\frac{\pi d_f^2}{4}.\sin\theta = \pi d_f\sigma\sin\theta + \pi d_c\sigma \tag{19}$$

A_c and A_j are the cross sectional areas of the control and main jets, respectively.

Generalization of the model presented in equations (18) and (19) can now be achieved through the introduction of suitable dimensionless variables [13], so that the resultant deflection angle model may be expressed as:

$$\frac{J(\tau_{yx_c})}{\mathrm{Re}_c} = \frac{\text{shear stress forces}}{\text{inertia forces}}\text{(control flow)} \equiv \beta_c.\iint_{Ac}\tau_{yx_c}.dA_c$$

$$\frac{J(\partial U_j/\partial x)}{\mathrm{Re}_j} = \frac{\text{viscous relaxation forces}}{\text{inertia forces}}\text{(power jet flow)} \equiv \frac{\beta_j}{4}\iint_{Aj}(\partial U_j/\partial x).dA_j$$

$J(U_{cn}.U_{ct})$ = nondimensional cross momentum correction factor (control jet flow)

$$\equiv \beta_c\int\int_{A_c} U_{cn}.U_{ct}.dA_c$$

$J(U_j^2)$ = nondimensional momentum correction factor (power jet flow) $\beta_j\iint_{A_j}U_j^2.dA_j$

Re = Reynolds number $\equiv \rho.d.\bar{U}/\mu$
We = Weber number $\equiv (d.\rho.\bar{U}^2/\sigma)^{1/2}$
Fr = Froude number $\equiv \bar{U}^2/d.g$
L_c' = nondimensional length ($L_c' \equiv L'/d_c$)
Ω = Ratio of nozzle diameters ($\Omega \equiv d_c/d_j$)

The model of equation (20) indicates that the deflection angle (θ) of two impacting axisymmetric, laminar, incompressible, transverse jets of Newtonian fluid is functionally dependant on both the control and power jet Reynolds numbers, the Weber and Froude numbers of the control jet, the ratio of control to power jet nozzle diameters and a set of dimensionless parameters which describe the flow field at each nozzle exit.

The nature of the velocity field at the control nozzle exit is of fundamental importance since the associated non-dimensional integral terms in J, [13], strongly influence whether the resultant jet deflection will be toward the control nozzle or away from it. The decaying velocity field at the power nozzle exit will be shown to be of lesser importance.

$$\theta = \tan^{-1}\left[\frac{J(U_{cn}^2) - 2\dfrac{J(\partial U_{cn}/\partial y)}{\mathrm{Re}_c} + \dfrac{J(P_c)}{2} - \dfrac{2}{\mathrm{We}_c^2}}{\dfrac{J(\tau_{yx_c})}{\mathrm{Re}_c} + 4\left(\dfrac{\mathrm{Re}_j}{\mathrm{Re}_c}\right)^2.\dfrac{J(\partial U_j/\partial x)}{\mathrm{Re}_j} - J(U_{cn}.U_{ct}) - \left(\dfrac{\mathrm{Re}_j}{\mathrm{Re}_c}\right)^2.J(U_j^2) + \dfrac{2}{\Omega\mathrm{We}_c^2} - \dfrac{L'_c}{\Omega^2\mathrm{Fr}_c}}\right] \tag{20}$$

let: $\beta_c = \dfrac{4}{\pi.\rho.\bar{U}_c^2.d_c^2}$; $\beta_j\dfrac{4}{\pi.\rho.\bar{U}_j^2.d_j^2}$

then: $J(U_{cn}^2)$ = nondimensional axial momentum correction factor (control flow) $\equiv \beta_c\iint_{A_c}.U_{cn}^2.dA_c$

$$\frac{J(\partial U_{cn}/\partial y)}{\mathrm{Re}_c} = \frac{\text{viscous dissipation}}{\text{inertia forces}}\text{(control flow)} \equiv \frac{\beta_c}{2}\iint_{A_c}(\partial U_{cn}/\partial y).dA_c$$

$J(P_c)$ = nondimensional streamline curvature pressure (control flow) $\equiv 2\beta_c\iint_{Ac}P_c^*.dA_c$

4 Solution of the Control Nozzle Exit Velocity Field

With the analytical model described in terms of equation (20) it yet remains to evaluate the non-dimensional integral terms at the control exit plane, namely $J(U_{cn}^2)$, $J(U_{cn}.U_{ct})$, $J(\tau_{yx_c})$, $J(\partial U_{cn}/\partial y)$ and $J(P_c)$.

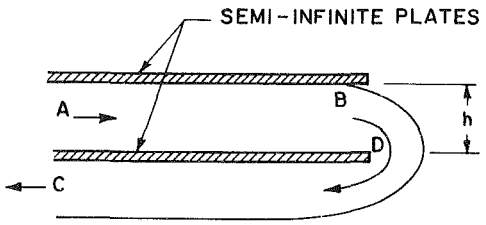

Fig. 3 Jet flow- one free surface

A potential flow approach together with a similarity solution for the velocity field is used, with due regard to limitations in not being able to directly account for the effects of viscosity, gravity and turbulence. This approximation to ideal flow is considered satisfactory since the flow is laminar, non axisymmetric in the interaction zone, and experimental results [13] show that at the control nozzle exit there is very little mixing at the interface between the two jets.

The development is based on the upper half solution of Keller's [12] hydrodynamic description of incompressible jet flow from a nozzle with one free surface, Fig. 3. The equations describing this flow are as follows:

$$z = -\frac{4h}{\pi}\log\cosh\left(\frac{\pi\omega}{4q}\right) \tag{21}$$

where z and ω are the complex variables

$$z = x + iy \tag{22}$$

$$\omega = \phi + i\psi \tag{23}$$

$$\Phi = \frac{\pi\phi}{4q}, \Psi = \frac{\pi\psi}{4q}, X = \frac{-\pi x}{4h}, Y = \frac{-\pi y}{4h} \tag{24}$$

x,y = physical coordinates
ϕ = velocity potential
ψ = stream function
i = imaginary number $\sqrt{-1}$
q = volumetric flow rate
h = separation of semi infinite plates

Equations (21) through (24) can be solved for the streamlines (25) and velocity potential lines (26), respectively.

$$X = \ln\sin\Psi - \ln\cos Y - \tfrac{1}{2}\ln(\tan^2\Psi - \tan^2 Y) \tag{25}$$

$$X = \ln\sinh\Phi - \ln\cos Y - \tfrac{1}{2}\ln(\tan^2 Y + \tanh^2\Phi) \tag{26}$$

The flow net, Fig. 4, is computed from equations (25) and (26) for increments in both ϕ and ψ of $q/10$.

Through application of the Cauchy-Riemann conditions [13] the nondimensional field velocities Vx and Vy are computed from the scalar velocity potential Φ and the stream function Ψ.

$$Vx = \frac{-e^{2X}(\tan^2 Y + \tanh^2\Phi)}{\tanh^2\Phi.\mathrm{Sech}^2\Phi(e^{2X} - \mathrm{Sec}^2 Y.\mathrm{Cosh}^4\Phi)} \tag{27}$$

$$Vy = \frac{\tan Y.\mathrm{Sec}^2 Y(\mathrm{Sinh}^2\Phi - e^{2X})}{\tanh^2\Phi.\mathrm{Sech}^2\Phi(e^{2X} - \mathrm{Sec}^2 Y.\mathrm{Cosh}^4\Phi)} \tag{28}$$

where:
$$Vx = v_x.\frac{h}{q}, Vy = v_y.\frac{h}{q} \tag{29}$$

Bernoulli's equation can be employed to derive the pressure profile from the velocity field:

$$P = Po + \rho\frac{Vo^2}{2}\left[1 - \left(\frac{V}{Vo}\right)^2\right] \tag{30}$$

where Po = reference pressure at $X = -\infty$
Vo = magnitude of velocity at $X = -\infty$
V = magnitude of velocity at the point of evaluation of P.

for $Po = 0$ and $Vo = 1.0$ at $X = -\infty$, then

$$P_c^* = 1 - (Vx^2 + Vy^2) \tag{31}$$

and
$$P_c^* = \frac{2P}{\rho Vo^2} \tag{32}$$

Computed nondimensional pressure profiles P_c^* are shown in Fig. 5 for $0.2 \geq X > 0$ confirming the hypothesis of the existence of a net suction pressure at the control nozzle exit.

With the development of expressions for the velocity field at the exit of the control nozzle, namely equations (27) and (28), it is now possible to solve the momentum flux balance for the control volume, equations (20). This procedure is detailed in [13]. From computer algorithms developed to solve these equations the values for the nondimensional parameters in J at the control nozzle exit plane ar tabulated as follows:

Table 1

$J(U_{cn}{}^2)$	$J(\partial U_{cn}/\partial y)$	$J\left(\tau_{yx_c}\right)$	$J(P_c)$	$J(U_{cn}.U_{ct})$
1.038	0.327	0.799	−0.514	0.277

4.1 Discussion of the Model

(*i*) *Power Jet Flow Parameters.* Laminar flow within the power nozzle will reach a proportion of the fully developed velocity profile given by the parabolic distribution

$$u_j = 2\bar{U}_j\left[1 - \left(\frac{2r}{d_j}\right)^2\right] \tag{33}$$

Langhaar [7] and Hornbeck [8], have shown that the actual profile at the power nozzle exit is dependent on the ratio

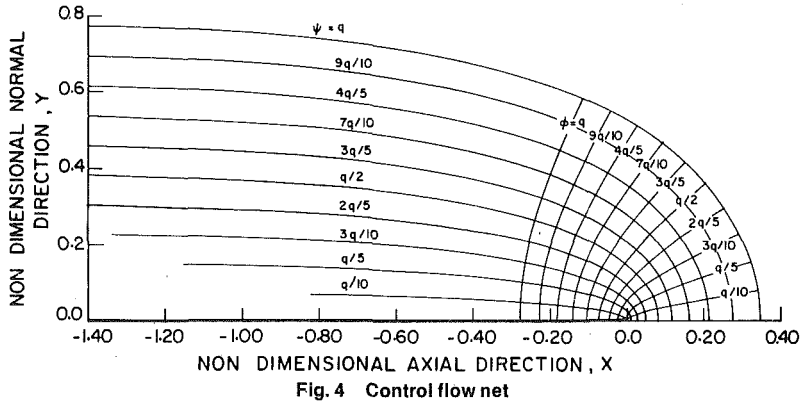

Fig. 4 Control flow net

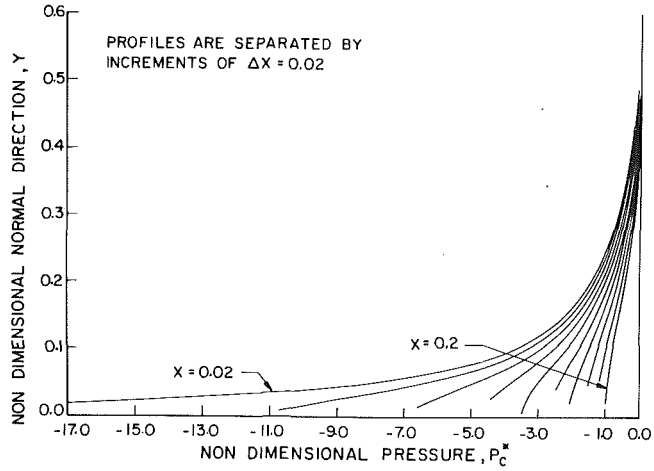

Fig. 5 Pressure profiles downstream of the control nozzle exit plane

$l/d_j.\mathrm{Re}_j$, where l is the power jet nozzle length. These results have implications on the solution of the non-dimensional power jet momentum correction integral $J(U_j^2)$. The paper of Beatty and Markland [14] gives a plot of $J(U_j^2)$ as a function of $l/d_j.\mathrm{Re}_j$. Based on the l/d_j ratio of 12:1 typical for the device illustrated in Figs. 1(*a*) – 1(*c*), the range of $J(U_j^2)$ is tabulated below as a function of the power jet Reynolds numbers (Re_j) used in this study.

Table 2

Re_j	$J(U_j^2)$	$J(\partial U_j/\partial x)$	$J(\partial U_j/\partial x)/\mathrm{Re}_j$
1000	1.245	1.6847	0.001685
2500	1.151	3.9031	0.001561
$\mathrm{Re}_c\min = 400$		$\mathrm{Re}_c\max = 1000$	

Upon ejection of the power jet into air the velocity profile is free to relax and assume uniformity some distance downstream. As the jet leaves the nozzle and the wall shear suddenly vanishes, the velocity profile will begin to relax in the power jet flow direction at a rate given by $(\partial U_j/\partial x)$. Thus in the vicinity of the power jet exit plane *j-j*, the non-dimensional normal relaxation stress $(\partial U_j'/\partial x')$ will be finite.

Gavis [9] gives an empirical formula for the integrated non-dimensional relaxation stress applicable at the power jet exit plane for a capillary jet of Newtonian fluid ejected into air as:

$$N \equiv \int_0^1 (\partial U'/\partial x').r'.dr' \equiv J(\partial U_j/\partial x) \tag{34}$$

where $$N = \frac{\mathrm{Re}_j}{8}\left[\frac{4}{3} - \left(1.10 - 0.23\exp(-60/\mathrm{Re}_j^{3/2})\right)^{-2}\right]$$

For the power jet Reynolds number range and the corresponding values of $J(\partial U_j/\partial x)$ and $J(\partial U_j/\partial x)/\mathrm{Re}_j$ (Table 2) it is apparent that the viscous relaxation forces are insignificant compared with the inertia forces at the power jet nozzle exit plane.

In addition, from equation (20) it can be seen that the factor $4.J(\partial U_j/\partial x)/\mathrm{Re}_j$ is approximately 0.5 percent of the non-dimensional power jet momentum correction factor $J(U_j^2)$ and can thus also be neglected.

(*ii*) *Control Jet Velocity Field Parameters.* Due to the assymmetry of the control nozzle exit flow there will be orthogonal velocity terms at the *c-c* cutting plane. The velocity components parallel to the normal of this plane are denoted U_{cn} while those tangential are denoted U_{ct}. Thus the non-dimensional integrals $J(U_{cn}^2)$ and $J(U_{cn}.U_{ct})$ are the normal velocity component and tangential velocity component momentum correction terms respectively. These have the usual meaning of when multiplied by the momentum computed using the average velocity in each case give the true momentum. The integrated normal flow relaxation stresses at the control jet exit are represented nondimensionally by $J(\partial U_{cn}/\partial y)$. Due to the tangential flow components a shear stress at the c-c cutting plane is introduced and is accounted for by the nondimensional integral term $J(\tau_{yx_c})$.

The importance of viscous relaxation and internal shear stress forces at the control jet exit plane can be studied with reference to Table 3.

Table 3

Re_c	$J(U_{cn}^2)$	$J(\partial U_{cn}/\partial y)/\mathrm{Re}_c$	$J(\tau_{yx_c})/\mathrm{Re}_c$
400	1.038	0.00082	0.0020
1000	1.038	0.00033	0.00080

In comparison to the case of power jet flow, the control nozzle inertia forces are much more significant than either viscous relaxation or the internal shear stresses. It can also be seen that each of the terms $J(\partial U_{cn}/\partial y)/\mathrm{Re}_c$ and $J(\tau_{yx_c})/\mathrm{Re}_c$ are at most 0.2 percent of the nondimensional axial control jet momentum correction factor $J(U_{cn}^2)$, and thus can also be neglected.

With the elimination of these three insignificant dissipative terms, the jet deflection model of equation (20) can be more simply described as follows:

$$\theta = \tan^{-1}\left[\frac{J(U_{cn}^2) + \frac{J(P_c)}{2} - \frac{2}{\mathrm{We}_c^2}}{-J(U_{cn}.U_{ct}) - \left(\frac{\mathrm{Re}_j}{\mathrm{Re}_c}\right)^2.J(U_j^2) + \frac{2}{\Omega\mathrm{We}_c^2} - \frac{L_c'}{\Omega^2\mathrm{Fr}_c}}\right] \tag{35}$$

4.2 Importance of Surface Tension and Gravitational Effects

The influence of surface tension and gravity forces in equation (35) manifest themselves through the terms containing the Weber number (We_c) and Froude number (Fr_c), respectively. A parametric study of these terms is made in Figs. 6 and 7.

The families of curves so generated are defined as follows:

$\theta(\mathrm{ALL})$ = deflection angles as described by equation (35), viz all terms included.

$\theta(\mathrm{We}_c)$ = equation (35), neglecting all terms in $J(P_c)$ and Fr_c.

$\theta(\mathrm{We}_c + \mathrm{Fr}_c)$ = equation (35), neglecting all terms in $J(P_c)$ only.

From Figure 6 it is evident that control jet surfaced tension effects are most dominant for low Re_j. Under these conditions power jet inertia forces are small and the mechanism for inwardly deflected jets is substantially controlled by the Weber number.

Comparison of Figs. 6 and 7 show that the gravitational effects tend to centralize deflection angles. The influence of the Froude number Fr_c is also most dominant for small power jet Reynolds numbers, Re_j.

4.3 The Control Nozzle Exit Pressure Term

A term of significant importance to the jet deflection model of equation (35) is the non-dimensional pressure integrated over the exit plane *c-c* of the control jet, namely $J(P_c)$. Control exit pressure profiles, defined by equations (31) and (32) are presented in Fig. 5.

As the momentum of the control flow increases and jet

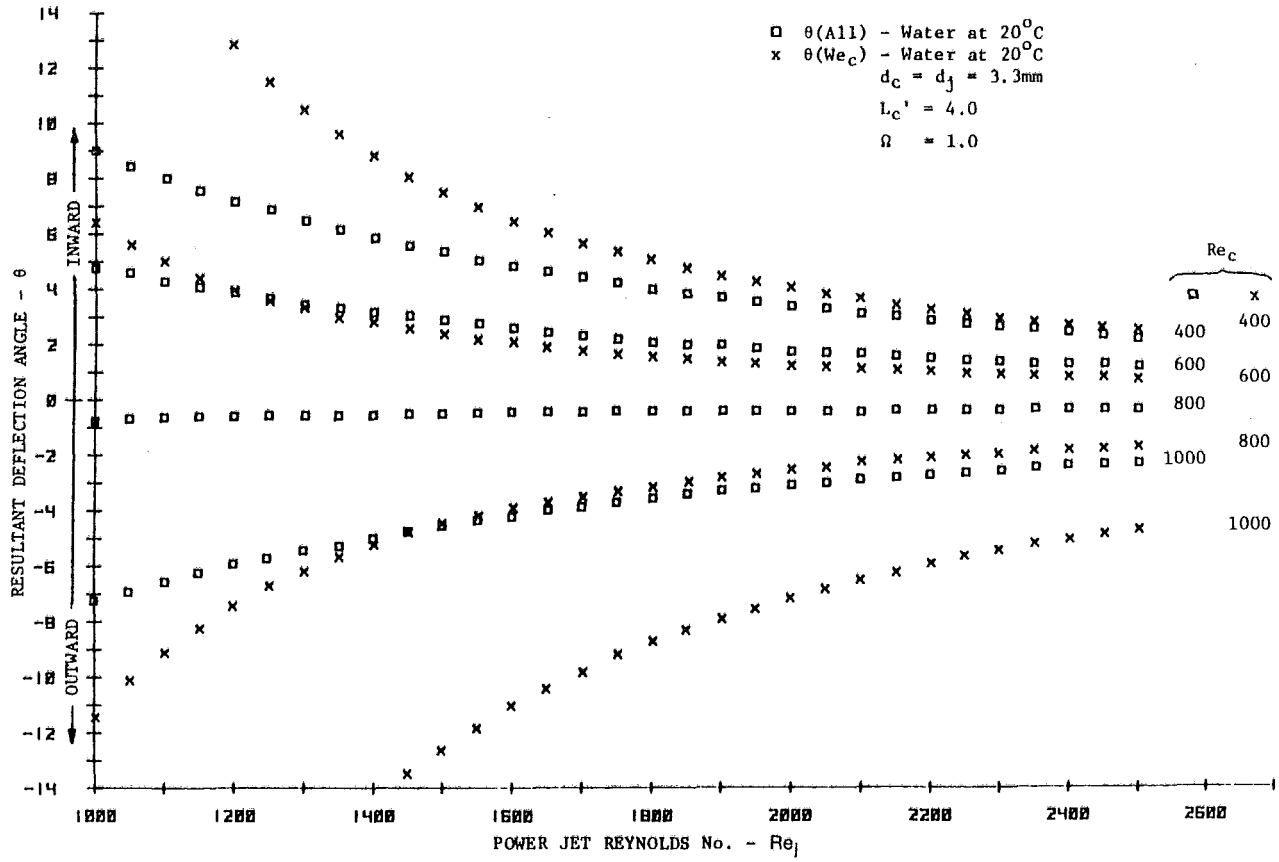

Fig. 6 Comparison of jet deflection characteristics θ(ALL), $\theta(We_c)$

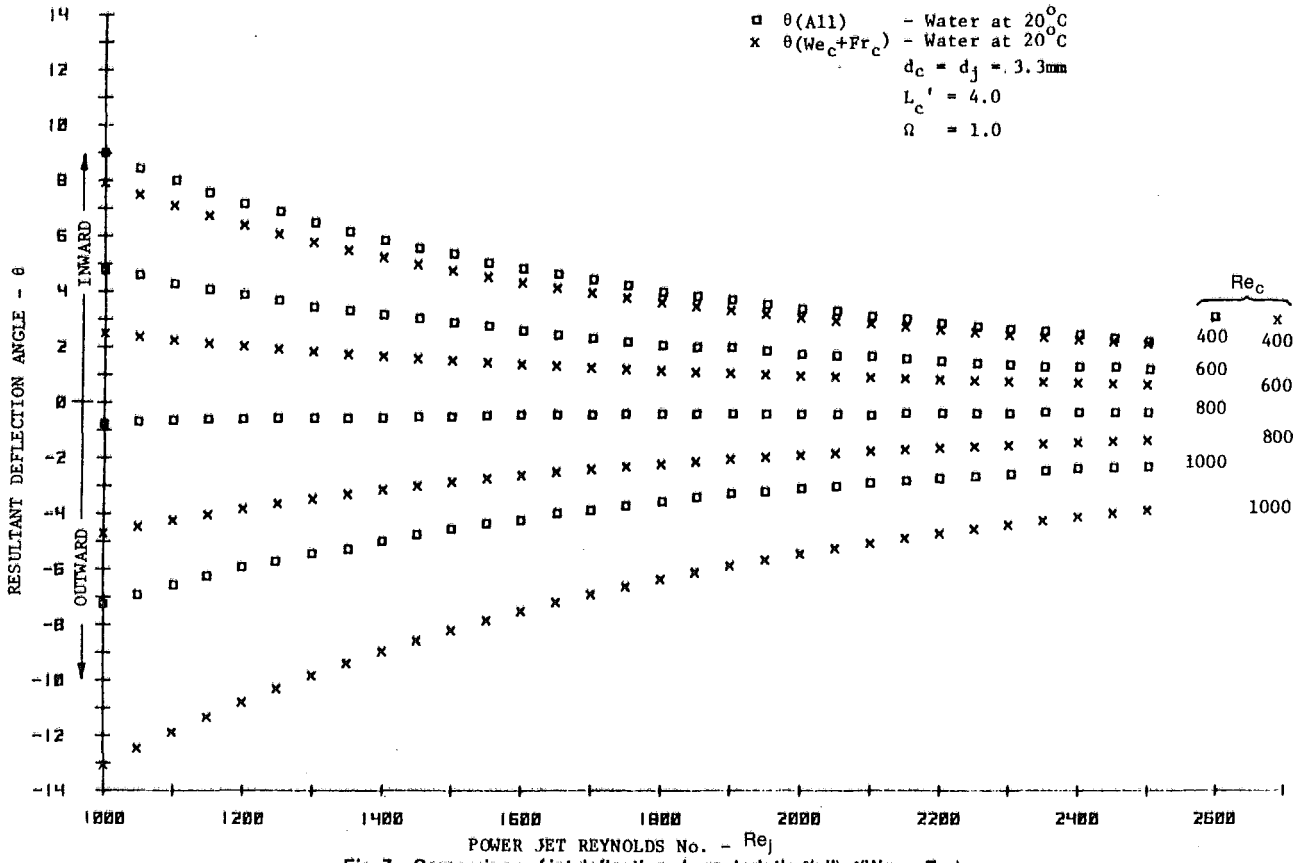

Fig. 7 Comparison of jet deflection characteristic θ(all), $\theta(We_c + Fr_c)$

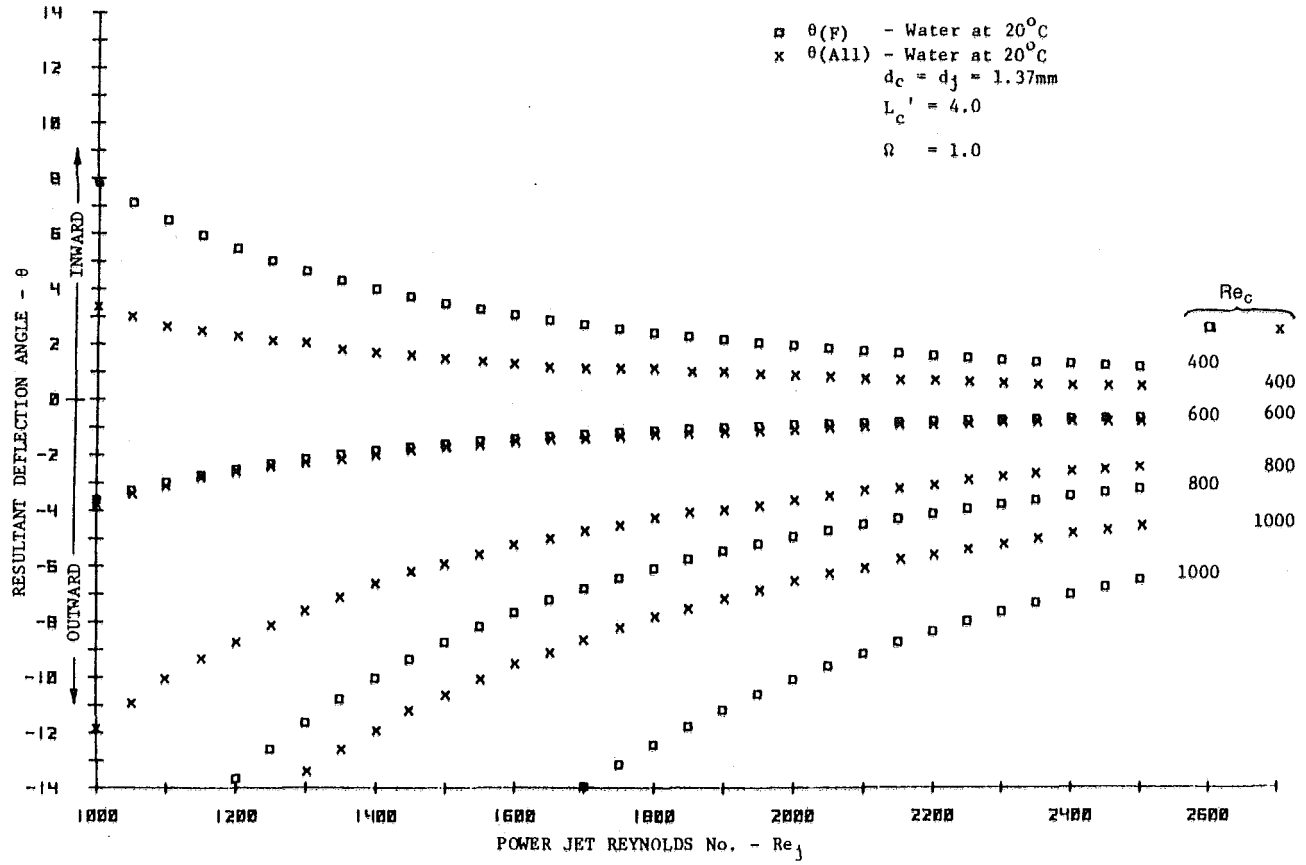

Fig. 8 Comparison of jet deflection characterisitcs θ(F), θ(All)

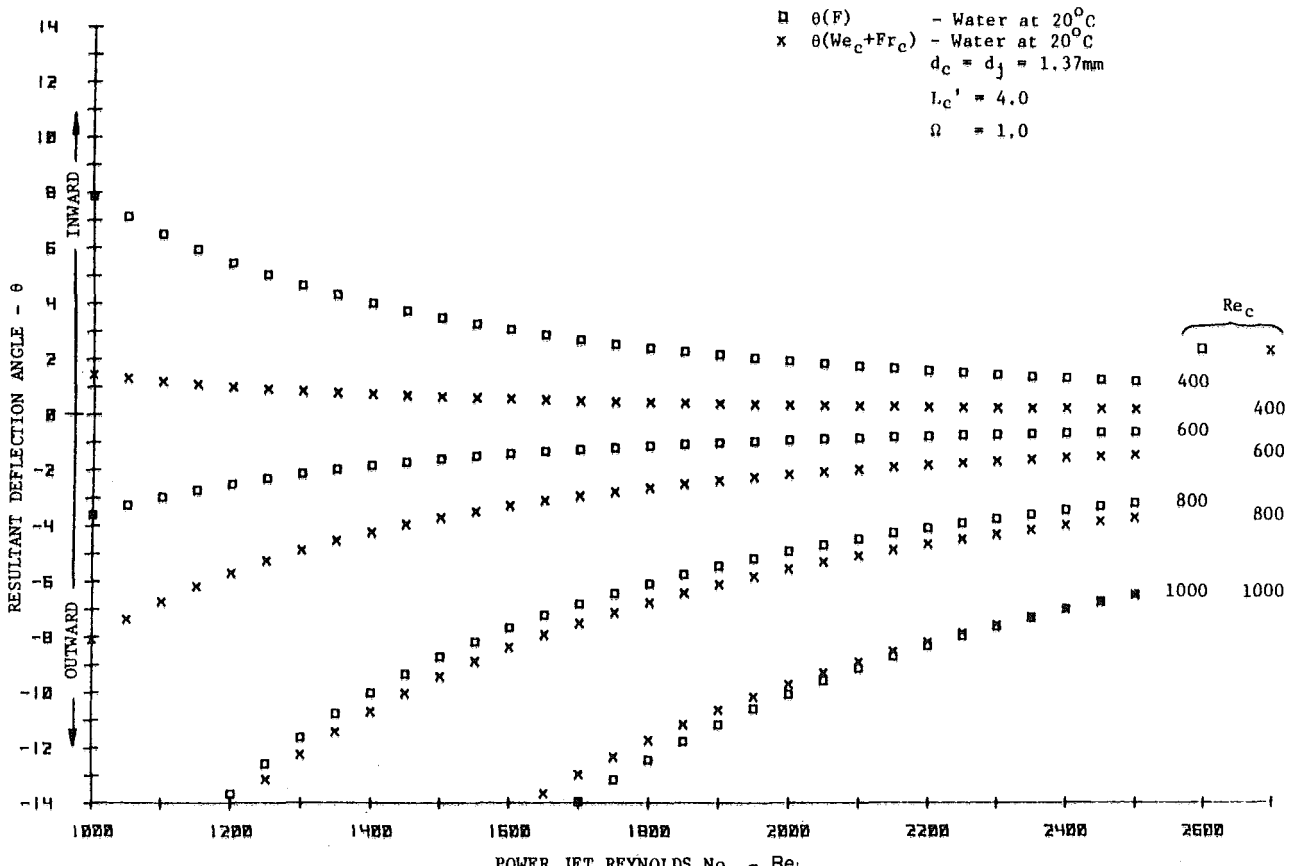

Fig. 9 Comparison of jet deflection characteristics θ(F), θ($We_c + Fr_c$)

deflection becomes increasingly negative, the magnitude of $J(P_c)$ will approach zero as the radii of curvature of the control nozzle exit streamlines become increasingly large. $J(P_c)$ is thus implied to be a function of θ. One limitation of the model presented in equation (35) is that the potential flow solution for $J(P_c)$ is deflection angle independent.

With regard to equation (35) the pressure term $J(P_c)$ must account for the shift in deflection angle plots of Fig. (7).

Good correlation between the empirical model for jet deflection of equation (35) and that of Friedman [1] was found to exist, especially for the medium to higher ranges of Re_c, by neglecting $J(P_c)$. For $Re_c > 800$, correlation becomes less satisfactory. These results are evident in Figs. 8 and 9, respectively. Friedman's empirical model of equation (36) is valid for the following conditions:

Working Fluid: Water at 20°C
Nozzle diameter ratio $\Omega = 1.0$
Tube diameter $d_c = d_j = 1.37$ mm

$$\theta(\mathrm{F}) = (2.97 \times 10^5 - \mathrm{Re}_c{}^2)/\mathrm{Re}_j{}^2 \tag{36}$$

Thus on the basis of Figs. 7, 8, and 9, the control nozzle exit pressure term $J(P_c)$ is most dominant under conditions of low power jet Reynolds number Re_j and of inward jet deflection (viz small Re_c).

4.4 The Outward Deflected Jet

As both the control jet and power jet Reynolds numbers become large in magnitude and the flow is turbulent, then equation (35) reduces to the model described by many authors for predicting jet deflection due primarily to momentum interaction. As the radii of curvature of the control nozzle streamlines approach infinity for large Re_c the following terms approach zero; $J(P_c)$ and $J(U_{cn}.U_{ct})$. Furthermore, both $We_c{}^2$ and Fr_c rapidly become large as Re_c increases and under these conditions equation (35) reduces to:

$$\theta = \tan^{-1}\left[-\frac{J(U_{cn}{}^2).\mathrm{Re}_c{}^2}{J(U_j{}^2).\mathrm{Re}_j{}^2}\right] \tag{37}$$

The terms $J(U_{cn}{}^2)$ and $J(U_j{}^2)$ are the momentum correction factors for the control jet and power jet flows respectively and approach 4/3 as each jet becomes fully developed at the exit.

Hence equation (35) becomes asymptotic with the conventional jet deflection model of equation (2) as Re_j and Re_c become increasingly large, viz:

$$\theta(c) = \tan^{-1}\left(-\frac{\mathrm{Re}_c}{\mathrm{Re}_j}\right)^2 \tag{38}$$

5 Conclusions

Motivated by requirements in the fields of industrial fluid mechanics and fluidics technology for devices which operate in the very low Reynolds number regime, this paper is an attempt to derive an adequate generalised mathematical model for the deflection of impinging liquid laminar jets.

The mathematical model is derived using both control volume and potential flow techniques. The case of inward jet deflection is highlighted, a phenomena which is instrumental in the performance of the fluidic logic device of reference [1]. Jet deflections are shown to be a function of inertia, surface tension and gravity forces in addition to a series of parameters which describe the velocity field at the exit of the control jet flow.

In particular, inward jet deflection is shown to be strongly influenced by control flow surface tension effects, gravity forces and a nett suction pressure at the control nozzle exit. Comparison of the model with empirical data of Friedman [1] shows good correlation over most of the flow range of interest. The model also is shown to asymptotically approach the conventional momentum based jet deflection model as the flow moves into the turbulent regime. Further insight into the mechanisms of jet interaction may be achieved with the development of a control jet potential flow model which is functionally dependent on resultant jet deflection, and is the subject of the next stage of investigation.

Acknowledgments

The authors would like to express their appreciation, to Professor G.M. Bragg who provided a keen insight into the problem and of the financial support from the National Research Council of Canada.

References

1 Friedman, S., and Martin, H.R., "Design Characteristics of a New Liquid Laminar Jet Fluidic Element," *Proc. Harry Diamond Labs.*, State-of-the Art Conf. on Fluidics, Paper #4, Washington, 1974.

2 Middleman, S., and Gavis, J., "Expansion and Contraction of Capillary Jets of Newtonian Liquids," *Phys. Fluids*, Vol. 4, No. III, 1961, p. 355.

3 Gavis, J., and Modan, M., 'Expansion and Contraction of Capillary Jets of Newtonian Liquids in Air: Effect of Tube Length," *Phys. Fluids*, Vol. 10, No. III, 1967, p. 487.

4 Winton, R.D., and Martin, H.R., "Predicting the Switching Times of Hydraulic Fluidic Elements from Static Characteristics," *Fluidics Quarterly*, Vol. 10, No. 2, 1978.

5 Malcolm, D., "On the Deflection of Free Jets by a Solid Surface," Can. Soc. Mechanical Engrs., paper 73, 1974.

6 Wille, R., and Fernholz, H., "Report on the First European Mechanics Colloquim on the Coanda Effect," *Brit. J. Fluid Mech.*, Vol. 23, 1965, p. 801.

7 Langhaar, H.J., "Steady Flow in the Transition Length of a Straight Tube," ASME *Journal of Applied Mechanics*, Vol. A-55, 1942.

8 Hornbeck, R.W., "Laminar Flow in the Entrance Region of a Pipe," *Appl. Sci. Res. A*, Vol. 13, 1963, p. 224.

9 Gavis, J. "Contribution of Surface Tension to Expansion and Contraction of Capillary Jets," *Phys. Fluids*, Vol. 7, 1964, p. 1097.

10 Friedman, S., and Martin, H.R., "Characteristics of a Liquid Laminar Jet Fluidic Element," I.S.A. Annual Conf., Houston, Texas, 1973.

11 Middleman, S., and Gavis, J., "Expansion and Contraction of Capillary Jets of Newtonian Liquids.," *Phys. Fluids*, Vol. 4, No. III, 1961, p. 355.

12 Keller, J.B., "Teapot Effect," *J. Appl. Phys.*, Vol. 28, No. VIII, 1957, p. 859.

13 Winton, R., "Dynamic Switching Characteristics of a Liquid Fluidic Jet Amplifier," M.A.Sc. thesis, University of Waterloo, Ontario, 1976.

14 Beatty, E.K., and Markland, E., "Feasibility Study of Laminar Jet Deflection Fluidic Elements," *Proc. of 3rd Cranfield Fluidics Conf.*, BHRA, 1968.

Journal of Fluids Engineering

Discussion

An Analysis of Uniform Shear Flow Past a Porous Plate Attached to a Plane Surface[1]

D. F. JAMES.[2] This is a good first study on the applicability of the wake-source model to shear flow around and through a screen. Since previous work [4] dealt with uniform flow, the authors have properly chosen shear flow as the next step in extending the work. Moreover, shear flow is probably more important than uniform flow in practical situations, and so this study should be of interest to designers who need quantitative information on the effectiveness of wind breaks and the like.

To be truly useful, however, this study should be continued in order to vary plate porosity and wind shear rate. The present experiments were carried out for a single plate and for one upstream velocity profile. The pressure-drop coefficient K for the plate was 18.1, which is higher than values for normal porous materials like woven screens, and the average shear rate G of the velocity profile was 216 s^{-1}, which corresponds to a moderate 53 percent change in velocity from the bottom to the top of the screen. These conditions produced a downstream velocity profile that was satisfactorily predicted by the wake-source model, but this tells us little about the accuracy of the model for other conditions. Additional experimental results would not only establish the range of validity of the model but would also provide useful data for design purposes. For the latter, the quantity of interest is likely the reduction of velocity produced by the windbreak, and thus it would be beneficial to have a plot, say, of mean velocity reduction as a function of the screen coefficient K, with G as a free parameter. I hope the present work is the initial step in an endeavour of this sort.

The authors do, in fact, infer that the study is being continued and to that end I would suggest several changes in future work. First, the mapping of the velocity field upstream of the plate is presently incomplete and the matching location too arbitrary. It would be interesting to learn, for example, the effect on predicted downstream profile if the matching were carried out at $x/h = -1.1$, say, and not at $x/h = -2.2$. Secondly, it should be straightforward to measure the plate's pressure-drop coefficient and so verify the value calculated in the text. Finally, it would be useful to investigate non-uniform shear flows. Uniform shear is the logical case after uniform flow, as mentioned above, but it is not true that the theory demands a uniform shear flow which has a constant vorticity. The model requires only that the flow be inviscid, not irrotational. Consequently the approaching flow may have vorticity, including non-constant vorticity. It appears that such non-uniformity can easily be incorporated in the authors' computational technique because the fundamental equation, (21), is nonlinear and must be solved numerically anyway. By a thorough testing with various velocity distributions, both uniform and non-uniform in shear, it should be possible to settle the question about the influence of the upstream profile.

Authors' Closure

The authors are grateful to the thoughtful discussion of Professor D. F. James. We agree to his comments and are trying to extend our research of the porous flow problem to the direction which he suggested.

Three-Dimensional Supersonic Flow Through a Cascade of Twisted Flat Plates[1]

J. MARTINON.[2] The development of three-dimensional calculation codes should help the designer in understanding essential phenomena of interaction between different radii and in improving low hub-to-tip ratio turbomachine design.

The discusser would like to thank the author for presenting the three-dimensional numerical results in this paper, and the very interesting conclusion that three-dimensional flows need modifications of the unique incidence concept.

The calculation of supersonic flows in linear cascades and rotating blade rows carried on at ONERA ([1,2]) led to a similar general conclusion. The method used was a fully three-dimensional, bicharacteristic one, and the computational domain was divided into distinct regions (each one comprising a blade-to-blade channel and an upstream extension), which were calculated in turn. The periodicity of the flow field in the inlet region was obtained after a few channels, but I also found it necessary in the most general case, as said in the above paper, to go on for a while with the calculation in order to obtain the flow conditions far upstream of the cascade (without using more than ten blades).

As in the twisted plate cascade presented by C.F. Grainger, for linear blade cascades with converging side walls the flow

[1] By M. Kiya, M. Arie, and K. Koshikawa, published in the June, 1980 issue of the ASME JOURNAL OF FLUIDS ENGINEERING, Vol. 102, No. 2, pp. 166–173.

[2] Professor, Department of Mechanical Engineering, University of Toronto, Toronto, Canada.

[1] By C. F. Grainger, published in the September, 1980 issue of the ASME JOURNAL OF FLUIDS ENGINEERING, Vol. 102, pp. 338–343.

[2] Laboratoire de Dynamique des Fluides, Ecole Nationale Superieure des Mines de Paris, 60, Boulevard Saint-Michel, 75272 Paris Cedex 06., France

blades before the 25th, the exponential shaped pattern from point E to the blades was invariant and in agreement with a simple model based on actutor disks, and the effect of the settling wave (D to E) was also almost invariant. We expected that the "infinite cascade" conditions would be obtained when the two exponential shaped patterns (from the ends of the blades) touched (at point E). In answer to the second query; the number of grid points used between walls was seven, with nine from blade to blade. We have no experimental results to compare with these numerical ones.

In response to Mr. Smith's queries, velocities U and V vary almost linearly with Y over the blade pitch except for discontinuities at the shocks. The averages (U, V) are (0.562, 0.863) at $Z = 0$ and (0.447, 0.867) at $Z = 5$. No results are yet available for the undersurface of the blade requested. However, a nearby blade had a jump in angle of about 1.5 degrees, as deduced by Mr. Smith.

Authors' Closure

The authors wish to thank Mr. Musgrave for his valuable comments on the paper. As he points out, additional measured data is required to unlock the true nature of the fluid flow inside the scroll passages.

It is important to note that, for example, in a simple pipe bend the high velocity would tend to move towards the outer pipe wall. However, in the case of this scroll the high velocity core is found to be near the inner scroll wall largely influenced by the position of the discharge nozzle. Hence the authors speculate that the flow would tend to oscillate about a certain line as shown in Fig. 15, sections 1 and 2. In the case of this scroll, one such line (section 1) happens to be the free vortex type of flow. This question would be resolved when more data are taken at some intermediate sections and perhaps beyond 184° as Mr. Musgrave pointed out.

Flow Measurement in a Turbine Scroll[1]

D. S. MUSGRAVE.[2] This paper is a welcome and notable addition to the limited published literature on the flowfield within a turbine scroll. The deviation from free vortex flow at section two underscores the complexity of this turbomachinery element. When additional measurements on the tangential and radial velocities at the sections become available the chaotic nature of scroll flow will be fully documented. Data on sections beyond 184° (almost half of the periphery) would also be of interest.

Since most scrolls are proceeded by burners or exhaust manifolds, it is likely that the velocity field is even more complicated than indicated in these measurements with a "clean" inlet.

Although the total pressure losses of a scroll can be 1 percent or less, the heavy boundary layer growth and the high asymmetry of the flowfield lead to significant incidence and secondary flow losses within the downstream nozzle. If the scroll generates a high level of vorticity it will imply a low deflection nozzle which is a type particularly sensitive to incidence. Thus, scrolls are not superior for radial turbines. The plenum requires, however, a stage layout that presents packaging problems for most vehicular gas turbine engines. The larger (low Mach number) scrolls tend to minimize the problems associated with scrolls in general, although with some cost in volume.

The authors' work, in concert with their previous papers, demonstrates that a careful coupling of analytical techniques with experimental information is underway. When one considers the difficulty of performing a fully three-dimensional viscous analysis and its sensitivity to inlet conditions, separation and boundary details, it is clear that a straightforward 3-D scroll design procedure similar to that developing for axial turbomachinery will not come into existence quickly. Nevertheless, turbomachinery for practical applications will continue to employ scrolls and the twin demands of high efficiency and compact design make the pursuit of this goal well worthwile.

[1] By W. Tabakoff, Y. Sheoran, and K. Kroll, published in the June, 1980 issue of the ASME JOURNAL OF FLUIDS ENGINEERING, Vol. 102, p. 290–296.

[2] Research Engineer, Power Plant Research, Chrysler Corp., Detroit, Mich. 48288.

Frictional Resistance of Enclosed Rotating Cones With Superposed Throughflow[1]

H. ITŌ.[2] The authors are to be congratulated on presenting useful experimental data concerning the effects of throughflow on the frictional moment of enclosed rotating cones. It is well-known that in the case of enclosed rotating disks with no throughflow, the modes of flow within the casing can be classified into four regimes,[3] i.e.,

Regime I. Laminar flow, merged boundary layers.
C_M is proportional to Re^{-1}.
Regime II. Laminar flow, separate boundary layers.
C_M is proportional to $\mathrm{Re}^{-1/2}$.
Regime III. Turbulent flow, merged boundary layers.
C_M is proportional to $\mathrm{Re}^{-1/4}$.
Regime IV. Turbulent flow, separate boundary layers.
C_M is proportional to $\mathrm{Re}^{-1/5}$.

Although the flow within the casing of an enclosed rotating cone is much complicated by the existence of Taylor-type vortices and a secondary flow shown schematically in Fig. 5, the following conclusions may be drawn from the authors' experimental results for turbulent flow in the case of $C_q = 0$.

(1) For the close clearance shown in Fig. 2, C_{M0} is nearly proportional to $\mathrm{Re}^{-1/4}$ in the region of higher Reynolds numbers. This fact means that in this region the Taylor-type vortices have no appreciable effect on C_{M0}, and the situation is similar to Regime III in case of the enclosed rotating disk.

(2) For $s/R \geqq 0.0160$ shown in Figs. 3 and 4, C_{M0} is nearly proportional to $\mathrm{Re}^{-1/5}$ in the region of higher Reynolds numbers except for the case of $\theta = 30°$ [1]. This proportionality corresponds to Regime IV in case of the rotating disk.

The authors state in the case of $s/R = 0.0400$ and $\theta = 30°$ shown in Fig. 4, C_M is proportional to $\mathrm{Re}^{-1/2}$ in the region of $4 \times 10^4 < \mathrm{Re} < 2 \times 10^5$. The fact that C_M is in proportion to $\mathrm{Re}^{-1/2}$ corresponds to Regime II in case of the rotating disk,

1 By Y. Yamada and M. Ito, published in the June, 1979, issue of the ASME JOURNAL OF FLUIDS ENGINEERING, Vol. 101, pp.

2 Professor, Institute of High Speed Mechanics, Tohoku University, Sendai, Japan.

3 Daily, J. W., and Nece, R. E., "Chamber Dimension Effects on Induced Flow and Frictional Resistance of Enclosed Rotating Disks," ASME *Journal of Basic Engineering*, Vol. 82, No. 1, Mar. 1960, pp. 217–232.

whereas in explanation of Figs. 6 and 7(*c*) the authors state that for the above configuration the flow is turbulent at Re = 10^5. Is it possible for C_M to be proportional to $Re^{-1/2}$ when the flow is turbulent? In this connection, presentation of a flow regime chart will be helpful to understand the possible modes of flow within the casing.

Authors' Closure

The authors appreciate Professor H. Ito's incisive comments. The authors are of the opinion that the gradient of the C_M-Re curve cannot always represent the mode of the flow within the casing of an enclosed rotating cone, because in our visual study of an enclosed rotating cone with no throughflow [1] the turbulent flow was observed even in the region where C_m was nearly proportional to $Re^{-1/2}$. The discusser may have misunderstood the explanation of Figs. 6 and 7(C). The authors stated there that the flow for $s/R = 0.0400$ was turbulent at Re = 10^5 in the case of $C_q \neq 0$. For the case of $C_q = 0$ we do not have enough data to draw a demarcation line between the laminar flow regime and the turbulent one in the flow regime chart.

A further study concerning this problem is now under way by the authors.

Combined Simultaneous Flow Visualization/Hot Wire Anemometry for the Study of Turbulent Flows[1]

P. BARDSHAW[2], K. C. MUCK[2], and H. M. TASI.[2] Dr. Falco is to be congratulated on the results of his latest work. The combination of visualization and quantitative techniques is very effective.

It is possible that the results of Fig. 12 may be pessimistic. Judging by the lack of high frequency in the signals the measurements must have been made at low Reynolds numbers, $R_\theta < 1000$. Also, the threshold values appear to be too high, although some obvious discrepancies in the traces (e.g. $uv = 0$ where $u, v \neq 0$) prevent detailed discussion. We have found good agreement at high Reynolds numbers (R_θ of order 5000) between (i) intermittency derived from temperature fluctuations in a heated flow (a technique that is closely equivalent to one-point measurements in oil-fog "smoke" except that the worry about Schmidt number is absent because the Prandtl number is nearly unity) and (ii) intermittency derived from the first *and second* time derivatives of uv, in a variant of the scheme used by Antonia. There are, inevitably, genuine regions of small turbulent activity within the marked fluid, usually in protruding fingers of decaying turbulence rather than in the interior of bursts as found by Dr. Falco. Even at low Reynolds numbers we [1, 2] have found adequately good agreement between the two techniques. Temperature tagging is more limited than smoke tagging because only point measurements can be made, but it is much easier to apply (especially at high Reynolds numbers), using standard wind tunnels and mounting a resistance thermometer ("cold wire") adjacent to, or at a distance from, the hot wire probe.

Additional References

1 Murlis, J., Tsai, H. M., and Bradshaw, P. "The Structure of Turbulent Boundary Layers at Low Reynolds Numbers," Submitted to *J. Fluid Mech.*, 1980.

2 Muck, K. C., "Comparison of Various Schemes for the Generation of the Turbulent Intermittency Function," Imperial College Aero Report 80-03, 1980.

S. J. KLINE.[3] Professor Falco's technique is a step forward in the state of experimental methods for study of turbulent flows. As noted in the motion picture, "Flow Visualization," and in many other places, turbulent flows often exhibit unexpected flow patterns; steady, two-dimensional boundary conditions can result in flows that are three-dimensional time-dependent motions. If these motions were either wholly random or wholly organized, at least many technically significant cases would have been the subject of completed, satisfactory analyses long ago since mathematical methods for both deterministic and wholly random processes are in relatively good order. Turbulent flows are not of either kind; typically turbulent flows contain quasi-coherent (or if you prefer quasi-random) structures with more random, usually smaller fluctuations superposed.

In some instances, it is not necessary to understand all the details of the structure, but for many technical problems we do not need to know the details of structure. Examples include combustion processes where structure controls the ignition range and probably other elements of structure control ultimate quenching. When we want to know about phenomena that often affect design such as: flow separation, reattachment, the nature of turbulence production, transition, laminarescence, or relaminarization, and many other effects, we need to understand structure. We also need structure data to interact with and complement current computer studies using "large eddy simulation" since no other data give sufficient details.

The output of hot-wires and visual studies complement each other strongly – each giving what the other does not. Either alone is often insufficient for obtaining clear data on quasi-coherent structure. The hot-wire is blind, totally insensitive to direction of flow normal to the wire, gives data only at a point. Visual studies have high uncertainties in both interpretation and numerical values, but give a good integrated picture of the flow. The two therefore complement each other strongly, and this complementarity is most effective when the two measurements can be taken synchronously on a single record. For all these reasons, Professor Falco's additions to the armentarium of experimental technique are very welcome.

Authors' Closure

We want to thank Professor Kline and Professor Bradshaw, et al., for their comments.

In reply to Bradshaw, et al., we must first note that the discrepancies they allude to in Fig. 12 are the result of errors in tracing over the computer plots, and are not a result of measurement errors. We have carefully checked this point. As

[1] By R. E. Falco, published in the June, 1980, issue of the ASME JOURNAL OF FLUIDS ENGINEERING, Vol. 102, pp. 174–182.

[2] Professor and Graduate Students, respectively, Department of Aeronautics, Imperial College, London, England.

[3] Thermosciences Division, Department of Mechanical Engineering, Stanford University, Stanford, Calif. 94305.

they surmised, our results were indeed at low Reynolds number, $R_\theta = 1230$. We are in agreement that the intermittency functions may not be seriously affected by the fact that the detector functions tried will go to zero within the "typical eddies." It has been known for some time that intermittency functions are insensitive to the choice of detectors used (also noted in reference [2]). However, as we indicated, information about the frequency of occurrence, and duration of turbulent regions, is highly sensitive to the detector and threshold levels used as well as the degree of smoothing, which inevitably accompanies these techniques. The problem with hot-wire detection functions is that "dropouts," regions in which the detector falls below the threshold, *often* occur within what appear to be large scale turbulent regions. In fact this is the central problem addressed by Muck [2]. We believe that the form of the uv signal within a "typical eddy" is one important cause of dropouts. Smoothing of the detector functions is the usual method used to eliminate dropouts. Muck has noted [2] that a practical smoothing window is often an order of magnitude larger than the Kolmogoroff length scale. Falco (unpublished) has calculated that the "typical eddy" scale is ~ 30 Kolmogoroff length scales at $R_\theta = 1, 300$. Looking at Fig. 12 it is clear that such smoothing will significantly improve the results. Furthermore, the fact that the "typical eddy" decreases as the Taylor microscale suggests that it will, at high Reynolds numbers, appear to contribute to the "high wave number intermittency" which the authors suggest is a major cause of the dropout problem. Finally, it should be noted that the scheme chosen in reference [2] was not tried on the "typical eddy" signatures. However, the use of the second derivative-or-the first derivative, does appear to be a more promising technique with which to detect eddies, and should be able to do so with significantly less smoothing than needed for techniques which use only the first derivatives.

Lower Mode Response of Circular Cylinders in Cross-Flow[1]

D. S. WEAVER.[2] The authors have reported a very interesting phenomenon and offered a plausible explanation of the mechanism. I agree that this phenomenon may have excaped previous attention in part as a result of the very low reduced damping in their experiments as compared with the majority of previous work. It is known that systems with small reduced damping are susceptible to oscillations not observed for cylinders with larger damping parameters. For example, King (author's reference [1]) has reported observations of serious in-line vibrations of piles in water which have not been observed for structures in air. Actually, the reduced damping parameter is the product of mass ratio and damping and, hence, very low values can be achieved by using heavier fluids rather than light cylinders. Perhaps further investigations of the present phenomenon could be conducted in water.

Of course, another reason why this phenomenon may not have been previously observed is that it occurs at flow velocities considerably in excess of those normally expected to cause serious vibration problems, i.e., three times the flow velocity required to produce resonant cross-flow oscillations in the fundamental mode.

It is a pity that the authors did not carefully examine the linearity of the damping of their cylinders. While non-linear damping would not change their basic conclusions, it certainly could make interpretation of the data more difficult. For example, the large amplitude fundamental mode vortex shedding responses shown in Fig. 3 are generally less than expected. A large number of experiments in both air and water from a variety of sources have indicated that the maximum resonant vortex excited amplitudes will be about one cylinder diameter for reduced damping (stability) parameters of the order of one. An empirical curve of amplitude vs damping parameter based on this data can be found in Fig. 10 of the paper by King cited above. The present author's experiments also show that some of their cylinders with larger damping parameters responded at larger amplitudes than others with smaller damping parameters which is certainly contrary to expectation. For example, the maximum fundamental mode response amplitude for test no. 4 is about twice that for test no. 1 even though the damping parameter is less in the latter case. In addition, the small amplitude "lower mode" response appears much less affected by changes in the damping parameter than is the normal vortex shedding response.

The latter observation together with the absene of response at $f_{s0} = 2f_n$ and the rather broad range of flow velocities over which "lower mode" response occurs are supportive of the self-excitation hypothesis. It would be interesting to compare wake turbulence spectra for free and rigid cylinders over this flow velocity range. Discrete periodicity in the wake of flexible cylinders which did not exist in the wake of rigid cylinders would be indicative of a motion dependent (self-excited) mechanism.

[1] By W. W. Durgin, P. A. March, and P. J. Lefebvre, published in the June, 1980, issue of the ASME JOURNAL OF FLUIDS ENGINEERING, Vol. 102, pp. 183-190.

[2] D. S. Weaver, Department of Mechanical Engineering, McMaster University, Hamilton, Ontario, Canada.

Comments on a Discussion

T. SARPKAYA.[1] The recent discussion of Professor John S. McNown [1] of the paper entitled "Two Dimensional Lateral Flow Past a Barrier," by Ramamurthy and Carballada [2] and the authors' closure [3] prompted this brief comment.

Professor McNown correctly stated that "Only for a single point on each of the curves presented in Figs. 6 and 8 *of Ramamurthy and Carballada* does the flow divide in the familiar form indicated by the line BD in Fig. A" (of McNown). All other cases lead to a lip cavity. The analysis of flows with such lip cavities is beyond the scope of the streamline theory.

The special stagnation condition which avoids the lip cavity has been discussed by Toch and Moorman [4], as pointed out by McNown. Even though the said condition for the special case of $K = 2$ has been given correctly by Toch and Moorman, it cannot be obtained in the manner suggested by them. Neither McNown in his discussion nor Toch and Moorman in their 1953 paper [4] gave a general rule for the derivation of the stagnation condition.

Sarpkaya [5] has shown that the said stagnation condition for combining or branching inviscid flows is given by

[1] Mechanical Engineering, Naval Postgraduate School, Monterey, Calif. 93940.

they surmised, our results were indeed at low Reynolds number, $R_\theta = 1230$. We are in agreement that the intermittency functions may not be seriously affected by the fact that the detector functions tried will go to zero within the "typical eddies." It has been known for some time that intermittency functions are insensitive to the choice of detectors used (also noted in reference [2]). However, as we indicated, information about the frequency of occurrence, and duration of turbulent regions, is highly sensitive to the detector and threshold levels used as well as the degree of smoothing, which inevitably accompanies these techniques. The problem with hot-wire detection functions is that "dropouts," regions in which the detector falls below the threshold, *often* occur within what appear to be large scale turbulent regions. In fact this is the central problem addressed by Muck [2]. We believe that the form of the uv signal within a "typical eddy" is one important cause of dropouts. Smoothing of the detector functions is the usual method used to eliminate dropouts. Muck has noted [2] that a practical smoothing window is often an order of magnitude larger than the Kolmogoroff length scale. Falco (unpublished) has calculated that the "typical eddy" scale is ~ 30 Kolmogoroff length scales at $R_\theta = 1, 300$. Looking at Fig. 12 it is clear that such smoothing will significantly improve the results. Furthermore, the fact that the "typical eddy" decreases as the Taylor microscale suggests that it will, at high Reynolds numbers, appear to contribute to the "high wave number intermittency" which the authors suggest is a major cause of the dropout problem. Finally, it should be noted that the scheme chosen in reference [2] was not tried on the "typical eddy" signatures. However, the use of the second derivative-or-the first derivative, does appear to be a more promising technique with which to detect eddies, and should be able to do so with significantly less smoothing than needed for techniques which use only the first derivatives.

Lower Mode Response of Circular Cylinders in Cross-Flow[1]

D. S. WEAVER.[2] The authors have reported a very interesting phenomenon and offered a plausible explanation of the mechanism. I agree that this phenomenon may have excaped previous attention in part as a result of the very low reduced damping in their experiments as compared with the majority of previous work. It is known that systems with small reduced damping are susceptible to oscillations not observed for cylinders with larger damping parameters. For example, King (author's reference [1]) has reported observations of serious in-line vibrations of piles in water which have not been observed for structures in air. Actually, the reduced damping parameter is the product of mass ratio and damping and, hence, very low values can be achieved by using heavier fluids rather than light cylinders. Perhaps further investigations of the present phenomenon could be conducted in water.

Of course, another reason why this phenomenon may not have been previously observed is that it occurs at flow velocities considerably in excess of those normally expected to cause serious vibration problems, i.e., three times the flow velocity required to produce resonant cross-flow oscillations in the fundamental mode.

It is a pity that the authors did not carefully examine the linearity of the damping of their cylinders. While non-linear damping would not change their basic conclusions, it certainly could make interpretation of the data more difficult. For example, the large amplitude fundamental mode vortex shedding responses shown in Fig. 3 are generally less than expected. A large number of experiments in both air and water from a variety of sources have indicated that the maximum resonant vortex excited amplitudes will be about one cylinder diameter for reduced damping (stability) parameters of the order of one. An empirical curve of amplitude vs damping parameter based on this data can be found in Fig. 10 of the paper by King cited above. The present author's experiments also show that some of their cylinders with larger damping parameters responded at larger amplitudes than others with smaller damping parameters which is certainly contrary to expectation. For example, the maximum fundamental mode response amplitude for test no. 4 is about twice that for test no. 1 even though the damping parameter is less in the latter case. In addition, the small amplitude "lower mode" response appears much less affected by changes in the damping parameter than is the normal vortex shedding response.

The latter observation together with the absene of response at $f_{s0} = 2f_n$ and the rather broad range of flow velocities over which "lower mode" response occurs are supportive of the self-excitation hypothesis. It would be interesting to compare wake turbulence spectra for free and rigid cylinders over this flow velocity range. Discrete periodicity in the wake of flexible cylinders which did not exist in the wake of rigid cylinders would be indicative of a motion dependent (self-excited) mechanism.

[1] By W. W. Durgin, P. A. March, and P. J. Lefebvre, published in the June, 1980, issue of the ASME JOURNAL OF FLUIDS ENGINEERING, Vol. 102, pp. 183-190.

[2] D. S. Weaver, Department of Mechanical Engineering, McMaster University, Hamilton, Ontario, Canada.

Comments on a Discussion

T. SARPKAYA.[1] The recent discussion of Professor John S. McNown [1] of the paper entitled "Two Dimensional Lateral Flow Past a Barrier," by Ramamurthy and Carballada [2] and the authors' closure [3] prompted this brief comment.

Professor McNown correctly stated that "Only for a single point on each of the curves presented in Figs. 6 and 8 *of Ramamurthy and Carballada* does the flow divide in the familiar form indicated by the line BD in Fig. A" (of McNown). All other cases lead to a lip cavity. The analysis of flows with such lip cavities is beyond the scope of the streamline theory.

The special stagnation condition which avoids the lip cavity has been discussed by Toch and Moorman [4], as pointed out by McNown. Even though the said condition for the special case of $K = 2$ has been given correctly by Toch and Moorman, it cannot be obtained in the manner suggested by them. Neither McNown in his discussion nor Toch and Moorman in their 1953 paper [4] gave a general rule for the derivation of the stagnation condition.

Sarpkaya [5] has shown that the said stagnation condition for combining or branching inviscid flows is given by

[1] Mechanical Engineering, Naval Postgraduate School, Monterey, Calif. 93940.

Journal of Fluids Engineering

Book Reviews

Injection and Mixing in Turbulent Flow, by Joseph A. Schetz, *Progress in Aeronautics and Astronautics*, Vol. 68, American Institute of Aeronautics and Astronautics, 1980, 200 pp., Price: $17 (AIAA Members), $27 (list).

REVIEWED BY PHILIP T. HARSHA

There is a long history of reviews of various aspects of turbulent flow phenomena. Most of these reviews have appeared as survey articles, and in fact this volume began as such a survey article. However, in describing the experimental and analytical aspects of the problems of injection and mixing in turbulent flow, Professor Schetz has gone far beyond the depth of material usually covered. Thus the importance of this work cannot be overstated: it belongs in the library of anyone interested in engineering problems which involve turbulent fluid flow.

Professor Schetz' intent is to review in depth the available experimental data for a variety of turbulent flows and the analytical techniques which have been used to predict them. This approach is necessary because the engineering solution of turbulent flow problems requires the use of both empirical and analytical techniques. An enormous variety of flows are covered in 200 pages: parallel jets, including constant-density flows and the effects of temperature and composition variations; flows with axial pressure gradients; zero net momentum defect cases; flows with swirl; two-phase flows; three-dimensional coaxial jets; transverse injection; buoyancy force effects; and viscous-inviscid interactions. In each case, experimental work is reviewed to establish the empirical data base and then the application of each of a hierarchy of turbulence models to prediction of the flowfield is examined. The experimental data include both mean flow and turbulence structure measurements, while the hierarchy of turbulence models ranges from algebraic eddy viscosity formulations through turbulent kinetic energy closures (both one-equation and two-equation) to Reynolds stress and direct turbulence models.

The amount of available data and the number of reported turbulence model applications varies widely for different flowfields, so that the depth of treatment in this volume varies with the subject considered. There are also, perhaps unavoidably, some gaps in the coverage of the various subjects: for example, while transverse injection into a supersonic stream is reviewed in detail, transverse injection into a subsonic stream is given only a brief mention. Nevertheless, Professor Schetz has succeeded admirably in what he sets out to do. The material covered in this volume provides an excellent introduction to turbulent mixing processes, while at the same time providing turbulence researchers with a complete overview of the current state-of-the-art. For the engineer concerned with examining a particular turbulent mixing process for a specific application, this volume provides the necessary review of the available experimental data and analytical techniques, while the 246 literature citations provide additional sources of information when further detail is required.

Wind Effects on Structures: An Introduction to Wind Engineering, Emil Simiu and Robert H. Scanlan, Wiley-Interscience, 1978, 458 pp. Price: $29.00

Wind Forces in Engineering (2nd Edition) Peter Sachs, Pergamon Press, 1978, 400 pp. Price: $40.00

REVIEWED BY OWEN M. GRIFFIN

Recent years have seen the growth of wind engineering as a technical discipline. Wind flow over buildings, cooling towers, bridges and other structures causes steady and unsteady loads and alters the atmospheric environment in the vicinity of the structure. For example, the need to know the effects of the wind on slender and flexible modern buildings has increased because most new high rise buildings have nonstructural curtain walls instead of massive masonry walls. The growth of wind engineering has been accompanied by an increased interest in the quadrennial International Conference on Wind Engineering, most recently held in 1979, which has evolved from earlier Conferences on Wind Effects on Buildings and Structures.

The two books reviewed here deal with the engineering aspects of wind forces and their effects on structures. Both were published in 1978, though the book by Sachs is a reissue of an earlier (1972) version. There is a definite distinction, however, between the two books and this can be seen from a comparison of the two Contents sections. The contents of the book by Simiu and Scanlan cover about two-thirds of a page and describe the book's eleven chapters by title. In contrast, the book by Sachs contains ten chapters but the Contents cover four pages; the book is arranged somewhat as a handbook (this is not meant in a particularly disparaging way) with the various topics discussed in each chapter listed in detail.

A chapter on wind tunnels is included by Sachs and is based largely upon the industrial aerodynamics program and experience at Great Britain's National Physical Laboratory. Chapters on Wind Data and Basic Shape Factors make up a large portion of the book. The latter is basically a compendium of drag and moment coefficients for almost every conceivable bluff body cross-section. Chapters 6,7,8 and 9 treat specialized applications to the wind engineering of Bridges, Buildings, Masts and Towers, and Special Structures. The latter include such things as cables, cooling towers,

and radar and communication aerials. The final chapter of the book is a discussion of several representative Codes of Practice, the subjects each contains, and to which chapter of Sachs' book a particular subject is related. This feature is a definite advantage for the designer, for whom the material in the book primarily is presented. The addition of the chapter on Codes of Practice seems to be the major difference between the 1972 and 1978 editions of Sachs' book (as noted in his Preface).

The book by Simiu and Scanlan is intended as a text for graduate engineering students and for practicing structural engineers and architects. It is organized accordingly into two parts: Part A, The Atmosphere and Part B, Wind Loads And Their Effects On Structures. Part A contains chapters on Atmospheric Circulations, The Atmospheric Boundary Layer, and Wind Climatology and Its Application to Structural Design. Part B consists of two sections. One section includes interesting and well-written chapters on Bluff Body Aerodynamics, Structural Dynamics, and Aeroelastic Phenomena. A second section is titled Applications to Design and it contains chapters on Along-Wind Tall Building Response, Across-Wind Tall Building Response, Across-Wind and Torsional Response, The Wind Tunnel as a Design Tool, Wind Induced Discomfort In and Around Buildings, and Tornado Effects. The coverage of topics by Simiu and Scanlan is not nearly so broad as that of Sachs, but the depth of coverage by the former is correspondingly greater. Numerous worked examples are distributed through the book by Simiu and Scanlan, but there are no problems at the ends of the chapters. All in all, however, these authors have succeeded admirably in producing an up-to-date text for the relatively new and still expanding field of wind engineering.

In summary it should be noted that both books have considerable merit. *Wind Forces in Engineering* by Peter Sachs contains a wealth of data (though much of it dates from a pre-1970 time frame) that is made available to the designer and that is coordinated with up-to-date engineering Codes of Practice. *Wind Effects on Structures* by Emil Simiu and Robert Scanlan represents a well-written and appealing new text for introducing wind engineering to graduate students and practicioners alike.

Applied Fluid Flow Measurement Fundamentals & Technology, by Nicholas P. Cheremisinoff, Marcel Dekker, Inc., Price: $23.75

REVIEWED BY RODGER B. DOWDELL

After having specialized in the field of flow measurement for thirty years, it is not often that I pick up a publication and learn some new facts. This book by N. P. Cheremisinoff is refreshingly different. His first two introductory chapters are excellent: not too much theory, but enough to present the concepts of Newtonian versus non-Newtonian fluids and the difference between the laminar and turbulent equations of flow. He even derives the law of the wall from Prandtl's mixing length theory in a page and a half. With these two chapter ingested, the practicing engineer should be able to calculate the pressure drops and design fluid systems.

Chapter 3 is devoted to pressure differential devices: the venturi tube, orifice and flow nozzle. The descriptions are excellent, and the reader can design a Herschel type venturi tube from the data given. However, this is not true for the orifice nor flow nozzle where the reader is given references for the design information. This chapter also sheds light on installation effects. The next two chapters are on positive displacement meters and mechanical flowmeters. Again these are well done with excellent tables on the choice of materials to use with various corrosive fluids.

Magnetic meters are described next, and this description is excellent right down to what materials should be used for the flow tube and electrodes. However more information could have been included on installation effects.

The final chapter on mass flow meters has a large omission in that no mention is made of the angular momentum principle, and meters based on this principle are being manufactured. However, this is a minor shortcoming when the book is viewed in its entirety. The 82 references will lead the reader to whatever additional information is required.

I highly recommend this book for engineers anxious to learn more about flow measurement.